Hybrid Ion-Kinetic, Fluid-Electron Modelling of Radial Plasma Flows in the Magnetospheres of the Outer Planets

Joshua Alexander Wiggs

Physics Department
Lancaster University
United Kingdom

This thesis is submitted in partial fulfilment of the requirements for the degree of Doctor of Philosophy

December 31, 2023

Declaration of Authorship

I, Joshua Alexander Wiggs, declare that this thesis titled 'Hybrid Ion-Kinetic, Fluid-Electron Modelling of Radial Plasma Flows in the Magnetospheres of the Outer Planets' and the work presented in it are my own. I confirm that:

- This work was done wholly or mainly while in candidature for a research degree at this University.
- Where any part of this thesis has previously been submitted for a degree or any other qualification at this University or any other institution, this has been clearly stated.
- Where I have consulted the published work of others, this is always clearly attributed.
- Where I have quoted from the work of others, the source is always given. With the exception of such quotations, this thesis is entirely my own work.
- I have acknowledged all main sources of help.
- Where the thesis is based on work done by myself jointly with others, I have made clear exactly what was done by others and what I have contributed myself.

Signed: _____

Date: _____

In dedication to Hazel Lee.
The brightest star in my night sky.

Abstract

Hybrid Ion-Kinetic, Fluid-Electron Modelling of Radial Plasma Flows in the Magnetospheres of the Outer Planets

Joshua Alexander Wiggs

The magnetospheres of the gas giants, Jupiter & Saturn, are both loaded internally with plasma. The source of this material in the Jovian system is the volcanic moon of Io and the icy moon of Enceladus in the Saturnian, creating the Io plasma torus and the Enceladus neutral torus. In both systems plasma is removed from these tori mainly via ejection as energetic neutrals and by bulk transport into the outer magnetosphere. The physical mechanism responsible for the bulk transport process is the radial-interchange instability (reviewed in §3).

In order to improve understanding of the bulk transport process a new hybrid kinetic ion, fluid-electron plasma model is constructed in 2.5-dimensions. The Jovian magnEtospheRIC kinetic-ion, fluid-electron Hybrid plasma mOdel, JERICHO, is detailed in §4 & 5. The technique of hybrid modelling allows for the probing of plasma motions from the scale of planetary-radii down to the ion-inertial length scale, considering constituent ion species kinetically, as charged particles, and forming the electrons into a single magnetised fluid continuum. Simulation results permit the examination of bulk transport on spatial scales not currently accessible with state-of-the-art models. To ensure JERICHO is physically accurate a series of physical benchmarks are examined in §6 and the parameter space within which it must be operated is identified.

Application to Saturnian magnetospheric system is presented in §7. Plasma injections are introduced and develop radial-interchange instabilities on spatial scales of 10^{-1} R_S. These motions create fingers of dense plasma interspersed with narrow tenuous plasma channels. A parameter survey is performed, varying the magnetic field strength & density of plasma injections. A potential link between the temporal scales of the instability and magnetic field strength is identified, however no correlation is found between either of these parameters and the spatial scales of the instabilities.

Acknowledgements

The completion of the work undertaken in the production of this thesis would not be possible without a number of mentors and collaborators or without the support provided by friends and family. Here I would like to indulge for a few brief paragraphs to thank them.

First, I would like to thank Dr. Chris Arridge for supervising this PhD and guiding me through the trials and tribulations encountered along the way. Over this course of the four years of this project the support provided has nurtured my scientific knowledge, enhancement my mathematical & computational abilities and allowed me to flourish into an independent researcher. It is safe to say that the work performed over the course of this project would not have been possible without this patient guidance.

Additionally, the support and guidance provided by Dr. Licia Ray over the course of my PhD studies has proved invaluable. Becoming a well rounded researcher requires more than the diligent investigation of interesting questions, it also needs you to be able to defend the results undertaken and disseminate the knowledge acquired to others. Whether through practice conference talks or in the labs, guidance provided has helped hone these skills.

A vast range of other PhD students, post doctoral researchers & academics at Lancaster University, specially within the physics department and Space & Planetary Physics Research Group, have both provided critique & guidance that have benefited the work in this thesis. But further they have provided the personal support and encouragement needed to get me to the completion of this PhD. Everyone in the B504 office over the course of this project has provided support in some-way, but in particular I would like to thank: Chris; George; Joe; Maria & Wayne.

PhD's do not just happen in the office, it requires a large amount of support (and patient understanding) from those around you. I would like to thank my family for all the personal support they have provided over the course of this PhD. Whether there to listen at the end of a long day or take my mind off matters and give me a break, without the help provided along the way the completion of this PhD would not have been possible. Teresa, John & Hazel Lee your nurture & guidance over the years have made it possible for me to complete this work. Harry, Lloyd & Nathan you have been the friends (and often source of tough love) that are needed to complete an undertaking of this magnitude.

Of course the personal support required to complete a PhD is not limited to colleagues & family. Sharon, Simon & Laura you each have my thanks for supporting me through this PhD. Ant, Tom & Joe you each have my thanks for often reminding to take a break from work.

I would like to thank Megan Bromiley who has been my constant companion throughout my PhD studies. I am sure at many points over the course of this process it has felt like you have been undertaking a PhD as much of me. Without your unfaltering partnership, support and motivation over the course of this project I would not have been able to complete it. You have often said it has felt like my head has travelled to Jupiter during this project, perhaps now it will able to visit Earth more often.

Finally, this work would not have been possible without the funding & support provided

by the Royal Society (RGF\EA\180320).

Contents

Declaration of Authorship **i**

Abstract **iii**

Acknowledgements **iv**

List of Figures **ix**

List of Tables **xxi**

Acronyms **xxii**

1 Introduction to Plasma Physics **1**
1.1 Space Plasma Physics . . . 2
1.1.1 Overview . . . 2
1.1.2 Drift Velocities . . . 5
1.1.3 Adiabatic Invariants . . . 8
1.1.4 Particle Distributions & Moments . . . 10
1.1.5 Generalised Ohms Law . . . 11
1.1.6 Plasma Parameters . . . 13
1.2 Modelling Plasma Physics . . . 17
1.2.1 Plasma Modelling Techniques . . . 20

2 Planetary Magnetospheres **25**
2.1 Overview . . . 25
2.1.1 Formation . . . 25
2.1.2 Structure . . . 29
2.1.3 Convection . . . 34
2.2 The Outer Planetary Systems . . . 36
2.2.1 Jovian System . . . 36
2.2.2 Saturnian System . . . 47

3 Radial Plasma Transport **57**
3.1 Theory . . . 58
3.2 Diffusion Models . . . 64
3.3 Observations . . . 66
3.4 Modelling . . . 75
3.5 Future Work . . . 80

4 Hybrid Modelling Numerics & Logic - A Recipe **82**
4.1 Model Equations . . . 83
4.2 Simulation via Numerical Differencing . . . 85

4.3 Main Loop Summary . . . 90

5 JERICHO - Model Description **92**
5.1 Overview & Computational Domain . . . 92
5.1.1 2.5-Dimensional Geometry . . . 93
5.1.2 Computed Domain Discretisations & Reference Frame . . . 96
5.1.3 Working in a Rotating Domain . . . 97
5.2 Macroparticle Motions & Moment Gathering . . . 99
5.2.1 Macro Particles . . . 99
5.2.2 Ionic Particle Motions . . . 100
5.2.3 Collecting Particle Moments . . . 101
5.2.4 Interpolating Fields . . . 103
5.3 Field Calculations and Numerical Differentiation . . . 104
5.3.1 Obtaining EM fields . . . 104
5.3.2 Numerical Differentiators . . . 106
5.3.3 Numerical Smoothing . . . 107
5.3.4 Low Density Regions . . . 108
5.3.5 Field Aligned Currents . . . 108
5.4 Initial Conditions & Particle Generation . . . 108
5.4.1 Domain Configuration . . . 109
5.4.2 Domain Population . . . 112
5.5 Boundary Conditions . . . 113
5.5.1 Periodic . . . 113
5.5.2 Hard (Specular) . . . 115
5.5.3 Open . . . 116
5.5.4 Recycle . . . 116
5.5.5 Inflow . . . 116
5.6 Architecture & Implementation . . . 117

6 JERICHO - Benchmarks & Validation **120**
6.1 Single Particle Motion . . . 121
6.1.1 Gyro-Motion . . . 121
6.1.2 ExB Drift . . . 123
6.1.3 ∇B Drift . . . 125
6.2 Energy Conservation . . . 126
6.3 Ion Acoustic Wave . . . 132

7 Application to Saturnian Magnetosphere **137**
7.1 A Saturnian Configuration for 7.5-9.5 R_S . . . 137
7.2 Simulation Results . . . 141
7.2.1 Links to Domain Resolution? . . . 150
7.2.2 Parameter Survey . . . 152
7.3 Discussion & Summary . . . 158

8 Summary **167**
8.1 Future Work . . . 170

Bibliography **172**

A JERICHO Variables **189**
A.1 Constants 189
A.2 Domain 189
A.3 Modelled Field Parameters 190
A.4 Modelled Particle Parameters 191

B Ion Equation of Motion in a Rotating Reference Frame **193**

List of Figures

1.1 The trajectories of ions (in blue) and electrons (in yellow) in four separate EM field configurations, with the directions of the fields shown to the left of these. Panel a) contains only an ion gyrating with a stationary guiding centre (indicated by a black dot) in a single component static magnetic field, b) shows both an ion & electron gyrating around a guiding centre drifting to the right (for both particles) via $\underline{E}\times\underline{B}$ drift, c) has the ion drifting to the left and the electron to the right with the guiding centres drifting due to some applied external force and d) the same directions of drift but a gradient in the magnetic field induces the drift. Adapted from Baumjohann and Treumann (1996). 5

1.2 View of the internal planetary field lines in the Jovian system obtained using a dipole field model by Ikuchi (Arridge and Wiggs, 2019). A planetary body is sat on a wireframe, constructed across the orbital plane. Four arrows can be seen emerging from the planet with the orange indicating the vector between the planetary centre and the Sun, red the rotation axis of the planet, blue the magnetic dipolar axis and green the orbital direction of the planet. Yellow field lines emerge from 6 locations equally spaced in longitude, these represent the magnetic field lines. Each of these sets contains 6 individual lines emerging from different latitudes. Another four green lines can be seen encompassing the planet, forming a set of concentric rings, these indicate the orbital paths of each of Jupiter's Galilean moons (Io, Europa, Ganymede & Callisto), small spheres represent the moons. . . 19

1.3 Description of which plasma modelling technique is appropriate for a typical magnetospheric plasma (n_i = 50 cm^{-2}, B = 50 nT & T_i = 100 eV) depending on the spatial & temporal length scales, L & T respectively, of the dynamics of interest. The ion & electron gyro-periods are indicated (Ω_i^{-1} & Ω_e^{-1}), as well as their gyro-radii (ρ_{te} & ρ_{ti}), with a t subscript indicating that typical thermal velocities have been used. For length scales below the ion gyro-radius ($< 10^2$ km) kinetic modelling is found appropriate, at much greater lengths ($> 10^4$ km) it is fluid (MHD) and for the lengths between (10^2-10^4 km) hybrid. Examining temporal scales shorter than the gyro-period ($< 10^0$ s) kinetic modelling is best suited, scales much greater than the ion gyro-period ($> 10^2$ s) are suited to fluid modelling and those between (10^0-10^2 s) are suited to hybrid (Winske and Omidi, 1996). . 21

2.1 A closed magnetosphere in the noon-midnight meridian plane with the solar wind entering from the left-hand side and encountering a planetary system in the centre. Solar wind flow is indicated by dashed white line and the different regions of space indicated by their colour. The interplanetary medium (light blue) is separated from the magnetosheath (dark blue) by the bow shock (green). Inside this the magnetopause (pink) contains the magnetosphere (varying shades of blue). The planetary magnetic field lines are shown surrounding (yellow). The arrow labelled R_{MP} indicates the distance from the planet to the magnetopause, often referred to as the stand-off distance (Bagenal and Bartlett, 2012a). 27

2.2 An open magnetospheric system, in the noon-midnight meridian plane, with the solar wind flowing towards the central planetary body from the left hand side. IMF field lines are seen and originate from outside the magnetospheric system. All magnetic field lines are indicated by solid black lines with arrows on them to indicate their directionality. Two seperatrices are indicated by dashed black lines, these confine different regions of the magnetosphere (Borderick, 2010). 29

2.3 A 3-dimensional overview of the terrestrial magnetospheric system. Solar wind can be seen flowing from the left-hand side of the diagram (white arrows). The position of the bow shock is indicated (solid white curve), created by the interaction between the magnetopause and the solar wind. Magnetic field lines are shown (black line with arrows) with the IMF also shown (recoloured white). The magnetopause (outer blue surface) extends outside the diagram to the right-hand side. A slice is taken from the magnetopause to allow for viewing of the internal magnetospheric structure, regions of which are indicated by different colours. The main current systems are shown (grey arrows). (Pollock et al., 2020) 30

2.4 Overview of the terrestrial magnetosphere in the noon-midnight median plane, with different regions of the magnetosphere coloured for emphasis. Solar wind enters from the left-hand side with the IMF shown outside the magnetopause (black lines with arrows), inside the magnetopause the planetary magnetic field is also indicated (black arrowed lines again). A pair of seperatrices (black dashed lines) are shown, with the outer indicating the bow shock and the inner the magnetopause. The magnetotail can be seen to taper as it increases in distance from the planet (round body). Reconnection events can be seen occurring between the IMF and planetary field at the sub-solar point, as well as in the magnetotail, with both field lines originating from the planetary dipole (Eastwood et al., 2015). 31

2.5 Structure of the Jovian magnetosphere, shown in the noon-midnight meridian plane, with the Sun to the left-hand side, hence the solar wind (red lines with arrows) arrives from the left. Interplanetary space (light green) can be seen outside the bow shock containing the IMF (white lines with arrows). The magnetosheath (green) is inside the bow shock (dark green line), further the magnetopause (dark purple) can be found inside bounding the magnetosphere (varying shades of blue). Magnetic field lines (white lines with arrows) are shown originating from the planetary body (red circle) and can be seen reconnection with the IMF in the lobes. The current sheet (yellow line) is indicated and the density of plasma inside the magnetosphere can be approximated by the darkness of blue (Bagenal and Bartlett, 2012b). 37

2.6 Comparison of acceleration provided by gravitational (blue) and centrifugal (orange) force/pseudo-force to material in the Jovian system from near the planets surface (1 R_J) into the outer magnetosphere (50 R_J). Gravitational force begins as the dominate and decreases with distance from the planet, inversely the centrifugal pseudo-force becomes larger as distance increases. At the critical value of approximately 2.2 R_J the two forces balance each other, indicated by the black dashed line. The magnitude of the accelerations are presented with the gravitational force acting in opposition to the centrifugal. 38

2.7 Two profiles of angular velocities of plasma in the Jovian magnetosphere as a function of distance given as a ratio to the planetary rotational velocity. $\Omega_J = 1$ represents rigid co-rotation with values greater than this indicating super co-rotational plasma and less than this indicating sub co-rotation. One profile (in blue) shows the variation in co-rotation by analysing the inertial balance of the system utilising a dipolar planetary magnetic field (Hill, 1979), the other (in orange) shows an updated profile, corrected by the inclusion of non-ideal terms in the planetary field model (Pontius Jr., 1997). Red dashed line indicated position of the outer edge of Io's plasma torus, placed at 6 R_J. Millas (2022) calculated profiles and provided data. . 39

2.8 Slice through the noon-midnight plane of the Jovian system, containing the Galilean moon Io and a cross-section of the associated plasma torus. Io is on the right-hand side of the plasma torus with the neutral cloud created by volcanic activity on the surface shown sing black dots. The plasma torus is seen on both the left and right-hand side of the central planetary body, with the cold & warm regions indicated. Additionally, approximate density gradients are indicated with denser areas shaded in darker. Labels indicate the approximate electron densities in the indicated regions, along with the corresponding plasma species and energies. The magnetic & spin axis are represented by arrows through the centre of the planetary body (adapted from Thomas et al., 2004). 41

2.9 Two flow diagrams detailing the transport of both material and energy through the Io plasma torus determined using a 0-dimensional neutral cloud model. Both diagrams follow the same flow structure, with the particle flow detailing the proportion of the total neutral material ionised to form the torus as a percentage of sulphur and oxygen atoms. The box contains (with hot electrons added) the neutral atoms in the model (S, O) along with the ion species included (O^+, O^{++}, S^+, S^{++}, S^{+++}) and electrons (e^-). Finally, the outflow mechanisms are indicated along with the percentage proportion of material removed via these. Beneath the energy flow through the Io plasma torus is shown, with inflow from ions freshly picked up after creation as well as from the addition of hot electrons. The energy within the torus is then transferred between the ions and electrons until a steady state is reached. Energy flows out of the system via a number of processes, with the amount contained within the two mechanisms associated with the removal of material given. Delamere and Bagenal (2003) (left), Delamere et al. (2007) (right) 45

2.10 Plasma flows within the Jovian magnetodisc as viewed from above (left) and in a series of meridional projections along the numbered solid lines (right). Double-tailed arrows indicate plasma flows in both panels. Field lines are indicated by solid lines in the meridional projections. Dotted and dashed lines (left) indicate the magnetopause and critical Alfven surface respectively. Magnetic X- and O-lines are indicated on the left-hand panel (Vasyliunas, 1983). 46

2.11 Side view of the Saturnian magnetodisk with solar wind (orange arrows) entering from the left. Magnetic field lines (in black) belonging to the IMF & the planetary field are shown. The magnetopause (purple surface) surrounds the planetary body (brown body) with a slice removed to allow for direct viewing of the contented magnetosphere (blue). Saturn is shown with aurorae present at the magnetic poles, the associated magnetotail extends in the anti-sunward direction to right-hand side (Bagenal, 2005). 47

2.12 Comparison of acceleration provided by gravitational (blue) and centrifugal (orange) force/pseudo-force to material in the Saturnian system from near the planets surface (1 R_S) into the outer magnetosphere (50 R_S). Gravitational force begins as the dominate and decreases with distance from the planet, inversely the centrifugal pseudo-force becomes larger as distance increases. At the critical value of approximately 1.9 R_S the two forces balance each other, indicated by the black dashed line. The magnitude of the accelerations are presented with the gravitational force acting in opposition to the centrifugal, directed towards the planets centre of mass. 49

2.13 Radial profile of the ratio of local plasma azimuthal velocity (ω) to co-rotational velocity (Ω_S) as a function of radial distance (ρ) in Saturnian planetary radii. Cassini mission data (black square) is input into the physical model utilised, as well as data from the Voyager mission (grey triangles). Thicker dark grey line, between $\approx 5 - 10$ R_S, is an empirical fit obtained by Wilson et al. (2008) using a subset of the data used by Achilleos et al. (2010) to obtain the full fit presented (thin black line). General trend of the fit indicated rigid co-rotation until approximately 5 R_S, this then begins to drop until 6 R_S where the plasma azimuthally accelerates again, recovering until approximately entering rigid co-rotation again at 15 R_S. After this second maximum then co-rotation ratio drops almost linearly until 27.5 R_S where a minimum of 0.6 ω/Ω_S is reached (Achilleos et al., 2010). 50

2.14 A flow diagrams detailing the transport of both material and energy through the Saturnian neutral torus as determined using a 0-dimensional neutral cloud model. Particle flow indicates the inflow of neutral material into the torus. The box contains (with hot electrons added) the neutral atoms & molecules included in the model (H, O, OH, H_2O) along with the ion species included (H^+, O^+, O_2^+, OH^+, H_2O^+, N^+) and electrons (e^-).The outflow mechanisms are indicated along with the percentage proportion of material removed via these also shown. Beneath the energy flow through the neutral plasma torus is shown, with inflow from ions freshly picked up after creation as well as from the addition of hot electrons. The energy within the torus is then transferred between the ions and electrons until a steady state is reached. Energy flows out of the system via a number of processes, with the amount contained within the two mechanisms associated with the removal of material given Delamere et al. (2007). 53

2.15 A flow diagrams detailing the transport of both material and energy through the Saturnian neutral torus as determined using a 0-dimensional neutral cloud model. Particle flow indicates the inflow of neutral material into the torus, with number density indicated inside the arrow and rate of total mass added below. The box contains the neutral atoms & molecules included in the model (O, H, H_2O, OH, H_3O, H_2) along with the ion species included (O^+, O^{++}, H^+, H_2O^+, OH^+, H_3O^+, H_2^+) and electrons (e). The outflow mechanisms are indicated along with the percentage proportion of material removed via these and the amount of mass that corresponds to per second. Beneath the energy flow through the neutral plasma torus is shown, with inflow from ions freshly picked up after creation as well as from the addition of hot electrons, the quantity of energy added by each of these processes is detailed below their corresponding arrow. The energy within the torus is then transferred between the ions and electrons until a steady state is reached. Energy flows out of the system via a number of processes, with the amount contained within the two mechanisms associated with the removal of material given, again quantities of total energy attributed to these are indicated below the arrows. Adapted from Fleshman et al. (2010). 54

2.16 Plasma flows in the equatorial plane of the Saturnian magnetosphere, the Sun is located below the figure. The planetary body with the dayside (white) and the night (black) is shown. The magnetopause surface (black line) is partially broken at its front by a series of X's. Inside magnetospheric plasma flows are indicated (solid and dashed arrowed black lines). Seperatrices (dashed black lines) are presnet between regions of separate dynamics. X lines related to the Dungey & Vasyliunas cycles are indicated, along with their corresponding O-line. A P-line is also shown which indicated the outer edge of a created plasmoid (Cowley et al., 2003). 55

3.1 Configuration for the interchange instability in a general planetary magnetosphere with a dipolar field, planetary field lines are black curved lines. Here it is shown that when interchange motions occur that the lower tube of force (magnetic flux tube), A, exchanges places with the upper tube, B, whilst unchanging the overall magnetic topologies. The planetary body can be seen as the circle on the left-hand side with a line through its magnetic dipole axis, from this the distance of the tubes is indicated by R_A & R_B (Gold, 1959). 59

3.2 Flow pattern created by continual random fluctuations of a plasma source to allow for the net outwards convection of plasma whilst generally preserving the magnetic topology of the region. The base of the wedge is at the Io plasma torus ($\sim$6 R_J) and extends to an arbitrary distance into the Jovian inner magnetosphere. Parcels of dense plasma are indicated by dark blue contours and lighter blue contours indicate lighter plasma parcels. Streamlines are shown in red to indicate the general flow pattern of material through the region, with arrows showing the direction of these flows. After Southwood and Kivelson (1989). 63

3.3 Configuration of geometry used for the construction of a diffusive model of plasma transport in a plasma environment like that surrounding Io, in which the flow pattern is random-like. The change in latitude of the inner & outer edge of a cell (semi-analogous to a flux tube) is seen as $\Delta\theta$ with the field lines traced into the planetary ionosphere. The subdivision of a eddy located at $R_J L$ into 4 cells is seen, with each cell the size ΔL and a height $\frac{1}{2}H^*$ (i.e. half the height of the plasma sheet). Adapted from Siscoe and Summers (1981). 65

3.4 Magnetometer data from Galileo on 7$^{\text{th}}$ December 1995 with the each component (r, θ, ϕ) in SIII coordinates shown along with the magnitude. a) shows the data between 17:30-17:35 UT, corresponding to radially distances of 6.08 R_J & 6.02 R_J. An anomalous period of data is shaded. b) shows the data between 17:33:45-17:44:30 UT. Entry & exit from the period of anomalous reading (17:34:08-17:34:18 UT) is indicated in the panel containing the magnitude of the field strength (Kivelson et al., 1997). 66

3.5 Measurements from the EPD & PWS instruments on Galileo on the 7$^{\text{th}}$ December 1995 between 17:33-17:36 UT, the translation into various other coordinates is shown below. Initial seven panels contain the count rates from various channels of EPD, with the label to the right of the plot corresponding to table 3.1. The bottom panel contains a spectrogram from PWS with the power indicated by the colour bar on the right (Thorne et al., 1997). 68

3.6 PWS & EDP data from the Galileo mission on 7$^{\text{th}}$ December 1995 between 17:00-17:45 UT. Top panel contains a spectrogram from PWS, with two events marked at 17:09 & 17:34 UT, the power is indicated by the colour bar to the right. The bottom two panels contain particle count rates from EPD, two channels, F0 & B1, are shown which both correspond to high energy electrons Bolton et al. (1997). 70

3.7 EPD measurements from Galileo on 353$^{\text{rd}}$ day, 18th December, of 1996 between 13:00-22:00 UT. Three 'injection' events are indicated by the curved black lines through the eight EPD electron channel intensities, with associated energies indicated on the left (Mauk et al., 1997). 71

3.8 Configuration of plasma in the equatorial plane of the Jovian system. PSD decreases as radial distance decreases, such that two surfaces can be creates with PSD1 encompassing PSD2, if the interface between these is perturbed then a plasma injection is generated and convects inwards moving through the azimuth to create a spiral Mauk et al. (2002). 72

3.9 Measurements from Cassini on the 30$^{\text{th}}$ October 2005 between 7:30-7:50 UT, of interest in the injection event with onset at ∼7:35 UT and lasting ∼5 minutes. Panels 1 & 2 contain electron fluxes & ion count rates respectively, over a broad range of energies with magnitude of count given by the colour bar to the right, additionally a black dotted line is included in panel 2 to indicate the ion detector's look direction. Panel 3 contains the magnetic field strength. Panel 4 contains electron number density (in blue) and temperature (in red), calculated from the CAPS data. Panel 5 contains a spectrogram from RPWS, with the upper hybrid (ω_{uh}) & electron cyclotron (ω_{ce}) frequencies marked, power is given by the colour bar to the right (Rymer et al., 2009). 73

3.10 Occurrence rate of the total number of interchange events observed at varying radial distances, binned at integer distance values 5-12 R_S, between 2005-2016. Total number of events at a radial distance is indicated by the dark blue bar, with confidence intervals shown, these are then subdivided into 4 categories (light blue, yellow, orange & red bars) using the mean partial pressure of the observed event, again with confidence intervals shown. It can be seen that the largest number of events are at 7-9 R_S. Spacecraft dwell time at a particular radial distance interval throughout the examined time-frame is indicated by the grey bars, this can be seen to be well distributed between each of the distance intervals (Azari et al., 2018). . . . 74

3.11 Flow diagram detailing the RCM's logical loop in order to progress temporally. The top panel (shaded dark grey) represents the magnetospheric portion of the model and the bottom (light grey) the ionospheric. The quantities both calculated (rectangles) and used as inputs (ovals) are included with black lines showing were inputs are inserted and the white arrows where computed values are passed. The magnetic field that connects the magnetosphere to the ionosphere is in the middle and is pre-defined though can vary in time. Adapted from Sazykin (2000). 76

3.12 Evolution of cold plasma edges associated with initial asymmetric longitudinal configuration for the Io plasma torus using the RCM-J. Coordinates are given in terms of the latitude & longitude that flux tubes containing plasma parcels map down to in the planetary ionosphere, this corresponding to modelling the entire torus (0-2 π) between 5-9 R_J. 4 panels are shown containing snapshots of the configuration at 0, 15, 20 & 22 hours, from top left to bottom right. The formation of several interchange fingers can be clearly, bent in the azimuthal direction against corotation Yang et al. (1994). 78

3.13 Outbreak of interchange fingers in the RCM-S with entire azimuthal domain (0-2 π) and inner boundary (2 R_S) to 12 R_S shown. A series of 6 snapshots are shown at 10, 22:25, 24, 26, 29 & 30:30 hours (labelled a, b, c, d, e & f respectively), from top left to bottom right. Colour of contour indicates the flux tube ion content (ions per Weber) with values indicated in colourbar on right of panel (Liu et al., 2010). 79

4.1 Logical cycle utilised to form a hybrid-PIC plasma model. A pair of concentric rings, the inner has fewer elements and contain a summary of the 3 major steps that are required to progress the model. The outer ring contains 8 more detailed elements, not equally distributed between the 3 summarised elements of the inner ring. Spokes can be seen to connect the more detailed step to the large summarised element it belongs in, colour is also used to indicate this. The time step within a logical cycle at which the detailed element occurs is shown at the base of its associated spoke. 91

5.1 Schematic of the planetary configuration considered when forming JERICHO's geometry. A meridian cross-section of the Jovian system with the Sun off to the right-hand side, the magnetic axis has been aligned with the planetary spin axis. The ionosphere can be seen surrounding the planetary body as a blue ring, with the magnetic field lines emerging through this region shown as yellow lines with arrows indicating orientation. The magnetospheric region of interest, the plasma sheet, is highlighted by the purple box, inside which the moons of Io, Europa, Ganymede & Callisto are shown. Credit: Arridge and Wiggs. 93

5.2 Schematic showing the 2.5D geometry exploited to construct JERICHO. Panel a) shows a side view of the configuration with the ionosphere unwrapped from the planet and flatten into a 2D plane represented by the blue line under the planetary surface, from this view the line shown is 1-dimensional with the second dimension extending into the page. Yellow field lines indicate the magnetic field, seen now to be confined to a single dimension orthogonal to the ionosphere. These dangle down, connecting into the purple magnetosphere, which has also been reduced to a 2D plane. b) shows the same set up from a 3D perspective. In this the 2d planes can be seen in both dimensions, situated on top of one another connected by the yellow field lines. In both panels the Galilean moons can be seen indicated in the magnetospheric planes. Credit: Arridge and Wiggs. 95

5.3 A schematic of the current system modelled by JERICHO to examine RI motions. The planetary body is seen on the left-hand side encompassed by a purple ionosphere. From the body the spin (and hence magnetic) axis is indicated, with the direction and rate of planetary rotation shown by Ω. Black magnetic field lines connect the ionosphere to the magnetospheric region of interest, in brown. The plasma in this region corotates with the planet giving it a flow velocity into the page, $\underline{U}$. The currents created by radial plasma transport are indicated by the blue lines, with arrows to indicate direction, FACs are shown flowing in two locations for simplicity, however this occurs along all magnetic field lines. Credit: Arridge and Wiggs. 96

5.4 A depiction of the computational domain constructed to model plasma in JERICHO. The discretised locations of the EM field can be seen as a series of regular points shown as blue dots, joined together by black horizontal and vertical lines to create the grid over the domain. The particles are shown as red dots, these can occupy any location in the domain and hence can be seen filling the grid cells constructed. Communicating particle distributions to the grid is essential for self-consistently progressing the simulation, therefore a method is needed to collect particle moments on the grid points, represented by the grey dot lines and a's in the bottom right cell. 97

5.5 2-dimensional representation of a macro-particle, with the red circle indicating the exterior boundary (or skin) of it and the green dots representing the constituent ions inside. 99

5.6 The index system used to identify and construct the cell which a particle (red dot) is located within, with the EM grid points shown as blue dots. Indexes i, j give the 'bottom left' grid point of the cell, with the 3 other vertices then located using $i+1, j$, $i+1, j+1$ & $i, j+1$. 101

5.7 First-order area weighting used to collect the moments of a particle, shown as a red dot, on the location of EM field discretisation, the blue dots. This area weight scheme subdivides a cell into 4 quadrilaterals, the areas of each are then used to determine the amount of a particle's moment allocated to each grid point. The closer a particle is to a point, the more moment it should be allocated, hence the area opposite a point is used to determine its portion of the moment. Therefore, a→A, b→B, c→C & d→D. 102

5.8 Panels showing the 5 different boundary conditions available for selection in JERICHO. Each shown is at a edge of the model domain, with the boundary under examination highlighted with a coloured line, particles are shown as red dots with grey lines showing their path and EM field discretisation locations in blue. Green dots indicate the creation of new particles as part of the boundary condition scheme. Panel a) shows a periodic boundary, b) a hard (specular) boundary, c) a outflow boundary, d) a recycle boundary and e) a inflow boundary. 114

5.9 Software architecture of the JERICHO software suite with the containers constituting the applications split into three categories and the flow of information between these indicate. The input category holds the containers that require a user to interact with before initialising a simulation run, JERICHO holds the core of the model and Outputs holds the containers associated with managing and writing data out of the model. The flow of information back into JERICHO from output indicates the capability to restore a simulation from the particle & EM field data. 117

6.1 Ray trace of a single ion's motions over 240 s, $\approx 3.6 T_g$, through a model domain containing a uniform magnetic field. Spatial coordinates are transformed using the analytic solution for the ion gyro-radii with the origin shifted to the centre of the particle's gyro-motion, indicated by a black cross and lines. 4 separate traces are visible with the blue, orange, green and red lines corresponding to a temporal resolution of 15%, 1.5%, 0.15%, 0.015% of the ion's gyro-period respectively. 122

6.2 Ray trace of a single ion's motion over 240 s through a model domain containing both a uniform magnetic and electric field, shown in the top left. Motions through the spatial domain are shown in (a), with coordinates transformed using the gyro-radii and the origin shifted to the initial guiding centre, and their corresponding position in velocity space in (b), with coordinates transformed using the ion's $\underline{\mathrm{E}} \times \underline{\mathrm{B}}$ drift velocity. A set of 4 traces can be seen in both (a) and (b) with the blue, orange, green and red lines corresponding to a temporal resolution of 15%, 1.5%, 0.15%, 0.015% of the ion's gyro-period respectively. The black line in (a) indicates the guiding centre of the ion as it moves through the domain and in (b) the black cross shows the centre of the ion's path through velocity space. 124

6.3 Ray trace of a single ion's motions over 240 s through a model domain containing a magnetic field with a uniform gradient, shown in the top left. Spatial coordinates are transformed using the analytic solution for the average ion gyro-radii with the origin shifted to the centre of the particle's initial guiding centre, indicated by a black dotted line. 4 separate traces are visible with the blue, orange, green and red lines corresponding to a temporal resolution of 10%, 1%, 0.1%, 0.01% of the ion's average gyro-period respectively. 125

6.4 Evolution of the electric field ($|\underline{E}|$, top row), ion charge (q, middle row) and magnetic field ($|\underline{B}|$, bottom row) over a period of 50 Ω_i^{-1} ($\sim$1.5 hr) with a 0.005 Ω_i^{-1} ($\approx$0.17 s) time-step (Δt). Modelled domain is from 49-50 $\mathrm{R_J}$ in both the x & y-coordinates with EM fields discretised on a 100×100 grid containing 50 macroparticles per grid cell (N_{PPC}), initialised with 0.01 β_i . 129

6.5 Percentage change in total energy (in $\%\times10^{-3}$) stored within the EM fields obtained in the simulation shown in figure 6.4 as it progresses. The change can be subdivided into 2 distinct epochs, switching at $\approx$20 Ω_i^{-1}, with these bounded by the vertical grey lines. Change between 0-20 Ω_i^{-1} relates to shot noise, where as change after this period, >20 Ω_i^{-1}, is related to centrifugal force. 130

6.6 Form of a perturbation with an amplitude of 10 m s^{-1} used to introduce an ion-acoustic wave within a simulated domain of 100×100 m. Panel a) shows the form in purely the x-domain and b) shows the contour of the perturbation in both the x & y-domains. 133

6.7 Automated detection of 3 ion acoustic waves moving through the model domain. Rate of change of mass density shown, with 1 s of simulation time against the line-of-sight integrated x-domain. The wave is identified by select points within the integrated domain that are $> 10^2$ above the median run value. The domain is then decomposed into 3 subdomains based on when the waves are launched with the wave speed obtained using linear regression on the points identified within an individual subdomain. . 134

6.8 Rate of change in mass density across a 100×100 m domain, line-of-sight integrated into x-plane, over a 1 s period, from 2 to 3 s, within which 3 ion acoustic waves are generated. Each panel shows a separate simulation run in which the magnitude of the initial perturbation is increased, from top left to bottom right. Red lines fit the path of each ion-acoustic wave front through the domain. 135

6.9 Speed at which ion acoustic wave front propagates across a 100×100m domain against the pressure in the region from which it was generated. 5 separate simulations are utilised with each containing 3 wave fronts, these 3 fronts are combined and averaged to yield a single value indicated by the blue crosses. A first-order polynomial is fitted to these values, the gradient of which is equal to γ_e determined to be 1.45 ± 0.28. The uncertainty in this value is a product of determining the path of the wave front. This is compared to a fluid with a γ_e equal to 2, indicated by the orange line. . . . 135

7.1 Profiles of plasma density and β as a function of radial distance in the Saturnian magnetosphere obtained using steady state modelling techniques to fit measurements made using in-situ spacecraft. a) is obtained by Persoon et al. (2020) using a diffusive equilibrium model and shows contours of water group ion density as both a function of radial distance and height from the equilibrium plane. b) is obtained by Wilson et al. (2017) using a forward modelling technique showing profiles of water group & hydrogen ion densities purely as a function of radial distance (top panel) and the profile of associated plasma β's (bottom panel). 140

7.2 BCs utilised in the configuration of the simulation domain in which RI instabilities are examined. The grid with red particles in the centre represents the domain constructed by the model framework with coloured bars placed on the edges to indicate BC. The x_{min} & x_{max} (left & right) edges have periodic boundaries (blue), y_{min} (bottom) has an inflow (green) and y_{max} has an open (red). Coloured arrows represents the general flow of particles at these edges. 141

7.3 Evolution of ion charge distribution (q) within a 2×1 R_S domain placed at 7.5-9.5 R_S. 21 panels, separated by 50 Ω_i^{-1}, show snapshots of the charge distribution over the course of the simulated 1000 Ω_i^{-1} period. Over this period 2 plasma 'injections' are introduced from the bottom boundary and can be seen to move through the y-domain (radially outwards) inducing RI instabilities both on their leading and trailing interfaces. 143

7.4 Evolution of electric field strength ($|\underline{E}|$) within a 2×1 R_S domain placed at 7.5-9.5 R_S. 21 panels, separated by 50 Ω_i^{-1}, show snapshots of the electric field strength over the course of the simulated 1000 Ω_i^{-1} period. The effects of two plasma 'injections' introducing RI instabilities on the electric field can be seen. 144

7.5 Evolution of the magnitude of current densities ($|\underline{J}|$) within a 2×1 R_S domain placed at 7.5-9.5 R_S. 21 panels, separated by 50 Ω_i^{-1}, show snapshots of the current densities over the course of the simulated 1000 Ω_i^{-1} period. The introduction of 2 plasma 'injections' from the bottom boundary can be seen to create RI instabilities on both the leading of trailing edges of these regions. 145

7.6 Induced magnetic effects (B_{z1}) within a 2×1 R_S domain placed at 7.5-9.5 R_S. 21 panels, separated by 50 Ω_i^{-1}, show snapshots of the perturbed magnetic field over the course of the simulated 1000 Ω_i^{-1} period. The effects induced by 2 plasma 'injections' introducing RI instabilities within the magnetic field can be seen. 146

7.7 A series of snapshots at 0, 250, 500 & 750 Ω_i^{-1} for ion charge distribution, electric field strength, magnitude of current densities and induced magnetic effects taken from the simulation run contained within figures 7.3-7.6. . . . 147

7.8 Two snapshots of ion charge distribution taken at 300 (left) & 650 (right) Ω_i^{-1} from the simulation run contained within figures 7.3-7.6. Key features related to the description of injected plasma region, as well as the developed RI motions are labelled. 148

7.9 Sketch of how plasma dynamics associated with developing RI motions effect EM fields, domain & magnetic configuration can be seen at the top of the panels. On the injection interface (left) it can be seen how the development of plasma fingers with channels in-between create oppositely directed electric effects. The deflection of the fingers on the leading & trailing edge (right) is caused by drifts induced by gradients in the magnetic field. Credit: Arridge and Wiggs. 149

7.10 Evolution of ion charge distribution (q) within a 2×1 R_S domain placed at 7.5-9.5 R_S utilising an increased spatial resolution of 500×250 cells. 21 panels, separated by 50 Ω_i^{-1}, show snapshots of the charge distribution over the course of the simulated 1000 Ω_i^{-1} period. RI motions are triggered on the leading and trailing edge of plasma injections. 151

7.11 Ion charge distribution at 700 Ω_i^{-1} taken from simulation performed in figure 7.10. Red lines highlight the large scale structures that smaller scale RI motions are coalescing into, found to be on length scales of $\sim 10^{-1}$ R_S. . 152

7.12 Evolution of ion charge distribution (q) within a 2×1 R_S domain placed at 7.5-9.5 R_S with the planetary dipolar field strength modified by a factor of $\mathcal{K} = 0.5$. 21 panels, separated by 50 Ω_i^{-1}, show snapshots of the charge distribution over the course of the simulated 1000 Ω_i^{-1} period, equating to $\approx$2 hrs. 154

7.13 Evolution of ion charge distribution (q) within a 2×1 R_S domain placed at 7.5-9.5 R_S with the planetary dipolar field strength modified by a factor of $\mathcal{K} = 1.5$. 21 panels, separated by 50 Ω_i^{-1}, show snapshots of the charge distribution over the course of the simulated 1000 Ω_i^{-1} period, equating to ≈0.75 hrs. 155
7.14 Evolution of ion charge distribution (q) within a 2×1 R_S domain placed at 7.5-9.5 R_S with the planetary dipolar field strength modified by a factor of $\mathcal{K} = 2.0$. 21 panels, separated by 50 Ω_i^{-1}, show snapshots of the charge distribution over the course of the simulated 1000 Ω_i^{-1} period, equating to ≈0.5 hrs. 156
7.15 Evolution of ion charge distribution (q) within a 2×1 R_S domain placed at 7.5-9.5 R_S with the density of plasma injections at 0-200 & 400-600 Ω_i^{-1} decreased by a factor $\mathcal{L} = 0.5$. 21 panels, separated by 50 Ω_i^{-1}, show snapshots of the charge distribution over the course of the simulated 1000 Ω_i^{-1} period. 159
7.16 Evolution of ion charge distribution (q) within a 2×1 R_S domain placed at 7.5-9.5 R_S with the density of plasma injections at 0-200 & 400-600 Ω_i^{-1} increased by a factor $\mathcal{L} = 5.0$. 21 panels, separated by 50 Ω_i^{-1}, show snapshots of the charge distribution over the course of the simulated 1000 Ω_i^{-1} period. 160
7.17 Evolution of ion charge distribution (q) within a 2×1 R_S domain placed at 7.5-9.5 R_S with the density of plasma injections at 0-200 & 400-600 Ω_i^{-1} increased by a factor $\mathcal{L} = 10.0$. 21 panels, separated by 50 Ω_i^{-1}, show snapshots of the charge distribution over the course of the simulated 1000 Ω_i^{-1} period. 161
7.18 Slices of ion charge taken on the leading edge of the first plasma injection from the simulation performed in figure 7.3. Each slice is comprised of the grid points at the indexes closest to the position in the y-domain that the front is calculated to occupy, with simulation time between 200-850 Ω_i^{-1} shown against the simulated x-domain. The perturbations that develop into fingers can be seen with initially wide regions of tenuous plasma that narrow to form diagonal tracks with a width of ∼0.02 R_S. 162
7.19 Snapshot at 650 Ω_i^{-1} selected from the simulation performed in figure 7.3 with panel a) containing the ion charge distribution and the red line at 9 R_S indicating where the cuts contained in panels b)-d) are taken. b) shows the ion charge against the simulated x-domain. c) shows the magnetic field (B_z) between 0.1-0.9 R_S with the average field value across these locations subtracted. Finally, d) shows the induced magnetic effects (B_{z1}) and is placed below b) to allow for direct comparison with ion charge distribution. The red dashed lines show the location of the isolated region of tenuous plasma in the snapshot. 164
7.20 Streamlines of ion flow velocity across the leading edge of the plasma injection contained within the simulation performed in figure 7.3 at 650 Ω_i^{-1}. Ion charge distribution is also shown to allow for comparison between the ion flows and the structures created on the edge. Ion flow velocities are transformed into a reference frame approximately at rest with the flows on the leading edge to prevent the bulk motion radially outwards overwhelming the finer dynamics created by RI instabilities, generating the clearly visible structures. 165

List of Tables

2.1 Summary of relevant planetary parameters for the Jovian system and the interplanetary medium, in the form of the solar wind, at Jupiter's orbital distance. Parameters are presented as a ratio to their corresponding terrestrial values in order to highlight key similarities and difference between the magnetospheric systems. Jovian parameters are obtained in System III coordinates as collated by Williams (2021a) and solar wind parameters are obtained by Slavin et al. (1985). 38

2.2 Summary of relevant planetary parameters for the Saturnian system and the interplanetary medium, in the form of the solar wind, at Saturn's orbital distance. Parameters are presented as a ratio to their corresponding terrestrial values in order to highlight key similarities and difference between the magnetospheric systems. Saturnian parameters are obtained in System III coordinates as collated by (Williams, 2021b) and solar wind parameters are obtained by (Slavin et al., 1985). 48

3.1 Selected channels from PWS on Galileo with particle channel labels, the species of the particle and their corresponding energy ranges. Additionally, the Larmor radius, gradient drift speeds and average bounce times are shown for these particles at 6.03 R_J. These channels are used in figure 3.5, with data for count rates of specific particles using the particle channel labels as identifiers (Thorne et al., 1997). 67

7.1 Comparison of key parameters considered when selecting, between Jupiter & Saturn, the initial system in which to simulate RI motions. Detailed overviews of the planetary systems can be found in §2.2.1 & 2.2.2. 138

Acronyms

BC Boundary Condition

CAM Current Advance Method

CAPS Cassini Plasma Spectrometer

CCMC Community Coordinated Modeling Center

CFL Courant-Friedrichs-Lewy

CHEMS Charge Energy Mass Spectrometer

EM Electromagnetic

ENA Energetic Neutral Atom

FAC Field Aligned Current

EPD Energetic Particles Detector

HPC High Performance Computing

IC Initial Condition

IMF Interplanetary Magnetic Field

JEMF JERICHO ElectroMagnetic Fields

JERICHO Jovian Magnetospheric Kinetic-Ion, Fluid-Electron Hybrid Plasma Model

JSON JavaScript Object Notation

KH Kelvin-Helmholtz

LFM Lyon-Fedder-Mobarry

MHD Magnetohydrodynamics

MMS Magnetospheric Multiscale Mission

ODE Ordinary Differential Equation

PDF Probability Density Function

PIC Particle-In-Cell

PSD Phase Space Density

PSP Parker Solar Probe

PWS Plasma Wave Subsystem

RAM Random Access Memory

RCM Rice Convection Model

RCM-J Rice Convection Model altered for Jupiter

RCM-S Rice Convection Model altered for Saturn

RI Radial Interchange

RPWS Radio Radio and Plasma Waves Sensor

RT Rayleigh-Taylor

SDO Solar Dynamic Observatory

SI International System

SIII System III

Stereo Solar Terrestrial Relations Observatories

Chapter 1

Introduction to Plasma Physics

In an ever increasing spacefaring age, our knowledge of perhaps our final frontier continues to expand rapidly as space-probes survey the solar system and beyond. Examining the medium that our universe is made from, it is found that the most prevalent state-of-matter is in fact plasma, making up over 99% of our observable universe. A striking example of a plasma construct rises and sets every day in our sky, the Sun, and in fact all stars, are comprised of this state-of-matter. However, probing the regions at the top of planetary atmospheres, and above, reveals an abundance of plasma and further this substance is found to tenuously fill inter-planetary space. Therefore, it is not surprising that when comprehending the machinations of our universe, even localised to individual planetary systems within our own solar system, it is essential to first understand the physics of plasmas.

In our solar system many planets internally generate strong magnetic fields which can be simply approximated as dipolar fields. This generated field interacts with the stream of particles continuously ejected from our Sun, the solar wind, balancing the dynamic pressure of the wind with the magnetic pressure of the planet's field to create regions of space surrounding these planets known as intrinsic magnetospheres. Of the eight recognised planets in our solar system six possess magnetic fields large enough to enter the class of the magnetised planets, these are: Mercury, Earth, Jupiter, Saturn, Uranus and Neptune. Each of these planets possess a magnetosphere, though the size, shape and dynamics of the complex regions varies vastly between them.

Our own planet, the Earth, is a member of the group of magnetised planets and therefore also the owner of an intrinsic magnetosphere. This is an important region of space as, focusing terrestrially, it acts to protect life and electronics on the ground and in orbit from harmful radiation that bombards us continuously from all directions. We can see evidence of this protection from the ground, at higher latitudes, by looking to the sky at night and witnessing the spectacular aurora borealis. Our planetary magnetic field causes charged particles to precipitate down and interact with molecules in our atmosphere, generating the light show. Looking to the stars in our sky once again, we find that our own planet is not unique in its possession of this light show, in fact all the magnetised planets, other than Mercury, have been observed to possess their own aurora's tied to their magnetospheres.

With its proximity and the convenience of data acquisition, our terrestrial magnetosphere is the most studied and best understood in the solar system. That is not to say that extra-terrestrial magnetospheric mechanisms have been ignored, rather it reflects the historic difficulty in analysing these regions. However, with the ever increasing sensitivity of terrestrial astronomical equipment and the advent of spacefaring probes able to travel to other planets in our solar system, measurements of and from these systems has become increasingly available. This has allowed insights that have vastly improved our

understanding of other-worldly magnetospheres.

Despite the ever increasing amount of data collected from magnetospheres at other planets, there are still profound limitations in the analysis that can be undertaking purely observationally. Looking at the gas-giants, Jupiter and Saturn (the classification of planet of particular interest in this thesis), outside of fly-bys by missions such as Pioneer and Voyager, there have been but two probes orbiting Jupiter for significant lengths of time, Galileo & Juno, and one at Saturn, Cassini. With both of Jupiter's orbiters in the system at different times it is only possible to analysis single point measurements inside the vast space of these magnetospheres.

Therefore, it is necessary to utilise techniques outside of remote & in-situ measurement taking in order to examine the physical dynamics and mechanisms at work in these other-worldly systems. A powerful technique for comprehending and exploring phenomenon that we are unable to direct observe is of course that of constructing a numerical description in order to explore through the medium of mathematics. However, early in the discovery and examination of magnetospheres it was determined that the construction of a complete set of equations able to exactly describe the entire system was unfeasible due to their complexity. Rather, simplification and assumptions must be utilised in order to form physics-based numerical models that could be used to examine a specific subset of questions.

In this chapter, we explore and begin to quantise the fundamental physics of space plasmas. This is done by examining precisely what a plasma is (§1.1.1) before describing the behaviour of single constituent charged particles that comprise the medium (§1.1.2 & 1.1.3). This is then generalised to examine a plasma as a continuum and obtain parameters that can be used to describe the expected behaviour of this as a whole (§1.1.4, §1.1.5 & 1.1.6) Finally, methods of plasma modelling, with specific application to space plasmas, are explored, including magnetospheric plasmas, §1.2.

1.1 Space Plasma Physics

1.1.1 Overview

Definition

Plasma is often referred to as the fourth state of matter, a fundamental form for material in our universe. The definition of the first three states of matter, these being solid, fluid & gas respectively, are well known, with a myriad of examples encountered in one's day-to-day existence. However, plasma is not so well known, with examples terrestrially limited to more specialised environments. Therefore, it is necessary to first define precisely want is described by the term plasma. Of course there is no single definition, so rather than select one, a range is collated and explored here.

Baumjohann and Treumann (1996, p. 1) state '*a plasma is a gas of charged particles, which consists of equal numbers of free positive and negative charge carriers*'. A concise definition that relates the state of plasma to one that is regularly encountered, gas. This analogy holds up to scrutiny for an enclosed system of plasma with only the external force of gravity acting upon it, extending to the second statement of equality between different signs of charge carriers. Boyd and Sanderson (2003, p. 1) introduces the ability of external forces, beyond those traditionally considered to act upon matter, to impact plasma by defining it such that '*we identify as plasma any state of matter that contains enough free charged particles for its dynamics to be dominated by electromagnetic forces*'. Finally, Priest (2014, p. 76) defines the state of matter using an intrinsic plasma quantity, that of its Debye Length, λ_D, by asserting '*a plasma may be defined as an ionised gas for which the number of particles in a sphere of radius λ_D is very large*'.

Plasmas have many properties that are useful when describing fundamental dynamics of a particular plasma filled region. These properties can relate to both a plasma's interaction with its constituent mass and charges, as well as that with the external electromagnetic forces acting upon it. The parameter used by Priest when defining the state of matter was its Debye Length, a measure of the spatial region into which a electric potential can penetrate before free charge carriers can act to neutralise it, effectively shielding the source of potential. This quantity can be calculated using

$$\lambda_D = \left(\frac{\epsilon_0 k_B T_e}{n_e e^2} \right)^{\frac{1}{2}} \tag{1.1}$$

where ϵ_0, k_B & e are the universal constants of the permittivity of free space, Boltzmann's constant & fundamental charge respectively, T_e & n_e are the electron temperature and density respectively. This formation for the equation of Debye length assumes quasi-neutrality and that constituent electron and ion temperatures are in approximate thermal equilibrium. In a three-dimensional system this can be readily utilised to create a region surrounding a potential known as a Debye sphere, where the radius of this sphere is equal to the Debye length.

Quasi-neutrality is a property that is often assumed when dealing with plasmas. The assertion that a plasma is quasi-neutral means that the amount of free ions and electrons contained is approximately equal, such that $n_e \approx n_i$, where n_i is the ion density. This means that on sufficiently large length scales the plasma appears neutral, however does not prohibit charge imbalances from occurring more locally within it.

Reflecting on the entirety of Priest's definition, it is possible to come to the natural realisation of what is typically referred to as the plasma parameter, Λ. The number of free charges inside a Debye sphere is obtained simply using $\frac{4\pi}{3} n_e \lambda_D^3$. Therefore, by isolating the variables in this definition the plasma parameter is found and is noted to be dimensionless in formation. By asserting that this dimensionless parameter is large Priest's definition of a plasma is satisfied, such that,

$$\Lambda = n_e \lambda_D^3 \gg 1. \tag{1.2}$$

The physical interpretation of this parameter is such that it ensures the dominant motions of the constituent species in a plasma are controlled by collective interactions rather than particle collisions.

Fundamental Motions

It is clear from the definitions explored that the charged particles that comprise plasma can be influenced by electromagnetic (EM) forces both applied externally as well as generated internally. Here we make the assumption that direct particle-particle interactions can be neglected when the inside a typical plasma (i.e. collisional frequency in the plasma is low), it makes sense to consider the dynamics of an individual charge responding to background EM fields when beginning to devise the motions of plasmas. The derivation of electrostatics, magnetostatics and electromagnetism is outside the scope of this thesis, but can be found in Shadowitz (1975) & Griffiths (2017) and key formulas are summarised in Huba (2013).

When formulating the equation of motion to describe the dynamics of the single constituent particle of the plasma, the forces acting upon it must be considered. Assuming that the particle is in a stationary reference frame, containing sufficiently large EM fields, it can be readily determined that the two forces acting are the Lorentz force, $\underline{F}_L$, and gravity, $\underline{F}_g$. When the contributions of these forces are considered it is found that typically the Lorentz force dominates gravity, such that $\underline{F}_L \gg \underline{F}_g$. Therefore, using Newton's

second law of motion the following formulation can be made

$$m_s \underline{a} = q_s \left(\underline{E} + \underline{v} \times \underline{B} \right), \tag{1.3}$$

where m_s & q_s are the mass & charge of the particle belonging to species s (i.e. proton, electron, ion), $\underline{a}$ & $\underline{v}$ are the particle's acceleration & velocity and $\underline{E}$ & $\underline{B}$ are the background electric & magnetic fields respectively.

Considering that the definitions for a plasma describe a region containing a distribution of charge carries able to respond collectively, it seems natural to explore the motions of a single particle in a complete euclidean space. A set of coordinates in this space are represented by $\underline{x}$, where $\underline{x} = (x, y, z)$, and using the well known $\dot{\underline{x}}$ & $\ddot{\underline{x}}$ representations for velocity & acceleration in eqn 1.3 it can be quickly seen that this is a second-order ordinary differential equation (ODE). Therefore, this formulation can be subjected to the usual mathematical tools (see Riley et al. 2002) in order to obtain the components of the particle's equation of motion.

The complexity of the particle's equation of motion is clearly dependant on the complexity of the EM fields within the region through which it traverses. Therefore, we will first consider a simple solution in a system which contains only simple fields. The electric field is considered negligible in comparison to the magnetic field and the magnetic field is aligned such that it is contained purely within the z-direction. This yields the following, simplified form of eqn 1.3,

$$\begin{aligned} \ddot{x} &= \frac{q_s}{m_s} B \dot{y} \\ \ddot{y} &= -\frac{q_s}{m_s} B \dot{x} \end{aligned}$$

where B is the strength of the magnetic field ($B = B_z$ in the described system). Examining the constants in the set of equations obtained it is determined that the velocity of both components is modified by the same constant value. Isolating this value, it is found to be of use when describing plasma motions generally and is known as the gyro-frequency, ω_g, defined as

$$\omega_g = \frac{q_s B}{m_s}. \tag{1.4}$$

Continuing the solution for the particle's equation of motion, examining the form of the set of equations it can be seen that they take that of a simple harmonic oscillator, with the particle following a circular trajectory from its initial position about a central point. The radius of this circular trajectory is known as the gyro-radius, r_g. This can be calculated by considering the velocity of the particle in the plane orthogonal to the magnetic field, $v_\perp = \left(\dot{x}^2 + \dot{y}^2 \right)^{1/2}$, such that,

$$\begin{aligned} v_\perp &= \left\{ \left[r_g \omega_g \sin(\omega_g t) \right]^2 + \left[r_g \omega_g \cos(\omega_g t) \right]^2 \right\}^{\frac{1}{2}} \\ v_\perp &= r_g |\omega_g| \\ r_g &= \frac{v_\perp}{|\omega_g|}. \end{aligned} \tag{1.5}$$

Further examination of the concept of a central point about which particles rotate finds it very useful when describing how a particle moves through a domain. This is because as a particle moves through a domain it continues gyrating as long as the magnetic field remains. Therefore, if some force is created or applied to begin moving the particle from its stationary orbit the path of its trajectory forms a helix, gyrating about this centre point. It is often easier to track the movement of this central point when considering the

general motions of the particle through a domain, as it takes the form of a line. The centre point is said to drift and forms the guiding-centre (Alfvén, 1950).

A natural result of the definition of the gyro-radius is the absolute being taken for the gyro-frequency. When the physical meaning of the gyro-frequency is considered, this being a measure of the time taken for the particle to complete a gyration, then it makes sense to discard the sign of the charge utilised when using eqn 1.4, as in a typical reference frame time only flows in a single, positive, direction. Further, whilst the gyro-frequency is a useful quantity for describing the motion of single particles, it can also be beneficial to re-express this as a period. The gyro-period, T_g, is typically the time taken for the particle to complete one fully rotation about its central point, however the gyro-frequency is in units of radians per second. Therefore, the following formulation is used to obtain it in units of seconds,

$$T_g = \frac{2\pi}{\omega_g} \tag{1.6}$$

1.1.2 Drift Velocities

The reintroduction of magnetic field components in the (x, y)-directions as well the electric field causes the particle's guiding centre to begin drifting, allowing the particle to move through the domain rather than just orbiting in place. The magnitude of the drift of the guiding centre can be obtained by building upon the solution used in describing a particle in a simple magnetic field. There are found to be several distinct drifts introduced depending on the configuration of the EM fields and here we will examine three fundamental to the work in this thesis.

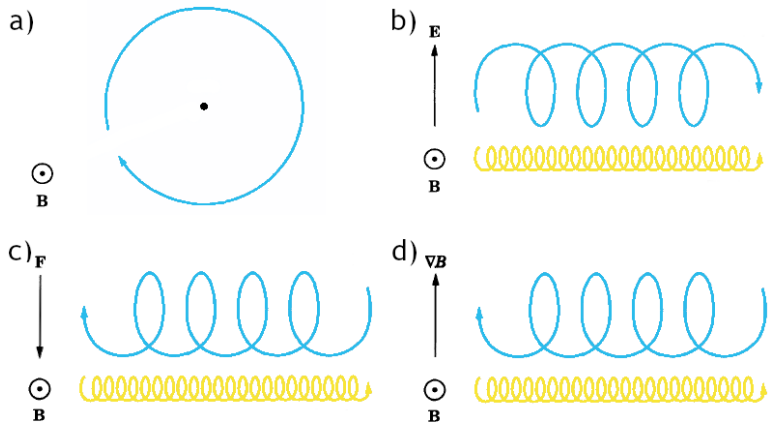

Figure 1.1: The trajectories of ions (in blue) and electrons (in yellow) in four separate EM field configurations, with the directions of the fields shown to the left of these. Panel a) contains only an ion gyrating with a stationary guiding centre (indicated by a black dot) in a single component static magnetic field, b) shows both an ion & electron gyrating around a guiding centre drifting to the right (for both particles) via $\underline{\mathrm{E}}\times\underline{\mathrm{B}}$ drift, c) has the ion drifting to the left and the electron to the right with the guiding centres drifting due to some applied external force and d) the same directions of drift but a gradient in the magnetic field induces the drift. Adapted from Baumjohann and Treumann (1996).

E×B Drift

Let us first examine the case in which an electric field is reimposed over the system but with components only in the plane orthogonal to the magnetic field (ie $\underline{E} = (E_x, E_y, 0)$).

Using the equation of motion determined in eqn 1.3, the following formalisation can be made for each component,

$$\begin{aligned} \ddot{x} &= \frac{q_s}{m_s} E_x + \omega_g \dot{y} \\ \ddot{y} &= \frac{q_s}{m_s} E_y - \omega_g \dot{x} \\ \ddot{z} &= 0. \end{aligned}$$

Taking the differential with respect to time of each component, and neglecting the z-direction, it is found that

$$\begin{aligned} \dddot{x} &= -\omega_g^2 \left(\dot{x} + \frac{E_y}{B} \right) \\ \dddot{y} &= -\omega_g^2 \left(\dot{y} + \frac{E_x}{B} \right). \end{aligned}$$

Examining the form of the equations above it can be seen that they are of the same form as the solutions obtained previously to describe particle gyro-motion where the guiding centre is stationary, with the addition of a linearly-superimposed second term dependent on the electric field. It is evident mathematically that this second term must be entirely responsible for causing the particle's guiding centre to drift and by isolating this term it is possible to exactly determine the velocity of this drift. This gives us the following description of the $\underline{\mathrm{E}}\times\underline{\mathrm{B}}$ drift velocity,

$$\underline{v}_{E\times B} = \frac{\underline{E} \times \underline{B}}{B^2}. \tag{1.7}$$

Hence, the particle gyrates about its guiding centre as the centre drifts according to the configuration of the EM fields, as seen in figure 1.1.

Generalisation

Using Coulomb's law (see Griffiths, 2017) along with the obtained equation for a particle's $\underline{\mathrm{E}}\times\underline{\mathrm{B}}$ drift velocity, it is possible to determine a generalised form of the drift velocity equation, applicable for any externally applied force. Assuming an electrostatic field, the Coulomb force F_c found to be acting on a single particle is

$$F_c = \underline{E} q_s.$$

Rearranging to isolate the electric field this can be substituted directly into eqn 1.7 yielding,

$$\underline{v}_F = \frac{1}{q_s} \left(\frac{\underline{F} \times \underline{B}}{B^2} \right). \tag{1.8}$$

The most obvious external force to apply to a plasma (particularly a space plasma) is that of gravity. This can be quantised using $\underline{F}_g = m_s \underline{g}$, where $\underline{g}$ is gravitational acceleration. The directionality of this force depends on the configuration of the plasma's reference frame, however eqn 1.8 can still be used to determine the contribution to the particles drift. This gives

$$\underline{v}_g = \frac{m_s}{q_s} \left(\frac{\underline{g} \times \underline{B}}{B^2} \right).$$

Recalling that the descriptions for the motions of a charged particle in a plasma so far have been constructed using Newton's second law, assuming the only force acting is the Lorentz force. Additional forces would be included mathematically by linear superposition

and would therefore take the form of a second term in the set of equations determined in the previous section. Utilising the same argument as when identifying the $\underline{E}\times\underline{B}$ drift velocity, it is evident that any additional forces would simply act to alter the drift of the guiding centre by constructing a linear superposition of all drift velocity terms. However, it is worth noting that unlike $\underline{E}\times\underline{B}$ drift there is a dependency on the sign of the particle's charge. This means ions & electrons drift in the opposite directions, once again dependent on the configuration of the fields, as seen in figure 1.1.

∇B Drift

The next drift is found by once again considering a set of temporally static EM fields and by setting the electric field to $\underline{0}$ across the domain in all directions. However, an inhomogeneity is introduced to the magnetic field in order to cause it to vary spatially. This is done by creating a gradient in the magnitude of the magnetic fields, restricted once again to a single direction such that $\underline{B} = (0, 0, B_z(y))$. It can be seen now that the magnetic field will vary in strength as the particle's position changes in the y-direction.

Mathematically, this change can be quantised using a first-order Taylor expansion (see Riley et al., 2002),

$$\underline{B} = \underline{B}_0 + \epsilon\underline{B}_1 + \mathcal{O}\left(\underline{B}_2\right), \tag{1.9}$$

where $\underline{B}_0$ is the background homogenous magnetic field, $\underline{B}_1$ is the first-order perturbation causing the gradient and ϵ is a collection of coefficients. Applying this to the described set up for the magnetic field it is determined that the following can be used in order to calculate the magnitude of the field 'felt' by the particle,

$$\underline{B} = \underline{B}_0 + \left(\underline{r}\cdot\nabla\right)\underline{B}_0,$$

where $\underline{r}$ is the position of the particle with the coordinate system transformed such that the origin is aligned with the guiding centre and ∇ takes its normal form from vector calculus. This alters the solution for a particle's gyro-frequency (eqn 1.4) such that it is a function of particle position rather than a constant.

Substituting the description for the magnetic field into the equation of motion to describe a particle (eqn 1.3) it can be found that the contribution from the gradient in the field can be isolated and treated as a drift (see Baumjohann and Treumann, 1996,Boyd and Sanderson, 2003). The drift velocity from this contribution can be calculated using

$$\underline{v}_{\nabla B} = \frac{v_\perp^2}{2\omega_g}\frac{\underline{B}\times\nabla B}{B^2}. \tag{1.10}$$

The physical mechanism for this drift is rooted in the varying of a particle's gyro-frequency and by extension its gyro-radii. When a particle moves into a region with a higher magnetic field strength its gyro-radii contracts and the inverse is true as it gyrates back into a region of weaker field strength. This causes a asymmetric orbit and results in the drifting of a particle's guiding centre as it completes multiple orbits. Again, there is a dependency on the charge of the particles, causing ions & electrons to drift in opposite directions, as seen in figure 1.1.

Additional Drifts

The drifts presented in this section are those that are pertinent to the work in this thesis, however that is not to say that they are a complete list of all drift motions. There do exist sets of further drift motions, such as polarisation & curvature that can be induced by specific configurations of the EM fields within a region of space. Additionally, there exist configuration of physical parameters outside of the electromagnetic that can cause

guiding centre of a particle to drift, such as the presence of pressure gradients within a region inducing a diamagnetic drift. However, once again these are outside the scope of this work.

1.1.3 Adiabatic Invariants

Along with the usual universal constants that demand conservation, such as energy and momentum, it is possible to determine other constant values in general mechanic systems. These are constructed by considering some parameter (or set of parameters), λ, that varies slowly in comparison with the characteristic temporal scale associated with particle motions in this system, T, hence (Landau and Lifshitz, 1976)

$$T\frac{d\lambda}{dt} \ll \lambda. \tag{1.11}$$

Therefore, it is apparent that term constant is inaccurate in describing these parameters, rather they are more commonly referred to as adiabatic invariants.

First Invariant

When considering motions that occur within a plasma which vary slowly in comparison to its characteristic temporal scale time scale, it is immediately reminiscent of drifts that occur perpendicular to the magnetic field. In recalling the case in which there are small inhomogeneities in the applied magnetic field, then the constituent particle species drift with a velocity prescribed by eqn 1.10.

Examining the form of eqn 1.10, it can be seen that if the magnitudes of the inhomogeneities in the field (∇B) are considered as the applied force and the general equation to describe drift motion is recalled (eqn 1.8), then the only difference remains in the collection of coefficients. Using the definition of the gyro-frequency (eqn 1.4) and observing that the kinetic energy of a particle can be obtained using $W = \frac{1}{2}mv^2$, these coefficients are

$$\frac{m_s v_{\perp}{}^2}{2B} = \frac{W_{\perp}}{B}. \tag{1.12}$$

Where $W_{\perp}$ is simply the kinetic energy of a particle orthogonal to magnetic field. If the gradients in the magnetic field are small, then the particle gyrates much more rapidly then its guiding centre drifts. Therefore, its trajectory can be found to create a circle that encompasses a surface with the magnetic field passing perpendicularly through. This is the definition of the magnetic moment, μ_B, such that,

$$\mu_B = \frac{W_{\perp}}{B}. \tag{1.13}$$

Considering the assumptions made in order to obtain the definition of the magnetic moment, it can be intrinsically seen that the drift motions must be on temporal scale shorter than the gyro-motions, meaning it is a adiabatic invariant. However, this assertion can be rigorously examined in order to ensure that these assumptions are physically accurate, these examinations can be found in a range of sources such as Baumjohann and Treumann (1996), Boyd and Sanderson (2003) & Somov (2006). By substituting the definitions of kinetic energy and momentum, into eqn 1.13, we obtain the expression of the first adiabatic invariant in its usual form,

$$\mu_B = \frac{k_{\perp}^2}{2mB}, \tag{1.14}$$

where $k_{\perp}$ is momentum orthogonal to the magnetic field.

Second Invariant

In a system containing diverging and converging field lines, such as that in a planetary magnetosphere, it is found that plasma particles drift along the field line as they converge until they reach a critical point. At this point the particle changes direction in order to conserve energy as well as the first adiabatic invariant, this critical value is known as the magnetic mirror point (see Baumjohann and Treumann, 1996, Boyd and Sanderson, 2003). After the particle's momentum has been turned it continues to travel as the field lines diverge and then converge at the other end, where the particle is mirrored again. Therefore, this set up is an oscillation as the particles travel from one end of the field to the other with a characteristic frequency, ω_b, known as the bounce frequency.

If we compare the drift of the particle to the frequency of its bounce we can construct an adiabatic invariant that is conserved as long as the bounce frequency remains low in comparison to its drift. The value of this invariant can be determined by examining the motion of a particle as it travels along the field line, which can be expressed in terms of its momentum parallel to the magnetic field. Since this invariant incorporates the entire field line and only the particle's guiding centre aligns with this at all times, then the value can be determined by integrating the particle's parallel momentum along the entire field line, $k_{\parallel}$, such that,

$$J = \oint k_{\parallel} ds. \tag{1.15}$$

Where J is known at the longitudinal invariant.

The second, or longitudinal, adiabatic invariant remains valid even if the particle's path is subjected to small variations, such as from weak interactions with other plasma components, as the EM field configurations in the bulk plasma will remain unchanged or is altered very slowly. If the fields in the bulk plasma begin to be altered more rapidly, with a frequency approaching or surpassing the bounce frequency, then the position of the mirror points will also rapidly alter, breaking the assumptions of the second invariant. It is also worth stating explicitly that as the second invariant is constructed utilising the first adiabatic invariant (conservation of magnetic moment), if the first invariant becomes invalid then the second is also violated.

Third Invariant

A particle bouncing between magnetic mirror points in the manner described in the previous section can also be found to drift from one field line to another. If the magnetic topology through which the particle travels in is axisymmetric, such as the case of a dipole planetary field, then the particle will eventually drift about the entire axis of symmetry creating another oscillatory motion. If we assert that this drift is slow enough that the longitudinal invariant is still constant, then, as a consequence of Liouville's theorem, it can be stated that in the presence of only weak electric fields that the surface enclosed by this drift possess a constant magnetic flux, Φ (Northrop, 1961, 1963).

In order to calculate this invariant then the magnetic field on the surface created by the drifting of the bouncing particle must be totalled. This can be simply done by integrating over the surface, denoted by $\underline{S}$,

$$\Phi = \int_S \underline{B} \cdot d\underline{S}. \tag{1.16}$$

This invariant, known as the third adiabatic or drift invariant, is demonstrated to hold constant in a range of literature including Northrop (1963) & Boyd and Sanderson (2003).

It is also found that the invariant is still constant if the EM fields are allowed to vary slowly. The fields must vary with a frequency less rapid than the frequency at which the particle completes its drift orbit about the line of axisymmetry. It should be noted that

if the EM fields vary more rapidly than this then the drift invariant is violated, but not necessarily the longitude or magnetic moment invariants, as the frequencies associated with these are higher (Northrop, 1963).

1.1.4 Particle Distributions & Moments

With an understanding developed of how individual charged particles move inside a plasma and how the forces externally applied alter the dynamics of them, we can now begin to consider plasma dynamics on a more macroscopic scale. It is often not convenient to describe a plasma by considering the motions of each constituent particle (although this can be done such as in the case of Particle-In-Cell modelling), but rather it is preferable to group particles together and consider them as a bulk. However, it is important to consider how it is possible to link individual particles that form a plasma, to any bulk description that is used.

By grouping particles together it is apparent that their characteristics can be treated stochastically and therefore it is possible to apply statistical techniques to understand the bulk properties of the plasma under examination (Piel, 2010). Examining the parameters of particles it is found that many, such as velocity, have a range of values that, when combined, create a distribution, the form of which is related to the plasma it is created from. Some properties, such as particle charge and mass in a single species plasma, do not have a range associated with them however this can simply be interpreted as another form of distribution, a Dirac delta function (see Riley et al., 2002). By examining the evolution of these distribution functions through time it is possible to comprehend the macroscopic dynamics observed in a plasma without having to be concerned with the motions of individual constituent particles.

Considering a plasma that occupies a 3-dimensional space, it is readily determinable that the distribution function that describes it can be written as

$$f(x, y, z, v_x, v_y, v_z, t). \tag{1.17}$$

From this function a 6-dimensional phase space, composed of the position and velocity components, is defined such that the state of any particle in the plasma is represented in this constructed region at time t. (Somov, 2006). It is worth noting that although it is trivial to construct a distribution function from a complete description of a plasma's constituent particles, it is not trivial to invert this process and obtain a set of particles with exactly the same parameters from knowledge of the constructed distribution function. Rather, it is possible to sample from the distribution and obtain a set of particles which form a plasma with the same statistical properties.

With the plasma now described using a distribution function it is possible to obtain a new set of parameters that describe the bulk dynamics. This can be done by taking the moments of functions constructed, essentially this involves integrating over the function with respect to its associated variable (see Riley et al., 2002). Using the distribution of velocity for example it is determined that the 1^{st} order moment yields the mean thermal velocity and the 2^{nd} yields the average kinetic energy of the plasma (Piel, 2010). Obviously these values could have been equally computed using each constituent plasma particle, but the calculation would have required a summation of all particles within the plasma which is usually not convenient.

Though to this point we have been considering a plasma to be described by a single distribution function, it is possible to subdivide regions of the plasma into smaller distributions that represent the region of phase space which they encompass. These smaller sections are also known as elements or parcels. The form of the distributions may change due to the subdivision, representative of some larger characteristic of the plasma. Obtaining the bulk properties of these sub-distributions, it is possible to determine the dynamics

of the subset of particles contained in relation to the larger plasma medium. This is immediately reminiscent of how fluids are treated, forming the constituent molecules in the substance into a single continuum that can be described as a whole in terms of mechanisms such as convection (see Kundu and Cohen, 2004).

In the case of plasma the dynamics of the formed continuum are described by a branch of physics known as magnetohydrodynamics (MHD). The postulations required to form the framework that describes plasma in this way is attributed to Alfvén (1942), with the simplest form being single-fluid ideal MHD. Essentially a plasma described using MHD is considered as a magnetised fluid, its mathematical descriptions are constructed using many equations from fluid dynamics as a basis, but altered to allow them to both respond to and induce EM fields (see Priest, 2014).

The equations that are derived to govern the dynamics of a MHD continuum are obtained by taking the moments of the distribution functions of the elements in combination with Maxwell's equations (the full derivation of these equations is outside the scope of this thesis, see Griffiths, 2017). This yields the continuity, momentum, induction and energy equations (presented in adiabatic form) as follows (Priest, 2014),

$$\frac{\partial \rho_m}{\partial t} + \nabla \cdot (\rho_m \underline{U}) = 0, \tag{1.18}$$

$$\rho \frac{D\underline{U}}{Dt} = -\nabla p + \underline{J} \times \underline{B} + \underline{F}, \tag{1.19}$$

$$\frac{\partial \underline{B}}{\partial t} = \nabla \times (\underline{U} \times \underline{B}) + \eta \nabla^2 \underline{B}, \tag{1.20}$$

$$\frac{D}{Dt}\left(\frac{p}{\rho_m^{\gamma}}\right) = 0. \tag{1.21}$$

where ρ_m is mass density of a element, $\underline{U}$ is the first moment of the velocity distribution in a element, equivalent to the macroscopic flow velocity, $\frac{D}{Dt} = \frac{\partial}{\partial t} + \underline{U} \cdot \nabla$ is the advective derivative, p is scalar pressure, $\underline{J}$ is current density, η is resistivity & γ is the adiabatic index. For this set of governing equations to remain valid it is determined that they must be applied to examining large length scales ($L >> \lambda_D, r_g$), low-frequency dynamics ($\tau >> \frac{1}{\omega_g}$) and remain firmly away from the bounds of relativity. Hence, this shows that when examining plasma at a macroscopic scales it is both permissible and advantageous to treat it as a bulk continuum (i.e. a fluid) rather dealing with each constituent particle.

1.1.5 Generalised Ohms Law

Derivation

Reflecting the start point for the determination of the equations of motion for single charged particles, seen in eqn 1.3, the momentum equation is first derived. Now, considering the plasma as a continuum, it is obvious that Newton's second law can no longer be simply applied, rather the Cauchy momentum equation (see Kundu and Cohen, 2004) must be utilised. This is recalled as

$$mn \frac{D\underline{U}}{Dt} = \nabla \cdot \underline{\sigma} + \underline{f}, \tag{1.22}$$

where $\underline{U}$ is flow velocity (called this henceforth), $\underline{\sigma}$ is the stress tensor, $\underline{f}$ is the linear superposition of all body forces and m & n have their usual meaning without subscripts.

Following §1.1.2 it is clear to see that different species of charged particle that constituent the plasma may behave differently when in the region of EM fields. Therefore, it is necessary to form each of these species into its own continuum when describing the bulk motion of particles within the plasma, giving a multi-fluid approximation. These fluids

can interact with one-another through EM effects as well as through elastic collisions, exchanging momentum from one fluid to the other to satisfy conservation laws.

The Cauchy momentum equation given in eqn 1.22 is modified to include the body forces acting upon the fluid as well as to include terms that allow for momentum transfer between fluids. Since we are interested in space plasmas a number of simplifications can be made when forming our modified momentum equation. First, we assume that the changes within the bulk of the plasma occur over spatial scales large enough to prohibit the formation of shears inside the fluids, meaning that the stress tensor contains effects purely arising from pressure, $\nabla \cdot \underline{\sigma} = \nabla \cdot \underline{P}$. It can also be assumed that the gravitational forces acting on the plasma are negligible, $\underline{F}_g = \underline{0}$. Finally, the plasma is in a true vacuum, therefore all momentum must be transferred between the constituent fluids only. The collisional term is

$$\underline{R}_{\alpha\beta} = n_\alpha m_\alpha \nu_{\alpha\beta} \left(\underline{U}_\beta - \underline{U}_\alpha\right),$$

where α & β are 2 generic fluid continuums and $\nu_{\alpha\beta}$ is the rate of collision between the fluids.

Using these of assumptions and asserting that the plasma is formed of only electrons and protons (denoted by the subscripts e & i respectively) the following set of equations is obtained (Baumjohann and Treumann, 1996; Somov, 2006),

$$\begin{aligned} n_e m_e \frac{D\underline{U}_e}{Dt} &= -\nabla \cdot \underline{P}_e - n_e e \left(\underline{E} + \underline{U}_e \times \underline{B}\right) + \underline{R}_{ei}, \\ n_i m_i \frac{D\underline{U}_i}{Dt} &= -\nabla \cdot \underline{P}_i + n_i e \left(\underline{E} + \underline{U}_i \times \underline{B}\right) + \underline{R}_{ie}, \end{aligned}$$

since the fluids can only exchange momentum between one-another $\underline{R} = \underline{R}_{ie} = -\underline{R}_{ei}$. However, it is noted that the plasma configuration of interest in this work is collisionless, hence collisional terms drop to 0 and the fluids are simply coupled through the EM fields. These two fluid equations are first multiplied by a factor of the mass of the constituent particle of the other fluid, before subtracting one momentum equation from the other.

From this point it can then be shown (see Shi, 2018; Baumjohann and Treumann, 1996) that generalised Ohm's law is defined as

$$\underline{E} + \underline{U} \times \underline{B} = \eta \underline{J} + \frac{1}{ne} \underline{J} \times \underline{B} - \frac{1}{ne} \nabla \cdot \underline{P}_e + \frac{m_e}{ne^2} \left[\frac{\partial \underline{J}}{\partial t} + \nabla \cdot \left(\underline{U}\,\underline{J} + \underline{J}\,\underline{U}\right)\right], \tag{1.23}$$

where

$$\begin{aligned} \underline{U} &= \frac{m_i \underline{U}_i + m_e \underline{U}_e}{m_i + m_e}, \\ \eta &= \frac{\nu_{ei} m_e}{ne^2}, \\ \underline{J} &= e\left(n_i \underline{U}_i - n_e \underline{U}_e\right), \\ n &= \frac{m_e n_e + m_i n_i}{m_e + m_i} \end{aligned}$$

and $\underline{U}$ returns to the bulk flow velocity of the single-fluid plasma (represented by the dropping of subscripts).

Physical Interpretations

Analysis of each term in eqn 1.23 can reveal their physical meaning as well as the parameters that control their influence on the overall description. Many sources include in-depth exploration of these terms, for example Shi (2018) provides an examination of them from a mathematical view point comparing the contributions of terms. Where as Vasyliunas

(1975) uses a more qualitative approach, defining their physical interpretations along with associated length scales. Of course discussion is not limited to these sources, but rather these represent two approaches to the examination.

Isolating the terms on the right-hand side of generalised Ohm's law, the first term, $\eta \underline{J}$, is found to be associated with finite resistivity. It is worth considering explicitly the case of an ideal MHD fluid, in which the conductivity tends to infinity, $\sigma \to \infty$, hence resistivity tends to zero, $\eta \to 0$. Hence, we obtain the following reductions to eqns 1.20 & 1.23 (Priest, 2014),

$$\frac{\partial \underline{B}}{\partial t} = \nabla \times (\underline{U} \times \underline{B}), \tag{1.24}$$

$$\underline{E} + \underline{U} \times \underline{B} = 0. \tag{1.25}$$

Considering the implications above it can be shown, using eqn 1.24, that for an enclosed surface the magnetic flux contained is constant and that the field lines on which the surface lies are also conserved. Hence, the frozen-in flux theorem (or Alfvén's theorem) is readily determined, this states that in the ideal limit the magnetic field lines are frozen into the plasma. Therefore, the magnetic field is moved along with the plasma and conversely changes to the magnetic field lines push the plasma (Baumjohann and Treumann, 1996).

A further consequence to the conservation of magnetic flux and field lines through a bounded surface in an ideal plasma is that by following the field lines a volume of space is identified throughout which flux is constant, this is known as a magnetic flux tube. As a consequence of the frozen-in theorem it is determined that the particles and magnetic flux inside the tube remain constant, even if the tube experiences motion and therefore remains characteristic of the region from which it originates (Baumjohann and Treumann, 1996).

The second term, $\frac{1}{ne}\underline{J} \times \underline{B}$, contains the contribution from the Lorentz force and is commonly referred to as the Hall term. This reflects that the contribution generated by this term is perpendicular to both the magnetic field as well as the current, similar to the Hall effect encountered when dealing with semiconductors (see Balkanski and Wallis, 2000). This term is found to be associated with a fundamental length scale tied to the kinetic motions of the ion constituents within the plasma known as the ion-inertial length scale, which is derived and discussed in §1.1.6.

Examining the third term, $\frac{1}{ne}\nabla \cdot \underline{P}_e$, it is determined that it communicates contributions caused by anisotropies and gradients in the electron pressure, giving rise to pressure gradients within the plasma. Like standard fluids, plasma acts to try and equalise pressure across its continuum in order to reach the lowest possible energy state, so tries to minimise these gradients. The length scale found to control this term is a product of the ion-inertial length scale along with the square root of another plasma parameter, the plasma beta, again derived and discussed in §1.1.6.

The fourth term, $\frac{m_e}{ne^2}\left[\frac{\partial \underline{J}}{\partial t}\right]$, is known as the inertial term and the fifth & sixth, $\frac{m_e}{ne^2}\left[\nabla \cdot (\underline{U}\,\underline{J} + \underline{J}\,\underline{U})\right]$, are the quadratic terms. Each of these terms contains a measure of the inertial effects contributed at the particle level to the bulk dynamics. These are associated with the electron inertial length scale (see §1.1.6) and are often neglected due to their small magnitude in comparisons to other terms.

1.1.6 Plasma Parameters

With it evidentially permissible to describe plasma on scales much larger than that of individual particles, it is logical to look to develop a set of properties that can assist in characterising the dynamics of the plasma as a whole. This set of properties is often referred to as plasma parameters, not to be confused with the plasma parameter defined in eqn 1.2.

Plasma Frequency

Considering the motions that single particles inside a plasma experience, with some drift directions possessing a dependency on the sign of particle charge, it is trivial to envisage a situation in which particles have moved to create a local charge imbalance. Particles then respond to neutralise this in response to the electric field, ensuring that globally the plasma remains neutral.

If first the electron constituents of the plasma are examined, they are determined to have a much lower mass than that of any of the ion species and hence a lower inertia. Therefore, when particles in the plasma move and then respond to induced EM effects, the electrons are able to change their velocity and position much more rapidly than the more massive ions. In effect, the ions can essentially be considered stationary whilst the electrons move to neutralise any charge imbalances. However, the electrons still have a finite quanta of inertia and are unable to instantly lose all momentum as they reach the position needed to full counter EM effects, overshooting and in turn generating new distributions of charge imbalances that require neutralising. The result of this process is the electron will oscillate at a fundamental frequency known as the electron plasma frequency, ω_{pe}.

The distance over which any charge is shielded inside of a plasma was obtained earlier as the Debye length, therefore any natural charge imbalances are intrinsically linked to this spatial scale. Since these perturbations require a response from all electrons in the medium, it makes sense to treat them statistically and obtain the average velocity of their motions. In order to obtain this the distribution of electron velocities must be determined, which is found to follow a Maxwell-Boltzmann distribution (Piel, 2010). It is in fact determined that both constituent ion and electron velocities follow a Maxwell distribution, therefore it is possible to describe any plasma species using

$$f\left(v_s\right) = 4\pi v_s^2 n_s \left(\frac{m_s}{2\pi k_B T_s}\right)^{\frac{3}{2}} e^{\left(-\frac{m_s v_s^2}{2k_B T_s}\right)}, \tag{1.26}$$

where $v_s = |\underline{v}_s|$ in spaces with more than 1-dimension and n_s & T_s are the number density & temperature of the selected particle species respectively. From our distribution function the most probable speed, $\tilde{v_s}$, can be determined in the usual manner ($\frac{\partial f}{dv_s} = 0$, Riley et al., 2002) yielding,

$$\tilde{v_s} = \left(\frac{2k_B T_s}{m_s}\right)^{\frac{1}{2}}. \tag{1.27}$$

Therefore, by comparing the average speed of a constituent particle species to the distance over which charges are shielded, it is possible to determine the fundamental frequency at which the plasma reconfigures itself to naturally occurring electrostatic effects. Using eqns 1.1 & 1.27 and selecting the electrons within the plasma yields,

$$\omega_{pe} = \frac{\tilde{v_s}}{\lambda_D} = \frac{\left(\frac{k_B T_e}{m_e}\right)^{\frac{1}{2}}}{\left(\frac{\epsilon_0 k_B T_e}{n_e e^2}\right)^{\frac{1}{2}}},$$

where the factor of 2 is dropped as it represents a selection of dimensionality in the examined space. This is trivially simplified to give,

$$\omega_{pe} = \left(\frac{n_e e^2}{m_e \epsilon_0}\right)^{\frac{1}{2}}. \tag{1.28}$$

A consequence of the fundamental oscillation of the electrons in the plasma is that any EM fluctuations applied to it at frequencies lower than the electron plasma frequency

cannot penetrate into the medium. This is because the electrons respond to neutralise them more rapidly than the field can change, negating its effects. More generally, the depth to which any EM radiation can penetrate into a plasma can be calculated by taking the ratio of the wave speed with the electron plasma frequency. Since we are dealing with space plasmas, it can be assumed that any EM radiation is travelling at the speed of light in a vacuum, c, giving

$$l_s = \frac{c}{\omega_{pe}}, \tag{1.29}$$

where l_s is more commonly known as the plasma skin depth.

On timescales much greater (or at much lower frequencies) than that of the oscillations of the electrons in a plasma, the constituent ion motions begin to become important again. Much like the electrons, ions move to neutralise charge imbalances that occur naturally in a plasma continuum, but are much slower to move to neutralise due to their larger mass. However, the fundamental frequency to these oscillations, known at the ion plasma frequency, ω_{pi}, can be calculated using the same process as utilised to form eqn 1.28. The difference is the ion species analysed, and this is reflected by using the charge and mass of the selected particle rather than that of the electron, giving the new definition,

$$\omega_{pi} = \left(\frac{n_i q_i^2}{m_i \epsilon_0}\right)^{\frac{1}{2}}, \tag{1.30}$$

where the subscript i denotes any ion plasma species (including protons).

Inertial Length Scales

Examining the form of eqn 1.29, the plasma skin depth, it becomes quickly apparent that this reveals more than simply the depth to which EM radiation can penetrate. The first subsequent conclusion that can be drawn is that l_s can be considered as a wavelength. Remembering that only EM waves with a frequency less than the plasma electron frequency can propagate into the medium, then this is the maximum wavelength that is permissible into the plasma.

Following this conclusion it is apparent that just as the plasma frequency is fundamental to the description of it, then this corresponding length also encapsulates some fundamental property of the plasma. Considering that the plasma frequency is the result of inertial effects, with charged particles in the plasma moving to neutralize imbalances, then this length represents the characteristic scale over which this occurs. Hence, this is referred to more often as the electron (or ion) inertial length scale, d_e & d_i respectively.

Since these length scales are fundamental to the constituent particle species forming the plasma, it is informative to express them in terms of the values of these particles. This can be done by taking the ratio of the speed of light to the plasma frequency of interest and re-expressing $c = \frac{1}{\sqrt{(\epsilon_0 \mu_0)}}$. Therefore,

$$d_e = \frac{(\epsilon_0 \mu_0)^{-\frac{1}{2}}}{\left(\frac{n_e e^2}{m_e \epsilon_0}\right)^{\frac{1}{2}}},$$

where μ_0 is the permeability of free space. Following this the simplified form readily obtained,

$$d_e = \frac{c}{\omega_{pe}} = \left(\frac{m_e}{\mu_0 n_e e^2}\right)^{\frac{1}{2}}. \tag{1.31}$$

The ion inertial length scale is determined using the same formulation, giving

$$d_i = \frac{c}{\omega_{pi}} = \left(\frac{m_i}{\mu_0 n_i q_i^2}\right)^{\frac{1}{2}}. \tag{1.32}$$

However, the implications of the value of this length scale are worth exploring. This is because the difference between the electron and the ion plasma frequencies is such that the ions can be considered essentially stationary when formalising the oscillatory motions of the electrons. Further, examining the magnitude of the inertial length scales associated with the particles it is found that the ion length is $\sqrt{m_i/m_e}$ larger than the electron length (assuming a quasi-neutral proton-electron plasma) (Tóth et al., 2017). Therefore, it can be demonstrated that the ion fundamental motion occurs over a larger spatial scale ($d_i > d_e$) with a lower frequency ($\omega_{pi} < \omega_{pe}$) than the electrons.

This means that when dealing with the dynamics of particles on spatial scales larger than that of the ion inertial then the electrons can be formed into a fluid continuum that is effectively decoupled from ion motions. This electron fluid fulfils the criteria for an ideal MHD fluid (Priest, 2014) and therefore has infinite conductivity. Hence, the fluid meets the frozen-in flux conditions and the magnetic field becomes linked to the motions of this electron fluid.

A final observation that can be made is that the ion inertial length can also be obtained by combining the definition for the Alfvèn velocity (see Priest, 2014),

$$v_A = \frac{B}{\sqrt{\mu_0 \rho_m}}, \tag{1.33}$$

with the ion gyroradius, eqn 1.5. If the velocity of the ion motion perpendicular to the magnetic field is allowed to reach the Alfvèn velocity, such that $v_\perp = v_A$, then,

$$r_{gi} = \frac{m_i}{q_i B} \frac{B}{(\mu_0 m_i n_i)^{\frac{1}{2}}}.$$

This can then be readily rearranged to yield the exact definition given in eqn 1.32.

Plasma Beta

Examining the fundamental motions of particles in the plasma continuum of gyro- and inertial-motions, it is apparent that both thermal and magnetic effects are important in the determination of the fundamental plasma properties. However, the question quickly becomes which of these effects is dominating the dynamics of a plasma under examination. In order to consider this the bulk medium must once again be analysed, and a pressure balance can be formed between these effects. This creates a ratio, the value of which is informative of which effect is dominant.

From the analysis of generalised Ohm's law (see §1.1.5), we know that the magnetic effects are contained within the Hall term. However, this term also includes current densities, which are undesirable when trying to isolate the magnitude of contributions from purely magnetic effects. Therefore, the low frequency Ampère's law (see Griffiths, 2017) is substituted in to allow for the re-expression of the current densities in terms of the magnetic field,

$$\underline{J} = \frac{1}{\mu_0} \nabla \times \underline{B}.$$

Using this substitution and commuting current density with the magnetic field yields,

$$\underline{J} \times \underline{B} = -\frac{1}{\mu_0} \underline{B} \times (\nabla \times \underline{B}).$$

Expanding this, using vector calculus identities, it can be readily shown that can be re-expressed in the more useful following form,

$$\underline{J} \times \underline{B} = -\nabla \left(\frac{|\underline{B}|^2}{2\mu_0} \right) + \frac{1}{\mu_0} \nabla \cdot (\underline{B}\,\underline{B}). \tag{1.34}$$

Recalling Cauchy's momentum equation (eqn 1.22), if we consider our bulk plasma in a steady state configuration, such that $\frac{\partial \underline{U}}{\partial t} = \underline{0}$, assume that shear is minimised in such a way that the stress tensor can be described purely in terms of pressure and the only body force is the Lorentz force, we obtain,

$$\underline{J} \times \underline{B} - \nabla \cdot \underline{P} = 0,$$

this is often referred to as the magnetohydrostatic equation. Where $\underline{P} = \sum \underline{P}_s$ is the sum of the pressures of all constituent plasma species. Substituting eqn 1.34 into this and rearranging yields,

$$\nabla \cdot \underline{P} = -\frac{1}{\mu_0} \nabla \left(\frac{|\underline{B}|^2}{2\mu_0} \right) + \frac{1}{\mu_0} \nabla \cdot (\underline{B}\,\underline{B}) \,.$$

If the form of the pressure is assumed to be isotropic and the magnetic field made homogeneous, then this simplifies further leaving,

$$\nabla p = -\nabla \frac{|\underline{B}|^2}{2\mu_0},$$

where p is the scalar pressure field. In the described plasma the total pressure is constant and the contributions from the kinetic effects described by the left hand side of the equation and the magnetic effects in the right. Therefore, by taking the ratio of these terms we can determine which effect is dominate in controlling plasma dynamics.

Utilising eqn 1.27 we already have a stochastic description of particle velocity. Therefore, we can readily obtain a value for the momentum in the bulk plasma using $k = \rho_m \tilde{v}_s$. Hence,

$$\beta = \frac{n k_B T}{\left(\frac{|\underline{B}|^2}{2\mu_0} \right)}, \tag{1.35}$$

where β is the dimensionless value known as the plasma beta.

The physical implications of this value are evident through its derivation. However, the mathematical values can now be examined and correlated to the physics. The values for the plasma beta can be categorised in three distinct manners, the first of these being $\beta \ll 1$. In this low beta regime the magnetic pressure is much greater than the thermal, therefore magnetic effects are dominate in controlling plasma dynamics. Conversely, in a high beta regime, $\beta \gg 1$, thermal effects control plasma dynamics. Finally, there is $\beta \approx 1$, in this regime the magnetic and thermal are approximately equivalent and neither dominate the dynamics.

1.2 Modelling Plasma Physics

Almost all physical phenomenon can be described through the use of mathematical equations, able to precisely capture and comprehend these phenomenon and able to predict the result of a set of parameters without the need to subject them to direct experiment in a laboratory. There are areas of physics that lie outside of exact solution through the use of mathematics and are rather better described statistically as a set of probabilities. This is of course most famously the case for the area of phenomenon and dynamics that fall under the branch of quantum physics (Griffiths and Schroeter, 2018). Whether this is due to the fundamental nature of these phenomenon or a incomplete understanding is still a matter for debate.

The matters in this thesis remain firmly in the realm of the determinable and therefore can be explored exactly through the use of mathematical theory and solutions. For phenomenon unable to be directly examined through the use of observation & experimentation, it is possible to explore them through the use of numerical techniques. This is not

to say that the data obtained through observation is not required when modelling, in fact it is often required for the configuration and parametrisation of numerical solutions and also allows for predictions made from these solutions to be tested and verified.

The mathematical technique we select in order to study the phenomenon of interest in this thesis, that being the mechanisms responsible for the radial transport of plasma in the magnetospheres of the outer planets, is the construction and utilisation of physics-based numerical modelling. By this it is meant that the laws of physics (as currently understood) will be utilised in order to construct a set of equations that describe a particular physical phenomenon. The precise reasons for this selection will be explored in more detail in later chapters (see particularly §3), but the distance of the systems of interest to this work, these being the Jovian & Saturnian, from the Earth clearly makes direct observation & experimentation challenging.

When constructing a model it is often not convenient or necessary to utilise every equation, or terms therein, therefore assumptions about the physical configuration of the system are made. This is beneficial in increasing the tractability of the model, however the trade for this is the enforcement of the assumption made in all solutions through the mathematics used. These limitations must be recalled and the impacts considered on all results obtained from the simplified implementation.

The problem then turns to the matter of the accuracy, storage and accessibility of these physical parameters and the solutions calculated using them, a matter vastly complicated when it is considered that matrices & vectors are means utilised to express these. Though it is permissible to envisage solutions being calculated for small systems, with few temporal steps, being determined manually. However, once this is applied to even small sections of a system as large and complex as a planet, it becomes obvious that some form of automation is required for the implementation of a described numerical model. With the advent of modern computational power and the general familiarity of mathematicians & scientists with programming languages, the development of software suites capable of performing simulations using physics-based numerical models is now a standard practice.

Of course it is possible to construct a set of equations which when solved yield a solution that describes a single state of a system with pre-defined boundaries in both the spatial & temporal domains. However, it is also possible to construct the logic of a model in such a way that the solutions obtained to previous equations can be utilised to update physical parameters which were used as input values to determine these solutions. Hence, the updated parameters can be re-utilised in the same equations in order to obtain a new set of solutions for the modelled system. The usual way to use this is to update parameters in the temporal domain, creating a model which is capable describing a system at particular points in time and simulating self-consistently the temporal evolution.

It is worth noting that the updating of physical parameters in an ordered manner to temporally progress model solutions, simulating the dynamical processes within a system, is not the only way in which physical parameters are varied to obtain a range of solutions from a models equations. Other techniques exist such as the Monte Carlo method (see Press et al., 2007), in which parameters are varied randomly in order to examine phenomenon of interest through statistical techniques. It should be noted that the combination of methods is often found beneficial in the construction of model logic. All of these methods are also enhanced through the use of modern computation, making modelling a staple of (current) research techniques across a broad range of topics.

A magnetospheric system is vast and incorporates a large range of physical phenomenon, a single model capable of capturing and quantising all of these would be incredibly complicated. In fact, 'obtaining an exact solution of the equations governing a system as complex as the magnetosphere is clearly impossible, and to construct a theoretical model the equations must be simplified (often drastically) to the point of tractability'

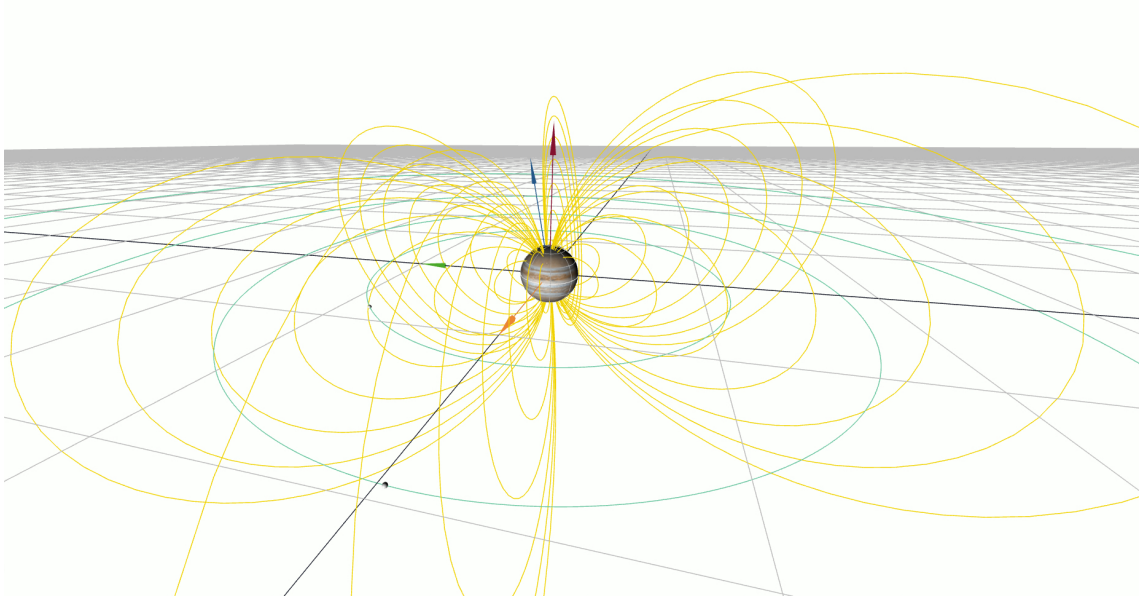

Figure 1.2: View of the internal planetary field lines in the Jovian system obtained using a dipole field model by Ikuchi (Arridge and Wiggs, 2019). A planetary body is sat on a wireframe, constructed across the orbital plane. Four arrows can be seen emerging from the planet with the orange indicating the vector between the planetary centre and the Sun, red the rotation axis of the planet, blue the magnetic dipolar axis and green the orbital direction of the planet. Yellow field lines emerge from 6 locations equally spaced in longitude, these represent the magnetic field lines. Each of these sets contains 6 individual lines emerging from different latitudes. Another four green lines can be seen encompassing the planet, forming a set of concentric rings, these indicate the orbital paths of each of Jupiter's Galilean moons (Io, Europa, Ganymede & Callisto), small spheres represent the moons.

(Vasyliunas, 1970, p. 61). Therefore, one must consider closely the physical phenomenon, dynamics and mechanisms, that they wish to capture inside a magnetospheric model in order to select the set of equations (and assumptions applied) before construction of said model can begin. A complete review of planetary magnetospheres, as well as a detailed examination of the Jovian & Saturnian systems, can be found in §2.

An example of how a magnetospheric system can be simplified and deconstructed into a number of base components that are combined in order to describe it, is to consider the planetary magnetic field. An internal planetary field can be approximated to the first order by using a simple dipole. Therefore, it is possible to construct a model of these internal fields by determining the solution to the set of equations that describe a dipole field, with the number of equations in the set equal to the number of spatial dimensions. This solution for the Jovian magnetic field is applied in figure 1.2, from the Ikuchi theoretical model (Arridge and Wiggs, 2019).

The solution presented in figure 1.2 for the approximated dipolar magnetic field at Jupiter can be seen as a set of 6 yellow lines surrounding the planet at the figure's centre. Each set of field lines consists of 6 field lines emerging from different latitudes, with higher latitudes corresponding to longer field lines which reach further radially from the planet. The planetary body is indicated, to scale, at the centre of the system with 4 concentric circles representing the orbital path of the Galilean moons. Moon location varies with time and accurately represents the position that would be expected at a given time.

1.2.1 Plasma Modelling Techniques

To model the dynamics found in planetary magnetospheres we must model them using an appropriate formulation. Since they are filled with plasma we must use equations that describe the behaviour of plasmas as discussed in section §1.1. Furthermore, for phenomenon we are investigating we must contemplate the regime of plasma physics in which it resides. For bulk plasma motions on temporal and spatial scales much longer than a gyro-period and gyro-radius, respectively, we can treat the plasma as a magnetised fluid using the framework of MHD, and on very short temporal and spatial scales we must treat the charged particles kinetically. For phenomena in-between we can treat one or more species kinetically and the rest as a fluid (Winske et al., 2003) in the so-called hybrid approach. We can use the plasma parameters defined earlier (see §1.1.6) to determine which approach is suitable for the regime within the domain we wish to examine.

The parameters that prove most useful for the determination of the appropriate modelling regime to utilise when identifying a particular phenomenon are the gyro-frequency (Ω_i & Ω_e), the gyro-radii (r_{gi} & r_{ge}) and finally the inertial length scales (d_i & d_e). By considering the spatial & temporal scales of the dynamics under examination in comparison to these parameters, it is possible to identify which modelling regime is required. Generally, for phenomenon and dynamics that occur on spatial scales much greater than the ion gyro-radii or on temporal scales much greater than the ion gyro-period then a fluid model is most appropriate (i.e. MHD). Dynamics that occur on spatial scales smaller than the ion gyro-radii or on shorter temporal scales than the ion gyro-period are best suited to full kinetic modelling (i.e. PIC). This leaves a mid-range on spatial scales above the ion gyro-radii but not much greater or longer than the ion gyro-period, this range is most suited for hybrid plasma models to be utilised (Winske and Omidi, 1996). The ion inertial length is also important when considering the implementation of a hybrid model as it dictates the length at which the ion motions decouple from the electrons.

In figure 1.3 the model regime which is most appropriate for a particular plasma over a range of spatial & temporal scales is shown. The plasma chosen has typical magnetospheric parameters with $n_i = 50$ cm^{-3}, $B = 50$ nT & $T_i = 100$ eV, quasi-neutrality and thermal equilibrium is also assumed. From these the electron gyro-period and radii can be readily calculated as 10^{-4} s & 0.7 km respectively, the same ion gyro-parameters are determined to be 0.2 s & 30 km. The gyro-parameters can be seen indicated in the figure and the ion values represent the upper limits for the ideal application of full kinetic modelling. The length scales ideal for MHD (fluid) modelling are much greater than these values and can be see to bound spatial scales above 10^4 km and temporal scales longer than 10^2 s. This leaves the gulf between these two modelling regimes that is occupied by hybrid plasma modelling, this can be seen to apply for spatial scales between 10^2-10^4 km and temporal scales between 10^0-10^2 s for the described magnetospheric plasma.

Fluid

With the appropriate circumstances for the use of fluid modelling techniques to be applied already identified, it is worth examining the application of established models to problems in space plasmas. When examining this subset of plasma models, it is found that a majority of modern codebases solve a set of the MHD equations (see Priest, 2014) in order to form their physical description of the material located inside their domains. Details on the specific construction & implementation of MHD models capable of resolving the dynamics of a magnetospheric system can be found in Raeder (2003). Additionally, details on the inclusion of physical effects beyond those contained with ideal MHD (i.e. Hall MHD) can be found in Huba (2003).

MHD models have been applied to a wide variety of plasma environments, with the

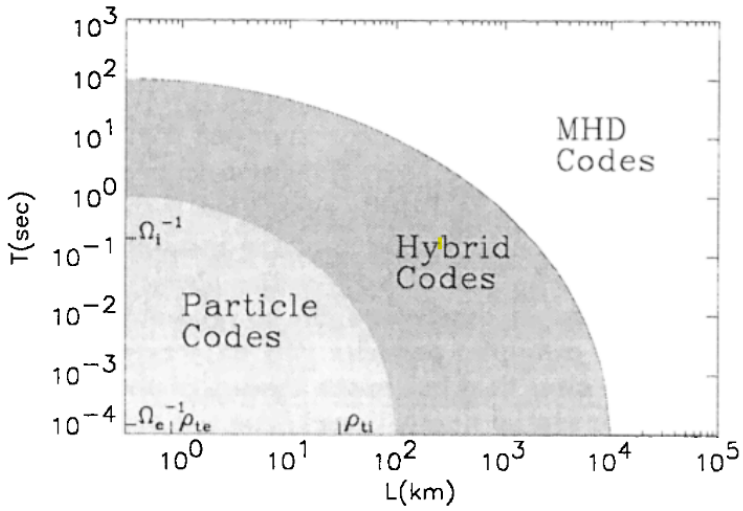

Figure 1.3: Description of which plasma modelling technique is appropriate for a typical magnetospheric plasma (n_i = 50 cm^{-2}, B = 50 nT & T_i = 100 eV) depending on the spatial & temporal length scales, L & T respectively, of the dynamics of interest. The ion & electron gyro-periods are indicated (Ω_i^{-1} & Ω_e^{-1}), as well as their gyro-radii (ρ_{te} & ρ_{ti}), with a t subscript indicating that typical thermal velocities have been used. For length scales below the ion gyro-radius ($< 10^2$ km) kinetic modelling is found appropriate, at much greater lengths ($> 10^4$ km) it is fluid (MHD) and for the lengths between (10^2-10^4 km) hybrid. Examining temporal scales shorter than the gyro-period ($< 10^0$ s) kinetic modelling is best suited, scales much greater than the ion gyro-period ($> 10^2$ s) are suited to fluid modelling and those between (10^0-10^2 s) are suited to hybrid (Winske and Omidi, 1996).

focus of this thesis being on solar system plasmas we can identify two regions of particular interest for study with these models. The first of these are the regions of the Sun and its atmosphere where, for example, analytic solutions to the set of perturbed & linearised MHD equations can be used in order to determine the propagation of different wave modes through a variety of magnetic topologies (i.e. McLaughlin et al., 2019).

The other set of space plasmas that are of particular interest to this thesis are those of the planetary magnetospheres. With the terrestrial magnetosphere being the most heavily studied and probed in the solar system, it is not surprising to find that the largest amount of attention has been given to this region for the construction of MHD magnetospheric models. Such models have become a staple for the examination of problems in the terrestrial magnetosphere, with a number even now utilised to aid the forecasting of space weather events (see Eastwood et al., 2017). With the popularity & vast scientific benefits of these models, centralised services, such as the Community Coordinated Modeling Center (CCMC) have been established to facilitate the usage of these model codebases throughout the scientific community. The models included in facilities such as the CCMC can of course be benchmarked against one another to identify which provide the most insights under a number of different circumstances (Ridley et al., 2016).

Selecting a single model from the range collated and contained within the CCMC for exploration, the Lyon-Fedder-Mobarry (LFM) is found to have been a work-horse magnetospheric simulation over the past 40 years. Initially developed at the National Research Laboratory, the model codebase has been continually updated over the course of its usage in order to incorporate the latest developments in MHD modelling and remain on

the cutting-edge (Lyon et al., 2004). Further, coupling with other models has allowed for the scope of the model to be expanded to include regions & dynamics typically unresolvable with traditional MHD modelling, such as the a number of current systems in the inner magnetosphere (Toffoletto et al., 2004).

Despite this continuous development, it has become necessary to rewrite the code in order to allow for the continued usage of the latest numerical methods, as well as for optimal use to be made of modern computational architectures (Lyon et al., 2017; Zhang et al., 2019). The application of the new model codebase, GAMERA, to simulating outer planetary magnetospheres will be examined in §2. However, this stands to highlight the versatility & adaptability of these codebases, with GAMERA also used extensively to perform analysis on terrestrial magnetosphere (i.e. Sorathia et al., 2020). Despite this versatility, there are still fundamental limitations on the spatial & temporal lengths of the dynamics that can be captured by them. Therefore, to examine scales below those accessible with MHD modelling other techniques are required.

Kinetic (Particle-in-Cell)

To examine plasma motions & effects on the shortest of spatial & temporal scales, the technique of full kinetic modelling is required. In order to construct these models the complete equations of motions for the constituent ions & electrons require solving, the solution to which can then be utilised to update particle positions. The complication with this technique then becomes immediately apparent, that is how to communicate the new distribution of the charged particles to one another in order to allow the plasma to respond to the new EM configuration. The most obvious option is to calculate the Coulomb force applied by each charge on all particles contained within the model, however when the number of computations required to do this is considered, it becomes obvious that this method is extremely inefficient.

The solution to this problem is found by constructing a grid over the model domain, on the vertices of which the EM fields are discretised upon and particle properties (such as charge) are collected on also. This allows for the updated charge distribution, after particles have been moved, to be communicated onto these grid points. These values are used to obtain updated EM field values, which are then interpolated back to the particles, allowing them to move in response to the new configuration. This technique creates a PIC model and vastly increases the computational efficiency of the codebase constructed to implement the model logic. Though to simulate large spatial domains or high density regions it is still necessary to introduce further simplifications, such as macroparticles, in order to make the problem tractable. Details on the specific construction of PIC models can be found in Birdsall and Langdon (1985), Pritchett (2003) & Schriver (2003).

Even with the improved efficiency provided by the methods described to create a fully kinetic PIC plasma model, applying one of these to a system as large as a planetary magnetosphere is still generally infeasible, though recent efforts have been made to apply this to small magnetospheres such as Mercury (Lapenta et al., 2022). Considering the vast computational power & resources available through the use of high performance computing (HPC) facilities, the total size of domain that can be simulated using this technique is now large and will continue to increase with the power of these facilities. However, when the dynamics best explored with kinetic modelling are considered, along with the corresponding computational overheads, it is clear that this technique is best explored to smaller sub-domains within a global system to investigate specific problems in plasma physics.

An example of a PIC modelling being currently utilised for the research of space plasma is the iPIC3d codebase (Markidis et al., 2010). This model has been applied to a number of problems identified as best analysed on the spatial & temporal scales

most suited to full kinetic modelling. The first of these processes is that of magnetic reconnection, which the model has been successful in analysing throughout the terrestrial magnetosphere (Olshevsky et al., 2013; Peng et al., 2015c). With reconnection near the sub-solar point in the magnetosphere being largely anti-parallel between the planetary field & the inter-planetary magnetic field, it is perhaps unsurprising to find that investigations have also been carried out into the interactions between plasma that forms the solar wind and that within the magnetosphere (Peng et al., 2015a,b). Further, the model has been used to investigate the phenomena of non-linear dynamics (i.e turbulence & shocks) that are often best examined on the spatial scales only accessible by full kinetic techniques (Pucci et al., 2021).

However, there are numerous physical processes and effects that occur in space plasmas that require examination on a large-to-global scale whilst maintaining the ability to examine the motions of particles without generalisation into a fluid. Therefore, it is apparent that a combination of the abilities of MHD (fluid) models to resolve larger system dynamics, on long spatial & temporal scales, whilst being able to track the motions of particles, on much shorter spatial & temporal scales, as they travel through the domain. This leads to the immediate realisation of the necessity of a modelling technique that bridges the gap between full kinetic & MHD.

Hybrid

The technique that bridges this gap is that of hybrid plasma modelling, the definition of which has been stated at the beginning of this section. It is worth noting however that there are several ways to treat the particles coupled to the fluid within the model. The most popular of these techniques is to use the PIC technique described in the previous section, with the fluid components within the model discretised and controlled along-side the EM fields on the grid vertices across the model domain (Winske et al., 2003). To examine another technique, the Vlasiator hybrid model, capable of simulating magnetospheres on an almost global scale, using a Vlasov description for the ions in the model, updating their distributions using a finite-volume method in 6-dimensions (von Alfthan et al., 2014) rather than the more common technique utilising the equation of motion to obtain velocity followed by position (i.e. PIC).

This modelling technique has been applied to a range of space plasma throughout our solar system including the solar wind (Ofman et al., 2011), Mercury (Kallio and Janhunen, 2003; Müller et al., 2011), Venus (Jarvinen et al., 2008), Earth (Swift, 1995; Battarbee et al., 2021; Shi et al., 2021), as well as the outer planets (Delamere et al., 2021; Müller et al., 2011; Liuzzo et al., 2015) and comets (Bagdonat and Motschmann, 2002), as they travel through the solar system. Therefore, it can be seen that this technique is suited for use in a wide range of environments in space plasmas.

The focus of this thesis is on the development, validation & benchmarking and implementation of a new hybrid plasma model at the outer planets for specific use in examining the radial plasma transport & the centrifugal interchange instability. Therefore, a review of the methods utilised in the application of this modelling technique will be reserved for discussion in later chapters (see §4 & 5).

An overview of planetary magnetospheres, followed by a detailed examination of the Jovian & Saturnian systems, is performed in the next chapter §2. This is followed by a detailed review of the theory, observations and modelling of the mechanism responsible for radial plasma transport at the outer planets, §3, with specific questions identified for examination through the use of a hybrid plasma model. A general recipe to construct the numerics and logic of a hybrid model are be detailed in §4, which are then utilised to create our plasma physics model in §5, with specific implementation detailed. This is followed by a set of physical benchmarks in §6 in order to ensure the accuracy of the results produced

as well as to gain an understanding of the limitations of its usage. Application of the model to the Saturnian magnetospheric system will be detailed in §7, with work done to address the research questions established in previous chapters. Finally, a summary of this thesis will be presented in §8.

Chapter 2

Planetary Magnetospheres

2.1 Overview

2.1.1 Formation

Solar Origins

Planetary magnetospheres, as the name suggests, are found in the regions of space surrounding planets contained within a solar system. However, the formation of these structures is not tied purely to the planetary body which they encompass, in fact the origins of all magnetospheres are intrinsically linked with the star about which they orbit. This is because stars not only emit EM radiation in the form of light, but also eject material in the form of the solar wind and also generates its own magnetic field via the solar dynamo which encompasses everything in the heliosphere. The heliosphere can be regarded as the magnetosphere of the Sun, its edge represents the radius at which the magnetic effects of our star intermingle with interstellar fields.

The edge of the heliosphere also represents an edge of our solar system though it is not the only one that can be defined, passing through which allows one to enter the interstellar medium and gain insights into physical properties of interstellar space. This new frontier of space exploration has been entered now by two space probes, Voyager 1 on 25^{th} August 2012 (Cowen, 2013) & 2 on 5^{th} November 2018 (Strauss, 2019). Despite the relatively short time these probes have spent in these regions, the results they continue to transmit have proved vital in developing our understanding of this region with instruments still measuring properties such as magnetic field strength and plasma densities (Burlaga et al., 2019; Gurnett and Kurth, 2019).

That is not to say that the only way to probe the heliosphere is through the use of in-situ measurements. In recent years instruments on spacecraft designed to investigate regions inside our solar-system have been co-opted and utilised as effective remote-sensing tools. An example of this is the use of the INCA camera onboard the Cassini mission in imaging energetic neutral atoms (ENAs) which originate from the heliosheath (Krimigis et al., 2009; Dialynas et al., 2022). These measurements are then combined with results from Voyagers 1 & 2 to create models of the shape of the heliosphere (Opher et al., 2020). This in many ways reflects how magnetospheres are generally probed, with a combination of in-situ and remote measurements required to yield the highest levels of understanding of the regions dynamics.

However, within the heliosphere, which each of the recognised magnetised planets firmly sit in, the interstellar medium cannot penetrate and the fields are dominated by those generated by the Sun. This means that external effects required to create a magnetosphere are almost always solely linked to our local star. Occurrences when other bodies can have an impact on the topology of a planetary magnetosphere are extremely limited

and transient in nature; an example of which is a convergence in which the gas giants of Jupiter and Saturn align in such a way that Saturn can enter Jupiter's magnetosphere (see Krupp et al., 2004).

The two main physical properties from the Sun which control the structure and size of magnetosphere are the extension of the Sun's magnetic field into the heliosphere, often referred to as the interplanetary magnetic field (IMF) and the solar wind. The solar wind is a continuous stream of plasma emitted from the solar surface, travelling with a velocity in the range of 200-800 km s^{-1} it falls into two distinct categories of slow and fast, hinting at acceleration by different physical mechanisms (see Priest, 2014). The solar wind decreases in density with distance from the Sun, more tenuous at the outer planets than the inner, and hence the dynamic pressure associated with this wind drops proportionally.

The solar wind can be considered constant in regards to large time scales, with the solar cycle seeming to provide some changes in the proportion of fast to slow wind (Tokumaru et al., 2010). However, the Sun itself is very dynamic, continually experiencing dramatic events such as coronal mass ejections and solar flares. If these occur in a position on the solar surface that propagates out to the position of a magnetised planet, then that body can find the stationary solar wind enhanced by increases in the density, temperature and velocities of the interplanetary plasma. These can have a profound impact on the structure and dynamics of a planet's magnetosphere, triggering events such as magnetic reconnection and geomagnetic sub-storms (see Hargreaves, 1992).

The connection between the terrestrial magnetosphere and our Sun through the interplanetary medium is what gives rise to the phenomenon of space weather. Like traditional weather this varies continuously and is the combination of numerous factors, not all of which are still fully understood. Further, there are concerted efforts to monitor and forecast the impact of the Sun on our magnetospheric system with a number of dedicated spacecraft monitoring it, such as the Solar Terrestrial Relations Observatories (Stereo) A & B (though B is now non-operational) (Biesecker et al., 2007) and the Solar Dynamic Observatory (SDO) (Pesnell et al., 2012). It is hoped that the continuing efforts to understand physical mechanisms that drive the dynamics observed on our Sun, by missions such as the Parker Solar Probe (PSP) (Fox et al., 2016) and Solar Orbiter (Müller, D. et al., 2020), will improve our ability to accurately forecast solar weather and its impacts on the terrestrial magnetosphere.

Despite the plethora of dynamics already outlined that can impact a magnetosphere, for the most simple approximation that will be utilised in this chapter the solar wind can be considered as providing an external source of pressure, known as the ram pressure. Treating the solar wind as a bulk plasma with the planets engulfed in its flows, then pressure can be obtained using the same expression as detailed in the previous section, hence

$$p_{sw} = n_{sw} m_{sw} v_{sw}^2. \tag{2.1}$$

Where the *sw* subscript denotes the solar wind.

Planetary Factors

The other main component in the construction of planetary magnetospheres is of course the planets themselves. In this thesis we shall focus upon the planets inside of our solar system, this is not to say however that planets in other systems, exo-planets, do not possess these regions of space. In fact the theory developed for the planets inside our solar system should be readily translatable to bodies in solar systems outside our own as the physical mechanisms responsible for the creations of magnetospheres are postulated to be universal in nature (ie Paty et al., 2020; Green et al., 2021).

Focusing initially on a simple magnetospheric topology, we consider the case of the closed magnetosphere which can be seen in figure 2.1. In a closed magnetospheric topology

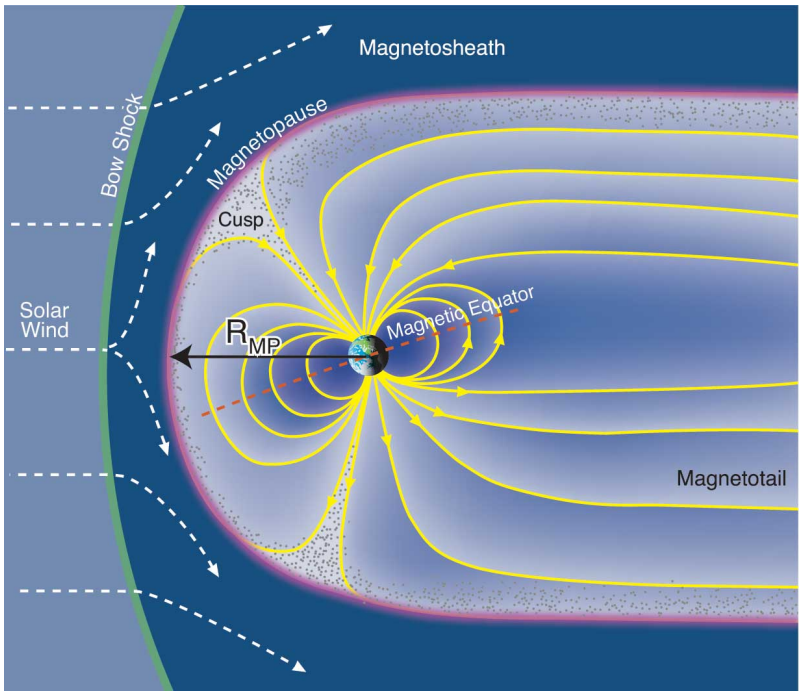

Figure 2.1: A closed magnetosphere in the noon-midnight meridian plane with the solar wind entering from the left-hand side and encountering a planetary system in the centre. Solar wind flow is indicated by dashed white line and the different regions of space indicated by their colour. The interplanetary medium (light blue) is separated from the magnetosheath (dark blue) by the bow shock (green). Inside this the magnetopause (pink) contains the magnetosphere (varying shades of blue). The planetary magnetic field lines are shown surrounding (yellow). The arrow labelled R_{MP} indicates the distance from the planet to the magnetopause, often referred to as the stand-off distance (Bagenal and Bartlett, 2012a).

the solar wind is separated from the magnetosphere entirely at the surface known as the magnetopause, this represents the outer-boundary of the magnetosphere and the position at which internal pressures balance with that applied by the solar wind. The magnetic field induced by processes localised to the planet in this set up is considered to be a perfect dipole, whose field lines are all connected inside the magnetosphere, ensure that Guass's law of magnetism is conserved.

It can be assumed that there are no strong plasma sources inside the closed magnetosphere, hence the dynamic pressure applied from the plasma contained within the region is negligible. Rather, the pressure to balance against the solar wind is provided by the magnetic field. Therefore, the distance at which the magnetic pressure equals that of the dynamic pressure of the solar wind can be obtained by taking the ratio of the magnetic effects of the planetary dipole to the kinetic effects of the solar wind. This is readily expressed in terms of the the radius from the planetary centre (Vasyliūnas, 2009), R_{MP},

$$\left(\frac{R_{MP}}{R_P}\right) = \left(\frac{\epsilon^2 B_{eq}^2}{2\mu_0 n_{sw} m_{sw} v_{sw}^2}\right)^{\frac{1}{6}}. \tag{2.2}$$

Where B_{eq} is the equatorial field strength of the planetary dipole and ϵ is a coefficient that accounts for additional terms enhancing pressure inside the magnetosphere. R_P is the radius of the planetary body under examination and hence the distance obtained is in units of this radii.

In order to understand the origins of the terms that can be summed and incorporated into eqn 2.2, first we must continue to examine the magnetospheric region bound by the magnetopause. With the solar wind encountering the boundary of the magnetopause and being unable to penetrate into the region surround the planet, the flow of plasma is instead redirected around the this separating surface. Therefore, the magnetosphere can be thought of as a cavity in the interplanetary medium inside which the dynamics are controlled by processes linked to the planetary system rather than the that of the interplanetary. We can begin to understand the dynamics in this separated region by considering that the it is the dynamic pressure of the solar wind balanced against the magnetic pressure of the planetary dipole. Recalling the definition of the plasma beta (eqn 1.35), this implies that the inter-planetary plasma has a high beta and the magnetospheric plasma has a low beta, though this assumption is found to be too simplistic within realistic systems.

Although the closed magnetospheric system lacks a strong plasma source, at least the simple one considered in this section, that is not to say that the cavity described is entirely devoid of material. The magnetopause is not completely impenetrable to the solar wind, though the physical mechanisms for this penetration are beyond the simple process described (Vasyliūnas, 2009). Additionally, the planetary atmosphere itself provides a source of material that flows into this region, though atmospheric processes are beyond the scope of this thesis (Russell et al., 2016). However, the plasma in the magnetospheric system can, and does, contribute to the pressure balance between the magnetosphere and the solar wind. This contribution is best described as a range of current systems.

Examining one of these current systems, the Chapman-Ferraro currents (Chapman and Ferraro, 1931), the mechanism for generation of these can be readily determined, even using our simplified closed magnetosphere assumption. These currents form on the surface created where magnetospheric pressure balances with that applied by the solar wind. Considering that the Lorentz force for a particle in a bulk plasma can be determined using $\frac{1}{q_s}(\underline{J} \times \underline{B})$ (see 1.1.5), it is readily found that particles entering this surface from the solar wind drift with a azimuthal velocity about the planet. Since the magnitude of this velocity is dependant on particle charge, ions and electrons move in opposite directions, establishing a current system. This current acts to add pressure to the magnetospheric portion of the pressure balance, being expressed by setting $\epsilon = 2$ in eqn 2.2 (Vasyliūnas, 2009), effectively inflating the size of the magnetosphere.

The assumption that the magnetosphere is completely separated from interplanetary fields and materials is clearly flawed, with processes such as magnetic reconnection allowing for the mixing of plasmas. If the systems were completely isolated then the IMF and planetary field lines would not be able to experience this reconfiguration in magnetic topology, removing a mechanism for the generation of magnetospheric dynamics. Magnetic reconnection itself is a driving mechanism for the Dungey cycle (Dungey, 1961), the effects of which are observable from the ground in the terrestrial system through the aurora. A diagram depicting an open magnetospheric topology can be seen in figure 2.2, with the solar wind flowing in from the left hand side and interacting with a planetary magnetic field to form a magnetosphere. In this figure it can be seen that the IMF has recently reconnected with a planetary field like, due to anti-parallel reconnection (see Hesse and Cassak, 2020), with the magnetic topology still in the progress of reconfiguration to minimise stress.

It can also be seen in figure 2.2 that the planetary magnetic field not only interacts with IMF at the front of the magnetosphere. Additionally, planetary field lines originating from high latitudes can also couple into the IMF. This preferentially happens in two locations, above the polar caps and down tail close to the magnetopause (Vasyliūnas, 2009). The implications of the open magnetosphere affect the structure and dynamics of this region.

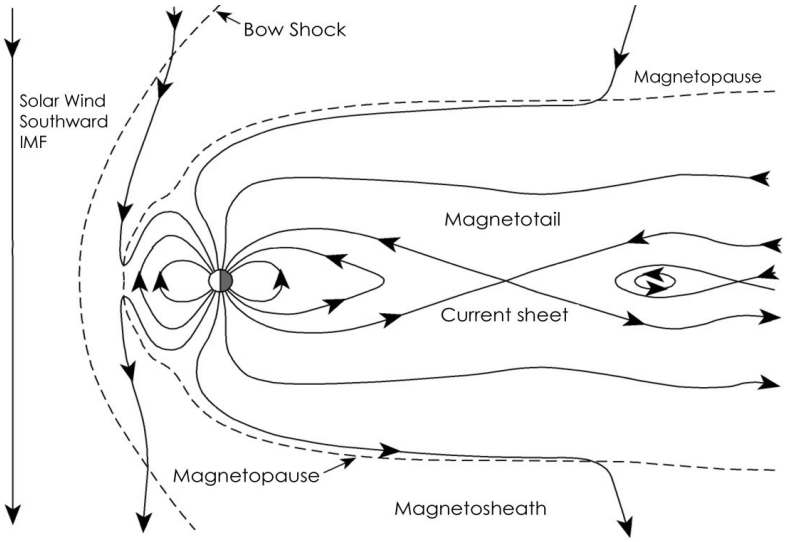

Figure 2.2: An open magnetospheric system, in the noon-midnight meridian plane, with the solar wind flowing towards the central planetary body from the left hand side. IMF field lines are seen and originate from outside the magnetospheric system. All magnetic field lines are indicated by solid black lines with arrows on them to indicate their directionality. Two seperatrices are indicated by dashed black lines, these confine different regions of the magnetosphere (Borderick, 2010).

2.1.2 Structure

Shape

The size of the magnetosphere is determined by the critical distance at which internal pressure from the planetary magnetic field balances with the ram pressure of the solar wind, calculated using eqn 2.2. This critical distance, more commonly referred to as the sub-solar point, describes the location of a single point, yet the magnetosphere is confined by a separating surface, the magnetopause. In order to determine the shape of the magnetosphere, this equation must be taken and generalised in order to calculate the location of the pressure balance at a range of locations.

If we consider the vector that points directly from the centre of the planetary body under examination to the Sun, in a simplified configuration where the spin and magnetic axis of the planet are at a right angle to this vector and the direction of orbit, then it can be seen that the stand-off distance determined lies upon on this. Taking a slice along this vector in the noon-midnight median plane, the shape of the magnetopause from $\sim \pi$-2π becomes readily obtainable by considering that pressure varies as a function of $\sin^2\theta$, where θ is the location on the separating surface. This gives an almost circular shape to the leading side of the magnetosphere (Russell et al., 2016). However, this approximation clearly begins to break down at locations close to orthogonal to the Sun-planet line, due to the simple expression devised for pressure balance becoming insufficient to describe the physics.

It is apparent that field lines with high degrees of inclination to the flow of the solar wind, which travels along the Sun-Planet vector in this example, provide only a small amount of magnetic pressure. Therefore, they become swept back in the anti-sunward direction, forming a long trailing region behind the planet known as the magnetotail (Sibeck and Murphy, 2021). To first approximation, as can be seen in figures 2.1 & 2.2, the sweeping back of these field lines can be considered to create an infinite straight set of boundaries aligned to the solar wind flow direction. However, this would imply that the magneto-

sphere contained an infinite amount of energy to continue providing pressure tangential to these swept field lines. Rather, it is determined that the pressure falls as a function of distance from the planet. Therefore, the tail thins as distance from the planet increases, eventually reaching a critical value at which the system closes. The physical mechanism responsible for determining the size of the magnetotail at any particular distance from the planet is the stress balance between that provided by the current sheet and the external magnetic pressure.

With a description now obtained for the magnetospheric structure in the 2-dimensional noon-midnight median plane, this can now be generalised for a 3-dimensional geometry. For the simple magnetospheric system that has been described, with a homogeneous and stationary IMF, the system becomes axisymmetric about the discussed Sun-planet line. This produces a spherical sunward facing side of the magnetosphere, often referred to as the dayside and a conic shaped structure on the trailing side, referred to as the night side. This topological setup is often considered as the 'traditional' configuration of a magnetosphere, resembling a tear-drop. The reason for this being the fundamental configuration is because it closely describes that of the terrestrial magnetosphere, with the ideal conditions being broken by the inclination of the magnetic and spin axis to the Sun-Earth vector.

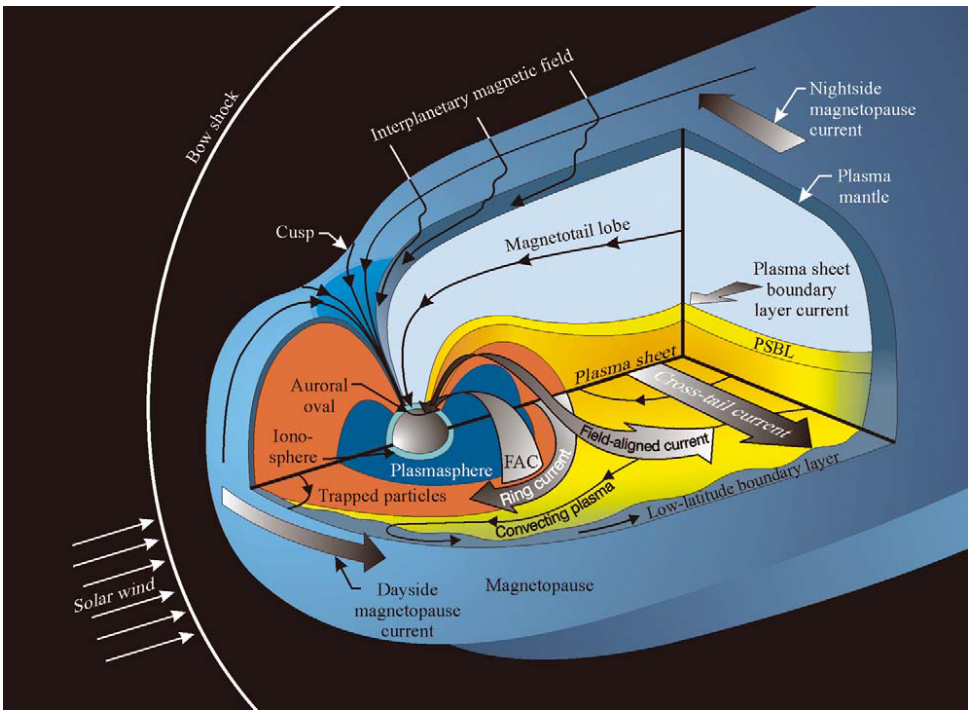

Figure 2.3: A 3-dimensional overview of the terrestrial magnetospheric system. Solar wind can be seen flowing from the left-hand side of the diagram (white arrows). The position of the bow shock is indicated (solid white curve), created by the interaction between the magnetopause and the solar wind. Magnetic field lines are shown (black line with arrows) with the IMF also shown (recoloured white). The magnetopause (outer blue surface) extends outside the diagram to the right-hand side. A slice is taken from the magnetopause to allow for viewing of the internal magnetospheric structure, regions of which are indicated by different colours. The main current systems are shown (grey arrows). (Pollock et al., 2020)

Figure 2.3 shows a 3-dimensional representation of the terrestrial magnetosphere. The solar wind flows from the left-hand side of the digram and encounters the planetary body in the centre. It can be seen that only the magnetospheric system close to the planetary body is depicted, hence the magnetotail appears not to thin as it has not moved sufficiently

far from the planet. The blue surface represents the magnetopause, out of which a section has been taken in order to allow viewing of different magnetospheric regions within. Grey arrows are also included that detail the main current systems within the terrestrial system, including: magnetopause currents (Chapman-Ferraro), ring currents, field-aligned currents and cross-tail currents. A complete review of current systems and their physical origins can be found in Ganushkina et al. (2018), however this falls outside the scope of this thesis.

Regions

Within the magnetospheric system it is possible to determine some indication of your position within the system without knowing your exact distance from the planetary body and the conditions of the solar wind & IMF. Rather, probing the material, mostly plasma, and EM fields in the position you occupy it is possible to determine at least an approximate location. This ability to classify different locations within the magnetosphere provides the necessary information required in order to subdivide the system into distinct regions.

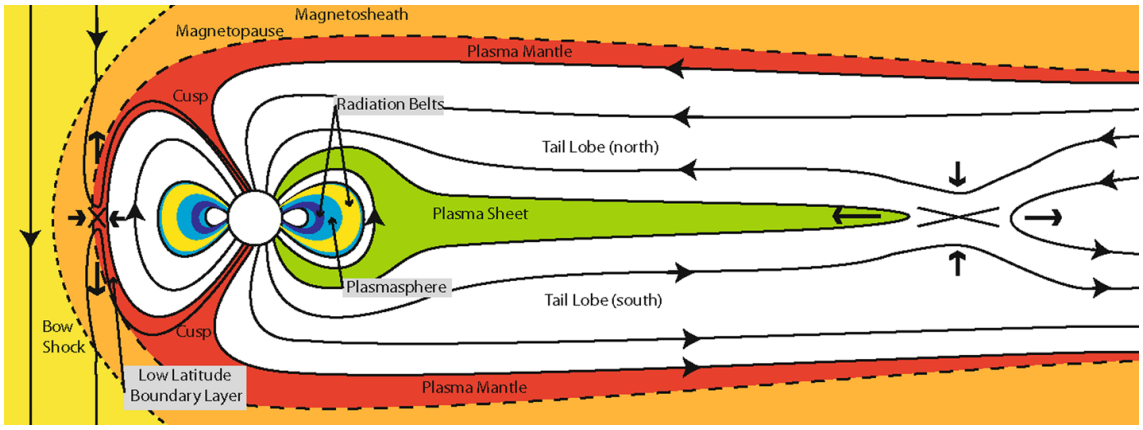

Figure 2.4: Overview of the terrestrial magnetosphere in the noon-midnight median plane, with different regions of the magnetosphere coloured for emphasis. Solar wind enters from the left-hand side with the IMF shown outside the magnetopause (black lines with arrows), inside the magnetopause the planetary magnetic field is also indicated (black arrowed lines again). A pair of seperatrices (black dashed lines) are shown, with the outer indicating the bow shock and the inner the magnetopause. The magnetotail can be seen to taper as it increases in distance from the planet (round body). Reconnection events can be seen occurring between the IMF and planetary field at the sub-solar point, as well as in the magnetotail, with both field lines originating from the planetary dipole (Eastwood et al., 2015).

Figures 2.3 & 2.4 both show the areas in the terrestrial magnetosphere that can be characterised as a distinct region. Figure 2.3 provides information of the 3-dimensional structure of these regions, however figure 2.4 is much clearer for the formal definition of them. Within figure 2.4 the global configuration is as would be expected after discussion in the previous section, with the figure taken in the noon-midnight median plane, much the same as those previously examined. However, an extra feature can be seen in this figure due to its extend view of the magnetosphere on the night side of the planet. This is as the tail moves further from the planet the straight edges of the magnetopause can be seen to taper, moving towards one-another. However, the figure is not extended far enough on the night side for the critical distance at which these meet to close the system can be observed. It is worth noting the tapering of these edges gives rise to the classically accepted tear-drop shaped system, however this configuration is not the only feasible solution (Macek et al., 1992)

A full and detailed examination of magnetospheric regions can be found in Russell et al. (2016) & Sibeck and Murphy (2021) and a brief history in the exploration & classification of them is provided by Southwood (2021). Here, a summary of the main regions will be presented from the point of view of the terrestrial magnetosphere, these will then be adapted for the outer planetary systems as necessary in the following section (§2.2). This approach is taken as the terrestrial system is often viewed as a generalised magnetosphere. Additionally, due to our location inside the magnetospheric system, it has the largest depth of examination and the most data available.

For our examination the system as presented in figures 2.3 & 2.4 shall be considered from left to right. This means we first consider the regions in which the solar wind encounters the planetary magnetic fields, before moving through the dayside of the magnetosphere towards the planet, into the nightside and finally down the tail. If we think of the solar wind as a stream flowing about the planet, then it is natural to conceptualise the dayside as upstream and the night as downstream.

Bow Shock

When the solar wind encounters the planetary obstacle in its flow path it is travelling at supersonic (and Alvènic) velocities and suddenly experiences rapid deceleration, to subsonic velocities, as its flow is redirected around the magnetopause. This rapid deceleration leads to the generation of a shock which propagates radially outwards from the magnetopause, but not inwards due to the impermeability of the magnetopause surface.

A thin transition layer, the Bow Shock can be represented by the black dashed line in figure 2.4 separating the yellow interplanetary space (the solar wind) from the magnetosheath in orange, both of which lie outside the magnetopause. Since this boundary layer can be considered a permanent feature it is clear that this region interacts with the solar wind, causing a shock inducing deceleration, before the incoming plasma can reach the inner magnetopause. However, the position of the region is not fixed and varies with solar wind conditions being able to be both expanded and compressed. Modern space technology has allowed for a series of missions to probe the bow shock, vastly improving our understanding of it, such as the Cluster and Magnetospheric Multiscale mission (MMS) detailed by Parks et al. (2021).

Magnetosheath

Between the bow shock and magnetopause is the region known as the magnetosheath. This can be seen in figure 2.4 as the orange region encompassing the entire boundary of the magnetopause. Solar wind transitions from the interplanetary medium into the planetary magnetosphere through the bow shock into the magnetosheath. Within this region the decelerated solar wind is slowed further causing a compression in both density, also furthering the compression of frozen-in IMF lines. This compressed plasma then flows around the impermeable magnetopause, convecting along the tail until it re-enters interplanetary space, rejoining the solar wind and effectively being ejected from the system.

The continual inflow of the solar wind experiences rapid deceleration, inducing shocks, along with compression due to the build up on the magnetopause, leads to a magnetospheric region with a myriad of turbulent processes. These processes include both the outbreak of plasma instabilities as well as the generation of different wave modes, which can cause wave-particle interactions. Despite the chaotic nature of this region its large-scale structure remains readily determinable with transient small-scale structures permissible within. Therefore, the magnetosheath provides the ideal laboratory for the examination and exploration of non-linear processes in plasma, with a number of space mission observing it and results compared with theory and models. Further discussions of observations

from this regions, as well as theoretical descriptions and models of it can be found in Lucek et al. (2005) & Narita et al. (2021).

Cusps

Above the magnetic poles of the planetary internal magnetic field are the regions known as the polar cusps, the northern polar cusp aligning, though not directly with the magnetic north and the southern polar cusp aligning with south. These regions can be seen in figure 2.4 inside the magnetopause, in the red coloured area above the magnetic poles. The configuration of planetary magnetic field in these regions allows for coupling to the plasma in the magnetosheath. Magnetosheath plasma can permeate into the cusps due to the lower magnetic field strengths in these regions as it convects around the magnetopause.

The polar cusps are inevitably tied to the conditions of the solar wind and the IMF, with reconnection occurring with the IMF in either a northern or southern configuration. The orientation of the IMF also controls the positions of the cusps in relation to the planet, varying in terms of both latitude and longitude (see Russell, 2000). Additionally, increased flow speeds or densities in the solar wind causes further compression in the magnetosheath leading to widening of the cusps. This region has been examined using various theoretical and numerical techniques as well as direct measurements taken by a range of space mission, a summary of this can be found in Lavraud and Trattner (2021).

Radiation Belts

The radiation belts constitute the region of the magnetosphere closest to a planetary body that will be covered in this section. These regions can be seen in figure 2.4 in a range of blues and a yellow bands either side of the planet and wrap around to create tori. Suggested by the name, these belts are not singular but rather represent a number of separate regions that can be classified together. These belts are separated, at least in the terrestrial case, into an inner and an outer belt, separated by a gap caused by pitch-scattering due to wave-particle interactions (see Lyons and Thorne, 1973).

The inner radiation belt, the smaller of the two, is made up of high-energy electrons (100's of keV) and protons (10-100's MeV). There are various mechanisms responsible for the population & energisation of plasma in this region such as energetic solar events. Additionally, material can be transported between the inner and outer belts, injecting fresh populations of plasma, triggered by events such as geomagnetic storms.

At the outer radiation belt, the larger region is contained a population of high-energy electrons (0.1-10's of MeV) as well as energetic protons and other ions from atmospheric sources. The size and particle flux in this region is extremely variable and have some dependence on solar cycle. This hints at the source for plasma in this region originating from the solar wind and diffusing inwards through the magnetopause to form this belt. Though radial diffusion alone is found to be insufficient to provide the entirety of the particle flux (Shprits and Thorne, 2004), hinting at local acceleration sources, such as wave-particle interaction. A more complete overview of the structure, dynamics and history of these regions is given by Li and Hudson (2019).

Plasma Sheet

Moving into the nightside of the magnetosphere, as previously discussed planetary field lines are swept back to form the magnetotail. In this stretched portion of the magnetosphere the planetary field lines can be found orientated away for the planet (anti-sunward) in one half of the tail and towards the planet (sunwards) in the other. These sections are separated in latitude along the equator of the planet by a theoretical surface at which the field strength is $\underline{0}$, known as the neutral sheet. Surrounding the neutral sheet is an

region containing distinct plasma properties known as the plasma sheet. This region of the magnetosphere can be seen as the green area in figure 2.4 on the night side of the planet, with a reconnection event occurring down tail and a resulting plasmoid being ejected (see Hones Jr., 1977).

The formation of the plasma sheet is a natural result of the magnetospheric configuration, the enhanced energy and density of the plasma in this region provides the pressure anisotropies & gradients required to prevent the return to a dipolar field (Bame et al., 1967). This region is formed either side of the neutral sheet and can be readily determined by the measure of the kinetic energy density of the plasma, inside the plasma sheet these are equal to the magnetic energy density, whilst they are much lower outer the sheet. Inside this region is a thinner sheet known as the cross-tail current sheet, through which another of the main current systems in the terrestrial magnetosphere flows (see Ganushkina et al., 2018).

Lobes

The regions either side of the plasma sheet, stretching the length of the magnetotail are known as the tail lobes. These can be seen in the white areas of figure 2.4 on the nightside of the planetary magnetosphere. The lobes are split into two sections, defined by the their latitude in relation to the field reversal that occurs either side of the neutral sheet. The northern lobes is above the neutral sheet (outside of the plasma sheet), in the noon-midnight meridian plane, with the magnetic field orientated towards the planet (sunwards) in this section. The southern lobe is conversely located below the neutral sheet with the field lines orientated away from the planet (anti-sunward). They both extend from the outside of the plasma sheet to the magnetopause, encompassing a large portion of the magnetosphere.

Plasma inside the northern and southern tail lobes is tenuous, with magnetic pressure dominate over thermal, as required for the low plasma-β assumption utilised to construct our magnetospheric topology. In order to sweep back the magnetic field lines and create the stretched magnetotail, there must be some interaction between the solar wind plasma and that contained within the magnetosphere, to impose this drag. Therefore, as the solar wind also carries the IMF (assuming frozen-in flux) in certain configurations there can be reconnection that occurs with planetary magnetic field lines in the lobes. Observations have been taken of the plasma in this region by a large number of space craft, such as by Coxon et al. (2016).

2.1.3 Convection

Though magnetospheres contain common regions that are readily identifiable, with the plasma in these indicative of the location occupied, this is not to say that the plasma contained within them is stagnant. Rather, these areas of space surrounding planetary bodies are so interesting to study precisely because of the range of plasma dynamics that can be observed to occur both within them and in the surrounding regions (i.e. the magnetosheath). However, the question arises of what mechanism is responsible for governing the flow of plasma through a magnetospheric system.

When considering the flow of plasma through a system as vast as a planetary magnetosphere, it is natural to reach for the framework of MHD to describe the motions (see §1.1.4), and in fact it is determined that magnetospheric configurations are well described by MHD (Bagenal, 2013). Further simplification is permissible with the ideal limit found to equally be able to describe these configurations. It is recalled that in this limit the magnetic field becomes frozen-in to the plasma and one moves with the other (see §1.1.5). Hence, the flows can be captured using eqn 1.25 and it is found convenient to rearrange

yielding (Baumjohann and Treumann, 1996),

$$\underline{E} = -\underline{U} \times \underline{B}_P. \tag{2.3}$$

With the electric field independent, it is permissible to use it to describe the flow of plasma through a magnetospheric system, as it intrinsically captures both the motions of the plasma and the planetary magnetic field. Immediately it is apparent that the choice of reference frame is important, as the flow velocity of the plasma is dependant on this choice. For example if an observer has the same reference frame as a plasma parcel (i.e. is placed in a parcel and allowed to flow with it), then they will see no motion associated with the parcel. Hence, the observed flow velocity will be $\underline{0}$ and the observer would experience no electric fields related to the flow velocity of the plasma parcel.

Turning to our idealised closed magnetospheric configuration described previously, it is clear that the only major source of momentum immediately available is the planetary body itself, representing a vast store of energy analogous to a flywheel. Recalling that the plasma is frozen-in with the planetary magnetic field lines then it is apparent that the connected plasma elements will be dragged along with the field as rotates with the planet and these elements are said to corotate with the body. For an observer in a non-rotational reference frame, then it is determine that the corotation electric field ($\underline{E}_{cor}$) generated by these motions is,

$$\underline{E}_{cor} = -\left(\underline{\Omega}_P \times \underline{r}\right) \times \underline{B}_P, \tag{2.4}$$

where $\underline{\Omega}_P$ is the rotational velocity of a generic planet P and $\underline{r}$ is a spherical coordinate system centred on the planet (Baumjohann and Treumann, 1996; Bagenal, 2013).

To identify a competing source of momentum for the transport of plasma then the assumption of the closed magnetosphere must be dropped, in order to allow for contributions from the solar wind. It has has already been discussed how Dungey cycle (Dungey, 1961) is created due to anti-parallel reconnection on the magnetopause. This allows plasma from the solar wind to enter the magnetospheric system, and which is then transported throughout the magnetosphere. A summary of the flow of plasma created by the cycle can be stated, unconcerned with physical mechanisms responsible for the generation of them, more complete descriptions can be found in Baumjohann and Treumann (1996) & Bagenal (2013). First, the plasma enters via reconnection on the magnetopause. It is then transported over the over the planetary poles and down the magnetotail until a critical distance is reached where the plasma elements are pushed together, creating an X-line (location of magnetic reconnection), this can be seen in figure 2.4. Reconnection in the tail releases a plasmoid that exits the magnetospheric system (down tail) and causes plasma to convect back towards the planet in the equatorial plane. Some of this precipitates down planetary field lines and the rest flows to the front (sunward side) of the magnetosphere.

The motions associated with this cycle of plasma through the magnetospheric system is captured in the convection electric current ($\underline{E}_c$). For an observer in a reference frame fixed with the planet, this can be obtained using

$$\underline{E}_{con} = -\underline{U}_{con} \times \underline{B}_P, \tag{2.5}$$

where $\underline{U}_{con}$ are the flows associated with the identified convection cycle (Baumjohann and Treumann, 1996). The importance of this convection in governing the flow of plasma through a magnetospheric system varies depending on the planetary body selected, see reviews at Mercury (Slavin et al., 2021), Earth (Eastwood et al., 2015) and Jupiter & Saturn (Badman and Cowley, 2007).

Plasma flow through magnetospheric systems is inevitably a combination of the two mechanisms captured in $\underline{E}_{cor}$ and $\underline{E}_c$. Examining 2.4 it can be obtained in the equatorial plane of the described ideal magnetospheric system as,

$$E_{cor} = \Omega_P B_{eq} / r^2, \tag{2.6}$$

where r is the radial distance from the planet. Hence, it can be readily determined that the strength of this corotation electric field falls with increasing radial distance from the planet. The region of space surrounding a planet in which plasma motions are controlled by the corotation electric field is known at the plasmasphere. The size of this region is hence controlled by the rate of planetary rotation and strength of magnetic field.

2.2 The Outer Planetary Systems

Each of the magnetised planets in our solar system has its own unique magnetosphere, representing a set of natural laboratories open for examination to gain further understanding of space plasmas. In the subset of outer planets known as the Gas Giants, both Jupiter and Saturn are situated at approximately 5.2 (Williams, 2021a) and 9.5 AU (Williams, 2021b) respectively. The two system share many similarities, with the planet at the centre of each being much more massive than the Earth, both in radius and mass, with strong internal magnetic fields and a gaseous surface. Each of the planets also rotate much more rapidly than then Earth. Hence, we group them together in this section, in which we examine the structure and dynamics of each system, highlighting similarities and differences between the two.

2.2.1 Jovian System

Jupiter's magnetosphere is a largest structure inside our heliosphere, if this expansive region of space was visible in the night sky it would be up to 3 times larger than a full moon to an observer gazing up. However, the magnetosphere, much like our own, is not visible for observation in the wavelengths of light perceivable by the human eye, rather more specialised instruments must be utilised to probe it. Despite this barrier, observations have been made since before the first space craft entered the Jovian system utilising radio emissions (Burke and Franklin, 1955) and found to be modulated by internal factors, such as the Galilean moon of Io (Bigg, 1964) as well as the solar wind (Terasawa et al., 1978).

The first in-situ observations from the system were provided when it was visited by the Pioneer 10 space probe in 1972, followed soon after by Pioneer 11 in 1973, performing flybys and utilising the planet's mass for a gravitational boost. Voyagers 1 & 2 were the next missions to visit the Jovian magnetosphere in 1979 during their grand tour of the solar system, a tour that still provides the only in-situ data we have for planets beyond Saturn. Ulysses was the next craft to visit in 1992, once again using the planet to gain for orbital purposes, this time to head back inwards to study the Sun. A dedicated mission to study the system was sent next, the Galileo space probe, arriving in 1995, however the mission results were limited due to a technical fault on its high gain antenna limiting bandwidth. Cassini flew though the system in 2000, en route to the Saturnian system, gathering data as it performed a fly-by (Bagenal et al., 2007). Finally, the most recent mission, Juno, another dedicated Jovian explorer, arrived in the system in 2016 and is still in operation at the time of this work.

The measurements taken from these missions, in combination with insights gained from observations made utilising remote sensing instruments in the terrestrial system, has provided a wealth of knowledge not only on the magnetosphere, but also on the planetary body itself as well as the satellites orbiting it. These have allowed for the structure and dynamics of magnetospheric mechanisms to be studied and classified, allowing for large scale temporally stationary features to be identified. Of course not all insights have been yielded through the acquisition and analysis of data, many mathematical and computational models of the region have been constructed providing a vital tool for understanding the mechanisms identified. Recent success in analysing the global magnetospheric system

has been found by the GAMERA MHD code (Zhang et al., 2019, 2021), examining how the global system impacts phenomena such as the aurora.

Magnetospheric Structure

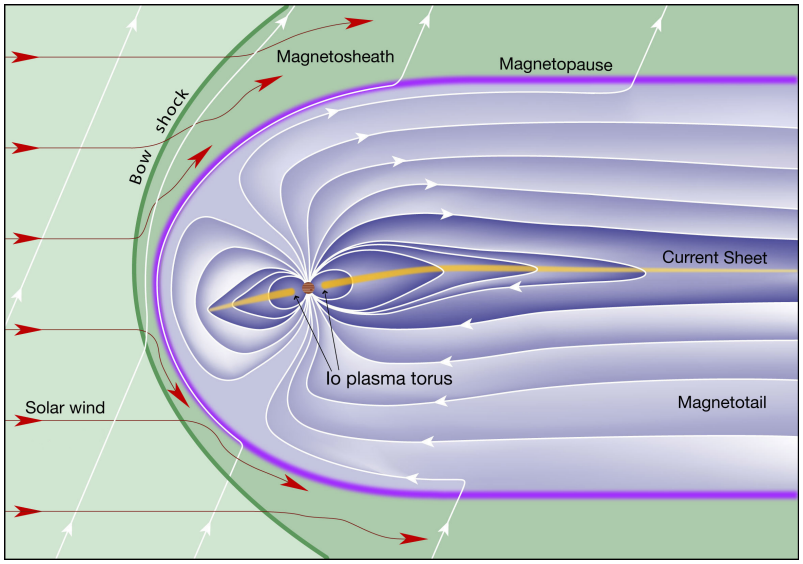

Figure 2.5: Structure of the Jovian magnetosphere, shown in the noon-midnight meridian plane, with the Sun to the left-hand side, hence the solar wind (red lines with arrows) arrives from the left. Interplanetary space (light green) can be seen outside the bow shock containing the IMF (white lines with arrows). The magnetosheath (green) is inside the bow shock (dark green line), further the magnetopause (dark purple) can be found inside bounding the magnetosphere (varying shades of blue). Magnetic field lines (white lines with arrows) are shown originating from the planetary body (red circle) and can be seen reconnection with the IMF in the lobes. The current sheet (yellow line) is indicated and the density of plasma inside the magnetosphere can be approximated by the darkness of blue (Bagenal and Bartlett, 2012b).

An initial overview of the Jovian magnetospheric structure, shown in figure 2.5, will find many similarities between it and the generic magnetosphere described in §2.1. When comparing the terrestrial magnetosphere to that of the Jovian the first, and most obvious, difference is that the latter is much larger than the former. When we consider our simple magnetospheric constructed in the previous section, the reason for this size difference begins to become apparent. This is because both the ram pressure of the solar wind is lower and the induced magnetic field strength is larger (see table 2.1). Using eqn 2.2 we can estimate the stand-off distance for the Jovian magnetopause (including Chapman-Ferraro currents) at $\approx$38 R_J, where R_J is the radius of the Jupiter in System III coordinates (see Seidelmann and Divine, 1977). However, when compared with the most probable locations of the magnetopause stand-off distance, 63 R_J & 92 R_J (Joy et al., 2002), determined by combining spacecraft observations with numerical modelling, it is readily seen that the simple pressure balance underestimates this distance. Therefore, it is apparent that mechanisms, beyond those required to construct our simple terrestrial magnetosphere, are necessary in order to explain that of the Jovian system.

Examining the planetary parameters in table 2.1, a key difference in the Jovian system is found, that is the planetary rotation rate is much greater than the that of the Earth, with a Jovian day being less than 10 hours long. Therefore, it is necessary to consider the contribution of the rotational force generated by the rapid spin of the Jovian planetary

Planetary Parameters	Jupiter	Ratio (Jupiter/Earth)
Mass (10^{24} kg)	1898.13	317.83
Radius (km)	71492	11.209
Equatorial Magnetic Field Strength (μT)	417	13.67
Day Length (hrs)	9.9259	0.414
Dipole Tilt (deg)	9.4	0.80
Solar Wind Dynamic Pressure (nPa)	0.092	0.039

Table 2.1: Summary of relevant planetary parameters for the Jovian system and the interplanetary medium, in the form of the solar wind, at Jupiter's orbital distance. Parameters are presented as a ratio to their corresponding terrestrial values in order to highlight key similarities and difference between the magnetospheric systems. Jovian parameters are obtained in System III coordinates as collated by Williams (2021a) and solar wind parameters are obtained by Slavin et al. (1985).

body on the material in the space surround. If a plasma is placed in the space surrounding Jupiter and the frozen in condition satisfied, then it will be accelerated and forced to co-rotate with the planet at its angular velocity. Under this assumption, a reference frame to examine the plasma can be selected such that it also perfectly co-rotates with the planet. In this frame the plasma will appear stationary in terms of the azimuthal direction, however will move towards or away from an observer based on the magnitude of the opposing gravitational and centrifugal force/pseudo-force (with Coriolis & Euler terms neglected).

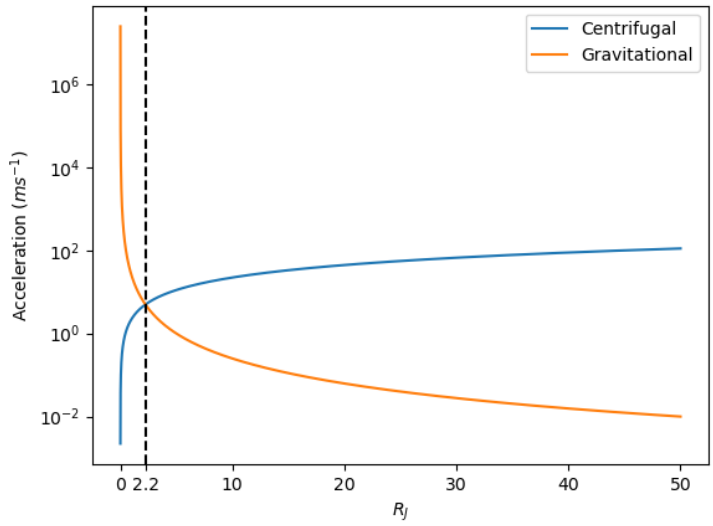

Figure 2.6: Comparison of acceleration provided by gravitational (blue) and centrifugal (orange) force/pseudo-force to material in the Jovian system from near the planets surface (1 R_J) into the outer magnetosphere (50 R_J). Gravitational force begins as the dominate and decreases with distance from the planet, inversely the centrifugal pseudo-force becomes larger as distance increases. At the critical value of approximately 2.2 R_J the two forces balance each other, indicated by the black dashed line. The magnitude of the accelerations are presented with the gravitational force acting in opposition to the centrifugal.

This force balance is shown in figure 2.6, it can be seen that the direction the plasma moves in a particular region of the system depends on its initial location. Material that is close to the planet will be moved towards it as the gravitational force is dominant,

material further away will be moved outwards as the centrifugal pseudo-force is dominant. The critical value that separates these regions of bifurcating dynamics is at approximately 2.2 R_J, the location at which the forces are equal, therefore material at this location is trapped and remains stationary.

The size of the Jovian magnetosphere has already been stated, and is clearly much larger than 2.2 R_J. Therefore, rotational forces are dominant over gravitational for a majority of the magnetospheric region and play an important role in dictating the physical dynamics of it. However, assuming frozen-in conditions for the entire plasma is in the magnetosphere is not reasonable and therefore our assumption of perfect co-rotation needs re-examining. Indeed when observational data is examined from spacecraft it is determined that rigid co-rotation is found close to the system but this rotational velocity falls further from it (Hill, 1980). However, the conclusion of the importance of rotational forces in the Jovian magnetosphere remains valid.

The profile of angular velocities as a function of distance from the planet for a plasma in the Jovian system can be obtained by considering inertia within the system. It is determined that at distances > 20 R_J that the angular velocity of the plasma begins to slow below that of the planetary rotation and hence begins to lag co-rotation, with the magnetic field and planetary atmosphere no longer able to provide the required forcing at above this distance (see Achilleos et al., 2021). This examination can also be performed by the utilisation of semi-empirical modelling, which allows for the incorporation of more plasma dynamics into the functions to obtain the angular velocity. An example of this is provided by Caudal (1986), in which a MHD model is constructed using initial conditions consistent with spacecraft data, using this model updated profiles of many key plasma parameters in the Jovian system were obtained.

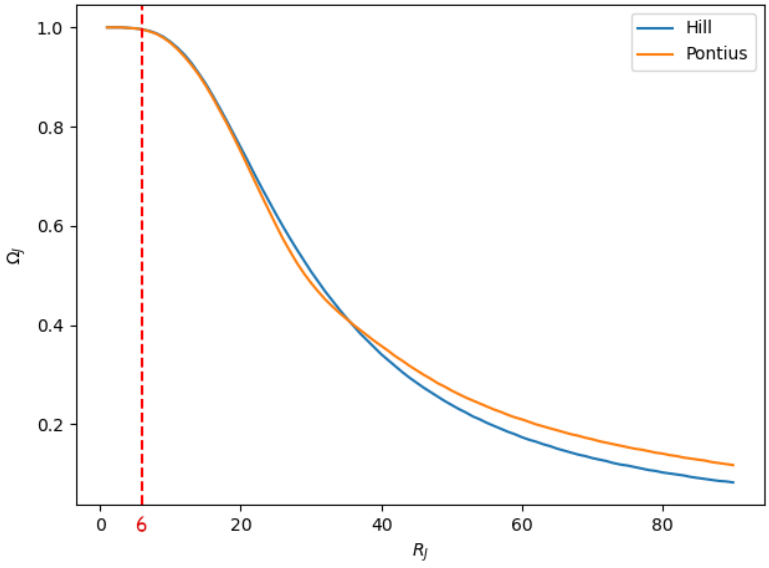

Figure 2.7: Two profiles of angular velocities of plasma in the Jovian magnetosphere as a function of distance given as a ratio to the planetary rotational velocity. $\Omega_J = 1$ represents rigid co-rotation with values greater than this indicating super co-rotational plasma and less than this indicating sub co-rotation. One profile (in blue) shows the variation in co-rotation by analysing the inertial balance of the system utilising a dipolar planetary magnetic field (Hill, 1979), the other (in orange) shows an updated profile, corrected by the inclusion of non-ideal terms in the planetary field model (Pontius Jr., 1997). Red dashed line indicated position of the outer edge of Io's plasma torus, placed at 6 R_J. Millas (2022) calculated profiles and provided data.

Figure 2.7 shows two profiles of the co-rotational velocity of plasma in the Jovian magnetosphere as a function of radial distance. These profiles are both determined by examining inertia through the system as a function of radial distance in Jovian radii. The blue profile is obtained following Hill (1979), in which the planetary magnetic field is assumed to be a simple dipole. The orange is a corrected profile following Pontius Jr. (1997), in which a more complete description of the planetary field is utilised. The angular velocity of the plasma is normalised in regards the rotational velocity of the planet, Ω_J, the velocity at which plasma moves when in rigid co-rotation with the planet. Therefore, when plasma examined using this normalised has values $\Omega_J > 1$ it is said to be super co-rotating, and when it has values $\Omega_J < 1$ it is sub co-rotating. Examining the form of the two profiles it can be seen that the corrections provided by the incorporation of a more complex magnetic field do little to change the overall trends. Both can be readily seen to be approximately constant, in rigid co-rotation, until 20 R_J. Between 20-40 R_J the angular velocity of the plasma decreases, leading it to sub co-rotate, in a linear manner, outside of 40 R_J the rate of decrease slows seeming to reach some minimum value far in the outer magnetosphere. It is worth noting however that in-situ measurements taken do not find the levels of sub-corotation determined using these models.

Analysing the plasma present in the Jovian system yields the presence of heavy ions in abundance, such as oxygen (O^+, O^{++}) & sulphur (S^+, S^{++}, S^{+++}) (see Khurana et al., 2004). This yields the question as to the origin of these ions. Examining the solar wind it is found that it is almost entirely comprised of hydrogen ions ($\approx 95\%$), with a small amount of helium ($\approx 5\%$) and trace amounts of heavier elements (Hundhausen, 1995). Turning to the planetary atmosphere it is also found to be primarily comprised of hydrogen ($\approx 86\%$) & helium ($\approx 13.6\%$), with trace amount of heavier elements and molecules (Taylor et al., 2004). Therefore, the source of the abundant oxygen & sulphur ions found in the Jovian magnetosphere is not immediately apparent.

The volcanic moon of Io is found to be a ready source of Sulphur Dioxide (SO_2), ejected into its atmosphere by continual volcanic activity generated by tidal heating (see Lellouch et al., 2007). Analysing the outflow of material from Io, it is determined that approximately 1000 kg s^{-1} is ejected from the moon (Broadfoot et al., 1979; Spencer and Schneider, 1996), forming a neutral cloud surrounding it. However, it is not only SO_2 that escapes from Io, rather a range of different molecules associated with volcanic activity are emitted, with sodium (Na) being the first element detected around the moon by analysing optical spectra (Brown, 1974). Optical detections of sulphur (S) are much more difficult due to the relative brightness of sodium emissions being much greater in comparison to these elements, with oxygen (O) emission almost completely lost, however some observations have been possible (see Thomas et al., 2004). In-situ measurements have proved much more beneficial in gaining insights into the distributions of S & O, and some of there associated ions (S^{++} & O^+ being exceptions to this), surrounding Io (in the vicinity of it orbital radius) (Bagenal et al., 1980; Bagenal, 1985, 1994; Bagenal et al., 1997) and beyond (Bagenal et al., 1992, 2016).

A portion of the neutral material surrounding Io is ionised through charge exchange and electron impact (Saur et al., 2003) as well as less prominent processes such as photo-ionisation. This freshly ionised material forms a plasma surrounding the moon that is now connected to Jupiter through the planetary magnetic field. The location of Io is indicated in figure 2.7, with the moon itself orbiting at approximately 5.9 R_J, and it can be seen that plasma in this region is accelerated to be in rigid co-rotation with the planet. Hence, the freshly ionised material is accelerated from the orbital velocity of Io, $\approx$54 km s^{-1}, to co-rotational velocities as dictated by radial location. Since the orbital velocity of Io is lower than that of the planetary spin then the plasma is accelerated around the planet to form a toroidal region of space known as the Io plasma torus Thomas et al., 2004;

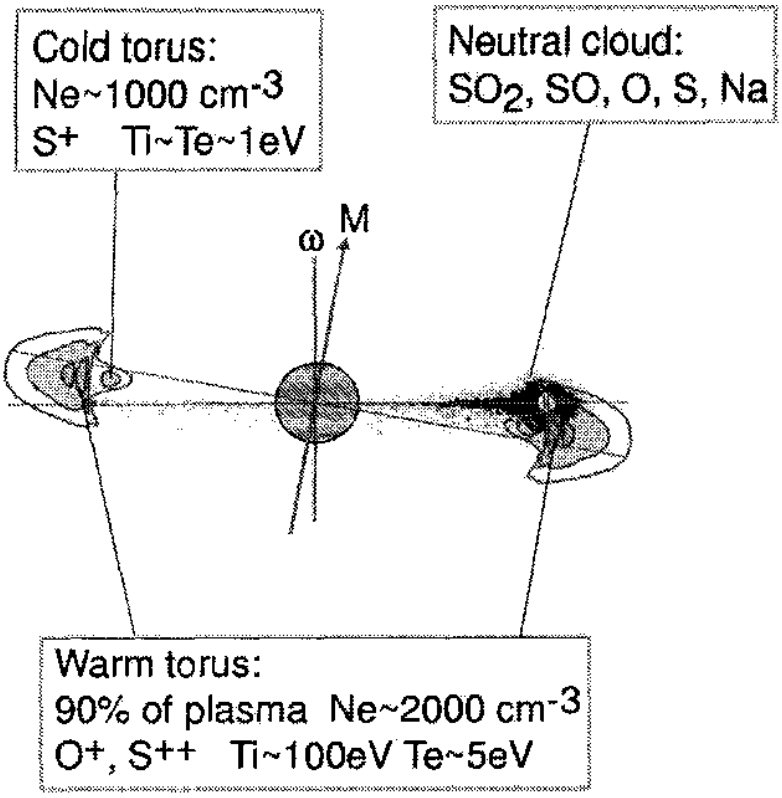

Figure 2.8: Slice through the noon-midnight plane of the Jovian system, containing the Galilean moon Io and a cross-section of the associated plasma torus. Io is on the right-hand side of the plasma torus with the neutral cloud created by volcanic activity on the surface shown sing black dots. The plasma torus is seen on both the left and right-hand side of the central planetary body, with the cold & warm regions indicated. Additionally, approximate density gradients are indicated with denser areas shaded in darker. Labels indicate the approximate electron densities in the indicated regions, along with the corresponding plasma species and energies. The magnetic & spin axis are represented by arrows through the centre of the planetary body (adapted from Thomas et al., 2004).

Schneider and Bagenal, 2007.

The Io plasma torus is commonly stated to extend between approximately 5-6 R_J and possess its own internal structure. The torus can be subdivided into 3 distinct regions: the cold torus, the ribbon and the warm torus, and these can seen in figure 2.8 with the ribbon being a thin region between the cold and warm tori. Despite the quoted upper limit of 6 R_J, just outside of Io's orbital distance, the actual outer edge of the torus is much harder to exactly locate. Rather the 5-6 R_J better summarises the distance from the centre of the cold torus (5.3 R_J) to the centre of the warm torus (5.9 R_J) (Phipps et al., 2020).

The cold torus represents the inner region of the overall structure, sometimes referred to as the disk, it is filled with plasma at lower energies ($\approx 1-2$ eV) than that of the outer portions, with the main constituent ion being S^+. The processes associated with filling this region are still unclear, however are thought to be connected to radial diffusion. The ribbon is usually the brightest region of the plasma torus when observed remotely, with S^+ being the dominant emitter. This region is clearly determinable in in-situ measurements as it represents a maximum in the electron number density in the torus. The mechanisms thought to be responsible for ribbon are associated with fresh plasma being continually sourced from Io, as well as the interaction of the moon with the plasma creating wakes

(see Saur et al., 2004). The warm torus constitutes the majority of the torus both in terms of space occupied and the amount of plasma contained within. This outer region is often referred to as the donut and contains higher energy plasma, of all constituent species, associated with outflow from Io's surface.

Plasma from the volcanic moon of Io, as well as from other sources such Callisto (though to a much lesser extent) (Liuzzo et al., 2015), provides a source of internal pressure changing the simple pressure balance utilised to construct eqn 2.2. This plasma inside the magnetosphere can by thought to push against the magnetopause, inflating the size of the magnetosphere. Though this is a highly dynamic contribution as the rate of mass loading from these satellites is variable and material moved & lost from the magnetospheric system by a variety of processes.

Focusing on the structure of the Jovian magnetotail, it is found to extend in the anti-sunward direction, with detections made by the Voyager missions at distances of approximately 7000 R_J (Khurana et al., 2004). A plasma & current sheet is found between two lobes through with cross-tail currents flowing. However, looking at the magnetic field lines in figure 2.5 they can be seen to be a different shape to the generic case previously examined. This is because the material ejected by Io, and then ionised, is moved radially outwards due to the strong rotational forces generated by the planetary spin. The outwards moving plasma can be thought to drag the magnetic fields lines out with it, causing them to become distended as they are stretched. When examining the exact physical mechanisms that cause this distension it is found to be a balance of the mechanical stress created by the centrifugal (rotational) force, pressure gradients & anisotropies against the restoring magnetic tension. The combination of these mechanisms is responsible for extending and creating the magnetotail, rather than open field lines connecting to the IMF as in the terrestrial system. This alternate mechanism for the creation of the magnetotail changes the overall structure of the magnetosphere, resulting in a much large system in which the magnetopause on the nightside of the planet remain relatively flat, this structure is known as a magnetodisk (Vasyliunas, 1983).

Considering the near equatorial current & plasma sheet and the tension required to balance magnetic effects, it is readily determinable that these sheets possess pressure gradients, gradients in the plasma flow kinetic energy & pressure anisotropies. In a rotationally dominant system these stresses are required to be perpendicular to the flow of plasma, partially controlling the shape and size of these important regions in the magnetospheric system (Vasyliunas, 1983). The contributions of pressure gradients and associated anisotropies were measured using data from the Voyager missions and it was determined that the pressure anisotropies provided the largest contribution compared with pressure gradients and centrifugal stresses (Paranicas et al., 1991). Additionally, computational techniques can be utilised through the development of numerical models in order to examine the contribution of these individual components to the total stress (Caudal, 1986; Nichols et al., 2015)

It is also worth noting that despite the assumption of a simple dipole to represent the planetary magnetic field, the structure of Jupiter's internal magnetic field is in fact much more complicated. To a first order, it can be determined that a dipole provides an adequate description, however a more detailed inspection requires higher order techniques to be utilised. Spacecraft measurements provide an excellent resource that can be analysed and fit to construct models of the field structure. This was done with results from the Pioneer missions by Acuna and Ness (1976) and a complete discussion of models in the pre-JUNO era can be found in Khurana et al. (2004). The orbital pattern selected for the JUNO mission, along with high cadence magnetometer measurements have allowed for more accurate models of the Jovian magnetic field to be constructed (Connerney et al., 2018, 2022), with work on-going to further improve these with the JUNO probe still in

operation at the time of this thesis.

When the effects, outside of the traditional magnetic pressure against the ram pressure of the solar wind, detailed in this section are utilised to adapted eqn 2.2 (see Vasyliūnas, 2009), a magnetopause subsolar distance is determined that sits within the range of observed values. However, the bimodal configuration determined using probabilistic modelling techniques with results from a variety of space probes (Joy et al., 2002; McComas et al., 2014) can not be captured by this simple force balance. Therefore, it is clear that dynamical processes both internal to the magnetosphere as well as in the solar wind are important to consider when examining processes. The magnetospheric regions of interest in this thesis are well inside the magnetopause, therefore focus will be given to the dynamics within.

The Io Plasma Torus and Magnetospheric Dynamics

When considering dynamics in the Jovian magnetosphere it is clear the planetary rotation rate does not vary temporally. Not only is this not observed using remote optical instruments, but also confirmed using in-situ data, such as the planetary magnetic field (Yu and Russell, 2009). Considered from an angular momentum point of view, the force required to either slow or accelerate the spin of a planet with the mass of Jupiter (see table 2.1) is truly astronomical. Therefore, we can conclude the temporal variation of the planetary spin is not of importance to the systems and dynamics we are interested examining.

Internal sources of plasma, particularly from the volcanic Galilean moon of Io, are found to be incredibly active (see Williams and Howell, 2007). However, material directly emitted from the moon does not directly enter the larger magnetospheric structure, as detailed previously. Rather neutral clouds form in the vicinity of the moon, proportions of which are then ionised and brought into co-rotation with the planet to form a plasma torus. Further, previous examination of the structure revealed that pressure gradients and anisotropies in combination with outwards plasma convection are responsible for contributing to the overall size of the magnetosphere, hence it is concluded that the plasma from this torus must be transported radially outwards by some mechanism. Clearly this must be the case as the Io plasma torus is not continually inflating and therefore must have mechanisms associated with it that allow for material to be removed. Therefore, it is natural to conclude that in order to fully understand the dynamics of global magnetospheric system, it is import to gain a detailed physical understand of the dynamics of internal plasma sources through to their sinks.

There are two main mechanisms found to be responsible for the removal of mass from the Io plasma torus (see Thomas et al., 2004; Rymer, 2021). The first of these is ejection of particles as energetic neutrals, this occurs as ions are accelerated to co-rotational velocities, as required to form the plasma torus, however these ions can still interact with both other charged particles in the system as well as neutrals. These interactions lead to charge exchange between atoms and can cause the co-rotating ions to become electrical neutral once again, hence these no longer feel the influence of the magnetic field but retain their kinetic energy. Therefore, these particles, known as energetic neutral atoms (ENAs), now follow a ballistic trajectory and are fired out the torus, whilst maintaining the total change density within these regions. It is possible to take in-situ measurements of these ENAs and use them to examine the regions from which they originate, in the Jovian system this has been done using both Cassini (Krimigis et al., 2002) & JUNO (Mauk et al., 2020), with the future JUICE mission also equipped with an ENA detector (Grasset et al., 2013).

The other main process for removing material from the torus is via bulk transport radially outwards. Outward motion is a natural consequence of the rotational forces applied by Jupiter through its magnetic field to its magnetospheric plasma, with the centrifugal pseudo-force, directed radially away from the planetary centre, being dominant

over gravitational forces at Io's orbit (as seen in figure 2.6). Of course though material is transported outwards, away from the planet, eventually being lost down-tail into the background interplanetary medium, the magnetic flux contained within the plasma must be returned to the planet in order to enforce magnetic flux conservation. The mechanism generally attributed to this is the radial (or centrifugal) interchange instability (see Thomas et al., 2004; Krupp et al., 2004; Achilleos et al., 2015). This process of plasma being transported radially outwards and the mechanisms associated with this constitutes the main topic of interest in this thesis, hence a detail discussion on this process can be found in §3.

The amount of material being transported by these two processes can be determined by the use of a 0-dimensional neutral cloud model. This model considers the following parameters in order to determine this: neutral source rate, O/S source ratio, transport loss, hot electron fraction, and hot electron temperature (Delamere and Bagenal, 2003). The results produced are verified by comparison with data collected from various space probes including, Voyagers 1 & 2 and Cassini. Utilising this modelling technique it is determined that of the overall neutrals emitted from Io between 20-37% are sulphur atoms and 63-80% are oxygen. Further, after ionisation 49-67% of the total plasma created is lost as ENAs, the remaining 33-51% is transported radially outwards (Delamere and Bagenal, 2003; Delamere et al., 2007). These processes can be seen summarised in figure 2.9 through the use of a flow diagram.

Additionally, it can be seen in figure 2.9 that a break down is given for the flow of energy through Io's plasma torus. An input of energy into the system occurs with the inflow of hot electrons (18-60%) along with the pickup of fresh ions (40-82%), this can be broken down by ionisation process to determine that electron-ion impact ionisation contributes a total of 17-19% & charge exchange reaction between 23-63%. Once ionised and accelerated energy is transferred between freshly picked up ions to electrons until a average steady state within the torus is reached. When plasma is removed via the two main mechanisms described 5-20% of energy flows out of the system via ENAs and 6-10% is removed with the plasma that is transported radially outwards. The remaining 69-89% of the energy with the torus is transmitted out by the excitation of ions from their base state, as these relax photons are emitted, removing the energy as UV radiation. A small proportion is additionally lost through inelastic collisions and through the excitation of neutrals, but account for only minor fractions of the total flow.

Loss of Internal Material

The global configuration of mass transport in the Jovian magnetosphere is described by what is now known as the Vasyliunas cycle (Vasyliunas, 1983). This details the process by which plasma is able to be transported anti-sunward, down the magnetotail and eventually released into interplanetary space, whilst allowing for the return of magnetic flux to the planet. It has been shown that as plasma moves radially outwards, away from the planetary body, it begins to sub co-rotate. On the dayside of the planet, it can be assumed that as co-rotation decreases, as function of radial distance from the planetary body, inwards stresses created by the solar wind applying pressure on the magnetopause provides the necessary force to ensure the plasma continues rotating around the planet. However, on the nightside of the magnetospheric system there are no stresses able to continue to enforce rotation and hence the flow path becomes almost straight at an adequate radial distance. The resulting flow pattern creates both X and O-lines in the magnetic field structure, along the X-line magnetic reconnection is permitted resulting in the release of a plasmoid. The plasma released by the creation of this plasmoid is no longer magnetically connected to the planet and hence can travel freely down-tail in the anti-sunward direction.

The flow pattern described by the Vasyliunas cycle can be seen detailed in figure 2.10.

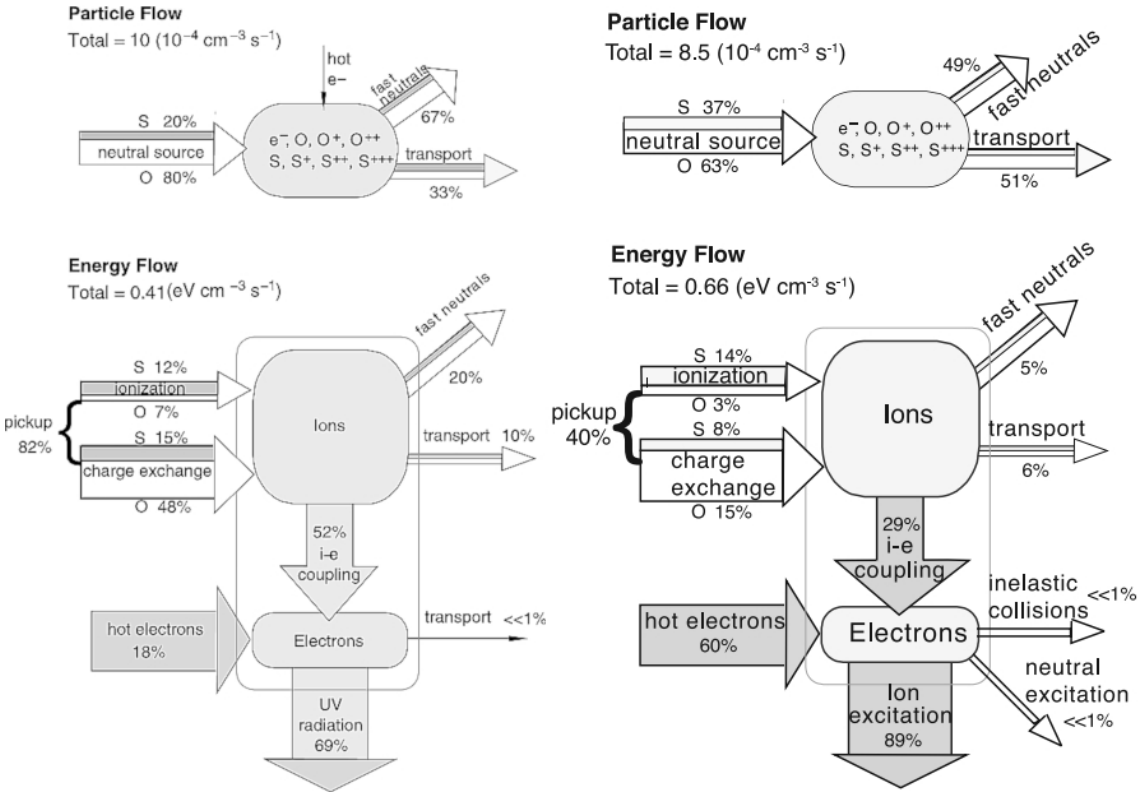

Figure 2.9: Two flow diagrams detailing the transport of both material and energy through the Io plasma torus determined using a 0-dimensional neutral cloud model. Both diagrams follow the same flow structure, with the particle flow detailing the proportion of the total neutral material ionised to form the torus as a percentage of sulphur and oxygen atoms. The box contains (with hot electrons added) the neutral atoms in the model (S, O) along with the ion species included (O^+, O^{++}, S^+, S^{++}, S^{+++}) and electrons (e^-). Finally, the outflow mechanisms are indicated along with the percentage proportion of material removed via these. Beneath the energy flow through the Io plasma torus is shown, with inflow from ions freshly picked up after creation as well as from the addition of hot electrons. The energy within the torus is then transferred between the ions and electrons until a steady state is reached. Energy flows out of the system via a number of processes, with the amount contained within the two mechanisms associated with the removal of material given. Delamere and Bagenal (2003) (left), Delamere et al. (2007) (right)

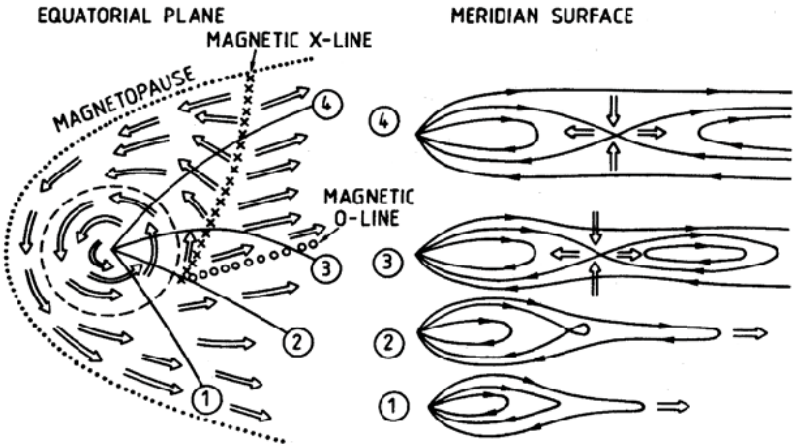

Figure 2.10: Plasma flows within the Jovian magnetodisc as viewed from above (left) and in a series of meridional projections along the numbered solid lines (right). Double-tailed arrows indicate plasma flows in both panels. Field lines are indicated by solid lines in the meridional projections. Dotted and dashed lines (left) indicate the magnetopause and critical Alfven surface respectively. Magnetic X- and O-lines are indicated on the left-hand panel (Vasyliunas, 1983).

The plasma can be seen flowing around the planet on the dayside inside the magnetopause and can be seen to be flowing more radially outwards in the magnetotail. The position of a X & O line is indicated in the pre-dawn sector, created by a bifurcation in flow direction being created a some critical radius, at which the plasma can no longer continue to rotate around the planet. Assuming that the plasma satisfies the conditions of ideal MHD, the magnetic field (and hence flux) is frozen into the plasma and therefore convects along within. Hence, at this this critical value a thinning of current sheet occurs as the magnetic field lines become stretched until magnetic reconnection can occur, this implies the existence of a O-line in order to ensure that Gauss's law for magnetic fields ($\nabla \cdot \underline{B} = 0$) is conserved. Slices through the indicated flow structure are shown on the right-hand side of the figure in the noon-midnight meridian plane, with the plasma flow into the X-point where reconnection occurs also indicated. Slices though the O-line are visible as circular magnetic field lines entirely contained within the magnetotail and no longer connected to the planetary body.

After reconnection has occurred the plasma remaining in the magnetosphere continues to be connected to the planet, however is now much more tenuous and heated (see Hesse and Cassak, 2020) by the reconnection event. Considering that magnetic flux is frozen into our plasma (assumed to return to obeying ideal MHD post-reconnection), it is readily determinable that a cylindrical region of space can be defined by inside which magnetic flux remains constant, assuming that the walls are determined by a closed set of field lines, known as a magnetic flux tube (see Priest, 2014). These tubes have an associated buoyancy (Parker, 1955) and in the rotationally dominated Jovian system the flux tubes filled with the depleted plasma are able to move radially inwards towards the planetary body, allowing the contained magnetic flux to move with the plasma. Hence, with the flux now returned to the planet the system is closed with all magnetic conservation rules conserved and internal material given a mechanism to escape the magnetospheric system (see Vasyliunas, 1983; Krupp et al., 2004; Rymer, 2021).

In-situ measurements provided by multiple missions have yielded observational evidence to support the existence of the Vasyliunas cycle. The Galileo mission found signature of strongly directed north & southward directed magnetic fields in the predawn section of the magnetodisk, strong evidence of recent reconnection in these plasma parcels

(Russell et al., 1998). A survey of reconnection events and their associated flows primarily comprised of data from the Galileo mission, though some from the Pioneer and Voyager missions is also included, is presented by Vogt et al. (2010). More recently data from the JUNO mission has provided further examples of reconnection events, along with associated enhanced radial flows (Vogt et al., 2020).

2.2.2 Saturnian System

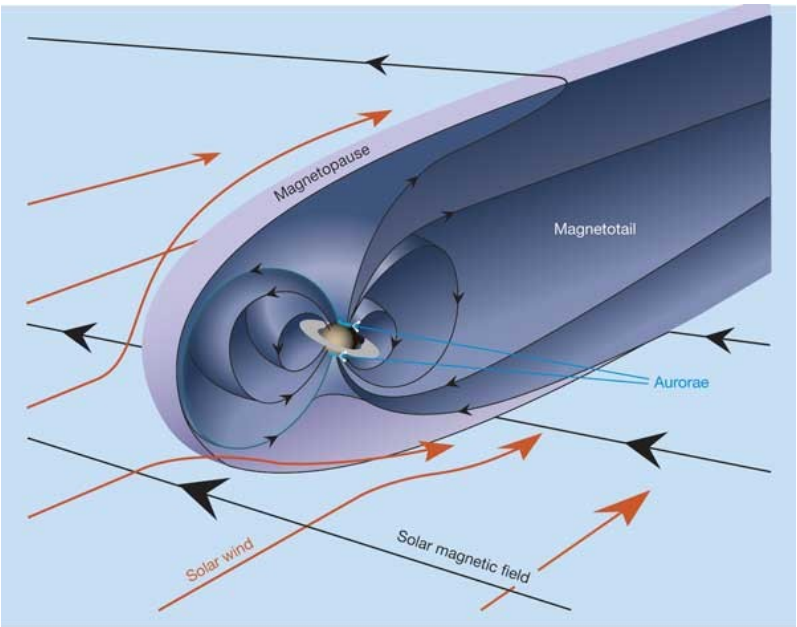

Figure 2.11: Side view of the Saturnian magnetodisk with solar wind (orange arrows) entering from the left. Magnetic field lines (in black) belonging to the IMF & the planetary field are shown. The magnetopause (purple surface) surrounds the planetary body (brown body) with a slice removed to allow for direct viewing of the contented magnetosphere (blue). Saturn is shown with aurorae present at the magnetic poles, the associated magnetotail extends in the anti-sunward direction to right-hand side (Bagenal, 2005).

The second gas giant in our solar system, the ringed planet Saturn, sits approximately 4AU outside of Jupiter's orbit as the sixth recognised planet in our solar system. A member of the subset of magnetised planets, the space around Saturn is also occupied by a magnetosphere. Much like Jupiter, the Saturnian (also known as the Kronian) magnetospheric system differs from the generic structure constructed due to strong rotational forces from the planetary body, as well as internal plasma sources. These processes have a similar effect on the system topology as a whole, hence Saturn's magnetosphere is also often referred to as a magnetodisk. The overall structure of this magnetodisk can be seen in figure 2.11 and the relevant planetary parameters are summarised in table 2.2.

The Saturnian system proved difficult to probe remotely before the insertion of early space-craft with the ability to take in-situ measurements. Emissions such as those in the radio wavelengths were much harder to detect, with those that were measured difficult to perform analysis upon, though eventually they were used to obtain an estimate of the planetary rotation period ($\approx 10.5 \pm 0.08$ hrs) (Smith and Carr, 1959; Brown, 1975). This is not to say that an extensive body of work performed using ground-based instrumentation focused on the Saturnian system did not exist prior to the insertion of various missions. Rather, measurements and analysis was constrained to the elements of the system that could be observed in spectrum's such as visible light, (i.e. the planetary body, the spec-

Planetary Parameters	Saturn	Ratio (Saturn/Earth)
Mass (10^{24} kg)	568.32	95.16
Radius (km)	60268	9.449
Equatorial Magnetic Field Strength (μT)	21.5	0.70
Day Length (hrs)	10.656	0.444
Dipole Tilt (deg)	$\approx$0	-
Solar Wind Dynamic Pressure (nPa)	0.027	0.011

Table 2.2: Summary of relevant planetary parameters for the Saturnian system and the interplanetary medium, in the form of the solar wind, at Saturn's orbital distance. Parameters are presented as a ratio to their corresponding terrestrial values in order to highlight key similarities and difference between the magnetospheric systems. Saturnian parameters are obtained in System III coordinates as collated by (Williams, 2021b) and solar wind parameters are obtained by (Slavin et al., 1985).

tacular rings and moons). Indeed, initial measurements of Saturn's composition were first obtained as early as 1905, with new data continually providing new insights and the elements comprising individual bands seen in the atmosphere identified in the 1930's (see Orton et al., 2009).

In 1979 the Pioneer 11 space-probe became the first to enter the Saturnian system, passing through the associated bow shock & magnetosheath, across the magnetopause and into the magnetodisk. Recordings from this mission allowed for in-situ measurements to be taken of the EM fields and contained materials allowing for formal confirmation of the magnetospheres existence (Wolfe et al., 1980). This was closely followed by the arrival of the Voyager 1 (Vogt et al., 1981) & 2 (Vogt et al., 1982) missions arriving in the system in 1979 & 1981 respectively, with the 3 spacecraft providing a vast quantity of data from the magnetosphere beginning to reveal the workings of space surrounding Saturn.

Post mission analysis on the results gathered from 1979-1981 made it clear that there was still much to learn about this enigmatic system, hence a dedicated orbital probe was designed and inserted into Saturnian magnetospheric space. The Cassini mission design, science objectives and specific instrumentation are detailed by Russell (2003) and a complete overview of the paradigm shifting results of the prime mission for the magnetospheric system provided by Gombosi et al. (2009), Mitchell et al. (2009) & Mauk et al. (2009). Initially inserted into Saturn's system in 2004, the mission continued successfully long after its envisaged completion date, being extended repeatedly until 2017, when it was eventually decommissioned in its so call 'grand finale', being crashed into the planetary surface for reasons of conservation (see Krupp et al., 2018; Spilker, 2019).

Magnetospheric Structure

Using equation 2.2 along with the planetary data presented in table 2.2, it is possible to calculate the Saturnian magnetopause standoff distance at approximately 17.3 R_S. This value is only marginally below the typical observed values of the standoff distance, obtained using measurements taken from the Cassini mission, of 18-25 R_S (Arridge et al., 2006; Achilleos et al., 2008; Jackman et al., 2019). However, when the solar wind ram pressure is observed for these values, it is found that 0.027 nPa is on the lower end of the range and hence the magnetosphere should be an expanded configuration for these values. It is therefore clear that internal sources of pressure are required in the Saturnian system, on top of the magnetic pressure provided by the internal field, in order to enhance those competing against the solar wind.

Analysing the gravitational force provided by the central planetary mass in the Sat-

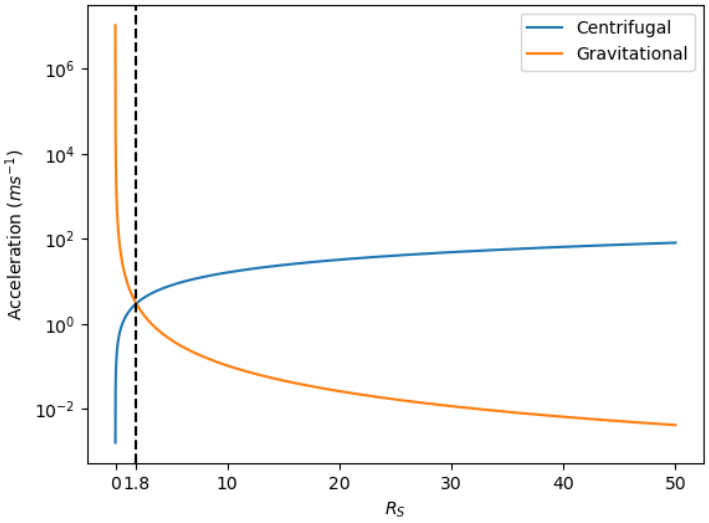

Figure 2.12: Comparison of acceleration provided by gravitational (blue) and centrifugal (orange) force/pseudo-force to material in the Saturnian system from near the planets surface (1 R_S) into the outer magnetosphere (50 R_S). Gravitational force begins as the dominate and decreases with distance from the planet, inversely the centrifugal pseudo-force becomes larger as distance increases. At the critical value of approximately 1.9 R_S the two forces balance each other, indicated by the black dashed line. The magnitude of the accelerations are presented with the gravitational force acting in opposition to the centrifugal, directed towards the planets centre of mass.

urnian system against the centrifugal pseudo-force generated from its planetary spin, it is possible to compare the magnitude of these in a plasma co-rotating with the planet following the method used in §2.2.1 for the Jovian system. The results of this comparison can be seen in figure 2.12, once again close to the planet gravitational forces dominate, but outside of a critical distance (approximately 1.9 R_S) rotational forces are found to be the dominant. Therefore, it is readily determinable that the magnetospheric system of Saturn is also rotationally dominated.

Using the same physical analysis as performed in the Jovian system, it is also determined that in order to fulfil inertial conservation the plasma must begin to sub-corotate in the middle & outer magnetosphere (Hill, 1979; Pontius Jr., 1997). Profiles of co-rotational breakdown as a function of radial distance are much difficult to produce at Saturn, this is exemplified by observations taken by the Cassini mission, observing turning points in the ratio of local azimuthal plasma velocity to the co-rotational velocity (Wilson et al., 2008). The reason for this difficulty is due to the overlapping of plasma sources with transport regions within the Saturnian system, altering the azimuthal velocity at these distances from the planetary body in a way that cannot be captured by simply considering the conservation of angular momentum from the planet's spin (Saur et al., 2004).

Still it has proved possible through the use of more sophisticated force-balance models to examine profiles of plasma co-rotation as a function of radial distance, this is accomplished through the modification of the Caudal model (Caudal, 1986) for the Saturnian system (Achilleos et al., 2010), as can be seen in figure 2.13. In this it can be seen that the magnetospheric plasma is in rigid co-rotation until approximately 5 R_S, at this radial distance the local azimuthal velocity drops causing the plasma to lag co-rotation. However, at 6 R_S the local azimuthal velocity can been seen to begin increasing again until approximately reaching rigid co-rotation again at 15 R_S. After this second maximum the

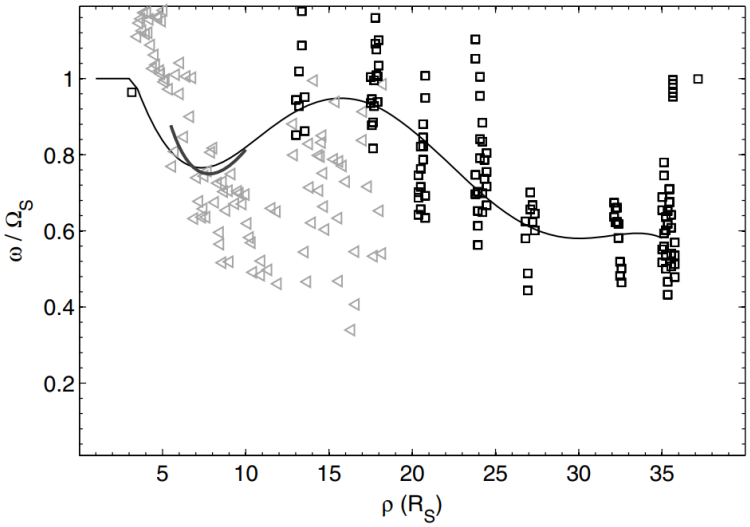

Figure 2.13: Radial profile of the ratio of local plasma azimuthal velocity (ω) to co-rotational velocity (Ω_S) as a function of radial distance (ρ) in Saturnian planetary radii. Cassini mission data (black square) is input into the physical model utilised, as well as data from the Voyager mission (grey triangles). Thicker dark grey line, between $\approx 5-10$ R_S, is an empirical fit obtained by Wilson et al. (2008) using a subset of the data used by Achilleos et al. (2010) to obtain the full fit presented (thin black line). General trend of the fit indicated rigid co-rotation until approximately 5 R_S, this then begins to drop until 6 R_S where the plasma azimuthally accelerates again, recovering until approximately entering rigid co-rotation again at 15 R_S. After this second maximum then co-rotation ratio drops almost linearly until 27.5 R_S where a minimum of 0.6 ω/Ω_S is reached (Achilleos et al., 2010).

local plasma azimuthal velocity once again begins to slow and lag co-rotation, this decrease continues almost linearly until 27.5 R_S where a minima of 0.6 ω/Ω_S is reached until the outer edge of the model is approached at 35 R_S. Further efforts have been made to create profiles fitting observations taken over the course of Cassini's 13 year orbital mission, the dynamical nature of the region however makes it difficult to produce these without the integration of a physical model.

Internal plasma is produced in the Saturnian system from its moons. Predominately, this is from the icy body of Enceladus, where the mechanisms responsible for the release of this material into the magnetospheric system differs from the Volcanic moon of Io. Rather, icy plumes originating from the moon are the source of the neutral material and the discovery of these constitute a major finding from the Cassini mission (Krupp et al., 2018). Though the precise mechanism for the generation of these plumes is still under discussion, the method that seems to be best supported by data is the tidal heating (Spencer, 2013) of a large salt water reservoir (Postberg et al., 2011). The amount of material added by these plumes is a dynamic process with short term variability of 4 orders of magnitude, in terms of the number of molecules, determined using a subsection of 7 months of data from Cassini (Saur et al., 2008; Smith et al., 2010). However, analysis of the data from the entire 13 year period of Cassini's occupation of the Saturnian system indicates that the moon ejects an average 300 kg s^{-1} of material within <15% variability (Hansen et al., 2020). Therefore, depending on the instrumentation and analytical techniques utilised, there is clearly a large discrepancy in the actual amount of variability in the source of material from Enceladus.

The material ejected from Enceladus is determined to be prominently water, H_2O ($\approx$ 91%), with small proportions of other molecules, such as ammonia. These then enter the

Saturnian magnetosphere creating a region known as the neutral torus, which extends from the orbital distance of Enceladus (≈4 R_S) to the middle/outer magnetosphere (see Krupp et al., 2018), with the middle magnetosphere encompassing 6-15 R_S and the outer beyond 15 R_S (Arridge et al., 2011). A distinction between Jovian and Saturnian magnetospheres is apparent from the name of the presence of a plasma torus in the former and a neutral torus in the latter. The neutral torus is much more extended and formed, rather than of plasma, due to the much smaller difference between Keplerian orbital velocity of neutral particles to the co-rotational velocity of ions (Wilson et al., 2009; Fleshman et al., 2012). The specific structure and dynamics of the torus will be discussed later in this section. Additionally, it is worth noting that despite the smaller total quantity of material injected into the magnetospheric system by Enceladus in comparison to Io, when this is compared with the overall size of the magnetosphere that mass loading is more significant in the Saturnian system than at the Jovian (Vasyliunas, 2008).

Additionally, it is worth noting that there are also measurable contributions to the neutral torus from the other satellites and structures in the Saturnian system. The first of these sources are the other icy moons: Mimas (≈ 3.2 R_S), Tethys (≈3.1 R_S), Dione (≈6.5 R_S) and Rhea (≈9.1 R_S). Other than Mimas, which sits just inside the lower boundary of the torus, each of these icy moons lie well within the radius of the neutral tori. However, no mass emission methods have been determined, such as the plumes at Enceladus, rather the material ejected from these bodies is generate though interactions with the surface (i.e. sputtering), therefore only proportionally small amounts of material are provided by these. At the outer edge of the neutral tori sits Titan (≈21 R_S), from this body measurable quantities of nitrogen and hydrocarbons, as well as other molecules, are ejected through processes such as hydrodynamic escape. Finally, there is evidence of contributions from Saturn's planetary rings, contributing small quantities of water group molecules (see Jurac et al., 2001; Gombosi et al., 2009; Tseng et al., 2011; Krupp et al., 2018).

Examining force balance models of the Saturnian magnetodisk it is determined that pressure gradients (Achilleos et al., 2010) & anisotropies play a key role in expanding the size of the Saturnian magnetodisk. These are key in providing the tension required to stretch the magnetotail in the anti-sunward direction, increasing the total size of the magnetodisk. It is also worth noting that the shape of the current sheet, and resultant plasma sheet, in the Saturnian system is warped past a critical distance to create a bowl shape (Arridge et al., 2008a,b). This is caused for the offset between planetary dipole and its orbital plane and hence the concavity of this warping is found to vary with the planetary season (Carbary and Mitchell, 2016).

The Neutral Torus and Magnetospheric Dynamics

Due to the lower differential between neutral Keplerian orbital velocity and ion co-rotational velocity the pickup temperature of freshly generated ions is much lower in the neutral torus than that of those found in the Io plasma torus. Further, comparing the material ejected it is apparent the cross-sectional area of water molecules is much smaller than that of sulphur dioxide, lowering the probability of collisions between neutrals and ions. Finally, due to cooler electron temperatures only the tail end of the distribution of the thermalised population have enough energy to ionise oxygen neutrals (Delamere et al., 2007; Fleshman et al., 2013).

Analysing the distribution of material through the neutral torus, it is found that, as would be expected, that the highest density of water molecules is at the orbital distance of Enceladus. Water molecules (H_2O) dissociate to create OH and also secondary O & H is produced via charge exchange, the peak of each of these created neutrals is also about Enceladus. Exploring the densities of each of these molecules (and element) as a function of radial distance, using neutral cloud modelling, it is determined that H_2O

drops much more rapidly than OH or O, with O becoming the dominant neutral beyond approximately 6.5 R_S. Additionally, it is determined at this outside of this critical location where O becomes dominant that amounts of OH and H_2O become approximately equal, at least to the outer boundary of the model at 20 R_S (Cassidy and Johnson, 2010; Fleshman et al., 2012).

The distribution of ions through the neutral cloud is determined using a 1D version of neutral cloud modelling (see Fleshman et al., 2013). When examining the ions in the Saturnian system it is usual to consider a group of different ionised molecules and elements known as the water-group ions, W^+, which contains O^+, OH^+, H_2O^+ & H_3O^+ (see Young et al., 2005). Analysing the ion densities as a function of radial distance it is determined that water-group ions peak in density just outside of Enceladus' orbit, decreasing as radial distance increases. However, proton density is found to increase as radial distance increases, with a peak between 5-6 R_S, after which the density decreases with distance. This peak corresponds with a local maximum in ion temperature (for both water-group and hydrogen species), outside of which remains almost constant until the boundary of the model are encounter. It is worth noting that even the peak density of hydrogen ions is at least an order of magnitude below even the lowest density region of water-group ions (Gombosi et al., 2009).

Using 0-dimensional neutral cloud models it is once again possible to determine the both the flow of material and energy into the neutral torus, as well as the rate at which these are then removed from the system and the proportion of each process responsible for this. The overall flow into the torus, followed by removal from this region, is summarised in figures 2.14 & 2.15.

Examining these flow diagrams we find that figure 2.14 considers a neutral source density of 4×10^{-4} cm^{-3} s^{-1}, including H, O, OH, H_2O. After the addition of a hot electron population, e^-, and the application of ionisation processes, a population of the following ions, H^+, O^+, O_2^+, OH^+, H_2O^+, N^+, are created. These are then removed from the the torus via the processes of ejection as ENAs and via bulk radial transport (Delamere et al., 2007). This can be compared with figure 2.15 which considers a neutral source density of 2×10^{-4} cm^{-3} s^{-1}, which equates to a total mass source of 125 kg s^{-1}. The models considers the follow neutrals, O, H, H_2O, OH, H_3O, H_2, which can be seen to differ slightly from the ones included in the previous. With the inclusion of an electron population, e, and subjected to the described ionisation processes, the following set of ions are then created, O^+, O^{++}, H^+, H_2O^+, OH^+, H_3O^+, H_2^+. These are then removed from the torus by the same two processes, but with the amounts of mass removed by these also detailed, ejections as ENAs, removing 110 kg s^{-1}, and bulk radial transport, removing 15 kg s^{-1} (Fleshman et al., 2010).

Further, energy flow is also examined in each diagram, with figure 2.14 considering an input energy density of 0.023 eV cm^{-3} s^{-1}. The vast majority of this energy, $\approx 99\%$ is input through the created of fresh pickup ions, with the remaining energy provided by hot electrons. A relatively small amount of the energy input, 3.5% is transferred from the ion to the electrons inside the torus, effectively heating a core thermalised electron population. ENAs remove a large proportion of energy, $\approx 92\%$ from the tours, with bulk radial transport only accounting for the removal of 4.5% of the total energy. The remaining 3.5% of the total energy is removed mostly via the excitation of neutral atoms from their base states, as well as small amounts via ion excitation and through inelastic collisions.

Figure 2.15 indicates the total amount of energy input into the torus per second, rather than energy density. The total can be seen with quantised along with their corresponding input flow, the proportion input in relation to the total energy is also indicated. Hot electrons account for 580 MW, or 1.8% of the total energy flow into the torus, pickup ions account for the remaining energy input, totalling $\approx$32 GW. It is determined in this model

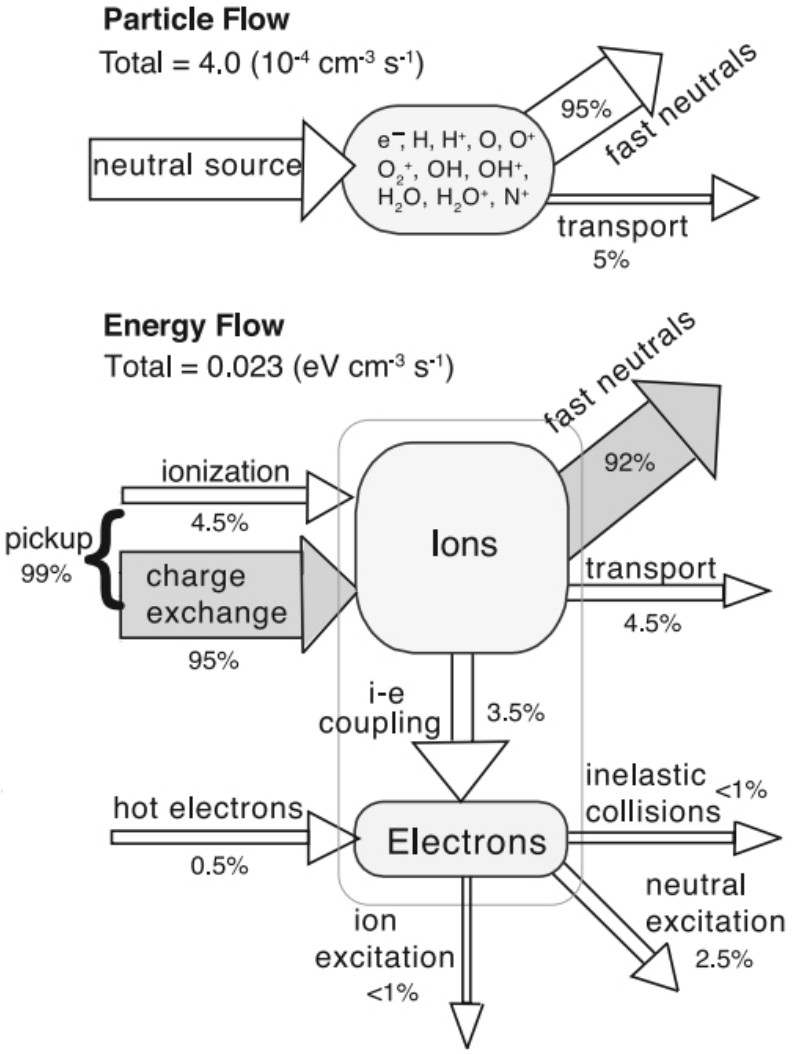

Figure 2.14: A flow diagrams detailing the transport of both material and energy through the Saturnian neutral torus as determined using a 0-dimensional neutral cloud model. Particle flow indicates the inflow of neutral material into the torus. The box contains (with hot electrons added) the neutral atoms & molecules included in the model (H, O, OH, H_2O) along with the ion species included (H^+, O^+, O_2^+, OH^+, H_2O^+, N^+) and electrons (e^-).The outflow mechanisms are indicated along with the percentage proportion of material removed via these also shown. Beneath the energy flow through the neutral plasma torus is shown, with inflow from ions freshly picked up after creation as well as from the addition of hot electrons. The energy within the torus is then transferred between the ions and electrons until a steady state is reached. Energy flows out of the system via a number of processes, with the amount contained within the two mechanisms associated with the removal of material given Delamere et al. (2007).

that 2.4% of the energy is transferred from the ion populations to the electrons inside the torus. Finally, it is found that ENAs account for a large majority of the energy lost from the torus, accounting for 27 GW of loss, a proportion of 83% of the total. Transport is found to carry more of the energy out the torus in this model, moving 4.2 GW from the system, equating to 13%. The remaining removal processes are grouped under radiation and are found to remove 1.2 GW, a proportion of 3.8%.

Focusing on the values of interest for this thesis, we isolate those relating to radial 'bulk' transport. From these figures, provided by Delamere et al. (2007) & Fleshman et al.

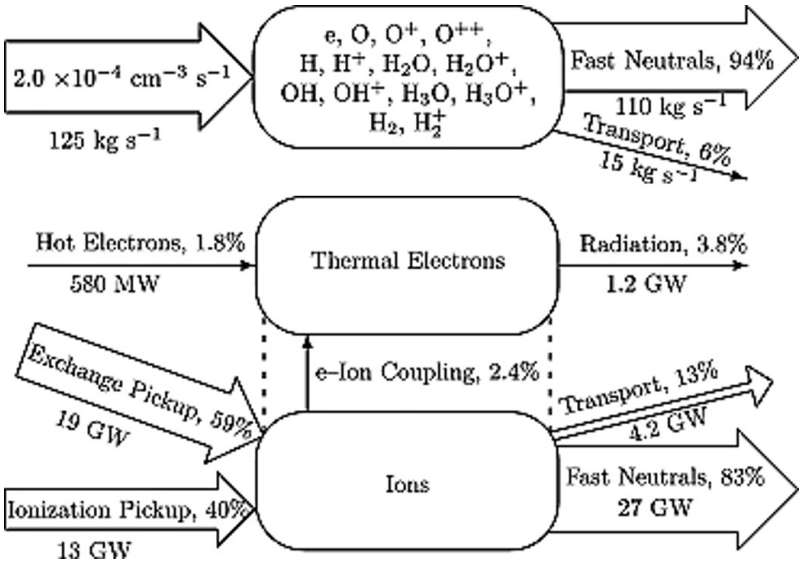

Figure 2.15: A flow diagrams detailing the transport of both material and energy through the Saturnian neutral torus as determined using a 0-dimensional neutral cloud model. Particle flow indicates the inflow of neutral material into the torus, with number density indicated inside the arrow and rate of total mass added below. The box contains the neutral atoms & molecules included in the model (O, H, H_2O, OH, H_3O, H_2) along with the ion species included (O^+, O^{++}, H^+, H_2O^+, OH^+, H_3O^+, H_2^+) and electrons (e). The outflow mechanisms are indicated along with the percentage proportion of material removed via these and the amount of mass that corresponds to per second. Beneath the energy flow through the neutral plasma torus is shown, with inflow from ions freshly picked up after creation as well as from the addition of hot electrons, the quantity of energy added by each of these processes is detailed below their corresponding arrow. The energy within the torus is then transferred between the ions and electrons until a steady state is reached. Energy flows out of the system via a number of processes, with the amount contained within the two mechanisms associated with the removal of material given, again quantities of total energy attributed to these are indicated below the arrows. Adapted from Fleshman et al. (2010).

(2010) respectively, a range for both the amount of material and energy removed from the Saturnian neutral torus can be determined. Removal of material via radial transport is found to account for between $5-6\%$ of the total mass lost from the region, with the process also responsible for the removal of between $4.5-13\%$ of the total energy. Therefore, it is determined that the models agree closely on the amount of material removed via radial transport, but diverge on the quantities of energy removed.

Loss of Internal Material

One way in which plasma transported through the Saturnian magnetospheric system is ultimately lost is much in the same way as in the Jovian magnetosphere, that being through the Vasyliunas cycle (see Krupp et al., 2018). Described in depth in the previous subsection, plasma transported outwards with frozen-in magnetic fields lines experience different levels of co-rotation, depending on radial location. This leads to regions, predominately on the dawn-side of the magnetotail, in which the magnetic topology configures in such a way as to create X-lines, where reconnection takes place. This creates a plasmoid, containing a corresponding O-line, that is decoupled from the field lines still connected to the planet, allowing it to move down tail & eventually enter into inter-planetary space. Depleted flux

tubes move radially inwards, due to magnetic buoyancy, returning magnetic flux back to the planet and ensure that conservation laws are satisfied.

However, it is also found in the Saturnian system that the Dungey cycle, discussed earlier in the setting of a generic (terrestrial) magnetosphere, is a contributing process for the removal of material. The use of data from pre-Cassini missions at the outer planets allowed for an assessment of currents produced by this cycle on the dynamics of the Saturnian system, with signatures identified to allow for the examination and quantisation of the effects provided. This lead to the determination of the Dungey cycle providing 100's kV to the magnetospheric system as well as allowing for the transport of significant amounts of flux in the outer magnetosphere Cowley et al. (2004); Badman and Cowley (2007). Using measurements collected over the course of the Cassini campaign analysis has been able to identify signatures of the Dungey cycle operating consistently in the Saturnian magnetospheric system, this being the the asymmetrically distributed suprathermal He^{++} (Dialynas, 2018). Hence supporting the assertion of the significance of the Dungey cycle at Saturn.

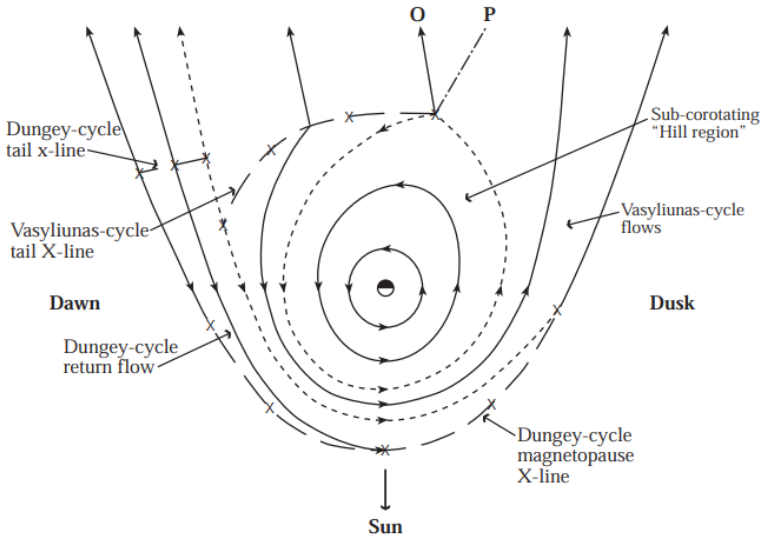

Figure 2.16: Plasma flows in the equatorial plane of the Saturnian magnetosphere, the Sun is located below the figure. The planetary body with the dayside (white) and the night (black) is shown. The magnetopause surface (black line) is partially broken at its front by a series of X's. Inside magnetospheric plasma flows are indicated (solid and dashed arrowed black lines). Seperatrices (dashed black lines) are presnet between regions of separate dynamics. X lines related to the Dungey & Vasyliunas cycles are indicated, along with their corresponding O-line. A P-line is also shown which indicated the outer edge of a created plasmoid (Cowley et al., 2003).

It is therefore necessary to adapt our schematic of large-scale plasma flows for the Saturnian system. This updated schematic can be seen in figure 2.16 and is, as expected, extremely reminiscent of the overview provided for the Jovian system in figure 2.10. Examining figure 2.16 the schematic is seen as a cross-section taken through the equatorial plane of the magnetospheric system, with the Sun located beneath the bottom of the figure. Plasma flows are represented by black lines, with dashed lines representative of seperatrices between regions of differing dynamics and arrows to indicate the directions of these flows. The outermost flow line can be interpreted as the location of the magnetopause, with a series of X's breaking it to show the region at which the Dungey cycle occurs. On the dawn side of the magnetotail the positions of X lines associated with both

the Dungey & Vasyliunas cycles are indicated. It can be seen that both occur preferentially on the dawn side with the Dungey cycle happening towards the outer-most edge of the magnetodisk. The corresponding O line generated by the Vasyliunas is also shown along with a P line which represents the outer edge of a released plasmoid.

Once again it is determined that internal plasma sources are not only present, but play an important role in the altering of an outer planetary magnetosphere, the Saturian, from the generic case developed initially. A proportion of plasma produced by these sources is once again transported through the magnetospheric region, with the radial-interchange instability thought responsible for this transport process. It is therefore now evident that this instability plays a vital role in the configuration of plasma dynamics within the magnetospheric regions of the outer planets. In the next chapter we will explore the precise mechanisms of this instability, including how to identify it within measurements taken from magnetospheric plasmas. Clearly plasma models play a vital role in our understanding of these regions, therefore the predictions made using computational simulations including the instability will also examined, with comparison to data. Finally, a list of open questions regarding it will be collated and the method for best answering them identified.

Chapter 3

Radial Plasma Transport

A general overview of internal sources of plasma in the outer planetary magnetospheric systems of Jupiter & Saturn have been discussed in the previous chapter, §2, along with associated mechanisms for transport away from their pickup regions and the ultimate fate of this material as it is removed from the system. These processes can be briefly summarised as follows. Material is ejected from the moon of Io at Jupiter and Enceladus at Saturn, this is then quickly ionised to form the Io plasma torus in the Jovian system, however ionisation occurs more slowly in the Saturnian system hence the Enceladus neutral torus is formed. Both of these structures contain a fixed total mass of plasma when considered in steady state, hence as material is continually sourced there must be mechanisms responsible for the removal of plasma, else these structures would be continually inflating. These mechanisms found responsible for removal are the ejection of material as ENAs and the bulk transport of plasma radially outwards. ENAs are neutral by definition and hence can be considered ballistic once created, released from planetary field lines. Plasma transported as a bulk radially outwards experiences corotation breakdown in order to conserve angular momentum, leading to removal via the Vasyliunas cycle, allowing plasmoids to be created that can enter the interplanetary medium.

Of the system of internal plasma flow from source to sink, it is the component of bulk transport radially outwards that is of particular interest to this thesis. This removal mechanism is thought to account for a total of 33-51% of material removed from the Io plasma torus, which when a steady state source of 1000 kg s^{-1} is considered equates to 330-510 kg s^{-1} of plasma flowing radially outwards (Delamere and Bagenal, 2003; Delamere et al., 2007). Examining this mechanism in the Enceladus neutral torus, it is determined to account for 5-6% of material removed, again considering a steady state source, approximately 300 kg s^{-1}, this is found to correspond to a total outflow of 25-30 kg s^{-1} (Delamere et al., 2007; Fleshman et al., 2010). Interestingly, when the proportion of energy removed by this mechanism from the two tori of interest is considered, it is determined that this is approximately equivalent in the two systems, with 6-10% removed via radial transport from the Io plasma torus and 4.5-13% removed from the Enceladus neutral torus.

Clearly the removal of both mass and energy via radial transport is an important process in controlling the flow of material inside the magnetospheres of the outer planets. It is worth recalling that this is not just of interest in terms of the plasma dynamics inside magnetospheric space, but these internal sources act to add pressure to the inside of the magnetopause, inflating the total size of the magnetosphere (see 2.1.1). Additionally, plasma flowing through equatorially aligned regions of the magnetosphere act, in combination with pressure gradients and anisotropies, to distend planetary magnetic field lines and contributing to the deformation of the overall magnetospheric structure into the magnetodisk configuration. Therefore, it can be readily seen that this flow created by bulk plasma transport is important in not only understanding the internal dynamics of

magnetospheric space, but also in understanding the overall geometry and topology of these systems.

The question that naturally follows these conclusions is how does plasma that is transported radially out of these tori, through the middle & outer magnetosphere, to its ultimate lose in sink regions, happen? Is the mechanism for this transport simply centrifugally driven diffusion or are there more structured processes at work? The importance of these fundamental questions on mechanisms for plasma transport is compounded by the requirement for the magnetic flux moved outwards by the plasma to be returned to the planet in order to conserve Gauss's law of magnetism ($\nabla \cdot \underline{B} = 0$). Therefore, any process is required to allow for the net outwards movement of mass whilst providing a mechanism for the return of magnetic flux.

The mechanism generally attributed as responsible for radial transport in outer-planetary systems is that of the centrifugal (radial) interchange instability (Achilleos et al., 2015). This chapter will first develop and examine the theory of interchange instabilities, §3.1, with specific application to the outer planetary presented and a brief overview of the inclusion of radial-interchange motions in diffusive models given, §3.2. This will be followed by a summary of observations made by space-craft that have visited these outer planetary systems, §3.3, before performing analysis on the results produced by previous attempts to model this mechanism in these systems, §3.4. Finally in §3.5, this chapter will specifically identify the questions that this thesis addresses, highlighting the need for the new hybrid plasma model developed throughout this work.

3.1 Theory

The centrifugal-interchange instability, often referred to as the radial-interchange instability, is a plasma specific instability which occurs in order to move a system into a state of lowest energy. Though both of these names for the instability are used through-out scientific literature produced on the topic, for this thesis a selection is made to use the radial interchange (RI) instability. This selection is made to reflect that the work undertaken to produce this thesis is interested in the overall radial transport of material through the magnetospheres of the outer planets.

With nomenclature addressed, next a definition is required of what precisely the RI instability encompasses. The first description of the RI instability was by Gold (1959), determined whilst examining magnetic flux tubes (tubes of force) in the terrestrial magnetosphere, postulated that a motion could occur that would allow a lower tube (A) to move into the place of an upper tube (B) and vice versa to the upper, the configuration of which can be seen in figure 3.1. Of interest was that the approximations made to obtain this description omitted the magnetic field and hence it was unchanged by the interchanging of tubes. The criterion determined for the triggering of this instability in this configuration was the decrease in energy density contained within a tube to be above a critical value, this would lead to fast adiabatic convection, triggering the RI instability. This form of RI is often referred to as spontaneous and it was quickly determined, at least in the terrestrial magnetosphere, that this process was unimportant to the redistribution of material (Sonnerup and Laird, 1963).

The description is summarised by Hill (1976) as 'the essential idea is that an insulating neutral atmosphere allows two neighbouring flux tubes to trade places without deforming the field and hence without encountering any opposing magnetic force'. This includes a component of interchange that was deliberately neglected when initially describing the process, that is the importance of the planetary ionosphere, to which the planetary field lines are connected. However, more detailed analysis of the impact of the ionosphere on the RI instability will be discussed later in this section after application to the outer

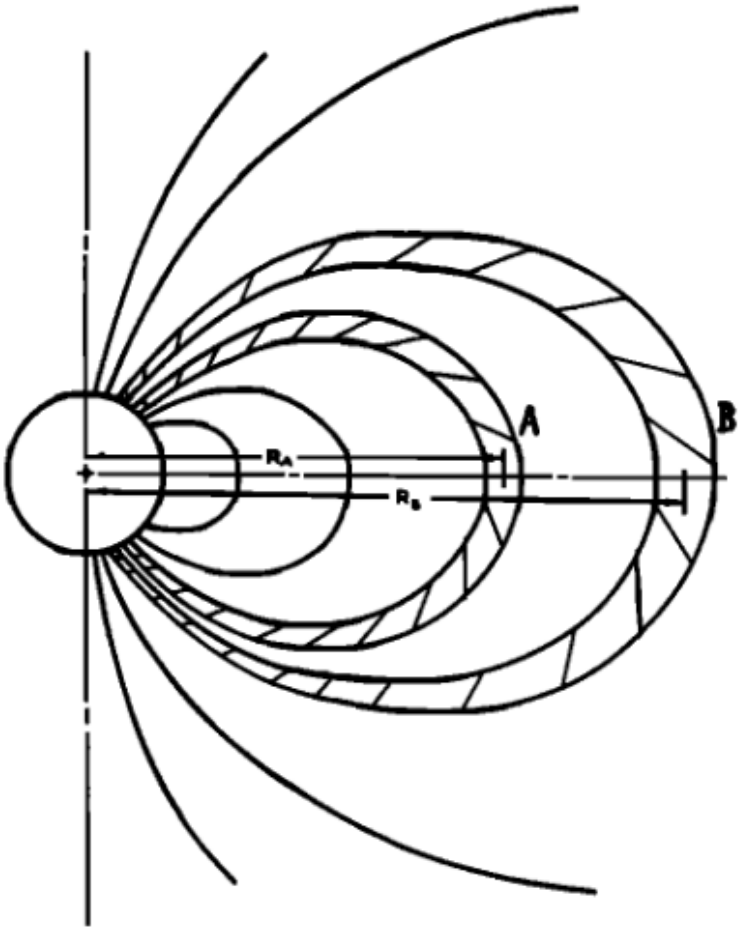

Figure 3.1: Configuration for the interchange instability in a general planetary magnetosphere with a dipolar field, planetary field lines are black curved lines. Here it is shown that when interchange motions occur that the lower tube of force (magnetic flux tube), A, exchanges places with the upper tube, B, whilst unchanging the overall magnetic topologies. The planetary body can be seen as the circle on the left-hand side with a line through its magnetic dipole axis, from this the distance of the tubes is indicated by R_A & R_B (Gold, 1959).

planetary systems.

Hill (1976) further provides a summary of the mathematical description of the interchange instability as determined within the terrestrial magnetosphere system such that, the reconfiguration results in a reduction of potential energy of the plasma within the two flux tubes,

$$\sum \Delta U < 0, \tag{3.1}$$

where U is the total potential energy contained within a flux tube. This can be obtained using,

$$U = \int \frac{ds}{B} \left(\frac{\gamma}{\gamma - 1} p - \frac{\rho_m G M_P}{R} - \frac{1}{2} \rho_m \omega_P^2 r^2 \right), \tag{3.2}$$

where ds is the element of length along the magnetic field line, γ is the adiabatic index, ρ_m is the mass density of the plasma, G is the constant of gravitation, M_P & ω_P are the mass & rotational frequency of planet (P) respectively, all other symbols have their usual meaning. A note must also be made here of the coordinate system this is defined in, that being spherical coordinates aligned with the planetary spin axis, hence R is radius from the planet & r is distance from the rotation axis.

Examining eqn 3.2 it is clear that in the terrestrial magnetosphere the final term, quantising the contribution of centrifugal force, can be neglected. However, as already discussed in the the previous chapter, in both the magnetospheres of Jupiter & Saturn, outside of distances very close to the planetary surfaces, rotational forces dominate over gravitational. Hence, this final term becomes important once again, dominating over the contribution of gravitational forces provided by the second term. In fact in the case of the outer planets it is determined that the centrifugal contributions become the most important at distances far from the planetary body (see figures 2.6 & 2.12), the distances that are of most interest to us when considering the transport of plasma from satellite based mass sources. Assuming that the plasma is connected to the ionosphere then the velocity distributions can be determined using two beams, one from each hemisphere, determining the continuity of field-aligned flow for each gives $\underline{B} \cdot \nabla (\rho_m r/B) = 0$ (Hill et al., 1974; Hill, 1976). Using this the following reduction to eqn 3.2 can be utilised yielding the centrifugal potential energy,

$$U = -\frac{1}{2}\left(\frac{\rho_{me}\omega_P^2 r_e}{B_e}\right)\int r ds,$$

where the e subscripts indicates the value at some position at the centrifugal equator.

Eqn 3.2 can be used to create a mathematical criterion for the interchange instability to occur, using eqn 3.1, in a rotationally dominated system. This is done by considering figure 3.1, we can now determine the total potential energy content in flux tube, A, in its initial position, also A, represented by U_{AA}. Hence, the following can be utilised to obtain the potential energy of a flux tube at a defined position,

$$U_{AA} = -\frac{1}{2}\left(\frac{\rho_{meAA}\omega_P^2 r_{eA}}{B_{eA}}\right) f(r_{eA}), \tag{3.3}$$

where function $f(r_{eA})$ encapsulates the integral component, such that, $f(r_{eA}) = \int r ds$. The total potential energy of the same tube can further be determined at location B, represented by U_{AB},

$$U_{AB} = -\frac{1}{2}\left(\frac{\rho_{meAB}\omega_P^2 r_{eB}}{B_{eB}}\right) f(r_{eB}).$$

Combining the potential energy of the initial flux tube configuration with that of the new can be now done simply,

$$\sum \Delta U = U_{AB} + U_{BA} - U_{AA} - U_{BB}.$$

Following this, a more generalised instability criterion can be determined by considering the change in flux tube content $\frac{\rho_{me} r_e g}{B_e}$ (where $g(r_e) = \int \frac{ds}{r}$) as a function of radial equatorial distance (Achilleos et al., 2015),

$$\begin{aligned} \frac{\partial}{\partial r_e}\left(\frac{\rho_{me} r_e g}{B_e}\right) &< 0, \\ \frac{\partial}{\partial r_e}(M_B) &< 0, \end{aligned} \tag{3.4}$$

where M_B is the flux tube content at the equatorial crossing. This instability criterion thus states that if in a corotating plasma the flux tube content decreases as a function of the equatorial crossing radius, then it is unstable to the interchange motions. It should be noted that this criterion assumes the tubes are in rigid corotation, however it is determined that this criterion holds if the plasma begins to sub-corotate.

The instability criterion provided above is intrinsically tied to a Jovian-like corotating plasma by the assumptions utilised when forming it. However, further mathematical

examination into the instability was performed in Southwood and Kivelson (1987, 1989). This analysis obtained a set of general stability conditions, based in a number of different system configurations, using a small perturbation in a plasma with isotropic pressure, but unrestricted to low-β approximations or specific field geometries. The derivation for these more general criterion is extensive (see Southwood and Kivelson, 1987), therefore a summary of the results most important to the work in thesis will be provided.

First, consideration is given to the inclusion of both gravitational & centrifugal forces acting upon the plasma. It is determined that when a plasma is considered in rigid corotation, with no Coriolis force so there are no perturbations in the azimuthal direction, then effective gravity, $\underline{g}_E$ is determined using,

$$\underline{g}_E = \underline{g} - \underline{\Omega} \times (\underline{\Omega} \times \underline{r}), \tag{3.5}$$

where Ω is angular velocity. If we recall the analysis performed in the previous chapters, it is determined that this neatly encapsulates the force balance examined in order to determine the importance of rotational forces in the Jovian & Saturnian systems.

In this derivation the plasma is described using the framework of MHD and is initially in equilibrium with only the effective gravitational force acting on it. A set of local coordinates are developed, (x_1, x_2, x_3), for the specific purpose of examining interchange instabilities. x_1 is aligned with the magnetic field (such that $dx_1 = ds/B$), x_2 is aligned with the direction of interchange motions and x_3 is orthogonal to these two to complete the set. Finally, a slightly altered definition for what precisely is meant by an interchange instability is made, to be exact, the overall magnetic topology is to remain unchanged but individual field components can change direction.

The case of most interest to this work is that of the low-pressure (low-β) centrifugal driven instability. Considering a worst case perturbation with pressure terms dropped, the following stability criterion is obtained,

$$\int \left(m\underline{g}_E \cdot \underline{U} \right) \left\{ (\underline{U} \cdot \nabla n) - n\underline{U} \cdot \left[\frac{(\nabla B)}{B} + \underline{c} \right] \right\} d\underline{V} > 0,$$

where $\underline{c}$ is the curvature $((\underline{B} \cdot \nabla \underline{B})/\underline{B}^2)$ of the magnetic field and all other symbols have their usual meanings. If it is assumed that the displacement is in the x_2 direction (again a worse case), recalling it is dependent on the magnetic field, and that effective gravity varies little over flux tube in the region of interest, then this simplifies to yield the following,

$$\frac{\partial \left(\int dx_1 n \right)}{\partial x_2} > 0. \tag{3.6}$$

This equation implies that a configuration is stable to interchange motions if the flux tube content increases in the direction of effective gravity. The inverse of the instability criterion determined in eqn 3.4 and hence equivalent.

A final derivation of the stability criterion for the RI instability is given by André and Ferrière (2004), that is not to say that this represents the entire breadth of literature in which this criterion is obtained, but rather that this is the final considered in this thesis. To obtain this solution once again the frame work of MHD is utilised, however the gyro-averaged Vlasov equation (see Boyd and Sanderson, 2003) is used to obtain a closure equation for the perturbations in parallel & perpendicular thermal pressures. Using the developed theory it is possible to obtain numerous low-frequency waves and instabilities, whilst considering only small perturbations. We shall concern ourselves only with the application of this to the Io plasma torus for the content of flux tubes on the surface of the magnetic equator (i.e. straight field lines). With these assumptions it is determined that the following inequality dictates the stability of plasma to interchange motions,

$$\underline{g}_E \cdot \nabla \eta_0 \geq 0, \tag{3.7}$$

where $\eta = \int (\rho_m/B)\, ds$. This states the now well known result that plasma is unstable to interchange if flux tube content decreases in the direction of effective gravity.

The reason for the presentation of this result is rather to highlight the exactness of the analogy usually made when describing the RI instability. This is that the RI instability is analogous to the Rayleigh-Taylor (RT), but with centrifugal force taking the place of gravity. When we consider this from a qualitative perspective, the validity of this assertion is immediately apparent. This is because the RT instability is well known to act in fluids (and other states of matter) to cause the mixing of more dense elements with lighter ones after an initial perturbation along their interface. The eventual result of the RT instability is the exchange of places of the heavy and light fluids, minimising the overall potential energy of the system. The RT instability in a plasma has the following stability criterion (Treumann and Baumjohann, 1997),

$$\underline{g} \cdot \nabla n_0 \leq 0, \tag{3.8}$$

which can be immediately seen as analogous to eqn 3.7.

With a firm understanding of the conditions in which the RI instability will occur for the contents of flux tubes in the magnetic equatorial region, consideration will now be given to the impact of the foot points of the flux tubes in the ionosphere. It should be recalled that a magnetic flux tube is defined as a set of surfaces, bound by frozen in field lines, through which flux is constant. The magnetic field through magnetospheric plasma originates from the planetary body, with generally flux tubes extending further into the magnetosphere corresponding to higher latitudes from which they emerge from the planetary surface. When plasma is brought into corotation with the planet, due to its connection to the magnetic field, the energy to acceleration charged particles to these velocities is provided from the ionosphere.

Therefore, it is important to determine the impact of ionospheric contributions on interchange motions, even at distances into the middle & outer magnetosphere. The first important result is that including consideration of the ionosphere in the mathematical frameworks used to obtain RI (in)stability criterion does not modify these solutions. This means it is purely the configuration of the magnetospheric plasma that determines whether a configuration is unstable to interchange motions or not. However, this is not to say these motions are entirely independent of the ionospheric influence. Rather, it acts to modify the growth rate of an RI instability, with flow perturbations and steady state velocities inversely proportional to ionospheric conductivity (Southwood and Kivelson, 1989).

The growth rate of the RI instability can be obtained using a Hamiltonian approach (i.e. Northrop and Teller, 1960), the full derivation for this quantity is extensive and can be found in Southwood and Kivelson (1989). We shall confine our examination of the Hamiltonian method to what is necessary in order to understand the obtained RI growth rate, γ_{RI}. First, the magnetic field is described using Euler potentials (see Stern, 1970), $\underline{B} = \nabla\alpha \times \nabla\beta$. Using these potentials with the adiabatic invariants, assuming the absence of source & loss terms, the distribution function for the particles at a particular time can be described using $f(\mu, J, \alpha, \beta, t)$. A partial Hamiltonian, $H = K - q\Phi$, is used to describe bounced-averaged motions, where K is the full Hamiltonian and the adjustment, $q\Phi$, is made using particle charge and the electric potential Φ in order to exclude electric field drift. Southwood and Kivelson (1989) show that under this framework the growth rate can be written as,

$$\gamma_{RI} = \left(\int d\mu dJ \frac{\partial f}{\partial \alpha} \frac{\partial H}{\partial \alpha} \Sigma_p^{-1} \right) \left(\frac{B_{ion}}{B_{mag}} \right) \left(\frac{h_\beta}{h_\alpha} \right)_{ion}, \tag{3.9}$$

where B_{ion} is the ionospheric field strength & B_{mag} is the magnetospheric field strength of the magnetic element in which a particle is situated, h_α & h_β are scaling factors such

that $h_\alpha h_\beta = B^{-1}$ and Σ_p is the ionospheric height-integrated Pedersen conductivity. Additionally, it is worth noting that the sign of γ is dependent on the non-electric drifts of a particle (i.e. gradient, curvature & general force) due to the proportionality of $\partial H/\partial\alpha$ on these.

With the conditions under which the RI instability will occur having been established, and with the growth rates of these instabilities also determined, it is clear that the plasma environments outside of the tori present in the Jovian & Saturnian systems are ideal for these instabilities. This is evident considering eqn 3.7 as flux tube content increases at radial distances close to these plasma sources with rotational forces dominant, hence satisfying the RI instability criterion.

However, we are yet to consider the large scale structure, the flow pattern, that is formed as material is transported by them. Of course, the nature of net motion of a plasma element radially outwards via an instability is difficult to capture in mathematics as it in a fundamentally non-linear turbulent process. That is not to say however it is entirely impossible to use the theory of RI, along with general observations of the plasma environments in the regions of interest, to qualitatively evaluate the most probable flow pattern for these motions.

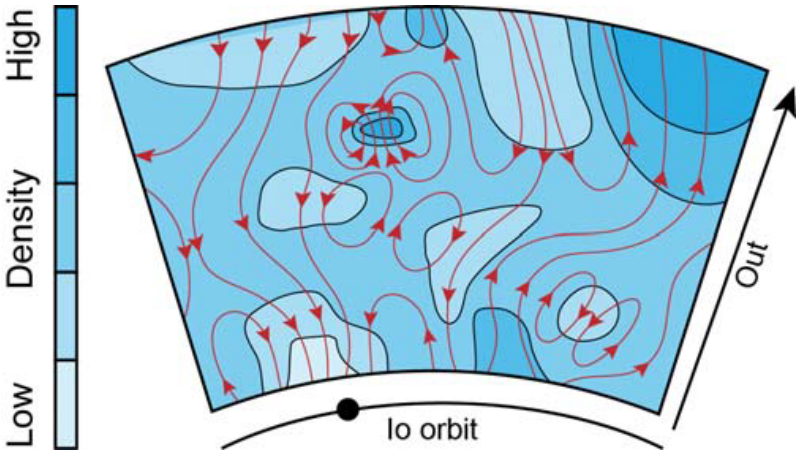

Figure 3.2: Flow pattern created by continual random fluctuations of a plasma source to allow for the net outwards convection of plasma whilst generally preserving the magnetic topology of the region. The base of the wedge is at the Io plasma torus (∼6 R_J) and extends to an arbitrary distance into the Jovian inner magnetosphere. Parcels of dense plasma are indicated by dark blue contours and lighter blue contours indicate lighter plasma parcels. Streamlines are shown in red to indicate the general flow pattern of material through the region, with arrows showing the direction of these flows. After Southwood and Kivelson (1989).

If one takes the region around Io, it is determined that from the plasma torus (∼6 R_J) to a distance of approximately 12 R_J that flux tube content falls monotonically, whilst the planetary magnetic field remains approximately dipolar in structure (Mauk et al., 1996). Therefore, a simple convective pattern from something like a two or multiple celled tori configuration can not be responsible, as this would have the effect of creating regions of large magnetic anomalies. Rather, the mechanism favoured upon review by Southwood and Kivelson (1989) was a source (Io) that continually fluctuates creating variations in density through the azimuth of the torus. The motions associated with a plasma element depends on whether it is heavier or lighter than its surrounding local medium, with the spatial scales of these regions determined by the random source. This creates a flow pattern that appears as a 'random walk', however is determinable purely by the variations in the plasma source. An example of this resultant seemingly random flow pattern is seen

in figure 3.2 and it should be noted that the indicated stream lines (in red) will continually vary in time.

Outside of these distances the flow structure is more difficult to precisely describe. Again, simple convection patterns have been suggested (i.e. Hill et al., 1981), however there exists little observational evidence to support this hypothesis. What seems most probable is there is a mixture of dense, cold plasma regions moving outwards with narrow regions of hot, tenuous plasma returning to the planetary surface. However, this process will only occur due to the RI interchange whilst the force of effective gravity is dominant over the internal pressure of the plasma, with effective gravity reducing as one moves further into the magnetosphere. Once contributions from internal pressure are substantive enough then the mechanism for plasma motions changes from the RI to the ballooning instability (Kivelson and Southwood, 2005). It is worth noting that the RI instability constitutes a special case derivable from the ballooning instability description in the case of low plasma pressure (Hameiri et al., 1991).

It is evident that the theoretical framework developed to describe RI motions leaves large questions remaining in how the instability is responsible for the transport of material in rotationally dominated systems and the global flow patterns that originate from these. Evidently in the case of the Io plasma torus there seems to be a change at some critical distance (perhaps 12 R_J) between a random-like walk of flux tubes, to larger scale convective motions. However, the flow patterns established in these two regions are still poorly understood, with the true transition zone between the patterns along with its size and structure also requiring investigation. A way in which the flow through the system can be investigated is by solving a diffusion equation to find the profile of parameters (such as ion density) when in steady state.

3.2 Diffusion Models

Due to the variability of the random source describing the addition of plasma from the Io plasma torus, it is possible to capture these motions, and hence interchange, mathematically using diffusion equations (through the inclusion of an additional coefficient, see Landau and Lifshitz, 1976). The development of this diffusion coefficient, specifically to encompass the contribution of driven interchange turbulence, is possible by constructing a diffusive model to examine this flow of material (Siscoe and Summers, 1981). Figure 3.3 shows the geometry for deriving the diffusion coefficient. A flux tube of radial width $2\Delta L$ ($L = R/R_P$) maps to a range of colatitudes $\Delta\theta$ in the ionosphere. The flux tube spans an azimuthal width $\Delta\phi$ and is split into four cells each of radial width ΔL

The general equation for time-dependant, axisymmetric cross-L diffusion is found to be,

$$\frac{\partial}{\partial t}\left(NL^2\right) = L^2 \frac{\partial}{\partial L}\left[\frac{D_{LL}}{L^2}\frac{\partial}{\partial L}\left(NL^2\right)\right], \tag{3.10}$$

where N is the number of ions in a flux shell per unit L and D_{LL} is the diffusion coefficient (see Siscoe and Summers, 1981). It can be seen that all parameters controlling the system, other than radial distance & ion distribution, must be incorporated into the diffusion coefficient, D_{LL}.

Siscoe and Summers (1981) show that this coefficient can be written as $(D_{LL})_\Omega = \left\langle (\Delta L)^2 \right\rangle / 2\tau$ where τ is a timescale for diffusion. Using this geometry for the interchanging cells, the gradient in mass per unit L and coupling with the ionosphere, they were able to show that the diffusion coefficient was equal to,

$$(D_{LL})_\Omega = -\frac{m^* \Omega^2 L^4}{4\pi \Sigma_p B_{ep}^2 R_P^2}\left(\frac{dNL^2}{dL}\right)\left\langle (\Delta L)^2 \right\rangle, \tag{3.11}$$

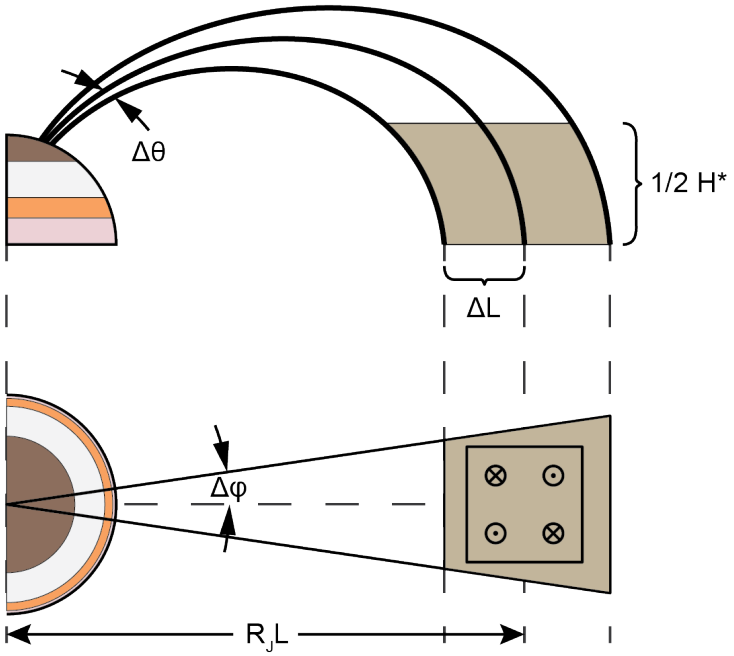

Figure 3.3: Configuration of geometry used for the construction of a diffusive model of plasma transport in a plasma environment like that surrounding Io, in which the flow pattern is random-like. The change in latitude of the inner & outer edge of a cell (semi-analogous to a flux tube) is seen as $\Delta\theta$ with the field lines traced into the planetary ionosphere. The subdivision of a eddy located at $R_J L$ into 4 cells is seen, with each cell the size ΔL and a height $\frac{1}{2}H^*$ (i.e. half the height of the plasma sheet). Adapted from Siscoe and Summers (1981).

where m^* is the average mass of the constituent plasma ions. If the mean size of the eddies as a function of L is written as a power law, $\left\langle (\Delta L)^2 \right\rangle = (\Delta L)_0^2 \, (L/L_0)^p$, eqn 3.11 can be written in compact form

$$(D_{LL})_\Omega = -k_\Omega L^{4+p} \frac{dNL^2}{dL} \tag{3.12}$$

where p is some free parameter and k_Ω incorporates all the constants. Hence, k_Ω becomes the parameter which controls the form of the system and therefore contains the physical description. Since NL^2 is representative of mass per unit flux, then it is clear from this equation that the system is unstable to interchange if this quantity decreases with distance (recall eqn 3.7). Further, the strength of the turbulence created is found to be proportional to rate of change of this quantity.

Fitting data from Voyager 1 between 6-8 R_J reveals that the value of the free parameter is $2 \leq p \leq 4$. Using typical values for the Io plasma torus with varying forms for the source function a negative feedback characteristic was determined, buffering density responses to source changes. Additionally, a travel time at 6 R_J was determined for the plasma at 2.7 days per R_J (Siscoe and Summers, 1981).

Further work on the usage of a diffusion model to examine plasma transport in the region around Io has successfully coupled a ring current with the Iogenic plasma, in order to examine the effects of the ring current pressure gradient (Summers and Siscoe, 1985). This was then generalised for centrifugally driven magnetospheres, with the results from the updated model seen to reproduce plasma densities (limited to the cool population) measured by the Voyager 1 probe to within an order of magnitude (Summers et al., 1988).

The system modelled using the detailed diffusive methods is one that has reached a

steady state, hence assuming the turbulence is both well evolved and mixed throughout the entire region. However, we are unable to resolve individual RI events (i.e. flux tubes trading places) or even quantise the size of the eddies produced in the creation of the system profiles. Therefore, we must find mathematical & experimental techniques that allow use to probe these plasma motions on spatial scales unavailable to diffusive models. Therefore, we will now examine measurements taken in-situ in order to gain further insights into the RI instability occurring within the Jovian & Saturnian systems.

3.3 Observations

With the discussed theory for RI largely developed in the 1980's, initial comparisons to observational data was largely limited to that provided by the Voyager missions. The arrival of the Galileo mission at Jupiter, along with data provided by Cassini's brief visit before its 13 year campaign in Saturn, fundamentally changed the landscape providing an abundance of high cadence data throughout these magnetospheric regions. In this section we will review observations of interchange events in both systems, starting at Jupiter then moving to Saturn, and present a summary of the insights gained from these.

Jupiter

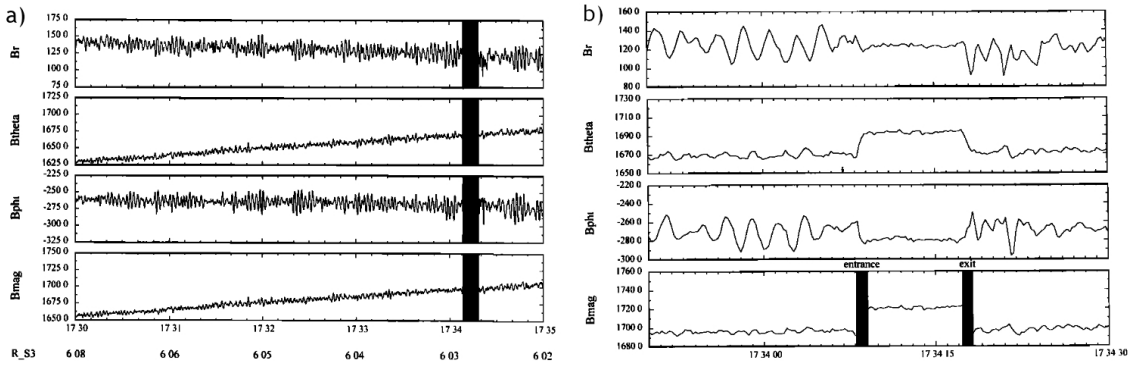

Figure 3.4: Magnetometer data from Galileo on 7$^{\text{th}}$ December 1995 with the each component (r, θ, ϕ) in SIII coordinates shown along with the magnitude. a) shows the data between 17:30-17:35 UT, corresponding to radially distances of 6.08 R_J & 6.02 R_J. An anomalous period of data is shaded. b) shows the data between 17:33:45-17:44:30 UT. Entry & exit from the period of anomalous reading (17:34:08-17:34:18 UT) is indicated in the panel containing the magnitude of the field strength (Kivelson et al., 1997).

Evidence for RI motions in the Io plasma torus was found in data gathered by Galileo in 1995, with signatures determinable in a range of the probe's instruments (Bolton et al., 1997; Kivelson et al., 1997; Thorne et al., 1997). The key observations from this range of instruments are present in figures 3.4, 3.5 & 3.6 and provided the first compelling in-situ evidence to support the theoretical description of plasma motions in this region. The broad interpretation of this event is the entry of the probe into a depleted flux tube originating from further out in the plasma torus. It should be noted that short anomalous signatures had previously been found (i.e. Kivelson et al., 1992), but these were deemed inconclusive to draw definite conclusions of interchange from.

Figure 3.4a shows an overview of the magnetometer data for the event when the spacecraft moved from 6.08 to 6.02 R_J (well within the plasma torus). The magnetometer data is presented in spherical polar coordinates (B_r, B_θ, B_ϕ) in System III (Seidelmann and Divine, 1977). With decreasing distance, the radial component is weakly falling but both

Channel	Species	Energy (MeV)	ρ_L (km)	v_{gc} (km s^{-1})	τ_B (s)
E0	electron	0.015-0.029	0.2	0.06	17
E2	electron	0.042-0.055	0.4	0.17	10
F1	electron	0.174-0.304	1.0	0.73	5
TP1	proton	0.8-0.22	23.3	0.34	313
TP3	proton	0.54-1.25	60.4	2.3	120
B0	proton	3.2-10.1	147	13.4	50
TO4	oxygen	1.8-9.0	440	7.5	260

Table 3.1: Selected channels from PWS on Galileo with particle channel labels, the species of the particle and their corresponding energy ranges. Additionally, the Larmor radius, gradient drift speeds and average bounce times are shown for these particles at 6.03 R_J. These channels are used in figure 3.5, with data for count rates of specific particles using the particle channel labels as identifiers (Thorne et al., 1997).

the polar and azimuthal components are increasing, as is the field strength as expected for a dipolar field. The identified interchange event occurs towards the end of the interval between 17:34 and 17:35 UT (Universal Time).

Figure 3.4b contains the details of the anomalous magnetic measurements, with the temporal resolution of the displayed data zoomed for a 45 s period (17:33:45-17:34:30 UT). Similarities between the radial and azimuthal coordinates is once again evident, with the values taking an average with decreased variability. The polar component and total magnitude demonstrate a sustained increase in strength, well above that of the general variability of the field strength, for a period of approximately 10 s between 17:34:08 and 17:34:18 UT. The magnetic field strength increased almost instantaneously by ∼25 nT, a increase of 1-2% of the total strength.

Although the anomalous magnetometer measurements are a strong indicator of local plasma dynamics, with RI motions postulated as being responsible for these, in isolation they are not enough to determine this is a definite signature of interchange. Figure 3.5 shows the count rates of a variety of energetic ions & electrons in the top seven panels, from the Energetic Particles Detector (EPD) (Williams et al., 1992), and the last panel contains the spectrum of powers observed by the Plasma Wave Subsystem (PWS) (Gurnett et al., 1992). All data in this figure is presented over a 3 minute interval (between 17:33-17:36 UT), corresponding to a radial positions of 6.04 R_J to 6.00 R_J. Additionally, SIII longitude (LonIII) as well as latitude in relation to both the rotational (LT) and magnetic (MLat) equators (Thorne et al., 1997).

Examining the count rates from EPD in figure 3.5, it can been seen that there is a increase in each of the included channels that corresponds exactly with the anomalous magnetometer readings (at ∼17:43:08 UT for ∼10 s). The energetic particles that a specific channel refers to is indicated by the label next to the data panel, with the channel specifics summarised in table 3.1. Each of the ion channels (TP1, TP3, B0, TO4) demonstrate a profound sudden increase in count rate, contained to the period corresponding with increased magnetic field strength, which quickly returned to the local rate after exiting this region. The exception to this is the TP1 channel (lowest energy protons) that display similar behaviour to the electron channels (E0, E1), a sudden increase with a slower relaxation to the background rate. It should be noted that the highest energy electron channel included (F1) only experiences a small enhancement in count rate. The increase in each of these count rates is related to a change in the loss cone for this parcel of plasma, this suggests a difference between the specific parcel to that of the surrounding 'local' medium. It is determined that these values are indicative of plasma at 6.3 R_J, indicating that this flux tube is filled with plasma adiabatically transported inwards from the outer-torus.

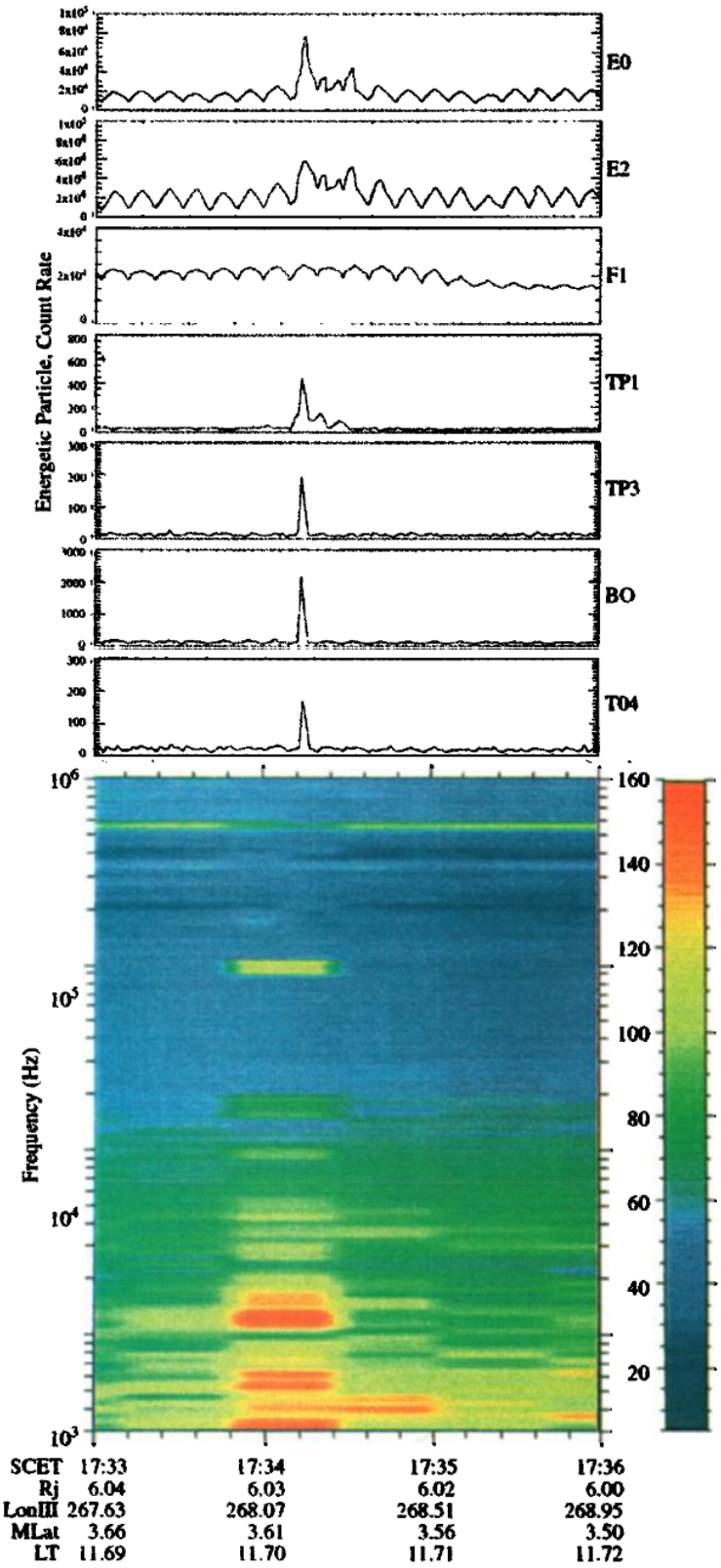

Figure 3.5: Measurements from the EPD & PWS instruments on Galileo on the 7th December 1995 between 17:33-17:36 UT, the translation into various other coordinates is shown below. Initial seven panels contain the count rates from various channels of EPD, with the label to the right of the plot corresponding to table 3.1. The bottom panel contains a spectrogram from PWS with the power indicated by the colour bar on the right (Thorne et al., 1997).

Examining the spectrogram from PWS in figure 3.5, it can be seen that once again there are dramatic changes to the plasma spectrum that corresponds almost exactly with the anomalous magnetometer & EPD data. There can be seen to be a clear enhancement in low frequency waves (<10 kHz), whilst a shift to lower frequencies in the wave line associated with the upper hybrid limit can be seen. It is this drop out in the upper hybrid line that is of particular interest as it would suggest a change in the number density in this flux tube from 3.7×10^9 m^{-3} to 9.5×10^7 m^{-3}, a decrease of approximately an order of magnitude. Combining the higher field strength with a much lower density (than the surrounding medium) would generate a flux tube that is magnetically buoyant and hence unstable to inwards interchange motions (i.e. $\underline{g}_E \cdot \nabla \eta_0 < 0$). It is determined by Thorne et al. (1997), using a time-of-flight approximation, that the approximate spatial scale of the encountered flux tube is 10^3 km with conditions sufficient to induce an inwards transport velocity of 10^2 km s^{-1}

Though a full review of plasma waves is outside the scope of this thesis, it is worth defining what the upper hybrid limit (or upper hybrid frequency) corresponds to. The physical origins of this fundamental plasma frequency is tied once again to natural oscillations that occur internally, detailed in §1.1.6, though the upper hybrid limit applies specifically to the subset of magnetised plasmas. Magnetism introduces the Lorentz force (eqn 1.3) to these oscillations, an additional restoring force, hence increasing the number of fundamental modes associated with these. The upper hybrid limit, ω_{uh}, specifically relates to the electron oscillations and can be obtained by combining their gyro-frequency (eqn 1.4) and plasma frequency (eqn 1.28) ,

$$\omega_{uh}^2 = \omega_{ge}^2 + \omega_{pe}^2. \tag{3.13}$$

Therefore, it can be readily seen that this fundamental mode is dependant both on magnetic field strength and plasma density (Baumjohann and Treumann, 1996).

The analysed event represents a single event in one fly-through of the Io plasma torus, selected for having the most distinctive data in the largest range of instruments. However, a number of other regions, distinct from the local background medium, were identified in one or more instrument data sets with varying strengths and temporal durations. There is strong evidence to indicate that at least a portion of these other events are RI motions, with various 'sources' in the outer torus. Figure 3.6 shows a spectrogram from PWS on the 7$^{\text{th}}$ December 1995 between 17:00-17:40 UT, corresponding data from EPD is shown in the two panels beneath, the selected channels (B1, F0) both show high energy electrons. Here, the 17:34 UT event can be seen, with only a small increase in high energy electrons. Another event can be seen at 17:10 UT which has a corresponding anomalous period in the magnetometer data. It is noticeable that the event is much longer (∼5 mins) starting at ∼17:09 UT and corresponds to a much larger increase in high energy electron count rates. Additionally, it is also readily seen that there is a broadband increase in low frequency plasma waves as well as a drop in the upper hybrid line which, when combined with the magnetometer data, gives a strong indication of also being a flux tube moving inwards under RI motions. This is due to the same reason as the single event identified previously, the flux tube now has a lower amount of content in a magnetic field with a larger strength, hence is magnetically buoyant inwards (towards the planet).

Moving out beyond the region of the Io plasma torus, it is predicted that this random-like outwards walk will transition into larger scale structures, sporadically spaced due to the nature of their creation (assuming a randomly varying source still). The creation of mass depleted, magnetically enhanced flux tubes is still required in order to enforce the conservation of flux on a global scale, providing a mechanism to return magnetic flux to the planet. Analysing Galileo's EPD data from beyond the plasma torus region >100 'injection' events are determined at distances between 9-27 R_J (Mauk et al., 1999).

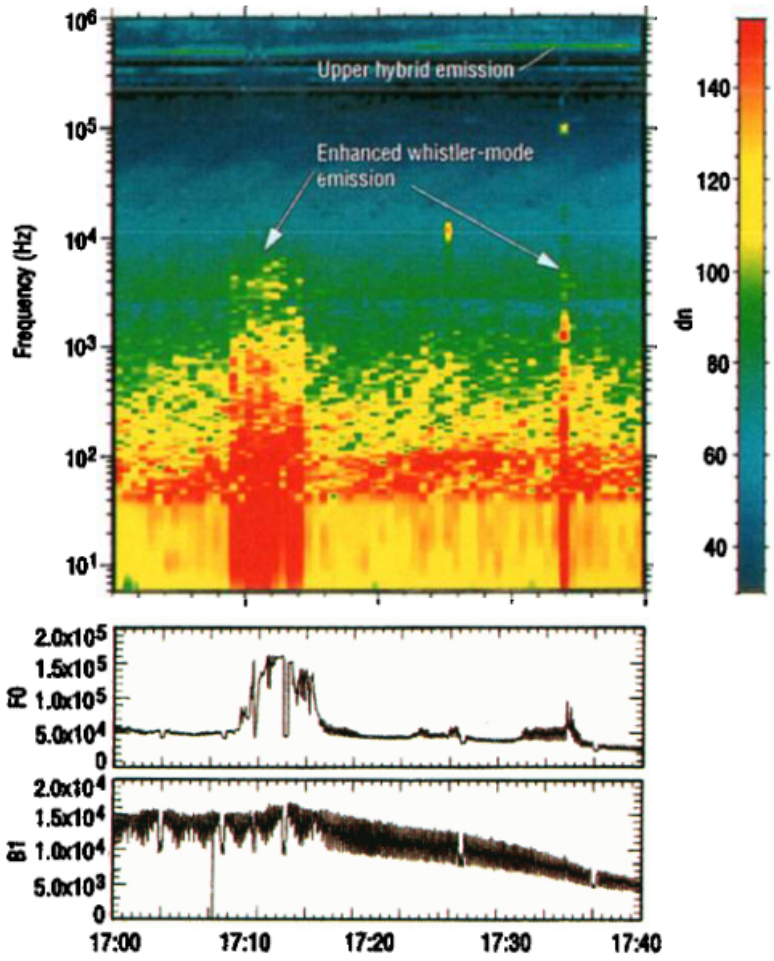

Figure 3.6: PWS & EDP data from the Galileo mission on 7$^{\text{th}}$ December 1995 between 17:00-17:45 UT. Top panel contains a spectrogram from PWS, with two events marked at 17:09 & 17:34 UT, the power is indicated by the colour bar to the right. The bottom two panels contain particle count rates from EPD, two channels, F0 & B1, are shown which both correspond to high energy electrons Bolton et al. (1997).

Injection events are so called due to their comparison with events by the same name in the terrestrial magnetosphere. They consist of energy-time dispersed charged particle signatures in both ion and electron data, though ion signatures are less organised (Mauk et al., 1997). Examples of injection events are seen in figure 3.7, where on 353$^{\text{rd}}$ day of 1996 three enhancements in a dispersed range of electron energies is seen. It is noted that the low energy increases are seen before the high and this can be used to determine the length of a injection event. Additionally, it is possible that there is correspondence between injection signatures and magnetometer anomalies, though these signatures precede these by $\sim 10^1$ hours and are hence challenging to correlate.

The cause of these injection events is determined to be some transport mechanism allowing a configuration, shown in figure 3.8, in which phase space density (PSD) decreases as location in radial distance from the planet also decreases (i.e. PSD1 > PSD2). PSD is a measure of particle intensity, in an invariant plasma (see §1.1.3), determined to be a function of $\frac{\mathcal{J}_\perp}{B^2}$ where $\mathcal{J}_\perp$ is the integral of particle flux perpendicular to the magnetic field (Gehrels and Stone, 1983). Hence, increases in PSD, correspond to more energetic (hotter), tenuous plasma parcels, which are unstable to inwards RI motions. These injections are much larger than the small parcels associated with the random-like walk in the Io

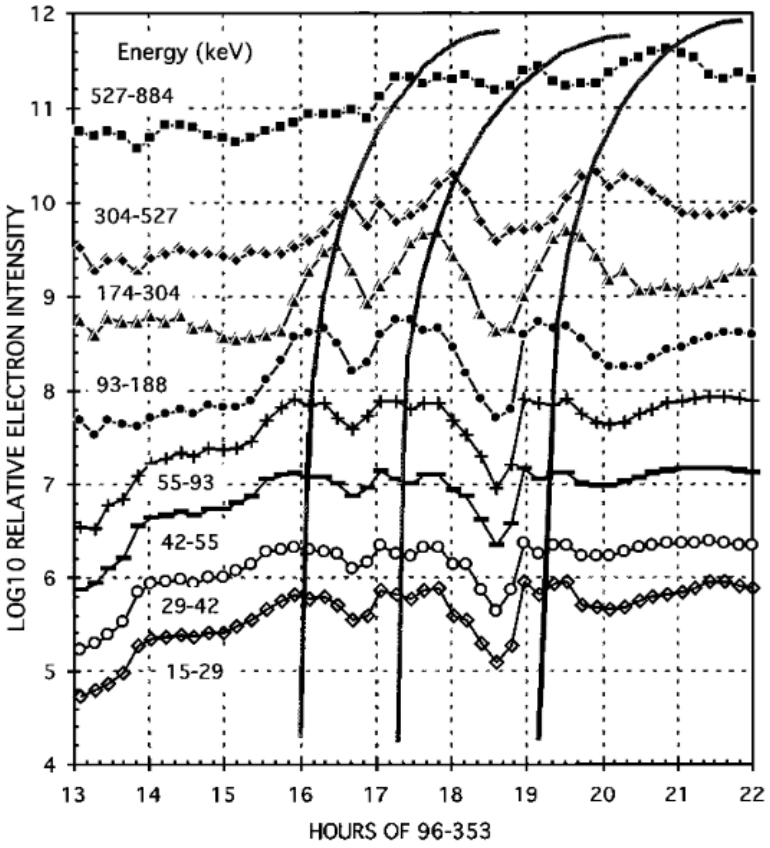

Figure 3.7: EPD measurements from Galileo on 353rd day, 18^{th} December, of 1996 between 13:00-22:00 UT. Three 'injection' events are indicated by the curved black lines through the eight EPD electron channel intensities, with associated energies indicated on the left (Mauk et al., 1997).

plasma torus, with azimuthal scales sizes of ∼5-15 R_J and potential radial displacements of potentially several R_J. The peak of these injections is determined to be at ∼11-12 R_J, the outer edge of the plasma torus, potentially indicative of a transition region. However, it should be noted that injections seem to occur over a wide range of longitudes and local times. Signatures of the injection events are also visible in the auroral regions, marking there similarity to the events at Earth (Mauk et al., 2002).

The mechanism for the generation of these injections is still a matter of discussion. There was suggestion that a connection could be drawn between these events and mass unloading, perhaps the natural results of the Vasyliunas cycle. However, to draw this conclusion definitively requires further work and falls outside the scope this thesis (Louarn et al., 2001; Achilleos et al., 2015). It should also be noted that injection signatures are less ordered in ion channels than the electron, again the cause of this is currently unknown, but could point to the impact of the ion-inertial length scale on the dynamic process (Mauk et al., 1997). The arrival of the Juno probe to the system provides the promise of more data to continue these investigation, to date ∼4 interchange events have been identified between 5-50 R_J (Daly et al., 2021).

Saturn

The Saturnian system, like the Jovian, was devoid of new data from which to search for RI motions until the arrival of the Cassini mission in 2004. The mission's high cadence in-

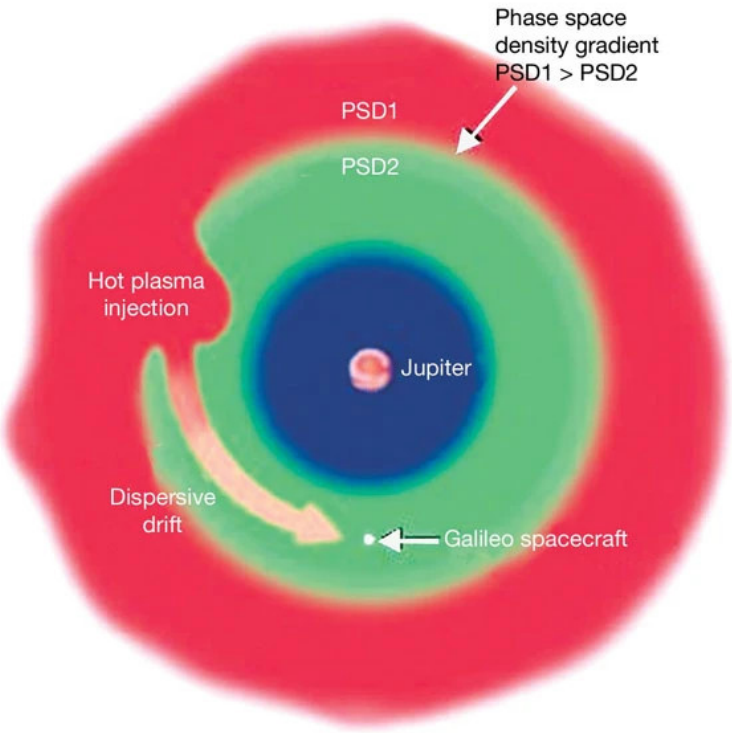

Figure 3.8: Configuration of plasma in the equatorial plane of the Jovian system. PSD decreases as radial distance decreases, such that two surfaces can be creates with PSD1 encompassing PSD2, if the interface between these is perturbed then a plasma injection is generated and convects inwards moving through the azimuth to create a spiral Mauk et al. (2002).

struments, along with its sustained 13 year observation campaign, provides a vast dataset of plasma & EM readings throughout large portions of the magnetodisk, the plasmasheet being the area of particular interest. It is therefore not surprising, considering the similarities between Jupiter's & Saturn's magnetosphere, to find that signatures of RI motions were quickly discovered after the arrival of Cassini into the system. In fact many more observations have been made in the Saturnian system than in the Jovian, the reason for this can be determined by first considering the larger dataset available, additionally the lower planetary magnetic field strength (see table 2.2) leading to lower ∇B drifts (see §1.1.2) making ion dispersion events easier to observe (Hill et al., 2005).

Initial observations of RI motions are found to be equivalent to the injection events identified at Jupiter, with a set of 48 events identified at distances between 5-10 R_S (Hill et al., 2005). It is worth initially defining exactly what is meant by injection in the Saturnian system, as it is suggested that there exists some disagreement in the literature, and in fact there are found to be two 'flavours' of injection:

- the localised presence of hot, tenuous plasma parcels moving inwards under RI motions
- localised particle accelerations associated with inward motions on the nightside after reconnection events

Whether these two flavours are distinct and indicative of separate plasma dynamics is debated (Mitchell et al., 2015), however the work reviewed in this thesis so far would suggest at least some connection between the two.

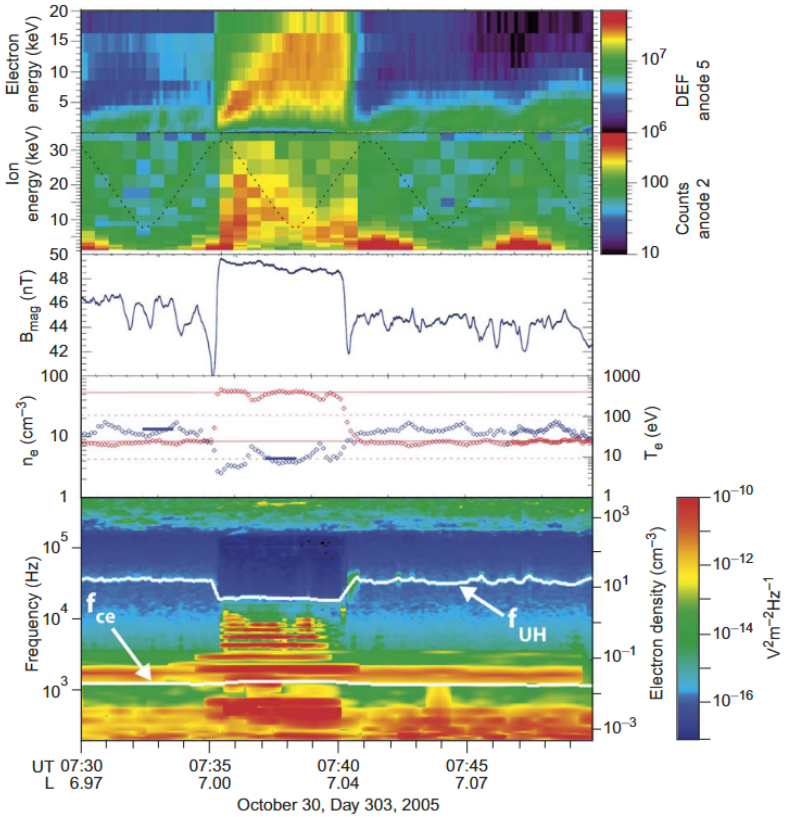

Figure 3.9: Measurements from Cassini on the 30$^{\text{th}}$ October 2005 between 7:30-7:50 UT, of interest in the injection event with onset at ∼7:35 UT and lasting ∼5 minutes. Panels 1 & 2 contain electron fluxes & ion count rates respectively, over a broad range of energies with magnitude of count given by the colour bar to the right, additionally a black dotted line is included in panel 2 to indicate the ion detector's look direction. Panel 3 contains the magnetic field strength. Panel 4 contains electron number density (in blue) and temperature (in red), calculated from the CAPS data. Panel 5 contains a spectrogram from RPWS, with the upper hybrid (ω_{uh}) & electron cyclotron (ω_{ce}) frequencies marked, power is given by the colour bar to the right (Rymer et al., 2009).

Examining the form of injection events identified, as seen in figure 3.9, there are found to be remarkable similarities between these events and the best interchange events analysed in the Jovian system. The data presented on 30$^{\text{th}}$ October 2005 between 7:30-7:50 UT, corresponding to a radial distance of 6.97-7.10R_S, contains one injection event occurring at ∼7:35UT and lasting ∼5 minutes. Panels 1 & 2 contain electron & ion data respectively from the Cassini Plasma Spectrometer (CAPS). An enhancement in both the electron fluxes and ion count rate is seen, however the form varies between the two. The electrons see a dispersed gradual onset to a peak value that suddenly disappears, whereas the ions see a sudden increase in a broad range of energies that decreases and increases over the course of the event, however this is found to be explained by the changing look direction of the ion detector. Magnetometer data is shown in panel 3, it shows a sudden increase in field strength, well above the prior variability of the data, that is sustained over the course of the 5 minute event. Panel 4 shows the electron density (in blue) and temperature (in red), calculated from the CAPS data, it can be seen that during the event the density drops by approximately a factor of 2 and the temperature increases by approximately an order of magnitude. Finally, panel 5 contains a spectrogram from the Radio and Plasma Waves Sensor (RPWS) in which broadband increase in lower frequency plasma waves is

observed, along with a drop out (reduction in frequency) in the line associated with the upper hybrid limit, suggesting a decrease in associated plasma density (Rymer et al., 2009).

Analysis of the detailed event reveals a 3 nT enhancement in the magnetic field strength from 46 to 49 nT, an increase of ∼6.5%. Combining the observation signatures with our developed theoretical framework provides strong evidence that this injection is a flux tube moving inwards under RI motions. The measured plasma properties, assuming the PSD is conserved, indicate an origin of $11R_S$ for the contained material, meaning that the tube has moved 4 R_S inwards. The radial velocity of this transport is difficult to determine exactly, especially considering all measurements are from a single spacecraft bound point, but seems to be on the order of 100 km s^{-1}, approximately consistent with velocities in the Jovian system.

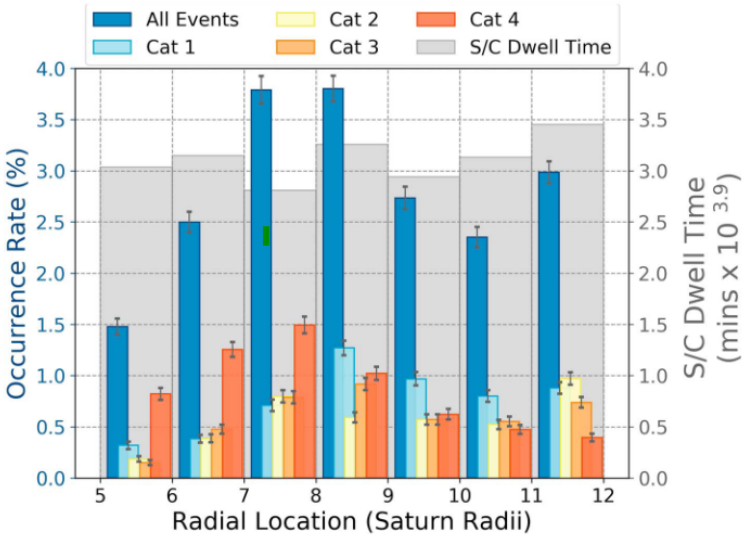

Figure 3.10: Occurrence rate of the total number of interchange events observed at varying radial distances, binned at integer distance values 5-12 R_S, between 2005-2016. Total number of events at a radial distance is indicated by the dark blue bar, with confidence intervals shown, these are then subdivided into 4 categories (light blue, yellow, orange & red bars) using the mean partial pressure of the observed event, again with confidence intervals shown. It can be seen that the largest number of events are at 7-9 R_S. Spacecraft dwell time at a particular radial distance interval throughout the examined time-frame is indicated by the grey bars, this can be seen to be well distributed between each of the distance intervals (Azari et al., 2018).

Collating interchange events observed over the course of the Cassini mission, it is found that the number identifiable is large enough to perform a statistical analysis. This is done by using data from the Charge Energy Mass Spectrometer (CHEMS) instrument, specifically using measurements of 3-22 keV H^+. A total of 663 events are determined to be permissible for comparison from a variety of previously conducted surveys (Chen and Hill, 2008; Kennelly et al., 2013; Lai et al., 2016) as well as newly identified (Azari et al., 2018). These events are then placed into categories 1-4 based on their pressure, starting at lower pressures and moving to high. The occurrence rate for the distance at which events are encountered is shown in figure 3.10 between 5-12 R_S, with the categories shown individually as well as summed. The dwell time that Cassini spent at each radial distance (S/C Dwell Time) is also shown and it can be clearly seen that this does not control the determined distribution of events.

From this statistical analysis it is determined that the peak in RI events occurs between

7-9 R_S, though some dependency is determined with an event's pressure such that higher pressure events occur at larger radial distances. It is also determined that the vast majority ($\sim$94%) of events are short in duration, <15 minutes, with a lower boundary also certainly provided by the cadence of observations. This supports the notion that injection events are narrow regions of hot, tenuous plasma being moved inwards by RI motions. Additionally, an estimate of the injection width is found as $\sim 10^{-1}$ R_S, again with some dependency on pressure (higher pressures having larger widths). Finally, it should be noted that injection events occur preferentially on the nightside of the magnetosphere. This is consistent with the ionospheric conductivity effecting RI instability growth rates, but also suggests that Vasyliunas reconnection events may be in part responsible for the generation of these hot, depleted flux tubes.

3.4 Modelling

The review of observation data has provided compelling evidence for the presence of RI motions throughout the inner & middle magnetosphere's of both Jupiter & Saturn. A number of measurements, calculations & conclusions have been made possible by these, including the determination of the average spatial scales and a confirmation of the link between ionospheric conductivity & growth times. However, due to the nature of single spacecraft measurements a number of questions remain unanswered which are fundamental to our understanding of the magnetospheric dynamics of the outer planets. Perhaps the most important of these is how precisely do the mechanisms of RI motions contribute/control the transport of plasma from the inner to outer magnetosphere? Here, the use of numerical models able to resolve large portions of the magnetosphere are necessary to gain insights into this question and more.

When global scale modelling of the magnetosphere is discussed, the most obvious candidate for usage is that of a MHD model. Indeed, these exist for both the Jovian (Ogino et al., 1998; Delamere et al., 2022; Sciola et al., 2022) and Saturnian (Jia et al., 2012; Rajendar, 2015) systems, though none of these models have been developed with the specific purpose of examining RI motions. Rather, these models have been extremely effective in capturing large scale dynamics, such as Kelvin-Helmholtz (KH) waves along the flanks of the magnetopause, along with the ejection of plasmoids from the middle magnetosphere down tail. That is not to say that these models are entirely unable to resolve RI motions or make predictions of the structures formed by them (see Kidder et al., 2009). However, the problem lies in that of the spatial scales on which RI motions are observed to occur on, with narrow inflows only fractions of a single planetary radii, they are difficult to determine when the models span 100's of planetary radii. This means these global scales models are limited to use grids with cells much larger than the length scales associated with RI motions, due to both the assumptions made in their formation and the limitations of modern computational resources.

A multi-fluid model that has been applied specifically to the problem of the RI instability and its associated motions at the outer planets is that of the Rice Convection Model altered for Jupiter (RCM-J). The RCM was initially developed for application to the terrestrial magnetosphere and exploits the notion that particle motions in the inner & middle magnetosphere can be treated adiabatically (Wolf, 1983). If an isotropic distribution is assumed in the plasma then its motions are representative of the motions of a whole flux tube, further by averaging over the tube the particles are effectively bounce-averaged. Plasma motions are self-consistently computed, along with electric fields, and these coupled down into the ionosphere along magnetic field lines for the inner & middle magnetosphere. The magnetic field typical utilised by the RCM is time dependant, however is pre-defined and hence not responsive to dynamics evolving within the model

(not self-consistent). Additionally, it is required that plasma convection speeds inside the model domain are much less than the fast (MHD) wave mode (Toffoletto et al., 2003).

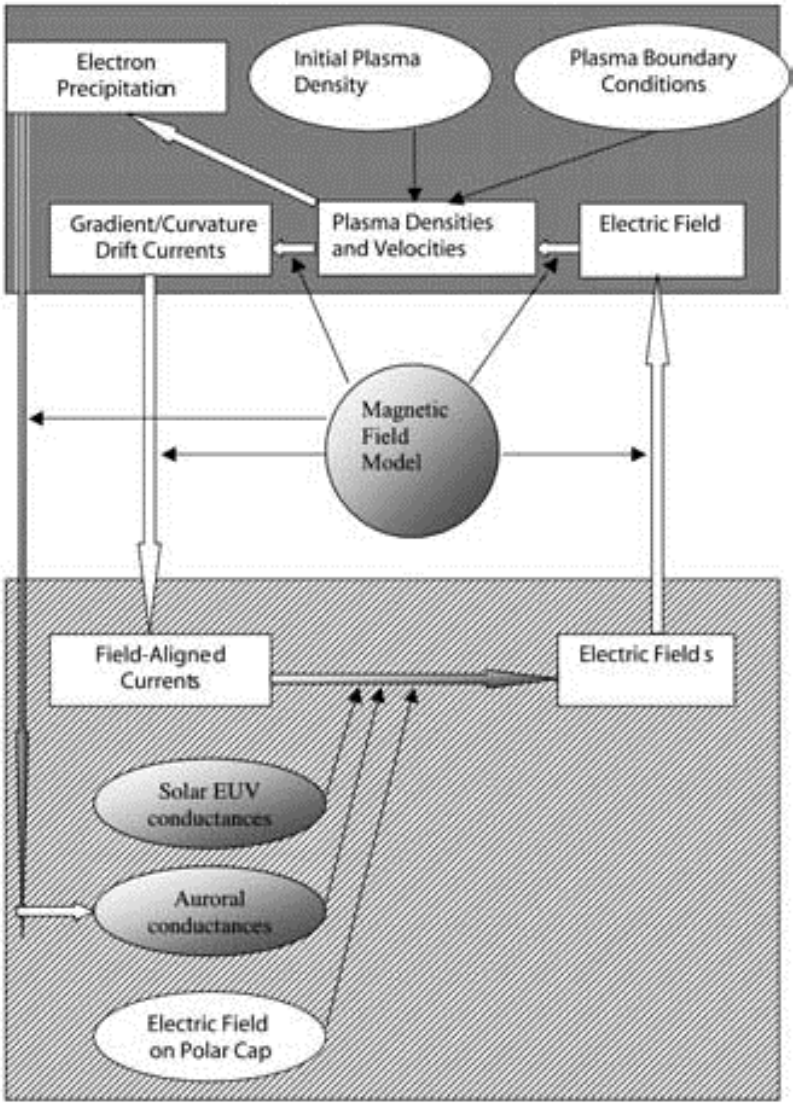

Figure 3.11: Flow diagram detailing the RCM's logical loop in order to progress temporally. The top panel (shaded dark grey) represents the magnetospheric portion of the model and the bottom (light grey) the ionospheric. The quantities both calculated (rectangles) and used as inputs (ovals) are included with black lines showing were inputs are inserted and the white arrows where computed values are passed. The magnetic field that connects the magnetosphere to the ionosphere is in the middle and is pre-defined though can vary in time. Adapted from Sazykin (2000).

The computational loop used by the RCM is based on the one first proposed by Vasyliunas (1970), with the complete updated model logic detailed in figure 3.11. From the initial configuration the plasma distribution is updated each time step (typically $\sim 10^0$ s) including gradient & curvature drifts, using the updated configuration the Vasyliunas equation (see Vasyliunas, 1970) is used and the field aligned currents (FACs) are calculated. These currents are then used to obtain the ionospheric electric potential and then calculate the ionospheric electric field, this is then communicated back to the magnetosphere along perfectly conducting magnetic field lines in order to obtain the magnetospheric electric field. We then arrive back at the beginning of the logical loop where the updated magnetospheric

electric field, along with gradient & curvature drifts update the plasma distribution once again (Toffoletto et al., 2003).

This allows for a model in which the ionosphere and magnetosphere can each be represented as 2-dimensional planes, connected by ideal magnetic field lines. In the magnetosphere, the flux tube content, η_s, and energy per unit flux tube volume, λ_s, for a particle of species s, are conserved quantities along a drift path. The thermal kinetic energy of a particle is then determined from λ_s as the flux tube volume from

$$W_s = \lambda_s \left(\int \frac{ds}{B} \right)^{-\frac{2}{3}},$$

where W_s is the thermal kinetic energy.(Harel et al., 1981).

The RCM model equations, which are seen to describe particle motions by following their analytical drift paths, are adapted for use at the outer planets through several major adaptions to its computations. First, it is assumed that $\underline{E} \times \underline{B}$ drifts follow ideal-MHD, hence the hot and cold plasma species drift together. Next, the centrifugal & Coriolis drifts (i.e. contribution from the centrifugal & Coriolis pseudo-forces), $\underline{v}_{cf,s}$ & $\underline{v}_{cor,s}$, are included to reflect the rotational dominance in the system using,

$$\underline{v}_{cf,s} = \frac{m_s \Omega_P^2 \underline{r} \times \underline{B}}{q_s B^2}, \tag{3.14}$$

$$\underline{v}_{cor,s} = \frac{-\left(m_s \Omega_P \times \underline{v}\right) \times \underline{B}}{q_s B^2}. \tag{3.15}$$

It is assumed that all particles associated with plasma/neutral tori are bound to the centrifugal equator for the purpose of determining their currents and their addition to the FACs. Hence, these currents, $\underline{J}_{cf}$ & $\underline{J}_{cor}$, are given by

$$\underline{J}_{cf,e} = \sum_s \eta_s \hat{b} \times \nabla_e \left(-\frac{1}{2} m_s \Omega_P^2 \underline{r}_e^2 \right), \tag{3.16}$$

$$\underline{J}_{cor,e} = 2 \left(\sum_s \eta_s m_s \right) \Omega_P \underline{v}, \tag{3.17}$$

where the e subscript denotes the equatorial plane (using Feynman notation for the ∇_e operator) and the unit vector $\hat{b} = \frac{B_e}{B_e}$. Further, it asserted that the there are no sources or sinks for plasma described by the model. The magnetic field and ionospheric conductances are altered to reflect those found at the outer planets. With these adjustments made it is determined that the assumption of flow speeds being less that the fast wave mode speed still holds, therefore model amendments are complete (Yang et al., 1992, 1994).

Early runs of the RCM-J examined plasma convection from the Io plasma torus radially outward. These runs determined that if the plasma was initialised with a longitudinal asymmetry, even small, that the convecting plasma would break up into fingers which transported it radially outwards, these can be seen in figure 3.12. The size of these fingers were at least partially a function of the radial density gradient in the torus, though it should also be noted that form of the finger configuration depends on the initial asymmetry introduced. Further, it is determined that the inclusion of the Coriolis pseudo-force acts to bend the fingers in the azimuthal direction to lag corotation, also visible in figure 3.12 with it most apparent in the final panel. (Yang et al., 1994).

Further work modelling the effects of transport via RI has been performed using the RCM-S, the RCM configured for the Saturnian system. Additional adaptations were made to the model computations in order to allow for the inclusion of a plasma source, obtained from neutral cloud theory, as well as a outflow boundary (a sink) placed well outside (at

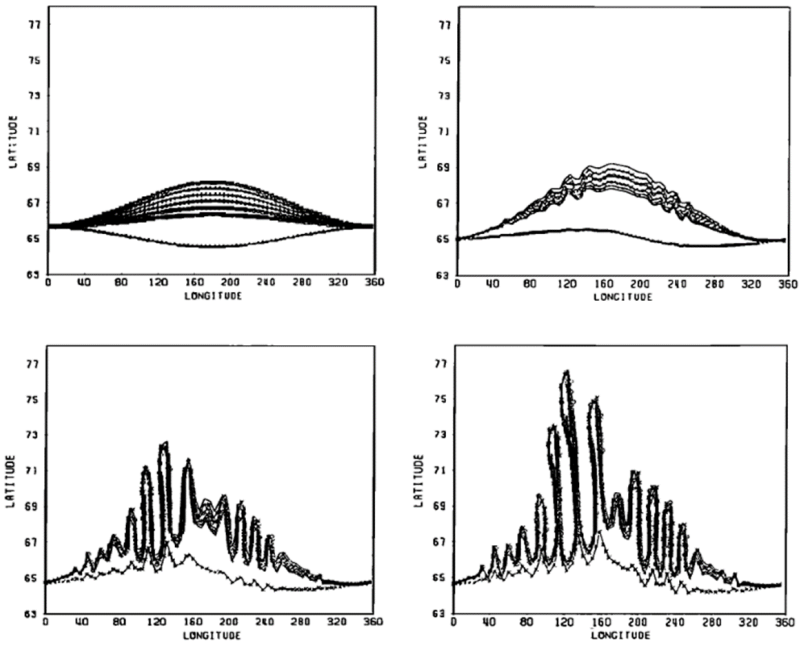

Figure 3.12: Evolution of cold plasma edges associated with initial asymmetric longitudinal configuration for the Io plasma torus using the RCM-J. Coordinates are given in terms of the latitude & longitude that flux tubes containing plasma parcels map down to in the planetary ionosphere, this corresponding to modelling the entire torus (0-2 π) between 5-9 R_J. 4 panels are shown containing snapshots of the configuration at 0, 15, 20 & 22 hours, from top left to bottom right. The formation of several interchange fingers can be clearly, bent in the azimuthal direction against corotation Yang et al. (1994).

40 R_S) of the region of interest (2-12 R_S). Also, the inclusion of a finite plasma pressure, with associated drift current, was found to be possible. Using these modifications it was determined that from initial configuration after several hours of plasma build up, at the position of maximum generation, the 'spontaneous' outbreak of interchange fingers was observed. This process can be seen in figure 3.13, these develop and reach out into the magnetosphere transporting plasma radially outwards via the RI instability and can be seen to be bent to lag corotation by the Coriolis force. However, it can also be seen as the simulation continues that this flow pattern evolves into a more chaotic structure, with clear interchange fingers difficult to identify (Liu et al., 2010). The inclusion of finite plasma pressure is found to enhance the instability growth rate by $\sim$50% (Liu and Hill, 2012).

Reviewing the simulations & their associated results provided by the RCM-J & -S, it is apparent that the work has had great success in beginning to improve our understanding of precisely how the RI instability orders plasma motions at the outer planets in order to accommodate bulk outwards transport. Although not specifically discussed alongside the presentation of the model's major results, these have been compared to theoretical predictions and observational data of the targeted regions, with model results being consistent, at least in part, with these (see Achilleos et al., 2015). There are of course still outstanding questions and fundamental limitations in the results produced by these simulations. Model configuration in the Jovian system is incredibly restrictive with no outflow boundary meaning that model run length is linked to the time taken for plasma to start to gather at this top boundary, which itself has EM effects as this represents a region of high electrical potential, produced from the created plasma pressure gradient that is then communicated to the ionosphere via FACs. This immediately leads to a second issue with the results for the Io plasma tori, the model predicts transport times on $\sim 10^1$ hours whereas

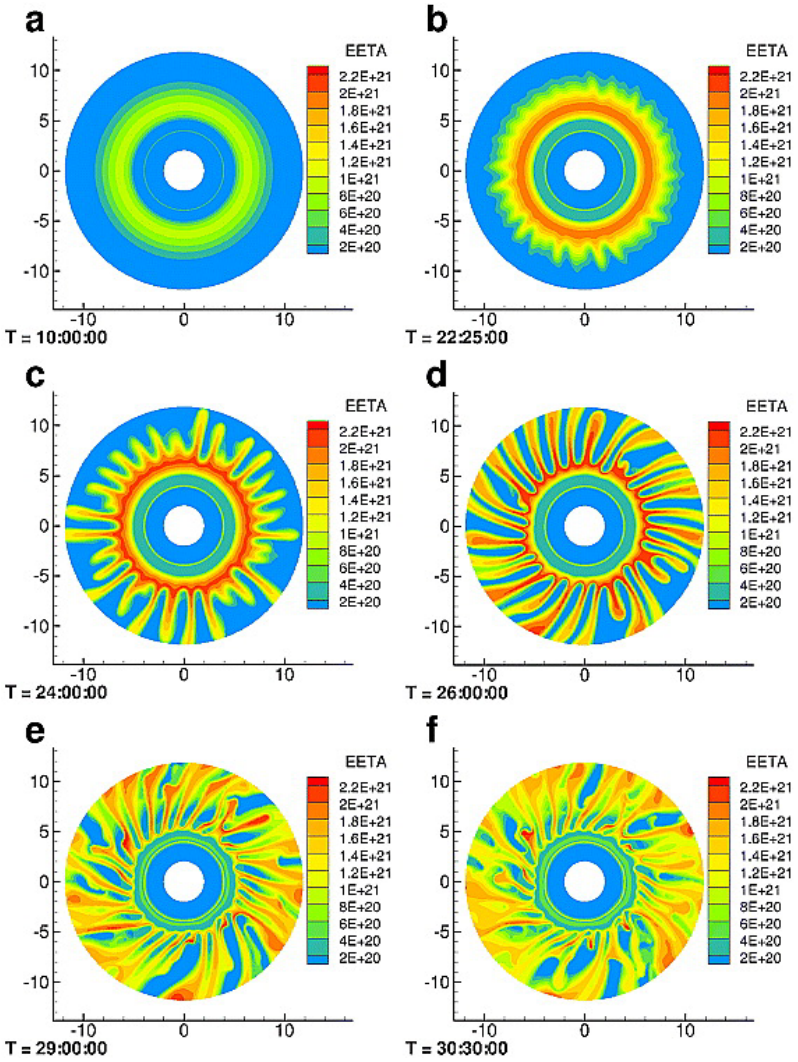

Figure 3.13: Outbreak of interchange fingers in the RCM-S with entire azimuthal domain (0-2 π) and inner boundary (2 R_S) to 12 R_S shown. A series of 6 snapshots are shown at 10, 22:25, 24, 26, 29 & 30:30 hours (labelled a, b, c, d, e & f respectively), from top left to bottom right. Colour of contour indicates the flux tube ion content (ions per Weber) with values indicated in colourbar on right of panel (Liu et al., 2010).

observational results have determined the true transport time for material to be $\sim 10^2$ hours (Thomas et al., 2004), meaning predicted plasma flows are a order of magnitude too fast. Examining the Saturnian results several of these issues are addressed, though the outer boundary at $\sim$40 R_S is well outside the range allowed by the assumptions used to build the model, potentially causing implicit erroneous numeric effects to be present though the entire run.

The major issue highlighted in the Saturnian results is that after the breakout of interchange fingers from an initial configuration the flows in the system tend to a more disorganised chaotic pattern, more reminiscent to of the random-like walk proposed in figure 3.2. This leads to the question being posed of are interchange fingers a natural occurrence we could observe at the outer planets, or are they purely a numeric result caused by the selection of initial conditions of the model, the link between finger structure and selected configuration would seem to support this notion. The conclusion that interchange fingers (at least of the form proposed by the RCM) are purely a numeric effect has been proposed by others also (i.e. Vasyliunas, 2019), and remains an open question that requires

further investigation.

It should be noted that additional work has been done to analyse the flow of material through the Saturnian system using multi-fluid modelling (Kidder et al., 2009), examining the system on global scales, allowing for coupling between magnetospheric dynamics with the solar wind. Simulations run using the model also find the outbreak of interchange fingers, with an interesting relation between the direction of the IMF & finger formation. This being that for parallel IMF configurations little finger development occurs, whereas for anti-parallel configurations production in maximised, finger width is linked to the density profile and they grow radially outwards up to distances of $\sim$20 R_S after which they disperse into the local plasma medium. This seems to imply that the process of radial transport via RI motions is in part linked with solar wind conditions outside the magnetosphere. Despite the results from this model, when the location of the RI motions with associated finger formation is considered, at 5-20 R_S on the equatorial plane, the likelihood of signifiant effects from IMF-magnetopause effects (i.e. Dungey cycle) is incredibly limited with the region well insulated from the IMF itself. It is therefore difficult to understand, with our present knowledge of magnetospheric dynamics, why IMF configuration would play such a fundamental role in the development of RI motions & the global transport of internally sourced plasma.

3.5 Future Work

Through the review of work in this chapter we have examined the theoretical formation of the RI instability and how this can be implemented in the rotationally dominated systems of the outer planets to transport plasma. Motions of individual pairs of flux tubes can be readily understood, but the flow patterns through large portions of the magnetosphere are more difficult to determine. At Jupiter it is proposed that there are rather two different regimes, a random-like walk in the region just outside the Io plasma torus, that changes to larger scales with a dense background medium containing hot tenuous plasma parcels moving inwards. The transition region between these two regimes is poorly defined with the exact mechanisms responsible for this change not well understood. The system at Saturn is thought to be somewhat simpler with just the large scale dense medium with narrow inflow channels.

Observations of the described regions provide evidence to support the theoretical results. The Galileo mission provided first evidence of inflow channels containing a plasma parcel transported from further into the torus, with the signatures obtained consistent with the random-walk assertion. Beyond the torus region at Jupiter and throughout the Saturnian system a substantial number of injections have been detected that are again consistent with hot, tenuous plasma parcels being transported through a dense local medium, with increased magnetic field strengths. The origins of these injections are suggested to be tied in both systems to Vasyliunas cycle reconnection events, creating mass depleted, magnetically enhanced flux tubes to be transported inwards under RI motions. However, once again more work is required to be sure of the exact mechanisms responsible for this.

Finally, model results have been presented, with hopes of gaining a better understanding of RI motions throughout large portions of a magnetosphere. Simulations at both Jupiter and Saturn have demonstrated how the RI instability can be responsible the bulk transport of plasma radially outwards. A major prediction from these modelling results is the outbreak of interchange fingers from asymmetric plasma configurations which are bent in the azimuthal direction to lag corotation by the inclusion of Coriolis effects. The limitations of these model results have been explored with concerns raised over the physical interpretation of the obtained results, with it demonstrated that this prediction is more uncertain then it first seems.

From this review we find that a number of open questions remain, with a selection chosen for investigation in this thesis. These can be summarised as:

- What are the local spatial & temporal scales of RI instabilities and which local plasma parameters control these?
- Are there ion-scale physical effects occurring in the plasma as flux-tubes are being interchanged and how do these alter RI motions from the theory?
- How can particle signatures be used to determine when an RI instability has occurred and how can we use these to obtain a measure of the event?
- What flow pattern is formed by RI motions and what local parameters control the regimes formed by these, additionally are interchange fingers a natural occurrence in these?

The method utilised to answer these question is the use of hybrid plasma modelling. This is selected for its ability to capture both large scale (in terms of multiple planetary radii) plasma flows, whilst being able to resolve physical effects down to the ion-inertial length. In the following chapter the numerics utilised to construct this model will be detailed, before the exact computational implementation is described. The model will be validated & benchmarked through a series of tests, before final application to the outer planetary systems for use in analysing interchange.

Chapter 4

Hybrid Modelling Numerics & Logic - A Recipe

The process of mass loading from internal sources in the magnetospheres of the outer planets has been examined in §2. The mass ejected from these sources forms either plasma or neutral tori, dependant on system specific factors. However, as these structures can be examined in a steady state without continual inflation then there must be loss processes associated with them. Bulk transport of plasma radially outwards is the process of particular interest to this thesis, with the mechanism responsible for this identified as the RI instability. This instability is examined in §3 and found to be important for the global transport of plasma through outer planetary magnetospheric systems. A number of questions fundamental to the understanding of these systems remain open, with it identified that hybrid plasma modelling will allow for insights and the answering of these questions.

Applications of hybrid plasma modelling to problems in space plasma physics has previously produced results integral to developing our understanding of these environments. A development of the theory of space plasmas, along with an examination of what parameters determine which modelling regime (i.e. kinetic, hybrid or fluid) has been presented in §1. In this a number of hybrid models applied to magnetospheric physics have been identified. However, none of these have been specifically designed for the examination of radial transport in rotationally dominated systems. Though adaption of current operational models is possible, the inclusion of rotational effects requires alteration of the fundamental equations used to form these. Therefore, would necessitate the re-derivation of solutions obtained, along with fresh computational implementations of these. Considering this, it is determined that a new hybrid plasma model would be most appropriate for use in answering the questions pertinent to this thesis.

Examination of the criterion for driven RI motions make it clear that the inclusion of rotational pseudo-forces (centrifugal, Coriolis & Euler) are fundamental to the development of the instability. It has been noted that observations of energetic ions & electrons generated by injections hint at different effects on ion length scales (see §3.3). Hence, a kinetic-ion, fluid-electron approach is selected for the development of this new model, with features on the spatial scale of the electron inertial considered unimportant in this work. This means that ions are treated kinetically, described using their full equation of motion, whereas electrons are formed into a neutralising fluid that follow the ion motions. Therefore, hybrid-PIC modelling is the technique identified for use.

In this chapter the basic model equations and logic for generic hybrid plasma modelling are presented. There exists a vast swathe of literature detailing the general formulation of a hybrid plasma model, the particular guides utilised in this thesis are Winske et al. (2003) & Bagdonat (2005). However, it is worth noting that the specific numerics utilised both vary & iterate on the guides given in these. Specific discussion of how these equations

& methods are adapted for specific modelling at the outer planets, with exact model geometry and solutions for computational implementation, follows in the next chapter.

4.1 Model Equations

We begin our exploration of the model equations by considering the ions, these are treated kinetically using their equation of motion (eqn 1.3) in order to obtain an individual particle's exact trajectory. This equation is utilised to calculate the velocity of each kinetic ion in the model quantising the effects of the surrounding EM fields on the particle. Here, the equation for the Lorentz force acting on a particle is restated. This is to bring the nomenclature for the variables contained in-line with that used throughout the model description. This will be repeated for all equations fundamental to model operation, with a list of model variables and their associated definition, found summarised in appendix A.

Therefore we restate,

$$\frac{d\underline{v}_i}{dt} = \frac{q_i}{m_i}\left(\underline{E} + \underline{v}_i \times \underline{B}\right), \tag{4.1}$$

where all symbols have their usual meaning, recalling the i subscript denotes ion species (including protons) of the plasma. The standard definition of velocity is utilised to obtain a particle's position once its velocity has been obtained,

$$\frac{d\underline{x}_i}{dt} = \underline{v}_i, \tag{4.2}$$

where $\underline{x}_i$ is the position of the particle. It is worth noting that the computational domain in which the particles are described is a complete Euclidean space inside which they are free to occupy any position.

Electrons are considered to form a continuum which can be treated as a fluid. It is important to note at this point that electrons are considered massless (i.e. $m_e = 0$, where e denotes an electron) in the model. Exploring the consequences of this on the motions of the electrons, as well as the plasma parameters, explored in §1.1.1 & §1.1.6, it is determined that both the electron gyro & plasma frequencies (ω_{ge} & ω_{pe}) become poorly defined and the gyro-radius & inertial length scale (r_{ge} & d_e) become 0. Therefore, any effects tied to fundamental oscillations of electrons in the plasma are equally poorly defined, limiting the range of wave modes permissible.

To describe the flow of this electron fluid the corresponding fluid momentum equation will be utilised, this has already been determined in §1.1.5 as,

$$n_e m_e \frac{D\underline{U}_e}{Dt} = -\nabla \cdot \underline{\underline{P}}_e - n_e e\left(\underline{E} + \underline{U}_e \times \underline{B}\right) + \underline{R}_{ei}.$$

The plasma contained within the model is considered to be collisionless (i.e. $\underline{R}_{ei} = 0$). Applying this condition along with asserting the massless nature of the electrons reduces the momentum equation to the following,

$$\underline{0} = -en_e\left(\underline{E} + \underline{U}_e \times \underline{B}\right) - \nabla \cdot \underline{\underline{P}}_e. \tag{4.3}$$

Both the electric and magnetic fields, $\underline{E}$ & $\underline{B}$ respectively, are fully described across the entire domain within the model. This is desirable over the utilisation of prescribed EM fields as these limit any model to being electro & magneto-static, unable to respond to the changing distribution of charged particles being described. Therefore, to be fully electrodynamic requires solving Maxwell's equations within each iteration of the model temporal step. The hybrid model under construction is required to be fully EM dynamic, hence equations are required to allow for their calculation as the ions & electrons move through the modelled domain.

This is essential when investigating any plasma as the motions of the charged particles contained themselves induce EM effects. Hence, the magnetic field is advanced numerically using Faraday's law of induction (see Griffiths, 2017),

$$\frac{\partial \underline{B}}{\partial t} = -\left(\nabla \times \underline{E}\right). \tag{4.4}$$

The obvious counterpart in the set of Maxwell's equations when determining the method for obtaining the corresponding electric field is the Ampère-Maxwell law (see Griffiths, 2017),

$$\frac{\partial \underline{E}}{\partial t} = c^2 \nabla \times \underline{B} - \frac{1}{\epsilon_0}\underline{J}. \tag{4.5}$$

However, for a quasi-neutral, collisionless plasma it is shown that Ampère's law is always in the low frequency limit (or Darwin limit) (Bagdonat, 2005). In this regime the displacement current associated with the law (i.e $\frac{1}{c^2}\frac{\partial \underline{E}}{\partial t}$) is much smaller than the current density ($\frac{1}{c^2}\frac{\partial \underline{E}}{\partial t} \ll \mu_0 \underline{J}$) and tends to zero in the calculations. Hence, we obtain the low frequency Ampère's law,

$$\underline{J} = \frac{1}{\mu_0}\nabla \times \underline{B}, \tag{4.6}$$

where $\underline{J}$ should be noted as being the total current density (i.e. $\underline{J} = \sum_s \underline{J}_s$, where s denotes all plasma species). The question then becomes, how does one obtain the electric field from this with the term now missing from this formulation?

Utilising the definition of current density,

$$\underline{J} = q_i n_i \left(\underline{U}_i - \underline{U}_e\right), \tag{4.7}$$

with quasi-neutrality applied to collect coefficients, low frequency Ampère's law is recast as

$$\nabla \times \underline{B} = \mu_0 q_i n_i \left(\underline{U}_i - \underline{U}_e\right), \tag{4.8}$$

note charge density $\rho_c = q_i n_i$ (with electron contributions neglected). Examining the form of our massless-electron momentum equation (eqn 4.3), we find it is possible to rearrange low frequency Ampère's law in terms of electron flow velocity ($\underline{U}_e$) and substitute it in to obtain an analytic solution for the electric field. Therefore,

$$\underline{U}_e = \underline{U}_i - \frac{\nabla \times \underline{B}}{\mu_0 q_i n_i}. \tag{4.9}$$

Substituting eqn 4.9 into 4.3 to eliminate U_e we find,

$$\begin{aligned} -en_e\left[\underline{E} + \left(\underline{U}_i - \frac{\nabla \times \underline{B}}{\mu_0 q_i n_i}\right) \times \underline{B}\right] - \nabla \cdot \underline{\underline{P_e}} &= \underline{0}, \\ -en_e\left[\underline{E} + \underline{U}_i \times \underline{B} - \frac{1}{\mu_0 q_i n_i}\left(\nabla \times \underline{B}\right) \times \underline{B}\right] - \nabla \cdot \underline{\underline{P_e}} &= \underline{0}, \end{aligned}$$

finally using quasi-neutrality,

$$\underline{E} = -\frac{1}{q_i n_i}\nabla \cdot \underline{\underline{P_e}} - \underline{U}_i \times \underline{B} - \frac{1}{\mu_0 q_i n_i}\left(\nabla \times \underline{B}\right) \times \underline{B}. \tag{4.10}$$

It is often convenient to recast this solution using the vector identity $\frac{1}{2}\nabla\left(\underline{A} \cdot \underline{A}\right) = \left(\underline{A} \cdot \nabla\right)\underline{A} + \underline{A} \times \left(\nabla \times \underline{A}\right)$, where $\underline{A}$ is some arbitrary vector. Hence,

$$\underline{E} = -\frac{1}{q_i n_i}\nabla \cdot \underline{\underline{P_e}} - \underline{U}_i \times \underline{B} + \frac{1}{q_i n_i}\left[\frac{\left(\underline{B} \cdot \nabla\right)\underline{B}}{\mu_0} - \nabla\left(\frac{B^2}{2\mu_0}\right)\right]. \tag{4.11}$$

Using this method to obtain the electric field has a number of implications for the model logic and numerics. The first of these is that the electric field can be obtained analytically, rather than numerically, by updating the variables used to calculate it. Next, since the electron flow velocity has been eliminated there is no need to update or track the fluid electron component of the hybrid model, rather the electron motions can be determined from the ions. Finally, a somewhat natural conclusion from the previous point, due to the application of quasi-neutrality the electron and ion densities are exactly equal at all times with the ion densities setting the quantity of electrons.

The final variable in the set of model equations that has not been acquired is that of the electron pressure. The selection made in this work is to simplify the electron pressure tensor into a scalar field, such that $\underline{\underline{P}}_e = p_e \cdot \underline{\underline{1}}$, where $\underline{\underline{1}}$ is a unit tensor. The first and most straight forward method for determining the electron pressure is by using an adiabatic equation of state using (Müller et al., 2011),

$$p_e n_e^{-\gamma} = \mathcal{C}, \tag{4.12}$$

where γ is the adiabatic index & $\mathcal{C}$ is a constant.

4.2 Simulation via Numerical Differencing

The key equations obtained in the previous section that can be solved iteratively in order to create a hybrid-PIC plasma model are collected,

$$\begin{aligned}
\frac{d\underline{v}_i}{dt} &= \frac{q_i}{m_i}\left(\underline{E} + \underline{v}_i \times \underline{B}\right), \\
\frac{d\underline{x}_i}{dt} &= \underline{v}_i, \\
\frac{\partial \underline{B}}{\partial t} &= -\left(\nabla \times \underline{E}\right), \\
\underline{E} &= -\underline{U}_i \times \underline{B} - \frac{\nabla p_e}{q_i n_i} - \frac{1}{\mu_0 q n_i}\left(\nabla \times \underline{B}\right) \times \underline{B}.
\end{aligned}$$

In order to progress the ion velocities & positions, as well as the magnetic field, it is necessary to advance them in time. This is done using a numerical approximation to obtain their updated values at some future position in the temporal domain. The reason this is considered an approximation is because the variables used to calculate the new value are fixed for the duration of the value advancement, therefore unable to capture any fluctuations that occur in the space moved through in a temporal step. The electric field is obtained analytically from a combination of ion flow velocity, magnetic field, electron pressure & charge density. Therefore it is only necessary to advance each of these variables and not the electric field itself, removing a source of numerical approximation, and hence error, from the simulation.

The technique selected for use in advancing both an ion's velocity and position is that of time-centred finite differencing. Using this, a forward differencing scheme progresses the selected quantity. The values of corresponding variables in its governing equation are at a time step centred between initial & final step of the selected quantity (i.e. $\underline{v}^{n-\frac{1}{2}} \rightarrow \underline{v}^{n+\frac{1}{2}}$ using $\underline{E}^n, \underline{B}^n$). Forward finite differencing uses (Press et al., 2007; Pletcher, 2013),

$$\frac{dA}{dt} = \frac{A^{n+\frac{1}{2}} - A^{n-\frac{1}{2}}}{\Delta t}, \tag{4.13}$$

where A is some arbitrary function with a time dependency and Δt is the length of the time step being taken. The superscripts denote its position in time, where n is an integer

representing the step in time the system is currently in. A full step in time (Δt) is indicated by the addition of one to the current step index (i.e. $n+1$), however it can been seen above that the differencing moves the function between half time steps.

The reason for obtaining particle velocities ($\underline{v}^{n+\frac{1}{2}}$) on the half integer time step is to offset their location in time from that of the particles position ($\underline{x}^{n+1}$). This is known as the 'leapfrog' method and has the benefit of increasing the accuracy to the second order (Horowitz et al., 1989). This is of course not the only numerical method for advancing a particles velocity & position, but rather selected for the provided balance between computational efficiency & resources utilised and accuracy of results produced. It should be noted that the second-order accurate central differencing scheme used in the next chapter for spatial derivatives is inappropriate for use here due to its limitation in capturing the dynamics of oscillating functions.

Forward differencing can be directly applied to the ion's equation of motion (eqn 4.1) in order to progress a particles velocities. This yields,

$$\underline{v}^{n+\frac{1}{2}} = \underline{v}^{n-\frac{1}{2}} + \frac{q_i \Delta t}{m} \left(\underline{E}^n + \underline{v}^n \times \underline{B}^n \right). \tag{4.14}$$

It is worth noting here that the EM fields at the current position in time are utilised in order to progress the ion velocities to the next. Although the velocity of the ions at their current time step is included (i.e. $\underline{v}^n$), this term can be eliminated using Lax's method as the velocities are never obtained on integer steps.

Lax's method uses the velocity of a particle at half integer time steps before and after the current step in order to calculate an average value at the integer value. This can be done using,

$$\underline{v}^n = \frac{1}{2} \left(\underline{v}^{n+\frac{1}{2}} + \underline{v}^{n-\frac{1}{2}} \right). \tag{4.15}$$

This is substituted into the ion's equation of motion to eliminate all velocity terms on full integer time steps, hence,

$$\underline{v}^{n+\frac{1}{2}} = \underline{v}^{n-\frac{1}{2}} + \frac{q \Delta t}{m} \left[\underline{E}^n + \frac{1}{2} \left(\underline{v}^{n+\frac{1}{2}} + \underline{v}^{n-\frac{1}{2}} \right) \times \underline{B}^n \right].$$

Clearly, this new form of the equation of motion requires rearrangement in order to collect the advanced value and obtain the updated particle velocities. This rearrangement is a non-trivial, lengthy derivation (see Horowitz et al., 1989; Bagdonat, 2005), with the final form presented here,

$$\begin{aligned} \underline{v}^{n+\frac{1}{2}} = K \Bigg\{ \left[1 - \frac{1}{4} h^2 \left(\underline{B}^n \right)^2 \right] \underline{v}^{n-\frac{1}{2}} + h \left(\underline{v}^{n-\frac{1}{2}} \times \underline{B}^n + \underline{E}^n \right) + \\ \frac{h^2}{2} \left[\underline{E}^n \times \underline{B}^n + \left(\underline{v}^{n-\frac{1}{2}} \cdot \underline{B}^n \right) \underline{B}^n \right] + \frac{h^3}{4} \left(\underline{E}^n \cdot \underline{B}^n \right) \underline{B}^n \Bigg\}, \end{aligned} \tag{4.16}$$

where

$$K = \frac{1}{1 + \frac{1}{4} h^2 \left(\underline{B}^n \right)^2}, \tag{4.17}$$

$$h = \frac{q}{m} \Delta t. \tag{4.18}$$

It should be noted that a more complete derivation of this formulation can be found in the following chapter where these equations are adapted for use at the outer planets.

Next, the definition of velocity (eqn 4.2) can be used to progress the ion's position. Since particle positions are required on full integer time step for our leapfrogging scheme, the following forward differencing is used,

$$\frac{dA}{dt} = \frac{A^{n+1} - A^n}{\Delta t}. \tag{4.19}$$

Combining with eqn 4.2 yields,

$$\underline{x}^{n+1} = \underline{x}^{n} + \Delta t \underline{v}^{n+\frac{1}{2}}. \tag{4.20}$$

It can be seen in this equation that the particle positions are advanced a complete time step by utilising the updated particle velocities on the half integer time step before, hence the name leap-frogging is given to the scheme.

The EM fields are required to be solved on integer time steps in order to be used to advance particle velocities in equation 4.14. However, since the magnetic field is advanced numerically using Faraday's law it is wholly dependant on the electric field which we currently only have also on a full integer time step. Approaching this problem from the other direction, if the equation used to obtain the electric field analytically is examined it is found to be dependant on the magnetic field, ion flow velocities and electron pressure gradients. Examining the temporal position of the variables we currently have, $\underline{B}^{n}, \underline{U}_{i}^{n+\frac{1}{2}}, p_{e}^{n+\frac{1}{2}}, n_{i}^{n+\frac{1}{2}}$, it is determined that by progressing the magnetic field by half a time step then the electric field can also be calculated at this time, $E^{n+\frac{1}{2}}\left(\underline{B}^{n+\frac{1}{2}}, \underline{U}_{i}^{n+\frac{1}{2}}, p_{e}^{n+\frac{1}{2}}, n_{i}^{n+\frac{1}{2}}\right)$. Therefore, the magnetic field is first advanced a half-time step, this advanced field is then utilised to calculate the electric field at plus a half time step, which in turn is then used to obtain the magnetic field on the full integer time step.

In order to progress our magnetic field a numerical technique must be selected, with the leapfrogging of particle positions & velocities making these solutions second order accurate. Therefore, we desire a scheme that ensures any progression of the magnetic field also remains second order accurate. The most obvious technique to apply to this is the time-centred finite differencing used to progress the particles, however this returns the leapfrogged parameters on time steps offset from one another. This is incompatible with the derived solutions for the EM fields as the electric field is solved analytically, requiring the magnetic field as a dependency, hence we require the magnetic field on both the half and full integer time-steps.

Therefore, another numerical scheme is required, with the method selected the MacCormack predictor-corrector scheme (Pletcher, 2013). This scheme uses two steps to first 'predict' the value of the progressed magnetic field, using forward differencing, before 'correcting' these initial estimated values, using backwards differencing. This method is second-order accurate and particular suited to application in non-linear equations, it should also be noted to not introduce diffusive errors into solutions produced. These two features are both desirable when attempting to determine the motions of enhanced fields within plasma parcels being transported via RI motions (i.e. a plasma instability). Further, it is found that as the solution to the electric field is analytic in form, the definition for this can be directly substituted into the equations used to progress the magnetic field by simply taking the curl of the analytic expression obtained (with dependent variables on appropriate temporal steps). Though the full solution with electric field will not be shown here (rather this is done exploiting the model geometry for simplifications in the next chapter), the variables used to obtain it will be indicated. Hence, the following is used to advance the magnetic field by a half time step, $(\underline{B}^{n} \rightarrow \underline{B}^{n+\frac{1}{2}})$,

$$\tilde{\underline{B}}^{n+\frac{1}{2}} = \underline{B}^{n} - \frac{\Delta t}{2}\left[\nabla \times \underline{E}^{n}\left(\underline{B}^{n}, \underline{U}_{i}^{n}, p_{e}^{n}, n_{i}^{n}\right)\right], \tag{4.21}$$

$$\underline{B}^{n+\frac{1}{2}} = \frac{\underline{B}^{n} + \tilde{\underline{B}}^{n+\frac{1}{2}}}{2} - \frac{\Delta t}{4}\left[\nabla \times \tilde{\underline{E}}^{n}\left(\tilde{\underline{B}}^{n+\frac{1}{2}}, \underline{U}_{i}^{n}, p_{e}^{n}, n_{i}^{n}\right)\right], \tag{4.22}$$

where $\tilde{\underline{B}}^{n+\frac{1}{2}}$ is the predicted magnetic field quantity.

With the magnetic field advanced by a half time step and the other quantities necessary to calculate the electric field already determined, we now obtain it using

$$\underline{E}^{n+\frac{1}{2}} = -\underline{U}_i^{n+\frac{1}{2}} \times \underline{B}^{n+\frac{1}{2}} - \frac{\nabla p_e^{n+\frac{1}{2}}}{q n_i^{n+\frac{1}{2}}} + \frac{1}{q_i n_i^{n+\frac{1}{2}}} \left[\frac{\left(\underline{B}^{n+\frac{1}{2}} \cdot \nabla\right) \underline{B}^{n+\frac{1}{2}}}{\mu_0} - \nabla \left(\frac{\left|\underline{B}^{n+\frac{1}{2}}\right|^2}{2\mu_0} \right) \right]. \tag{4.23}$$

It is now possible to use the predictor-corrector scheme detailed in eqn 4.21 & 4.22 to advance the magnetic field onto the full integer time step. This is done using,

$$\begin{aligned} \tilde{\underline{B}}^{n+1} &= \underline{B}^{n+\frac{1}{2}} - \frac{\Delta t}{2} \left[\nabla \times \underline{E}^{n+\frac{1}{2}} \left(\underline{B}^{n+\frac{1}{2}}, \underline{U}_i^{n+\frac{1}{2}}, p_e^{n+\frac{1}{2}}, n_i^{n+\frac{1}{2}} \right) \right], \\ \underline{B}^{n+1} &= \frac{\underline{B}^{n+\frac{1}{2}} + \tilde{\underline{B}}^{n+1}}{2} - \frac{\Delta t}{4} \left[\nabla \times \tilde{\underline{E}}^{n+\frac{1}{2}} \left(\tilde{\underline{B}}^{n+1}, \underline{U}_i^{n+\frac{1}{2}}, p_e^{n+\frac{1}{2}}, n_i^{n+\frac{1}{2}} \right) \right]. \end{aligned}$$

However, obtaining the electric field on the whole integer time step is still not possible since it is not only dependent on the magnetic field, but also the ion flow velocity, electron pressure gradients and charge density. Using the adiabatic equation of state to obtain the electron pressure it is found that this is wholly dependant on the ion distribution, hence are directly obtained at n_i^{n+1} and Lax's method is applied to obtain these on the half integer step. The ion flow velocities are not so easy to calculate with the quantity obtained from the particle velocities in the modelled domain, a quantity only determined on the half time step. Techniques for calculating the electric field on the integer time step are non-trivial and are the area in which most hybrid models diverge in method in a substantial sense (Winske et al., 2003).

It is apparent that in order to complete the advancement of the electric field the flow velocities at the full integer time step must be obtained. One simple method for calculating the flow velocities is utilising the values on the previous two half integer time steps, $\underline{U}_i^{n+\frac{1}{2}}$ & $\underline{U}_i^{n-\frac{1}{2}}$. The advanced flow velocities are then obtained using

$$\underline{U}_i^{n+1} = \frac{3}{2}\underline{U}_i^{n+\frac{1}{2}} - \frac{1}{2}\underline{U}_i^{n-\frac{1}{2}}. \tag{4.24}$$

The accuracy of this technique can only be considered to be to a first-order approximation. A more accurate formulation of this technique can be made by including additional flow velocity values from previous time steps, i.e. $\underline{U}_i^{n-\frac{3}{2}}$. However these techniques require additional computational memory usage to store these values. The increase in accuracy must be carefully weighed next to the additional computational expense in order to determine the feasibility of these formulations (Winske et al., 2003).

However, the methods utilised in model progression to this point have been second-order accurate in the temporal domain, therefore a technique is required that preserves this level of precision. The technique identified for obtaining the required parameters to advance the electric field onto the full integer time step is to use the Current Advance Method (CAM), detailed by Matthews (1994). This obtains the parameters by calculating a mixed time electric field description, $\underline{E}^*$, and using this to progress the current densities. These are utilised with updated charge densities to calculate ion flow velocities at the complete time step. Hence, providing all the parameters needed to calculate the electric field.

Another improvement provided by the CAM technique, in terms of computational efficiency, is seen in the determination of the ion flow velocities on the half time step. Rather than determining the advanced particle position & velocity distribution (achieved by looping through a list containing all particle information), then using Lax's method

to obtain the positions on the half time step and using these to calculate the current density and hence ion flow velocity. This method calculates the current densities at mixed time steps and combines these. The benefit of this is it can be done in concert with the calculations of the particles velocities & positions. These mixed current densities are determined as,

$$\underline{J}_i^- \left(\underline{x}^n, \underline{v}^{n+\frac{1}{2}}\right), \tag{4.25}$$

$$\underline{J}_i^+ \left(\underline{x}^{n+1}, \underline{v}^{n+\frac{1}{2}}\right), \tag{4.26}$$

where they are functions of the position & velocity distribution. The gathering of particle moments to compute these is dependant on the model geometry and hence will be detailed in the following chapter.

The pair of mixed current densities can then be combined to determine the ion flow velocities on the half integer step using,

$$\underline{U}_i^{n+\frac{1}{2}} = \frac{1}{2}\left(\frac{\underline{J}_i^-}{\rho_c^n} + \frac{\underline{J}_i^+}{\rho_c^{n+1}}\right). \tag{4.27}$$

This method follows the reformulation postulated by (Bagdonat, 2005), rather than following the method proposed by (Matthews, 1994) exactly. The formulation above can be seen to eliminate 'shot noise', a term for numerical noise introduced by the use of a finite number of particles to represent ion position and velocity distributions. This can lead to the development of unphysical, numerical effects and can ultimately lead to simulations becoming unstable, hence should be reduced where possible.

These mixed current densities can be used to calculate an electric field also composed of a mix of temporal time steps, $\underline{E}^*$. To do this the mixed ion flow velocity, $\underline{U}_i^+ = \frac{\underline{J}_i^+}{\rho_c^{n+1}}$, is utilised, with all other variables on the full integer step. Hence, using the solution given by eqn 4.23,

$$\underline{E}^* = -\underline{U}_i^+ \times \underline{B}^{n+1} - \frac{\nabla p_e^{n+1}}{q n_i^{n+1}} + \frac{1}{q_i n_i^{n+1}}\left[\frac{\left(\underline{B}^{n+1}\cdot\nabla\right)\underline{B}^{n+1}}{\mu_0} - \nabla\left(\frac{\left|\underline{B}^{n+1}\right|^2}{2\mu_0}\right)\right]. \tag{4.28}$$

This mixed electric field can now be combined with two new values determined from the collection of particle moments, $\Lambda^{n+1}\left(\underline{x}^{n+1}\right)$ & $\underline{\Gamma}\left(\underline{x}^{n+1}, \underline{v}^{n+1}\right)$ (see §5.2.3 for collection method), to correct the mixed step current density, $\underline{J}_i^+$. Therefore, it is determined that $\underline{J}_i^+$ is representative of the 'free-streaming' currents (Matthews, 1994). These are the currents that would arise from particle motions if they were force free, hence the corrections applied represent the contributions from the EM fields on these. Ion current densities on the full integer time step, $\underline{J}_i^{n+1}$, can be determined using

$$\underline{J}_i^{n+1} = \underline{J}^+ + \frac{\Delta t}{2}\left(\Lambda^{n+1}\underline{E}^* + \underline{\Gamma}^{n+1}\times\underline{B}^{n+1}\right). \tag{4.29}$$

The fully progressed ion flow velocities, $\underline{U}_i^{n+1}$, are determined in the usual fashion,

$$\underline{U}^{n+1} = \frac{\underline{J}^{n+1}}{\rho_c^{n+1}}. \tag{4.30}$$

With the magnetic field, ion flow velocities, electron pressure gradients & charge densities now obtained at the full integer time step it is possible to calculate the fully advanced electric field. This is done once again with the solution determined in eqn 4.23,

$$\underline{E}^{n+1} = -\underline{U}_i^{n+1}\times\underline{B}^{n+1} - \frac{\nabla p_e^{n+1}}{q n_i^{n+1}} - \frac{\underline{B}^{n+1}\times\left(\nabla\times\underline{B}^{n+1}\right)}{\mu_0 q n_i^{n+1}}. \tag{4.31}$$

With the obtention of the electric field at a fully progressed temporal position, each of the values in the key equations summarised at the beginning of this section have been calculated ($\underline{v}_i^{n+\frac{1}{2}}, \underline{x}_i^{n+1}, \underline{B}^{n+1}, \underline{E}^{n+1}$). Therefore, the model has completed one step forward in time and the logical cycle begins again to progress by another time step. To indicate this, each of the superscripts are re-indexed to allow the same state of formulations to be used (i.e. $\underline{v}_i^{n+\frac{1}{2}} \rightarrow \underline{v}_i^{n-\frac{1}{2}}, \underline{x}_i^{n+1} \rightarrow \underline{x}_i^{n}$, etc), essentially moving to the next iterator in the temporal loop. Hence, the logical cycle necessary to construct a self-consistent hybrid-PIC model has been formed.

4.3 Main Loop Summary

The hybrid-PIC plasma model described in the previous section is progressed through time by cycling through the equations described above. Each part of this cycle that can be readily broken down into a step is summarised and listed in order of operation below. These steps are:

1. Update particle velocities, $\underline{v}^{n+\frac{1}{2}}$, using their equation of motions (4.16).
2. Move particles, $\underline{x}^{n+1}$, using the differenced definition of velocity (4.20).
3. Gather particle moments (charge & current density, CAM moments), ρ_c^{n+1}, $\underline{J}^{n+1}$, Γ^{n+1}, $\underline{\Lambda}^{n+1}$.
4. Advance the magnetic field by initial half time step, $\underline{B}^{n+\frac{1}{2}}$, using Faraday's law (4.21 & 4.22).
5. Calculate updated electric field, $\underline{E}^{n+\frac{1}{2}}$, using the electron momentum equation (4.23).
6. Advance the magnetic field ($\underline{B}^{n+1}$), using the updated electric field, to obtain it at the full time step (4.21 & 4.22).
7. Calculate mixed time step electric field $\underline{E}^*$ (4.28) in order to correct free-streaming currents $\underline{J}_i^+$ (4.29) and obtained fully advanced ion flow velocities $\underline{U}_i^{n+1}$ (4.30).
8. Calculate the electric field, $\underline{E}^{n+1}$, using the updated magnetic field, ion flow velocities & electron pressure gradients, $\underline{B}^{n+1}$, $\underline{U}^{n+1}$ & p_e^{n+1} (4.31).

This overview is limited to detailing the steps required to update each of the key values summarised at the beginning of the previous section, ($\underline{v}_i, \underline{x}_i, \underline{B}, \underline{E}$) rather than a detailed examination of every step in the hybrid method. The logic presented in this list is cyclical in nature and is required for the model to be able to self-consistently progress through time. Therefore, it is both possible and convenient to present these steps as components that can be moved through in order to complete a cycle, this is seen in figure 4.1. In this figure it can be seen that there are a pair of concentric rings, with the outer more detailed than the inner. If one begins at the green 'update velocities' segment and follows the flow of logic, it is found that each step detailed in the list above corresponds to the section of the ring moved into.

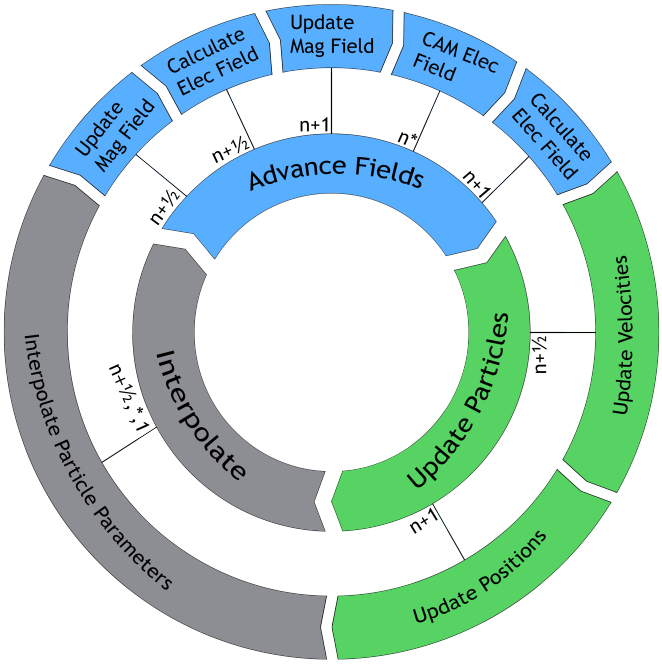

Figure 4.1: Logical cycle utilised to form a hybrid-PIC plasma model. A pair of concentric rings, the inner has fewer elements and contain a summary of the 3 major steps that are required to progress the model. The outer ring contains 8 more detailed elements, not equally distributed between the 3 summarised elements of the inner ring. Spokes can be seen to connect the more detailed step to the large summarised element it belongs in, colour is also used to indicate this. The time step within a logical cycle at which the detailed element occurs is shown at the base of its associated spoke.

Chapter 5

JERICHO - Model Description

The previous two chapters (§2 & 3) reviewed important scientific questions and the physical constraints within the Jovian and Saturnian systems leading to the need for a hybrid plasma model within their magnetospheres. Chapter 4 described the essential physics of a hybrid model and in this chapter the application of these ideas to produce the **J**ovian magn**E**tosphe**RIC** kinetic-ion, fluid-electron **H**ybrid plasma m**O**del (JERICHO) will be described in detail. The remainder of this thesis will detail the model description, verification & validation, and present initial results examining RI motions in Saturn's magnetosphere.

Specifically, in this chapter the exact geometry selected for the model is detailed, along with the form of the computational domain, with the reasoning for the use of these configurations examined. Next, the adaptions required to alter the numerics of a general hybrid model for use at the outer-planets are provided, before the full exact solutions utilised are presented with the numerical differentiators. We then examine the methods for initialising the model, those required to reduce the number of particles to an amount suited to the power of the hardware in use and for dealing with particles & fields at the model boundaries. Finally, a brief overview of the structure of the software created to both initialise and run the adapted model, as well as store results produced in simulation runs. Clearly the variable names used in this chapter cannot be used in JERICHO's software, appendix A provides a table to allow for reference between the variables used in this thesis and those used in the codebase.

5.1 Overview & Computational Domain

When constructing a numerical model it is imperative that extensive consideration is given to both the geometry & dimensionality of the domain. In the examples of plasma codes already presented there are models that operate in 1, 2 & 3 spatial dimensions along with using a range of Cartesian and curvilinear coordinates. It is natural when first examining a problem to consider a 3-dimensional system, most intrinsically familiar to us from everyday experiences. However, when the development of mathematical solutions with efficient computational implementations is examined, it is often determined that a reduction of model dimensionality can offer vast benefits. This is not limited to an increase in efficiency through a reduction in the number of computations, but extends to increased physical exactness with conservation laws able to be enforced by definition within solutions.

The selection of coordinate system used by a model is often best informed by consideration of the shape of the overall system. Therefore, when constructing a global magnetospheric model it seems natural to select a system which is able to capture the stretched spherical shape (i.e. the traditional tear drop or disk-like) of the cavity, such

as polar-cylindrical or spherical. However, when the translation of these into the model mathematics and the computational implementation is considered, it is once again determined that polar coordinate systems lead to more complex solutions and introduce problems computationally. Hence, one must ensure that the benefits provided by the use of any particular coordinate system are not out-weighed by its corresponding draw-backs.

5.1.1 2.5-Dimensional Geometry

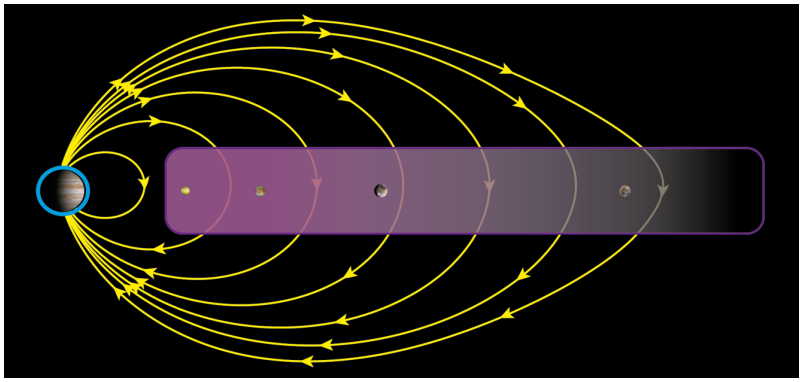

Figure 5.1: Schematic of the planetary configuration considered when forming JERICHO's geometry. A meridian cross-section of the Jovian system with the Sun off to the right-hand side, the magnetic axis has been aligned with the planetary spin axis. The ionosphere can be seen surrounding the planetary body as a blue ring, with the magnetic field lines emerging through this region shown as yellow lines with arrows indicating orientation. The magnetospheric region of interest, the plasma sheet, is highlighted by the purple box, inside which the moons of Io, Europa, Ganymede & Callisto are shown. Credit: Arridge and Wiggs.

An overview of the system which is of interest when examining RI motions at the outer-planets is seen detailed in figure 5.1. In this, the magnetospheric section containing the plasma sheet is seen in purple with yellow field lines, representing the intrinsic planetary magnetic field, connecting into the blue ionosphere. Examining the figure, a number of the model assumptions are immediately apparent from an inspection of figure 5.1. The first of these is that the planetary field is described as a perfect dipole, meaning the inclusion of higher order moments (finer structure) has been prohibited with the distension of field lines ignored. The validity of this assumption, along with the magnetospheric distances these correspond with, have been previously discussed in §2. It was found that this assumption is most valid in the inner magnetosphere, but breaks down as the middle magnetosphere is entered, then becomes poorer at larger radial distances. However, it should be noted that this assumption is contained to the construction of the magnetic field initially provided to the model. Solutions used to evolve and progress the modelled plasma and EM responses are free from this. Additionally, more complex magnetic fields can be introduced to the model purely through modifications of the initial conditions (ICs) or by evolving background field contributions.

The next assumption is the alignment of both the planetary magnetic and spin axis, aligning the rotational equator with that of the magnetic. This means that both the plasma and current sheet are perfectly aligned along the 0° latitudinal line for the entire extent of the magnetosphere. Examining the deviation from the actual planetary systems this assumption represents, it can be determined (using tables 2.1 & 2.2) the dipole tilts (offset) are 9.4° at Jupiter and ≈0° at Saturn. Hence, it can been seen that this assumption more accurately reflects the Saturnian system than that of the Jovian. The impacts of this are

intrinsically linked to the model solutions obtained, with the equations derived and utilised in model construction incorporating the assumption of the magnetic & centrifugal equators being aligned. If inclination was included, it would effectively scale the field strengths at the equatorial crossing surface and rotate the vector of the field line, therefore inclusion of this would require the re-derivation and implementation of the model solutions.

Turning now to the selection of model geometry, initially one must consider both the vast spatial scales of outer-planetary magnetospheres and the dimensionality of the dynamics of interest. From previous analysis of the size of these systems (see §2), where a single planetary radii is $\sim 10^8$ m, the magnetodisk can be approximated of having a radius of $\sim$100 R_P and a height of $\sim$10 R_P. These spatial scales require comparison with the gyro-parameters (controlled by the magnetic field, see §1.2) in order to determine the amount of computational resources required. The strong planetary fields in both the Jovian & Saturnian systems mean that even a MHD model would require a phenomenal amount of computational resources to create a full 3-dimensional simulation of the entire magnetospheric system, with a hybrid model requiring even more. However, we note that the dynamics of interest to this work can be largely confined to the centrifugal equator and hence the plasma sheet, which has been shown can be approximated as a thin sheet (Vasyliunas, 1983). Hence, we integrate over a thin 3-dimensional plasma sheet (by height) to reduce this region to a 2-dimensional plane which lies aligned along the centrifugal & magnetic equators. The same argument is made to integrate over the height of the ionosphere. This can then be unwrapped and formed into a second flat 2-dimensional plane.

Now considering how the magnetic field and ionosphere connect & interact with the magnetospheric plane, it is found that due to the alignment of spin & magnetic axes, assuming a perfect dipole, that the field lines intersect perpendicularly. Hence, the magnetic field lines are reduced to a set of 1-dimensional lines that are perpendicular to the coordinates describing the plane. These 1D lines interact with the plasma contained within the magnetosphere at discretised locations, from these locations the lines can be followed back to their foot-points in the ionosphere. This has the effect of unwrapping the ionosphere forming it into the same shape of as the magnetosphere, yielding a pair of 2D planes stacked on top of one another.

The described geometry can be seen in figure 5.2, with 5.2a showing the plane containing the magnetosphere represented by the purple line at the bottom, connected along the straight yellow field lines to the blue line, representing the ionosphere. A perhaps more informative view is provided by 5.2b, showing the pair of 2D planes stacked over top of one another, connected by the suspended magnetic field lines between them.

The described configuration forms the 2.5D geometry in which JERICHO is constructed, with the selection made for the pair of coordinates describing the planes to be (x, y) and the perpendicular coordinate describing the field line to be z. This set of coordinates alludes to the selection of coordinate system for the model, a set of Cartesian coordinates rather than polar-cylindrical or spherical. These are selected despite the apparent natural affinity between the system described in the model and the polar coordinates. The reason for this selection is tied to the computational implementation of the methods and solutions utilised to construct the model, with the simplicity provided by Cartesian out-weighing the benefits of the polar in terms of model stability (Simon, 2019).

Examining the implications of the selection of a Cartesian coordinate system, upon which modelled parameters are discretised forming a regular grid (see next section for detail), it is determined that beyond making the construction of the computational domain easier, it vastly simplifies the derivation of the solutions for particle motions, the interpretation of particle distributions & the EM fields (in the magnetospheric plane). However, this is traded for complexity with calculating potentials in the ionosphere in response to

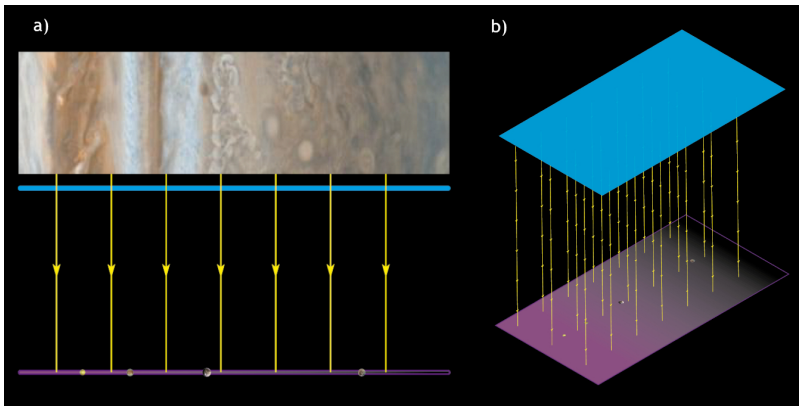

Figure 5.2: Schematic showing the 2.5D geometry exploited to construct JERICHO. Panel a) shows a side view of the configuration with the ionosphere unwrapped from the planet and flatten into a 2D plane represented by the blue line under the planetary surface, from this view the line shown is 1-dimensional with the second dimension extending into the page. Yellow field lines indicate the magnetic field, seen now to be confined to a single dimension orthogonal to the ionosphere. These dangle down, connecting into the purple magnetosphere, which has also been reduced to a 2D plane. b) shows the same set up from a 3D perspective. In this the 2d planes can be seen in both dimensions, situated on top of one another connected by the yellow field lines. In both panels the Galilean moons can be seen indicated in the magnetospheric planes. Credit: Arridge and Wiggs.

the magnetospheric motions. This is because the Cartesian grid upon which the EM fields are discretised maps to an irregular latitude-longitude grid, upon which it is difficult to perform the required calculations. A solution for this would be a method to interpolate the values obtained on the regular magnetosphere grid onto a regular grid in the ionosphere, however the derivation of this method is not trivial and would require considerable effort to implement in a 2.5D geometry.

Focusing purely on the structure of the domain in the magnetospheric plane, a Cartesian grid lends itself to the creation of quadrilateral surfaces. Further, for computational ease it is preferential to use even grid spacing in a spatial-dimension, though mathematically this is not required. Hence, the shape of the computational domains created are either square or rectangular. Clearly, these shapes do not naturally align with the typical polar-cylindrical/spherical geometry of the magnetospheric systems. A solution to this is to vary the width of the domain with height, whilst holding the grid-spacing constant, creating a trapezoid shaped domain with stepped edges, approximating a wedge of magnetospheric space. However, this approach creates difficulties in handling kinetic particles, as well as solving the EM fields at the stepped edges and these are not trivial to solve. Additionally, the sources of material in the systems of interest are found to be tori (see §2.2.1 & 2.2.2), hence any inflow at domain boundaries is more natural if it is curved.

Considering the flow of plasma outwards in the radial direction, along with feedback via FACs into the planetary ionosphere as a system of currents, a complete diagram of these can be created. This is shown in figure 5.3 with the ionosphere now indicated as the purple region surrounding the planet connecting the the brown plasma sheet. The systematic picture here is consistent with that described in §4 with net plasma flow being radially outwards, hence current also moves outwards, and magnetospheric distributions & ionospheric response communicated along field lines by FACs.

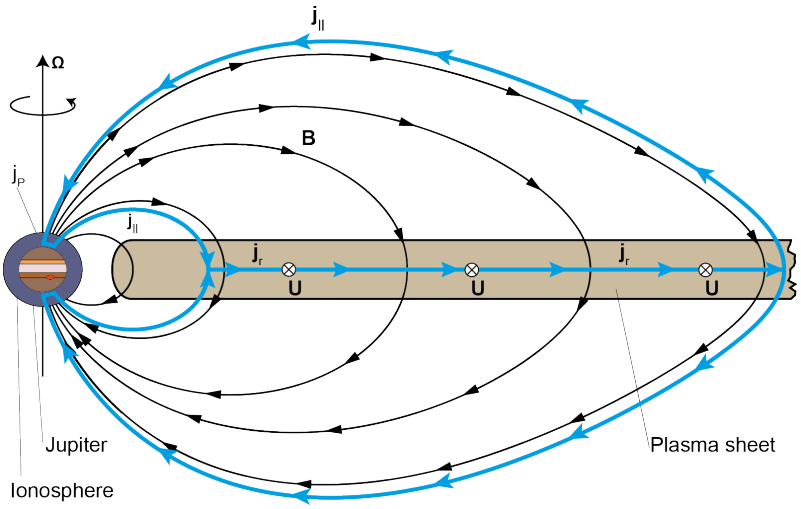

Figure 5.3: A schematic of the current system modelled by JERICHO to examine RI motions. The planetary body is seen on the left-hand side encompassed by a purple ionosphere. From the body the spin (and hence magnetic) axis is indicated, with the direction and rate of planetary rotation shown by Ω. Black magnetic field lines connect the ionosphere to the magnetospheric region of interest, in brown. The plasma in this region corotates with the planet giving it a flow velocity into the page, $\underline{U}$. The currents created by radial plasma transport are indicated by the blue lines, with arrows to indicate direction, FACs are shown flowing in two locations for simplicity, however this occurs along all magnetic field lines. Credit: Arridge and Wiggs.

5.1.2 Computed Domain Discretisations & Reference Frame

JERICHO progresses self-consistently through the temporal domain from a provided initial configuration, populating the magnetospheric plane with ions (kinetic particles) and describing the EM configuration. The domain occupied by the particles populating the simulated region in the model is simply connected and complete with them able to be located in any position within the plane. Of course a model simulates only a bounded region of space, so the question becomes what happens to the particles at the edges, this is discussed in the boundary condition (§5.5) section later in this chapter.

The electric and magnetic fields could be discretised onto a non-uniform or adaptive mesh but for simplicity we discretise onto a single uniform grid. There is no theoretical limitation that requires the points on which field values are calculated to be uniformly spaced, although this is computationally desirable. In fact many modern hybrid plasma models take advantage of this with adaptive meshes. These decrease the spatial separation of field points to increase the resolution in regions of the model in which interesting small scale dynamics are occurring. Conversely, for computational efficiency, these adaptive meshes can decrease the spatial resolution in regions exhibiting little interest. In the interest of simplicity in JERICHO, a uniform distribution is utilised.

Joining each point on which field values are calculated to its nearest neighbours in all dimensions, a grid is constructed throughout the entirety of the simulated space, this can be seen in figure 5.4. On each vertex of a grid cell is a field calculation location, these will be known as the grid points. It is evident that all particles within the model occupy one of these described grid cells. The particles populating the model and the EM fields within it communicate with one another via these grid points. This is achieved by gathering particle moments (such as charge) on the grid points, once particle moments are collected they can be used in field calculations. Updated fields can then be interpolated back to the particles allowing them to 'feel' EM forces. This is a commonly utilised PIC modelling

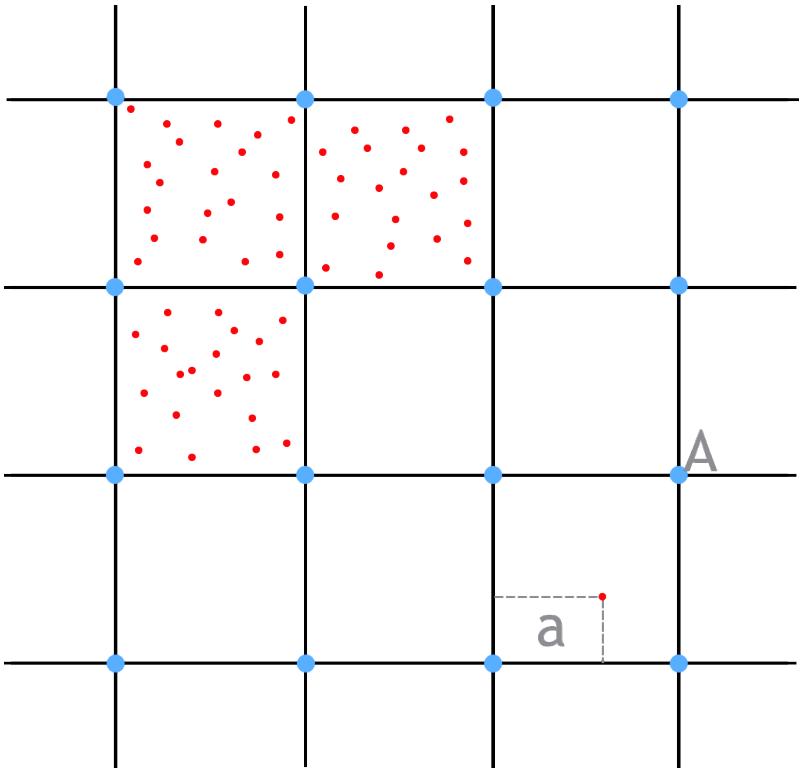

Figure 5.4: A depiction of the computational domain constructed to model plasma in JERICHO. The discretised locations of the EM field can be seen as a series of regular points shown as blue dots, joined together by black horizontal and vertical lines to create the grid over the domain. The particles are shown as red dots, these can occupy any location in the domain and hence can be seen filling the grid cells constructed. Communicating particle distributions to the grid is essential for self-consistently progressing the simulation, therefore a method is needed to collect particle moments on the grid points, represented by the grey dot lines and a's in the bottom right cell.

technique, and as already been discussed, can be used on its own to move all particles in a model, or used in the construction of hybrid plasma models.

5.1.3 Working in a Rotating Domain

It has been detailed how the plasma in the outer-planetary magnetospheres is accelerated by the planetary magnetic field to possess the same angular velocity as the planet, hence corotating with the body. Therefore, it is advantageous to work in a frame rotating with the planet. The 2-dimensional magnetospheric plane perfectly corotates with the planet, meaning that the model domain does not need to encompass a full 2π azimuthal section of of the magnetosphere. Further, the 1-dimensional field lines remain straight and connected with the same corresponding ionospheric region, as previously discussed.

In the rotating reference frame the velocity of the ions is,

$$\left\{\frac{d\underline{x}}{dt}\right\}_s = \left\{\frac{d\underline{x}}{dt}\right\}_r + \underline{\Omega} \times \underline{x}$$

where the subscript s denotes the stationary reference frame and r the rotational. Hence yielding the transformation operator

$$\left\{\frac{d\underline{x}}{dt}\right\}_s = \left(\left\{\frac{d}{dt}\right\}_r + \underline{\Omega}\times\right)\underline{x}. \tag{5.1}$$

Applying this operator to itself gives the acceleration,

$$\begin{aligned}\left\{\frac{d^2\underline{x}}{dt^2}\right\}_s &= \left(\left\{\frac{d}{dt}\right\}_r + \underline{\Omega}\times\right)\left(\left\{\frac{d}{dt}\right\}_r + \underline{\Omega}\times\right)\underline{x}, \\ \left\{\frac{d^2\underline{x}}{dt^2}\right\}_r &= \left\{\frac{d^2\underline{x}}{dt^2}\right\}_s + \underline{\Omega}\times(\underline{\Omega}\times\underline{x}) + 2\underline{\Omega}\times\frac{d\underline{x}}{dt} + \frac{d\underline{\Omega}}{dt}\times\underline{x}. \end{aligned} \tag{5.2}$$

Substituting this definition into Newton's second law gives us it in the rotational reference frame (dropping the subscripts now the transformation is complete),

$$m\frac{d^2\underline{x}}{dt^2} = \underline{F} - m\underline{\Omega}\times(\underline{\Omega}\times\underline{x}) - 2m\underline{\Omega}\times\frac{d\underline{x}}{dt} - m\frac{d\underline{\Omega}}{dt}\times\underline{x}. \tag{5.3}$$

The RHS contains any force applied to the particles, such as the Lorentz force or gravity, and three pseudo-forces:

- the Centrifugal force, $\underline{F}_{cf} = -m\underline{\Omega}\times(\underline{\Omega}\times\underline{x})$
- the Coriolis force, $\underline{F}_C = -2m\underline{\Omega}\times\underline{v}$
- the Euler force, $\underline{F}_E = -m\frac{d\underline{\Omega}}{dt}\times\underline{x}$, note this is only present in systems with a time dependant rotation rate.

The equation to obtain particle velocities in JERICHO, recalling the only force included in our original recipe is that of the Lorentz, is,

$$\frac{d\underline{v}}{dt} = \frac{q}{m}(\underline{E} + \underline{v}\times\underline{B}) - \underline{\Omega}\times(\underline{\Omega}\times\underline{x}) - 2\underline{\Omega}\times\underline{v}, \tag{5.4}$$

where the Euler force has disappeared due to Jupiter & Saturn having constant rotational rates. Expanding the centrifugal term using the vector triple product, using forward differencing and applying (3.13-3.15) we find,

$$\underline{v}^{n+\frac{1}{2}} = \underline{v}^{n-\frac{1}{2}} + \frac{q\Delta t}{m}\left[\underline{E}^n + \underline{v}^n\times\underline{B}^n\right] - 2\Delta t\,(\underline{\Omega}\times\underline{v}^n) + \Delta t\,|\underline{\Omega}|^2\,\underline{x}^n.$$

Angular velocity does not have a superscript n as planetary spin rate is not time dependant. By splitting the particle velocities on the integer time step into half-integer steps using Lax's method, as before, the following is obtained,

$$\begin{aligned}\underline{v}^{n+\frac{1}{2}} - \frac{q\Delta t}{m}\left[\underline{v}^{n+\frac{1}{2}}\times\left(\frac{1}{2}\underline{B}^n + \frac{m}{q}\underline{\Omega}\right)\right] = \\ \underline{v}^{n-\frac{1}{2}} + \frac{q\Delta t}{m}\left[\underline{E}^n + \underline{v}^{n-\frac{1}{2}}\times\left(\frac{1}{2}\underline{B}^n + \frac{m}{q}\underline{\Omega}\right)\right] + \Delta t\,|\underline{\Omega}|\,\underline{x}^n.\end{aligned}$$

This can be rearranged to yield,

$$\begin{aligned}\underline{v}^{n+\frac{1}{2}} = K\Big\{\left(1-h^2\alpha^2\right)\underline{v}^{n-\frac{1}{2}} + h\left[\underline{E}^n + 2\alpha\left(\underline{v}^{n-\frac{1}{2}}\times\hat{\underline{z}}\right)\right] + h^2\alpha\,(\underline{E}^n\times\hat{\underline{z}}) \\ +\Delta t\,|\underline{\Omega}|^2\left[\underline{x}^n + (\underline{x}^n\times h\alpha\hat{\underline{z}})\right]\Big\},\end{aligned} \tag{5.5}$$

where

$$K = \frac{1}{(1+h^2\alpha^2)}, \tag{5.6}$$

$$\alpha = \frac{1}{2}B_z^n + \frac{m}{q}\Omega_z, \tag{5.7}$$

$$h = \frac{q\Delta t}{m}. \tag{5.8}$$

It is noted that this rearrangement is not a trivial process, details on how to perform it can be found in appendix B.

Since the centrifugal pseudo-force dominates the gravitational attraction of Jupiter & Saturn after a short distance from the planetary body, the term has not been included in the construction of the solution above. However, if it is required it can be simply incorporated by adding this term to the right hand side of equation 5.5,

$$-K\left\{\Delta t G M_P\left[\frac{\underline{x}^n}{|\underline{x}^n|^2}+\left(\frac{\underline{x}^n}{|\underline{x}^n|^3}\times h\alpha\hat{\underline{z}}\right)\right]\right\}, \tag{5.9}$$

where G is the gravitational constant.

5.2 Macroparticle Motions & Moment Gathering

5.2.1 Macro Particles

Taking a thin plasma sheet configuration at Jupiter of just 1 R_J in height (not concerned with the physical implications of this) and placing a 1x1 R_J model domain at a radial distance of 10 R_J, the total number of heavy ions is already 10^{28} (Huscher et al., 2021). It was previously discussed how the majority of the run time of a hybrid model is occupied by particle operations (see §1.2), clearly it is important to ensure that an appropriate number of particles are utilised. The number of particles usually used in JERICHO ranges from $10^6 - 10^{10}$, which would seem to vastly limit the size of the permissible computational domain.

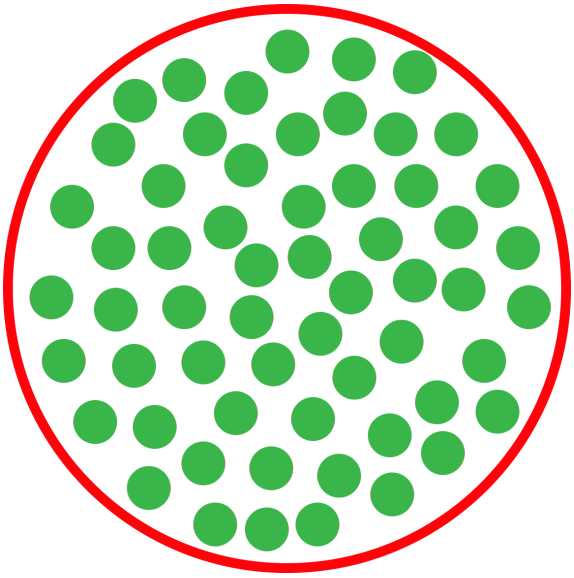

Figure 5.5: 2-dimensional representation of a macro-particle, with the red circle indicating the exterior boundary (or skin) of it and the green dots representing the constituent ions inside.

Therefore, a compromise is required that allows for the simulation to cover the area of interest, whilst containing a physically accurate number of particles. This is achieved through the introduction of macro-particles (or super-particles), allowing for a reduction in the total number of particles in the computational domain by grouping ions together inside a singular 0-dimensional construct. A 2-dimensional representation of a single macro-particle can be seen in figure 5.5, with a pre-defined number of ions (green dots) placed inside the larger macro-particle (in red).

Although macro-particles are easiest to conceptualise in 2 or 3-dimensions, all particles in JERICHO are assumed to have an exact position on the computational domain, with the precision of this limited only by the data-type selected for storage. Hence, it is said that the particles are 0-dimensional. With the position of the macroparticles known exactly, it is clear the minimum size of a spatial step that can be taken by a particle is only limited by the precision of memory type used to store its location in each dimension.

This description of the particles used in JERICHO is clearly a divergence from what is observed, with the introduction of macro-particles only serving to increase the size of the assumption. Clearly, the larger the number of ions contained within the macro-particle, the greater amount of space it should occupy. However, when we consider the physical implications of this assumption, recalling that we are describing a plasma that is already collisionless, it is determined that as long as the macro-particles are much smaller than the resolution of our spatial grid, then it has no impact on the operations of the modelled domain.

The question then turns to how to determine the number of ions that should be contained in a macro-particle within a simulation run. The method selected to calculate this is utilising the number density, n_i, defined upon initialisation of the model along with the desired number of particles, T_{PPC}, within the computational domain. From these quantities a value known as the macro-number is calculated,

$$M_N = \frac{(x_{max} - x_{min})\,(y_{max} - y_{min})}{T_{PPC}} n_i. \tag{5.10}$$

This value is used to scale the size of particles after their position both on the computational domain and in velocity phase space has been determined by being applied as a multiplier to the mass & charge. Using this method it is not necessary to have a separate macro-number for multiple ion species as this ratio can be controlled by the number of a particular species created at the time of initialisation. Using this technique the original species of ion can be determined by simply dividing the particles mass or charge by the macro-number.

5.2.2 Ionic Particle Motions

The first step in JERICHO's simulation (the step we select to begin with) is to update the particle velocities by half a time step, $\underline{v}^{n+\frac{1}{2}}$, using the solution to the equation of motion in a rotating reference frame (eqn 5.5). For a plasma contained within the 2-dimensional magnetospheric plane described in our 2.5D geometry, particle velocities are determined using,

$$\begin{aligned}
v_x^{n+\frac{1}{2}} &= K\left[\left(1-h^2\alpha^2\right)v_x^{n-\frac{1}{2}} + h\left(E_x^n + 2\alpha v_y^{n-\frac{1}{2}}\right) + h^2\alpha E_y^2 + \Delta t\Omega_z^2\left(x^n + h\alpha y^n\right)\right], \\
v_y^{n+\frac{1}{2}} &= K\left[\left(1-h^2\alpha^2\right)v_y^{n-\frac{1}{2}} + h\left(E_y^n - 2\alpha v_x^{n-\frac{1}{2}}\right) - h^2\alpha E_x^2 + \Delta t\Omega_z^2\left(y^n - h\alpha x^n\right)\right]
\end{aligned}$$

The leapfrog technique, described in the previous chapter, is then used to progress the particle positions a complete integer time step, $\underline{x}^{n+1}$, using the updated velocity from the half integer time step before ($\underline{v}^{n+\frac{1}{2}}$). This is done using

$$\begin{aligned}
x^{n+1} &= x^n + \Delta t v_x^{n+\frac{1}{2}}, \\
y^{n+1} &= y^n + \Delta t v_y^{n+\frac{1}{2}}.
\end{aligned}$$

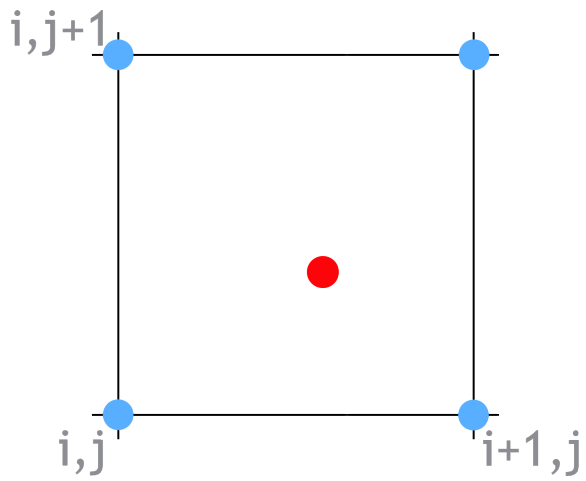

Figure 5.6: The index system used to identify and construct the cell which a particle (red dot) is located within, with the EM grid points shown as blue dots. Indexes i, j give the 'bottom left' grid point of the cell, with the 3 other vertices then located using $i+1, j$, $i+1, j+1$ & $i, j+1$.

5.2.3 Collecting Particle Moments

Once the positions and velocities of the ions have been updated, their effects on the fields must be calculated. This process can be done using numerous methods depending on the accuracy desired for the model. However, the way in which particles are assigned to a set of grid points based on its location must be formalised. Grid points located throughout the simulated space, no matter if the distribution is uniform or not, can be indexed using the natural numbers such that $(i, j, k) \in \mathbb{N}$, where (i, j, k) are the grid point indexes. These indexes are assigned to grid points by increasing the index number as the location changes in the corresponding dimensional vector. The indexes are associated to their dimensions by (i, j, k) corresponding to (x, y, z). Particles are assigned to the grid point, in the set that form the cell, with the lowest index in each dimension, the complete set can then be obtained using $\sum_{a,b,c=0}^{1} (i+a, j+b, k+c)$. This can be seen applied to our 2-dimensional plane in figure 5.6, with a set of 4 grid points forming a cell which a particle inhabits with the following set of indices $\{(i, j), (i+1, j), (i+1, j+1), (i, j+1)\}$.

Because the JERICHO grid is uniform the bottom-left grid index for each particle can be found trivially from,

$$i = \left\lfloor \frac{x_p - x_{min}}{\Delta x} \right\rfloor, \tag{5.11}$$

$$j = \left\lfloor \frac{y_p - y_{min}}{\Delta y} \right\rfloor, \tag{5.12}$$

where the subscript p denotes the parameters association with a specific particle.

Now the gathering of particle moments onto the grid points constituting the cell in which it resides can be specified. In order to distribute a particle's moments a weighting scheme must be formulated to account for the position of the particle within the cell, with grid points located closer to it requiring more of the moments to be allocated than those further away. This notion can be simplified through the use of zeroth order weighting which is also the least computationally expensive distribution scheme. This is because rather than subdivide and distribute a particle's moments, the entirety of these are collected and allocated to the so called 'bottom left' grid point of a cell. However, clearly this scheme fails to capture the full physical contributions of the position of a particle in a cell, essentially reallocating each one to a position aligning exactly with a grid point.

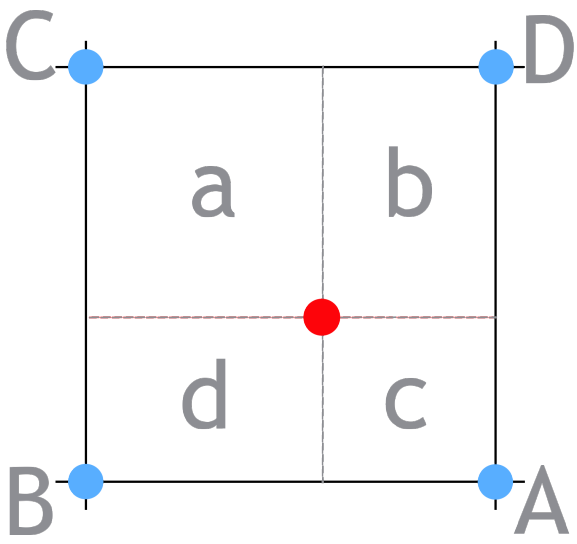

Figure 5.7: First-order area weighting used to collect the moments of a particle, shown as a red dot, on the location of EM field discretisation, the blue dots. This area weight scheme subdivides a cell into 4 quadrilaterals, the areas of each are then used to determine the amount of a particle's moment allocated to each grid point. The closer a particle is to a point, the more moment it should be allocated, hence the area opposite a point is used to determine its portion of the moment. Therefore, a→A, b→B, c→C & d→D.

Therefore, it is necessary to use a higher-order weighting scheme to communicate the impact of a particle's position within a cell and allow for a high resolution interpretation of overall particle distributions. First-order weighting (also called bi-linear weighting or area weighting) allocates portions of a particle's moments to the 4 grid points constituting its cell. This is done by sub-dividing the cell into 4 quadrilaterals based on the location of the ion within the cell and then using the relative areas to weight the ion's moments. The resultant configuration is shown in figure 5.7, with the 4, area variant, quadrilaterals created labelled a, b, c, d. It is seen that the largest areas occur for the quadrilaterals opposite to the grid points the particle is closest in proximity too, hence the area of a is used to determine the amount of the moment allocated to grid point A. This is repeated such that $a \rightarrow A$, $b \rightarrow B$, $c \rightarrow C$ & $d \rightarrow D$. These created quadrilaterals are known as the shape factors and are calculated according to the shape function, $\mathcal{F}$, to give a geometric interpretation for moment weighting.

First-order weighting is the most commonly used method for collecting particle moments in modern PIC codes and also is the method selected for use in JERICHO. Generally, this technique subdivides the particle moment being allocated into 2^n different areas, where n is the number of dimensions being modelled. The exact shaping function for determining the area of each of these weighting quadrilaterals can now be determined for our 2.5D geometry. Our plasma is confined to a 2-dimensional plane, hence we created 4 sub-cells, the size of allocations determined by these weightings on the grid point located at indexes (i, j) using $f_{i,j}$. $f_{i+1,j}, f_{i+1,j+1}, f_{i,j+1}$ are required to complete the set and yield our overall shape function. The total areas of each created sub-cell set are normalised such that when totalled they equal,

$$\mathcal{F}\left(\underline{x}_p^n\right) = \sum_{a,b=0}^{1} f_{i+a,j+b} = 1. \tag{5.13}$$

Each of these allocations of a particle's moments to the surrounding grid cells is obtained

using (Birdsall and Langdon, 1985),

$$f_{i,j} = \frac{(\Delta x - x_p)(\Delta y - y_p)}{\Delta x \Delta y}, \tag{5.14}$$

$$f_{i+1,j} = \frac{x_p (\Delta y - y_p)}{\Delta x \Delta y}, \tag{5.15}$$

$$f_{i+1,j+1} = \frac{x_p y_p}{\Delta x \Delta y}, \tag{5.16}$$

$$f_{i,j+1} = \frac{(\Delta x - x_p) y_p}{\Delta x \Delta y}. \tag{5.17}$$

With the exact configuration & corresponding mathematics obtained for the use of first-order weighting to allocated particle's moments to surrounds grid points, the question turns to the matter of what moments require gathering. The standard moments gathered in hybrid-PIC plasma modelling are the charge & current densities, ρ_c & $\underline{J}$ respectively. Using the shaping function determined these are obtained following Bagdonat (2005) but in 2-dimensions rather than 3, hence,

$$\rho_c^n = \sum_p \frac{q_p}{\Delta x \Delta y} \mathcal{F}(\underline{x}_p^n), \tag{5.18}$$

$$\underline{J}^{+,-} = \sum_p \frac{q_p \underline{v}_p^{n \pm \frac{1}{2}}}{\Delta x \Delta y} \mathcal{F}(\underline{x}_p^n). \tag{5.19}$$

The summation here shows how the surface charge & current densities at any particular time step can be obtained by using these shape functions to determine the contributions of all particles in the model collected on the grid points. Of note is the mixing of the temporal position of the particle velocities and positions when determining the current densities, therefore these are obtained at mixed time steps and the combination for using these to determine the currents on exact time steps has been previously detailed.

JERICHO utilises the CAM method, as detailed in the previous chapter, to obtain the fully advanced current densities and corresponding ion flow velocities. Therefore in addition to the standard moments gathered from the particle distributions, we additionally require the gathering of another pair of moments for specific use in correcting our free-flowing currents. These are obtained using (Matthews, 1994),

$$\Lambda = \sum_p \frac{q_p^2}{m_p} \mathcal{F}\left(\underline{x}_p^n\right), \tag{5.20}$$

$$\underline{\Gamma} = \sum_p \frac{q_p^2 \underline{v}_p^{n+\frac{1}{2}}}{m_p} \mathcal{F}\left(\underline{x}_p^n\right). \tag{5.21}$$

5.2.4 Interpolating Fields

With particle moments gathered, communicating their distributions to the EM fields, it is now possible to update these fields, with the solutions utilised to do this detailed in the following section. Looking forward, once the fields have been updated their new configurations and magnitudes require communicating back to the particles so that these can be progressed via their equation of motion. This is a process known as interpolation and will be done using a first-order scheme which mirrors the weighting used to collect moments.

Therefore, the weights determined in equations 5.14, 5.15, 5.16 & 5.17 are stored and reused to weight the values of the field at the grid points surrounding a particle when

performing interpolation. Hence, for a generic field $\mathcal{A}$ the value of it 'felt' at the position of a particle within the domain, $\underline{x}_p$ is determined using

$$\mathcal{A}_p = \mathcal{A}_{i,j} f_{i,j} + \mathcal{A}_{i+1,j} f_{i+1,j} + \mathcal{A}_{i+1,j+1} f_{i+1,j+1} + \mathcal{A}_{i,j+1} f_{i,j+1}, \tag{5.22}$$

where the subscript p here denotes the value of the field at the particle's location and the indexes indicate the value of the field at that discretised grid point. This is of course not the only way to interpolate field values to the particles, however it is the method utilised in JERICHO.

5.3 Field Calculations and Numerical Differentiation

5.3.1 Obtaining EM fields

Recalling the flow of model logic detailed in figure 4.1, we find that two of the three broad steps described have been completed. The remaining step is that of advancing the fields within the model, with it notably containing the largest number of sub steps. It should be noted however that despite this, field operations do not occupy a majority of the computational run time. This is because fields are treated as matrices that can be operated on through the usual principles of linear algebra (see Riley et al., 2002) with the concept of vectorisation applied computationally to enhance efficiency, whereas each particle must be looped through individually to be progressed and then again to construct the parameters from updated distributions.

From the recipe provided in §4 we find that it is necessary to first progress the magnetic field by half a integer time step. The numerical progression is achieved through the use of the detailed MacCormack predictor-corrector scheme applied to Faraday's law, with it noted that as the electric field is an analytic solution it can be substituted directly into this equation. The geometric framework of 2.5D allow for a vast number of simplifications to be made after this substitution and further means it is only required (and in fact permissible) to calculate the magnetic field in the z-direction.

Substituting eqn 4.11 into the predictor-corrector scheme detailed in eqns 4.21 & 4.22. Looking at the form of each of these equations, it is apparent that obtaining a solution to $\nabla \times \underline{E}$ allows for the immediate obtention of the final form of these. Hence,

$$\begin{aligned}
\nabla \times \underline{E} &= \frac{1}{q_i n_i} \nabla \times \nabla p_e + \nabla \times (-\underline{U}_i \times \underline{B}) + \frac{1}{\mu_0 q_i n_i} \left(\nabla \times (\underline{B} \cdot \nabla) \underline{B} - \nabla \times \nabla \frac{|\underline{B}|^2}{2} \right), \\
\nabla \times \underline{E} &= \nabla \times (-\underline{U}_i \times \underline{B}) + \frac{1}{\mu_0 q_i n_i} \left(\nabla \times \nabla \frac{|\underline{B}|^2}{2} \right).
\end{aligned} \tag{5.23}$$

Here it can be seen that the third term on the RHS, corresponding physically to magnetic tension, disappears as all components are equal to 0. When the physical implications of this are considered the reason for this becomes clear as it is dependant on the curvature of magnetic field lines, with 2.5D confining field lines to a single dimension they are unable to be curved and hence the magnetic tension disappears. Additionally, it is seen that the electron pressure term is set to 0, this is an assumption made when choosing model logic rather than a physical consequence of the current configuration. This is not to say that JERICHO is free from pressure, but rather that it is not considered when determining the distribution of particles on the EM fields. The physical interpretation for this is that (kinetic) pressure terms are negligible in comparison to bulk flows and magnetic pressure.

Completing the substitution of the curl of the electric field into Faraday's law, the

following is readily determined,

$$\begin{aligned}
\tilde{\underline{B}}^{n+\frac{1}{2}} &= \underline{B}^{n} - \frac{\Delta t}{2}\left[\underline{B}^{n}\nabla\cdot\underline{U}_{i}^{n} + (\nabla\underline{B}^{n})\cdot\underline{U}_{i}^{n}\right], \\
\underline{B}^{n+\frac{1}{2}} &= \frac{\underline{B}^{n} + \tilde{\underline{B}}^{n+\frac{1}{2}}}{2} - \frac{\Delta t}{4}\left[\tilde{\underline{B}}^{n+\frac{1}{2}}\nabla\cdot\underline{U}_{i}^{n} + \left(\nabla\tilde{\underline{B}}^{n+\frac{1}{2}}\right)\cdot\underline{U}_{i}^{n}\right].
\end{aligned}$$

Isolating and solving for the single directional component of the magnetic field, B_z, yields,

$$\begin{aligned}
\tilde{B}_{z}^{n+\frac{1}{2}} &= B_{z}^{n} - \frac{\Delta t}{2}\left[B_{z}^{n}\left(\frac{\partial U_{i,x}^{n}}{\partial x} + \frac{\partial U_{i,y}^{n}}{\partial y}\right) + U_{i,x}^{n}\frac{\partial B_{z}^{n}}{\partial x} + U_{i,y}^{n}\frac{\partial B_{z}^{n}}{\partial y}\right], \\
B_{z}^{n+\frac{1}{2}} &= \frac{B_{z}^{n} + \tilde{B}_{z}^{n+\frac{1}{2}}}{2} - \frac{\Delta t}{4}\left[\tilde{B}_{z}^{n+\frac{1}{2}}\left(\frac{\partial U_{i,x}^{n}}{\partial x} + \frac{\partial U_{i,y}^{n}}{\partial y}\right) + U_{i,x}^{n}\frac{\partial \tilde{B}_{z}^{n+\frac{1}{2}}}{\partial x} + U_{i,y}^{n}\frac{\partial \tilde{B}_{z}^{n+\frac{1}{2}}}{\partial y}\right].
\end{aligned}$$

Once again refreshing our recollection of our hybrid model recipe, we find that with the magnetic field advanced by a half time step, we can now use this, in combination with the charge densities and flow velocities collected (and calculated) from the particle distributions, to analytically determine the electric field also on the half integer time step. Reviewing briefly the physical interpretations of the simplifications found in eqn 5.23 we find they are entirely independent of the mathematical operation being applied. Therefore, when using eqn 4.11 to obtain the electric field the same formulation can be used. Hence, obtaining the electric field in 2-dimensions in which it is permitted in our 2.5D geometry we find,

$$\begin{aligned}
E_{x}^{n+\frac{1}{2}} &= -U_{y}^{n+\frac{1}{2}}B_{z}^{n+\frac{1}{2}} - \frac{1}{\rho_{c}^{n+\frac{1}{2}}}\frac{\partial}{\partial x}\left(\frac{\left|B_{z}^{n+\frac{1}{2}}\right|^{2}}{2\mu_{0}}\right), \\
E_{y}^{n+\frac{1}{2}} &= U_{x}^{n+\frac{1}{2}}B_{z}^{n+\frac{1}{2}} - \frac{1}{\rho_{c}^{n+\frac{1}{2}}}\frac{\partial}{\partial y}\left(\frac{\left|B_{z}^{n+\frac{1}{2}}\right|^{2}}{2\mu_{0}}\right).
\end{aligned}$$

With the electric field obtained at the temporal position of a half time step it can immediately be used to progress the magnetic field a further half time to, once again using our predictor-corrector scheme. This is done with

$$\begin{aligned}
\tilde{B}_{z}^{n+1} &= B_{z}^{n+\frac{1}{2}} - \frac{\Delta t}{2}\left[B_{z}^{n+\frac{1}{2}}\left(\frac{\partial U_{i,x}^{n+\frac{1}{2}}}{\partial x} + \frac{\partial U_{i,y}^{n+\frac{1}{2}}}{\partial y}\right) + U_{i,x}^{n+\frac{1}{2}}\frac{\partial B_{z}^{n+\frac{1}{2}}}{\partial x} + U_{i,y}^{n+\frac{1}{2}}\frac{\partial B_{z}^{n+\frac{1}{2}}}{\partial y}\right], \\
B_{z}^{n+1} &= \frac{B_{z}^{n+\frac{1}{2}} + \tilde{B}_{z}^{n+1}}{2} - \frac{\Delta t}{4}\left[\tilde{B}_{z}^{n+1}\left(\frac{\partial U_{i,x}^{n+\frac{1}{2}}}{\partial x} + \frac{\partial U_{i,y}^{n+\frac{1}{2}}}{\partial y}\right) + U_{i,x}^{n+\frac{1}{2}}\frac{\partial \tilde{B}_{z}^{n+1}}{\partial x} + U_{i,y}^{n+\frac{1}{2}}\frac{\partial \tilde{B}_{z}^{n+1}}{\partial y}\right].
\end{aligned}$$

We now reach the step identified as the main problem in EM field progression when constructing hybrid-PIC models. The is how to obtain the electric field on the fully advanced time step without the current densities (and hence flow velocities) at this time. The method we identified and selected when writing our recipe was that of the CAM scheme (see Matthews, 1994), where a mixed time level electric field is calculated and combined with the collected particle moments identified in eqns 5.20 & 5.21. Using the

solution for the electric field our 2.5D geometry, we can calculate the components of the mixed time step field using,

$$\begin{aligned} E_x^* &= -U_y^+ B_z^{n+1} - \frac{1}{\rho_c^{n+1}} \frac{\partial}{\partial x} \left(\frac{\left| B_z^{n+1} \right|^2}{2\mu_0} \right), \\ E_y^* &= U_x^+ B_z^{n+1} - \frac{1}{\rho_c^{n+1}} \frac{\partial}{\partial y} \left(\frac{\left| B_z^{n+1} \right|^2}{2\mu_0} \right). \end{aligned}$$

These field solutions are then used with the scalar field constructed from the specified particle moment to adjust the free-streaming currents onto the fully advanced temporal position. Hence,

$$\begin{aligned} J_x^{n+1} &= J_{i,\,x}^+ + \frac{\Delta t}{2} \left(\Lambda^{n+1} E_x^* + \Gamma_x^{n+1} B_z^{n+1} \right), \\ J_y^{n+1} &= J_{i,\,y}^+ + \frac{\Delta t}{2} \left(\Lambda^{n+1} E_y^* - \Gamma_y^{n+1} B_z^{n+1} \right) \end{aligned}$$

With the CAM scheme yielding the fully progressed current densities, these are then combined with charge density (already gathered at the full integer time step) to determine the required flow velocities. With these obtained, all the dependants of the electric field are possessed at the appropriate temporal position, therefore the fully progressed field components are calculated via

$$\begin{aligned} E_x^{n+1} &= -U_y^{n+1} B_z^{n+1} - \frac{1}{\rho_c^{n+1}} \frac{\partial}{\partial x} \left(\frac{\left| B_z^{n+1} \right|^2}{2\mu_0} \right), \\ E_y^{n+1} &= U_x^{n+1} B_z^{n+1} - \frac{1}{\rho_c^{n+1}} \frac{\partial}{\partial y} \left(\frac{\left| B_z^{n+1} \right|^2}{2\mu_0} \right). \end{aligned}$$

An issue that requires addressing is the deviation of conserved physical quantities from their definite values due to the use of numerical approximations. In this section we have used the method of a predictor-corrector scheme to progress the magnetic field twice doubling the opportunities for errors to be introduced into the solutions. The main conserved quantity of interest when examining the magnetic field is $\nabla \cdot \underline{B} = 0$, the accuracy of which is of extra importance in this thesis as the conservation of magnetic flux is a key principle in the application of RI motions to the outer-planetary magnetospheres. Conveniently, it is found that in the prescribed 2.5D geometry used to construct JERICHO that this conservation law is enforced by definition,

$$\nabla \cdot \underline{B} = \frac{\partial}{\partial x} 0 + \frac{\partial}{\partial y} 0 + 0 B_z = 0. \tag{5.24}$$

The use of numerical approximations when progressing parameters inevitably leads to the introduction of numeric errors to the solutions obtained. Reducing these errors to 0 is impossible, however the use of higher order solvers, when done well, generally leads to more accurate results being produced. The important metric to examine when considering these errors is that over the course of a simulation run, of the temporal length of interest, that these do not alter the form of the dynamics observed. This will be examined and verifications made for over progressed parameters in JERICHO in the follow chapter.

5.3.2 Numerical Differentiators

Both the solutions used to numerically advance the magnetic field and to analytically obtain the electric field contain spatial derivatives. The general method used to solve

these throughout the model is that of centre differencing, second-order accurate in space. The exception to this are the derivatives in the predictor-corrector scheme used for the magnetic field, as previously alluded to, in this forward differencing is used in the predictor and backwards in the corrector. Using this combination of methods along with predicting then correcting makes this magnetic solution second-order accurate in both space and time.

These finite differencing schemes are obtained through the application of a Taylor series in order to expand the derivative. Therefore, the solutions obtained can be applied generally to each spatial direction permitted for a parameter in a models geometry. Hence, rather then repeat the exact same equation with only the spatial direction changed within we introduce a variable to represent a generic spatial dimensional vector (i.e. can be x, y or z in Cartesian), ξ, as well as one for all velocity vectors (i.e. v_x, v_y or v_z), ζ. These will now be used in this work inside equations that can be applied to any spatial direction without alteration.

Forward Differencing

Assuming an arbitrary function, $\mathcal{G}(\xi)$,

$$\mathcal{G}(\xi_i + \Delta\xi) = \mathcal{G}(\xi_i) + \dot{\mathcal{G}}(\xi_i)\,\Delta\xi + \mathcal{O}(2) \tag{5.25}$$

$$\begin{aligned} \mathcal{G}(\xi_i + \Delta\xi) &\approx \mathcal{G}(\xi_i) + \dot{\mathcal{G}}(\xi_i)\,\Delta\xi, \\ \dot{\mathcal{G}}(\xi_i) &\approx \frac{\mathcal{G}(\xi_i + \Delta\xi) - \mathcal{G}(\xi_i)}{\Delta\xi} \end{aligned} \tag{5.26}$$

$$\frac{\partial}{\partial\xi}\xi_i = \frac{\xi_{i+1} - \xi_i}{\Delta\xi} \tag{5.27}$$

Backwards Differencing

$$\frac{\partial}{\partial\xi}\xi_i = \frac{\xi_i - \xi_{i-1}}{\Delta\xi} \tag{5.28}$$

Central Differencing

$$\frac{\partial}{\partial\xi}\xi_i = \frac{\xi_{i+1} - \xi_{i-1}}{2\Delta\xi} \tag{5.29}$$

5.3.3 Numerical Smoothing

When selecting the solver for the EM fields in the development of our hybrid recipe, the use of a MacCormac predictor-corrector scheme was found beneficial as it did not introduce numerical diffusion into the solutions produced. The electric field is calculated analytically and therefore also unable to introduce a source of dispersion into the fields. This is beneficial from a physical point of view as signatures of RI instabilities are thought to be small regions of enhanced magnetic field strength being transported inwards.

However, from a computational point of view it is beneficial to allow for some diffusion in the magnetic field in order to prevent large sudden gradients being created between grid points. Numerical solvers struggle to resolve large gradients and these can lead to numerical instabilities being generated that feedback into the solvers and are a cause of simulation results diverging from their true solutions. Typically the larger these gradients, the more error introduced via this mechanism and this can quickly over-power the true

physical dynamics being modelled. Hence, we introduce a parameter when initialising the model that allows for the inclusion of a controlled amount of numerical smoothing, N_{NS}, reducing the size of gradients between individual points.

The scheme devised for use in JERICHO is tailored specifically to allow for the reduction of gradients between neighbouring grid points. This is done by combining a portion of a grid point's value with an average of its neighbouring 4 grid points, hence creating a star smoothing scheme. This method can be expressed mathematically, in our 2.5D geometry, as,

$$\mathcal{A}_{i,j} = (1 - N_{NS})\,\mathcal{A}_{i,j} - \frac{N_{NS}}{4}\left(\mathcal{A}_{i+1,j} + \mathcal{A}_{i,j+1} + \mathcal{A}_{i-1,j} + \mathcal{A}_{i,j-1}\right). \tag{5.30}$$

It is apparent that the function of N_{NS} is to define the amount of the smoothed value that is provided by the target grid point and the amount contributed by its neighbours, hence this value must always be unity or lower, with a value of 0 turning off our artificial smoothing function.

5.3.4 Low Density Regions

It has been described how the amount of numerical noise introduced into the model is in part a function of the number of particles contained in each grid cell. JERICHO uses a statistical method (see §5.4.2) to seed each grid cell with approximately the same number of particles (the same if the number of particles tends to infinity). However, the model is allowed to evolve self-consistently without any limits placed on the number of particles required in each cell. The question then becomes what happens if the number of particles in a cell becomes very low or even drops to 0. Examining the solution used to calculate the electric field we find that it is dependent on the inverse of the charge densities, hence if density tends to 0 then the physical description becomes poorly defined.

A number of solutions are used to remedy or prevent this effect in PIC and hybrid-PIC modelling. These include methods such as pausing the model when densities become low or splitting particles to ensure that a large enough number remain throughout the model domain. The approach taken in JERICHO is to use a different solution to obtain the electric field in cells where the densities become low. This is done by solving $\nabla^2 \underline{E} = 0$ across the model domain and replacing any values where $q_{i,j} < 0.1 q_p$ with the solution to this equation.

5.3.5 Field Aligned Currents

For coupling to a planetary ionosphere it is necessary to obtain a value for the amount of current flowing along the planetary field lines. Since all particle motions are contained within a 2D plane orthogonal to the 1D field lines clearly no particles can actually flow along these lines. However, it is still possible to obtain a value for the FACs using (Vasyliunas, 1970),

$$\nabla \cdot \underline{J} = 0. \tag{5.31}$$

From this it is apparent that the divergence of the current densities in the magnetospheric plane is equal to that along the field lines. Hence, by obtaining the magnetospheric current density divergence and integrating along the length of the field line one obtains,

$$J_z = \frac{B_z}{B_{ion}}\left(\frac{\partial J_x}{\partial x} + \frac{\partial J_y}{\partial y}\right). \tag{5.32}$$

5.4 Initial Conditions & Particle Generation

With the specific operations now obtained to implement the model logic described to allow for the progression of a hybrid-PIC model through time, it is now necessary to examine the

process of constructing the initial domain. This configuration can be left to evolve purely in response to effects introduced via its construction (i.e. present at $t = 0$) or can have external effects introduced, such as sources of fresh plasma. The methods for introducing these effects vary depending on the selected technique, in JERICHO the introduction of freshly ionised plasma is necessary and is incorporated by placing a source at the base of the model domain. This is equivalent to allowing particles to flow in through a porous boundary and hence will be described with the rest of the model's boundary conditions.

It is important to note that particles are seeded throughout the constructed domain by randomly sampling a function across it, however as a finite number of particles are used there is inevitably the introduction of numerical effects. These effects are known as shot noise and it important to ensure that dynamics observed in simulations are not purely a function of these. This is often achieved by allowing a model a period of 'start-up' time, in which the modelled particles can reconfigure themselves into a lower energy state before introducing effects to trigger dynamics of interest. The CAM scheme used by JERICHO introduces a mixed time step method for obtaining the flow velocities, one of the benefits of this technique is the removal of shot noise from the particle distributions.

5.4.1 Domain Configuration

When initialising a model domain with JERICHO it is necessary to select which planetary magnetosphere one wishes to examine. This allows for the definition of several key variables to be made that are utilised throughout the solutions of the model. These variables are that of the planetary mass, radii, spin velocity and equatorial field strength (M_P, R_P, ω_p & $B_{eq,P}$ respectively), with the choice of planet represented by the subscript attached to these variables (J for Jupiter & S for Saturn). These values are given in the International System of (SI) units and predefined using values provided by Williams (2021a) at Jupiter and Williams (2021b) at Saturn.

A selection of SI units for these values reflects the use of SI units for all quantities used throughout the model. Therefore, it is convenient to also predefine a number of physical constants that are also present in model solutions since these constants are universal in nature. Hence, the values of fundamental charge, the permittivity & permeability of free space and Boltzmann's constant (e, ϵ_0, μ_0 & k_B) are defined according to values provided by Huba (2013).

Additionally, the atoms & molecules of particular note in the outer-planetary systems, sulphur dioxide & water group ions, are known. It is also convenient to predefine the atomic masses of oxygen, sulphur and a proton as these can be used in combination to determine the values of needed for particle mass within the model domain. These are simply calculated using values from the periodic table.

With universal constants defined throughout the model domain, the size of the space is determined by first selecting the minimum & maximum positions of each of the co-ordinates that describe the 2D plane containing magnetospheric plasma. Therefore, these are set and contained within the following four variables, x_{min}, x_{max}, y_{min} & y_{max}, with any particle with a position outside of these no longer being described by the model. It should be noted that the length of the magnetic field lines is not required by any of the solutions determined to form the model and hence is not specified, though these could be calculated using the magnetic field model (a simple dipole) and the radially position of the line.

Now our domain has been described, the locations at which the EM fields are discretised upon require determination by the construction of a grid across it. The grid we construct in JERICHO is Cartesian & regular in spacing and hence is defined by selecting the number of points that the EM fields require discretisation at. The number of points in the x-direction is described by N_x and in the y-direction by N_y, with there no need for these

numbers to be equal (i.e. both square & rectangular cells are permissible). The number of grid points along with the minimum & maximum positions of the domain are used to calculate the spacing between each point using

$$\Delta\xi = \frac{\xi_{max} - \xi_{min}}{N_\xi - 1}. \tag{5.33}$$

With the spatial domain of model defined, it is now necessary to construct the temporal domain that the model is progressed through in order to form it into a simulation. Like the spatial domains the temporal also requires discretisation in order to determine the size of step taken each time the model progresses. Typically in numerical modelling the maximum size of this step is dictated according to the Courant-Friedrichs-Lewy (CFL) condition (Press et al., 2007). This dimensionless value, C_{CFL}, is required to be less than or equal to unity in order for the results produced by a model to be accurate, with the value determined by

$$C_{CFL} = \frac{U_\xi \Delta t}{\Delta\xi}.$$

A linear superposition of the different spatial-dimensions incorporated by ξ is used where dimensionality is greater than 1. Hence, in JERICHO

$$C_{CFL} = \Delta t \left(\frac{U_x}{\Delta x} + \frac{U_y}{\Delta y} \right). \tag{5.34}$$

It is determined for hybrid models that the gyro-parameters of the kinetic-ions are also important when determining the magnitudes of the steps in both space & time. The parameter that is important for the spatial scales is that of the gyro-radius, with the spatial step required to be shorted than this to properly capture the oscillatory motions (and associated drifts) of the ions. If the spatial steps are larger than this radius then the model is in a semi-fluid regime where the ion motions begin to reflect that of fluid elements, rather than single kinetic particles. In the temporal domain the important parameter is the gyro-period, with it necessary for multiple steps per period in order to accurately capture kinetic motions. It is determined for JERICHO that temporal steps at 1% of a gyro-period give solutions that are indistinguishable from analytic, see the follow chapter for detail on how this is determined.

The dependency of temporal discretisation on the gyro-period of kinetic-ions within the model means that the maximum value of the magnetic field, B_{max}, is required to determine the size of a time step. Since we assume the internal magnetic field is described by a dipolar this value can be determined using,

$$B_{max} = B_{eq,P} \frac{1}{\left[\left(x_{min}^2 + y_{min}^2 \right)^{\frac{1}{2}} \right]^3}. \tag{5.35}$$

Using this value the size of a temporal step is determined using,

$$\Delta t = \frac{T_{g,i}}{100}. \tag{5.36}$$

By defining a start and end time for the simulation using t_{min} & t_{max}, the number of steps is calculated by determining the amount needed to move from the minimum position in the temporal domain to the maximum.

Now both the spatial & temporal dimensions used to construct the model domain have been defined and discretised, the magnetospheric plane requires populating with kinetic-ions. There are a vast number of different ion species present in the magnetospheric plasma populations of both the Jovian & Saturnian systems. However, JERICHO typically is filled

with a single species of interest, with these already identified in each system. That is not to say that JERICHO is only capable of modelling the dynamics of a single species, with the initialiser capable of handling multiple species defined within a vector. Macroparticles within JERICHO are defined using 6 variables, or particle parameters, that are stored and updated as required over a simulation. These parameters are the particle's position, (x_p, y_p), velocity, $(v_{x,p}, v_{y,p})$, charge, $M_N q_p$ and mass $M_N m_p$. From these it is possible to completely describe a particle's motions, determine its precise position on the domain and perform calculations to collect its moments onto the EM grid points.

The initial positions and velocities of the particles require varying in order to fully populate a 4-dimensional phase space, (x, y, v_x, v_p). Hence, functions must be sampled randomly across these spaces in order to ensure they are fully populated. However, with simulated ion species required to be pre-defined before model initialisation and a particle's mass & charge being fixed once it is initialised, it is possible to assign these values before the positions and velocities by allocating the particle to a ion species. In the case of single ion species plasma (the type utilised in this thesis) the following statement is possible

$$\begin{aligned} q_p &= q_s, \\ m_p &= m_s. \end{aligned}$$

In order to fully populate the described 4-dimensional phase space we require the definition of additional physical values in order to construct the functions needed. The values required are that of the number density of the selected ion species within the domain, n_p, and the plasma beta of the associated ions, β_i. Additionally, it is found convenient to calculate some physical values to help describe the dynamics of the plasma contained within the model, these are the gyro-frequency, $\omega_{g,p}$, and the Alfvén velocity, v_A, obtained using

$$v_A = \frac{B_{max}}{(\mu_0 m_p)^{\frac{1}{2}}}. \tag{5.37}$$

Using the Alfvén velocity it is trivial to calculate the Alfvén time for a particle to cross a grid cell. These quantities are both useful in understanding the import physical factors defined by our models parameter space. Since JERICHO is typically operated in low β environments, then it is found beneficial to ensuring the Alfvén time remains below that of the model temporal step, Δt.

Finally, before populating our domain it is necessary to make some computational definitions, required to determine the number of times a function is sampled and to ensure that the random sampling is repeatable. Since we have a 4-dimensional phase space the constructed function require sampling 4 times for each macroparticle that is included in the model, hence by defining the number of macroparticles in the model do we determine the number of samples. This is defined by the number of macroparticles that each cell contains, N_{PPC}. The reason for defining the number of macroparticles in our hybrid model in this manner is that the amount of noise created by using a finite number of macroparticles is directly proportional to this value, with energy conservation also being closely associated with it (Matthews, 1994). Therefore, it is convenient to directly scale the number of macroparticles in the model using this value (N_{PPC}) rather than selecting an arbitrary number of total macroparticles. Hence, the total number of macroparticles in simulation is calculated using

$$N_{TPPC} = N_{PPC} \left(N_x - 1\right) \left(N_y - 1\right). \tag{5.38}$$

The repeatability of the random samples taken to populate phase-space is ensured between simulations by the definition of a seed used in the random generators. These generators use the random library from the standard set of libraries of their respective

programming language (either Python or C++), with both languages using a standard Marsene twister engine to generate the random numbers (see ISO/IEC TR 19768:2007, 2007). The seed used in the random engines takes the form of an integer and defined as N_{RS} in JERICHO.

It should be noted that an additional functionality that can be provided when initialising the model is the inclusion of background fields, beyond a typical dipolar. This is extremely useful when the model domain represents a small section of a much larger system which enforce global fields independent of effects induced by modelled plasma motions. Though defined in the initialisation there is no need for these background fields to be constant in time, rather these fields can change at every time step if that is desired, however they must be fully prescribed before the model begins to self-consistently evolve. These background EM fields are described by $\underline{E}_{back}$ & $\underline{B}_{back}$ and are still bound to the 2.5D geometry of the model.

5.4.2 Domain Population

Will all the physical parameters now obtained that are required for the population of the described 4-dimensional phase-space, we can now define how this is accomplished. The method used to populate the (x, y) dimensions are identical and the methods used to populate (v_x, v_y) are also. It is recalled that each macroparticle requires the random sampling of functions across these phase-spaces 4 times to obtain the values for a single macroparticle. Here, the method for taking these samples are described for a single macroparticle and these are then repeated in the model for every macroparticle, making the total number of samples equal to $4N_{TPPC}$. From this point all the operations described are within the confines of JERICHO's framework, hence all particles created are by their nature macroparticles, as previously described, hence for simplicity they shall just be referred to as particles.

First, the process for obtaining the position of each particle is described, yielding x_p & y_p. The relation between the number of particles within a computational grid cell and the amount of numerical noise in the model has been discussed. For this reason initially it is desirable to try and ensure each cell contains the same number of particles. Of course since we are randomly sampling functions to populate these domains there is no guarantee that each cell will contain exactly the same number of particles, however statistically we would like a cell to contain N_{PPC} particles. Therefore, a pair of uniform distributions are constructed across the x & y-domains to satisfy this need for initial uniformity. The probability density function (PDF), $\mathcal{P}$, for each of the spatial dimensions is given by,

$$\begin{aligned} \mathcal{P}(x) &= \begin{cases} \frac{1}{x_{max}-x_{min}} \text{ for } x \in [x_{min}, x_{max}] \\ 0 \text{ for } x \notin [x_{min}, x_{max}] \end{cases}, \\ \mathcal{P}(y) &= \begin{cases} \frac{1}{y_{max}-y_{min}} \text{ for } y \in [y_{min}, y_{max}] \\ 0 \text{ for } y \notin [y_{min}, y_{max}] \end{cases}. \end{aligned}$$

These functions cover the entirety of the computational domain, hence particles cannot exist outside of this domain as the functions are equal to 0 by definition.

The particle velocities can be initialised with a uniform distribution but in JERICHO they are typically initialised with a Maxwell-Boltzmann distribution set to the temperature

of the plasma. This is done by modifying a normal distribution, with PDFs,

$$\mathcal{P}(v_x) = \frac{1}{\frac{k_B T_i}{m_p}(2\pi)^{\frac{1}{2}}} e^{-\frac{1}{2}\left(\frac{v_x - U_x}{\frac{k_B T_i}{m_p}}\right)^2},$$

$$\mathcal{P}(v_y) = \frac{1}{\frac{k_B T_i}{m_p}(2\pi)^{\frac{1}{2}}} e^{-\frac{1}{2}\left(\frac{v_y - U_y}{\frac{k_B T_i}{m_p}}\right)^2},$$

where T_i is the temperature of the ion species. When written in this form it can be readily seen that the mean (μ) is equal to the bulk flow velocity ($\underline{U}$) and the standard deviation (σ) is equivalent to $\sqrt{\frac{k_B T_i}{m_p}}$. This allows a standard normal distribution generator from the standard programmatic libraries to be used.

Temperature is used to determine the PDFs used to obtain the velocities, yet we have not explicitly calculated this value. It should be noted that temperature is not a parameter supplied when initialising the model domain, rather it is controlled by the plasma beta, β_i. The reason for this selection is that when setting the β_i it allows for a better physical understanding of which effects will be dominant in a plasma contained within the model (see 1.1.6). From the plasma beta temperature is calculated as follows,

$$T_i = \frac{\beta_i m_p v_A^2}{2k_B}. \tag{5.39}$$

5.5 Boundary Conditions

Extensive discussion has been provided on the initialisation and operations of particles and fields inside the constructed model domain. However, what happens to these as they approach or even enter a space outside of that described by this domain? The set of schemes that deal with this are known as the boundary conditions (BCs) and determine precisely what happens at these critical locations to model operation.

It is convenient when describing the operation of the BCs to introduce two new subscripts. The first of these denotes the spatial location of the boundary which is being approached, indicated by B. The other represents the location of the other boundary associated with the one being approached, or the alternate boundary AB. Hence, if a particle was crossing outside of the domain via the boundary located at x_{max}, then this would be x_B and the boundary at x_{min} would be x_{AB}.

JERICHO contains five different types of boundary conditions for the treatment of particles that exit the model domain and two for the fields. These are titled the Periodic, Hard, Open, Recycle & Inflow for the particles, with the function of each of these shown in figure 5.8, labelled a-e respectively. The EM fields simply have Periodic & Hard, these will be defined along with the particle boundary of the same name.

5.5.1 Periodic

The first boundary condition examined is that of the periodic, this condition essentially warps the domain such that one edge wraps around to touch its alternate boundary. This means when a particle passes over this boundary it reappears on the other side of the domain, with all particle parameters conserved apart from position, hence the momentum and charge of the particle are both conserved. This boundary is seen in figure 5.8a, where the trajectory of the particle can be seen to take it over the domain, hence it is re-inserted at the same position on the opposite domain where it continues on its path.

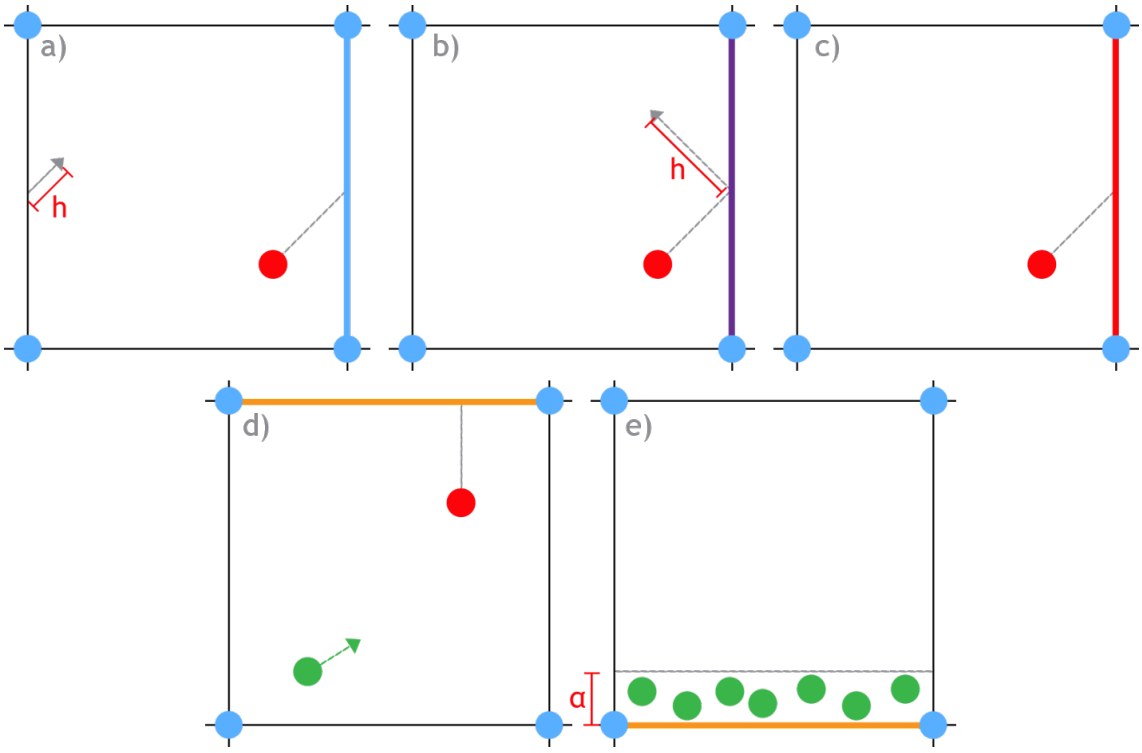

Figure 5.8: Panels showing the 5 different boundary conditions available for selection in JERICHO. Each shown is at a edge of the model domain, with the boundary under examination highlighted with a coloured line, particles are shown as red dots with grey lines showing their path and EM field discretisation locations in blue. Green dots indicate the creation of new particles as part of the boundary condition scheme. Panel a) shows a periodic boundary, b) a hard (specular) boundary, c) a outflow boundary, d) a recycle boundary and e) a inflow boundary.

The mathematical solutions used to operate this scheme within the model logic can been seen below, detailed at each of the 4 boundaries of the domain. When the condition specified by the inequality associated with a solution is satisfied, then the corresponding equation is used to move the particle. The set of inequalities and solutions are as follows,

$$x_p \leq x_{min} \quad : \quad x_p = x_{AB} - |x_p - x_B| \,, \tag{5.40}$$

$$x_p \geq x_{max} \quad : \quad x_p = x_{AB} + |x_p - x_B| \,, \tag{5.41}$$

$$y_p \leq y_{min} \quad : \quad y_p = y_{AB} - |y_p - y_B| \,, \tag{5.42}$$

$$y_p \geq y_{max} \quad : \quad y_p = y_{AB} + |y_p - y_B| \,. \tag{5.43}$$

These equations can be summarised as follows,

$$\xi_p = \xi_{AB} + h \tag{5.44}$$

where h is the remaining distance moved in time step once boundary is reached, calculated by subtracting the boundary location from the particle's position.

Now we must consider how to update the values of the EM fields discretised that are located along these boundaries. The problem arises due to the use of numerical differentiators when determining the spatial derivatives in the solutions used to obtain these fields, as these sample the grid points either side of a specific index to determine its value (i.e. central differencing). With these grid points lying on the very edge of the domain, clearly they are unable to be resolved by the numerical scheme devised previously, hence a selection of boundary condition is made to update these.

With the domain warped such that the two boundary edges are touching one another, when considering how to handle EM grid points at these locations it makes sense to allow for communication between the two edges. Hence, the values of EM fields on the boundary opposite the one being updated are used to take the place of the indices missing to allow for the numeric scheme to be completed.

5.5.2 Hard (Specular)

Rather than warp the computation domain allowing for particles to move from one side of the domain to the other, the boundaries can be made to behave as a wall on which particles elastically collide and bounce off. The elastic collision does not alter the magnitude of a particle's velocity, only its direction. Therefore, momentum is not fully conserved, however both the kinetic energy & charge of the particle are. The collision of a particle with a hard boundary is shown in figure 5.8b where the trajectory of the particle can be seen to be deflected at the point of incidence with the edge of the domain.

This scheme is implemented in the model using the following set of inequalities and equations,

$$x_p \leq x_{min} \quad : \quad x_p = x_B + v_{x,p}\left(\Delta t - \tau\right), \tag{5.45}$$

$$x_p \geq x_{max} \quad : \quad x_p = x_B - v_{x,p}\left(\Delta t - \tau\right), \tag{5.46}$$

$$y_p \leq y_{min} \quad : \quad y_p = y_B + v_{y,p}\left(\Delta t - \tau\right), \tag{5.47}$$

$$y_p \geq y_{max} \quad : \quad y_p = y_B - v_{y,p}\left(\Delta t - \tau\right). \tag{5.48}$$

Once again it can be seen that when a particle position moves to a location that is outside of the model domain, the associated scheme is applied to move it back inside the defined region. τ is calculated using

$$\tau = \frac{\xi_B - (\xi_p - \Delta t \zeta_p)}{\zeta_p},$$

with it immediately apparent that this value is equal to the amount of time taken for a particle to reach the boundary on its current trajectory. This value is then combined with the total length of a temporal step to calculate the distance travelled away from the boundary after deflection. Hence, the equations used to operate the condition can be summarised as follows,

$$\xi_p = \xi_B + \zeta_p\left(\Delta t - \tau\right), \tag{5.49}$$

where

$$h = \zeta_p\left(\Delta t - \tau\right)$$

can be asserted to make the form identical to that used in the periodic boundaries.

After the particle's position has been updated its velocity must also reversed to reflected the collision with the boundary. This is simply done using

$$\zeta_p = -\zeta_p \tag{5.50}$$

in which the direction of the velocity that is altered is the same as the dimension in which the boundary was encountered.

With the boundaries of our domain now not wrapping to connect one side to the other, it no longer makes sense to allow the EM grid points to access those on the alternate boundary to calculate their values. However, it is noted that JERICHO's domain typically only covers a small portion of a much larger magnetospheric environment. Typical values for the particle distributions and magnetic field, from which the initial electric field is calculated, through these sections of the magnetosphere are well known with analysis of spacecraft measurements able to obtain steady state solutions for them through the

system. Hence, when using hard boundaries, or any of the BCs after this point, the EM field values are set and held constant by these well known steady-state solutions. This has the additional benefit of providing some restoring mechanisms to prevent simulation results from straying to far from typical magnetospheric configurations.

5.5.3 Open

Both BCs discussed already enforce a constant number of particles within the model domain, not allowing for any source or sinks of fresh particles. The open boundary addresses the latter proportion of that critique allowing for the removal of particles from the simulated domain. This boundary simply destroys any particle that passes out of the boundaries on which it operates, in computational terms, removing the object containing the particle parameters from the list of particles. Figure 5.8c shows this with the particle and its associated trajectory disappearing once it encounters the edge of the domain.

The consequence of this is of course that none of a particle's momentum, energy or charge is conserved, with this BC representing a sink for total energy and number of charge carriers from the model domain. Therefore, one must be careful when using this BC to ensure that the rate of particle loss from the model does not leave the domain depleted of both energy and charge carriers to an extent where physical assumptions break down. Despite this caveat, these BCs are essential to the physical modelling in JERICHO, this is because the simulated domain occupies a fixed location within the magnetosphere, hence plasma enters and exits the region over the course of run time. Without particle removal plasma would gather at the outer boundary (radially) creating large electrostatic effects that would dramatically alter the dynamics within the model region.

5.5.4 Recycle

A simple way to reduce the impact of net energy and number of charge carriers changing is the use of the recycle BC. This scheme initially operates in the same way as the outflow condition, but finishes by reinitialising the same number of particles on the alternate boundary as it has removed. The operation of this BC is seen in figure 5.8d, with the initial red particle removed from the simulated domain, but a new green particle is placed at the alternate boundary. In order to mitigate the electrostatic effects of a large number of particles being injected at the same location, the particle initialisers (detailed previously) are reused, with a injection range specified from the boundary to a distance α, typically the length of one spatial step $\Delta\xi$.

The benefit of using this scheme is that total number of charge carriers is conserved for all time throughout the model domain. The velocity initialisers using the same temperature and bulk flow velocity as defined in the model configuration stage and therefore total momentum and energy is not explicitly conserved. However, if the model has not statistically varied by any great amount from this initial configuration then these quantities can be approximated as being conserved.

5.5.5 Inflow

The final BC utilised by JERICHO allows for a source of fresh ions that is independent from the sink schemes. This BC scheme operates by assuming a solid emitter is placed at the edge of the domain, injecting particles into the model with a specified flux. Just like the recycle BC the location at which these particles are injected is varied over a range α in order to prevent any large electrostatic accumulation effects. The generation of the fresh ions is demonstrated in figure 5.8e, with the solid emitter creating a hard boundary for particles that encounter that edge. Alternatively, this boundary can be thought of a porous wall through which plasma can only flow in one direction, into the model domain.

Just like the outflow boundary, the inflow boundary does not act to conserve net momentum, energy or number of charge carriers, increasing the magnitude of these quantities rather than decreasing them. Once again the initialisers for populating the domain as a whole are reused to generate these new particles, with their temperature and bulk flows set by the values used in the configuration stage. Computationally, this BC adds fresh ions by creating and appending new particle objects to the list of total particles, hence the codebase must be able to dynamically alter the length of this particle list. If the rate of outflow at some boundary is approximately balanced by the rate of inflow then the conserved quantities of momentum, energy & charge remain constant, along with the length of particle list remaining stationary.

5.6 Architecture & Implementation

JERICHO has codebases in both Python and C++, with the former developed before the latter to allow for the rapid prototyping of different physical contributions. One would expect that the codebase developed second would be the more sophisticated of the two and this is true, though differences are of course inevitable due to the nature of C++ being a lower-level programming language (i.e. the need for explicit data-typing). However, both versions of the codebase follow the same general architecture in the design of their software, which can be seen summarised in figure 5.9.

In order to describe the piece of software that operates our computational model, we shall decompose the suite into elements. There are a number of approaches to this decomposition, with the selection largely based on the level of detail one wishes to explore a software suite in. For this explanation we shall use the language of C4 modelling (Brown, 2019). Specially, the definition of a container, an application or data store inside the software, and a component, a group of related functionality, will be utilised. The containers (black boxes in figure 5.9) used to construct the software suite which comprises JERICHO can be grouped in three categories: input, outputs & JERICHO.

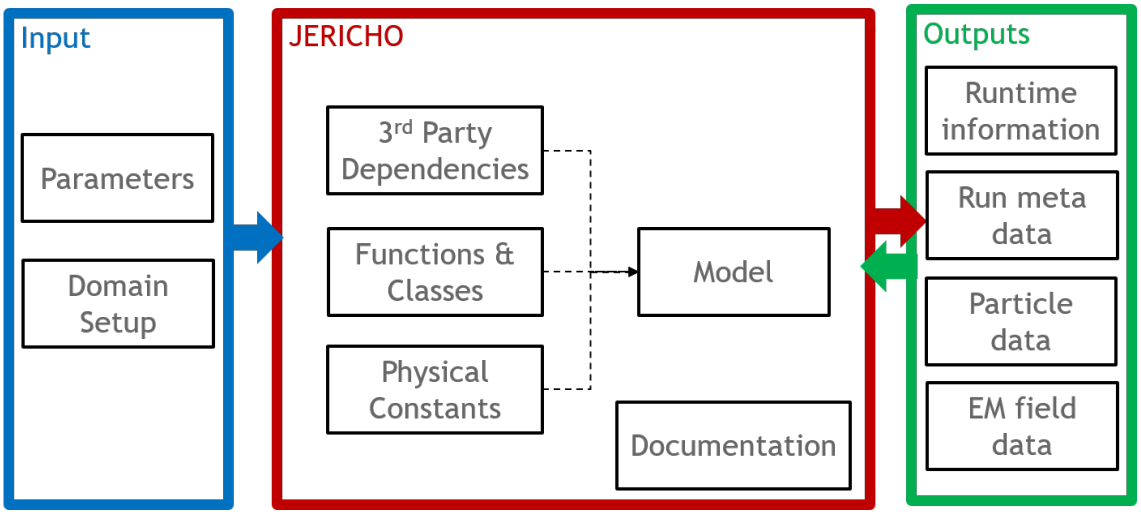

Figure 5.9: Software architecture of the JERICHO software suite with the containers constituting the applications split into three categories and the flow of information between these indicate. The input category holds the containers that require a user to interact with before initialising a simulation run, JERICHO holds the core of the model and Outputs holds the containers associated with managing and writing data out of the model. The flow of information back into JERICHO from output indicates the capability to restore a simulation from the particle & EM field data.

Beginning with the inputs there can be seen to be two containers that constitute this part of the software, categorised together as both require configuring by the model user before a simulation is initialised. These are the parameters and domain setup. Examining the parameters first, this is found to contain all the definitions required to construct the computational domain, such as the size of both spatial directions, the number & species of particles and the temporal discretisation. Domain setup contains an array of switches that can be used to control the physical features included within the simulation, such as whether a dipolar magnetic field is used. Although these containers are separate they are intrinsically linked, with the features selected in the domain setup described in parameters.

The containers defined in input are then passed into the section of the software contained within JERICHO (the programmatic logical detailed in this chapter), so titled as this what most people would recognise as the model itself. Along with the user defined variables, the model has a core of additional components required to construct the computational framework necessary for operation. This core is the foundation of the computational model, taking the user defined inputs and using these to form a simulation.

Three containers comprise the core that can be seen flowing into the main model, the first of these being 3rd party dependencies. Examples of these dependencies vary depending on the language of the codebase, but would be libraries such as Numpy in Python (Harris et al., 2020) and Eigen3 in C++ (Guennebaud et al., 2010). The other two containers hold custom modules built specifically for JERICHO, with functions & classes being comprised of components such as the numerical differentiators and particle objects. Physical constants is much smaller in scope, responsible for the provision of all the required values of physical constants into global namespace in appropriate units.

The components within the model container are responsible for the actual operation of the logic required to perform a hybrid plasma simulation. First the model domain is constructed, then populates with a particle population, this initial distribution with the magnetic field definition is used to obtain a full set of discretised EM fields. The logical loop that forms the back-bone of JERICHO's operation can then be entered (see 4.3), with a selection made to start by updating the particle velocities & positions, though the loop could be entered at any step in its overall cycle.

It is notable that there remains one container in the JERICHO category that is yet to be touched upon, this is that of the documentation. This is because although present throughout all containers comprising the JERICHO software suite, it is not responsible for the operation of any component required for the computational model. Rather, it is created from inline code comments alongside the specific code they pertain to in order to automatically generate a guide for users when required. This functionality is provided using Sphinx (Developers, 2022) in the Python codebase and Doxygen in C++ (van Heesch, 2022).

The third category holds the containers responsible for managing and writing outputs from JERICHO as it runs. These containers are more specifically responsible for a wide breadth of functionality and generate any messages or data seen by a user. It is worth stating explicitly that though this category is placed after JERICHO that is not to say that data is only written to disk once a simulation is complete, rather these components can be accessed during a logical cycle in order to write whilst the model is still running. Following the order containers are displayed from top down in figure 5.9, first is runtime information. The components in this container allow for useful metrics to be displayed in the application console (screen terminal), updating whilst the simulation is in progress. There are a number of automated tests performed whilst using these metrics, with errors raised if behaviour is exhibited outside of what is expected (i.e. CFL condition violated).

In order to understand the importance of the components, forming run meta data, it is necessary to first examine the structure used to write data to a mounted volume. Upon

initialisation of a simulation a new directory is created at a specified location, inside this all data from that run is written to. Once a simulation has been configured and initialised the run meta data is written, containing all the key information provided by a user as inputs. This is stored as a JavaScript Object Notation (JSON) file, providing the benefit of being both human & machine readable. This allows it to be utilised by the visualisation suite to automatically populate plots with labels corresponding to a runs configuration. Further, to ensure the integrity of data sets a unique reference is contained within the meta data that can be checked against all data files within a directory, providing a mechanism for finding the particular run from which a data set originates.

Within the created directory all data associated with the particles and EM fields written. It is convenient to save particle data separately from field data as the former requires much more memory (disk space) than the latter. Particle lists/vectors allow for the serialisation of the data forming the list of objects containing macroparticle information, with this list written to disk at the end of a logical loop. The file format selected to do this is binary in order to minimise the amount of space needed to write these. EM field data allows for the writing of all fields required to calculate any value utilised in a model cycle into a data cube (though flat as only a single time step is written) of values for that cycle. These fields are the EM fields and the current densities. The fields are written to a custom file format, JEMF (JERICHO ElectroMagnetic Fields), which essentially writes the field in binary but in a known structure. With the field data being much lighter than the full list of particles and essentially containing the particle information collected on the spatial grid, usually the EM field container is called with a much higher cadence than the particle data.

The code is also written to be able to restart from a saved state - but this requires both a full set of fields and particles in order to restart. Thus, writing out particle files at a very low cadence will impact the point at which a simulation can be restarted.

Chapter 6

JERICHO - Benchmarks & Validation

All numerical models inevitably introduce errors as they move through time, simulating the dynamics of a true physical system, this is due to the solutions being used to advance through times being approximations, rather than exact or analytical in nature. The order of accuracy used in the derivation of the numerical methods is a reflection of both the size of effects that can be captured within the model, as well as the accuracy of the values determined. In theory, the higher the order of solvers used, the smaller the error introduced at each time-step. However, this is often complicated by higher-order effects introducing dynamics into a model domain that themselves can cause the solutions to diverge from the exact (i.e. turbulence). In §5, JERICHO is shown to be second-order accurate in both the spatial & temporal domains.

The important metric to consider when examining the performance of a numerical model is not the total mitigation of numerical errors, but rather to ensure that the size of errors introduced into the solutions do not alter the dynamics of the effects of interest in a simulated domain. When we recall the values needed to progress JERICHO, these being the particle distribution in configuration and velocity space, the current densities and the EM fields, the exactness of the solutions can be measured using the total energy. Since the domain constructed for our hybrid plasma simulation is largely isolated from the global system in which it is embedded, with effects introduced adiabatically, energy should be conserved. Therefore, by measuring the total energy within the simulation as it progresses, we gain an understanding of the size of errors introduced.

Of course even a model that perfectly matches an analytic solution as it progresses is not useful if the methods used to determine these are so restrictive as to prevent the dynamics of interest from occurring. The motions of interest in this thesis are those associated with the RI instability, as described in §3. In order to ensure the effects produced by a model are physical, it is necessary to induce higher-order effects with well known analytically obtained parameters within the simulated domain. To do this a wave will be induced in a domain with known parameters which can be used to calculate analytic properties of the wave, with wave speed being the specific property of interest, which is then compared to the behaviour observed within a simulation run. This provides confidence that those effects that are less readily parametrised are also physical.

It is not that the physical tests performed on the model codebase in this chapter are the simplest that can be used to determine the exactness of model operations, with it obviously simpler to compare the solutions produced by the solvers in known configurations to sets of pre-calculated solutions. Of course this relies on one knowing the exact values of all field components and can only be performed for a single step in time. However, these simple tests are still of use to ensure the integrity of the model codebase, particularly when it

is being deployed on new computational systems. Hence, these are wrapped into a set of unit tests that are included in the software suite that contains JERICHO.

In this chapter we will first analyse the accuracy of the solutions used to advance the modelled particles positions and velocities. Performing this analysis allows for the identification of the parameters set when constructing JERICHO that control the overall accuracy of the solutions produced. Then, the total energy contained within the model domain is analysed over periods of time of interest to RI motions. Finally, the ability of the model to resolve higher-order effects is verified through the introduction of an ion-acoustic wave, using a density perturbation at one edge of the model domain.

6.1 Single Particle Motion

Perhaps the most fundamental physical test of any hybrid plasma physics model is its ability to accurately reproduce physical motions. With a kinetic-ion, fluid-electron model it is necessary to capture the motions of single particles (ions) within the domain. The analysis of an individual particle's motions in the domain allows for the measuring of a solution's accuracy as it progresses both through the spatial & temporal domains of the model. This allows for more rigorous testing of the physical accuracy of the simulation which is both more informative and expansive than a unit test will permit. That is not to say that the testing of single particle motions on their own is enough to determine the physicality of the entire model. In fact, in order to resolve the parameters of interest with single particle motion, the gyro-parameters, either the particles in the model must be prevented from communicating electrostatically (i.e. insulated from one another) or the density vastly reduced. The reason for this is particle-particle interactions will deflect the smooth 'orbits' assumed in the formation of the gyro-parameters, making the comparison impossible.

Therefore, the tests performed in the validation of single particle motions select to use a modified EM configuration, with both fields set to prescribed configurations and held constant throughout the test run. The reason for this selection is that it is far simpler to implement computationally than the two physically accurate options. This is because in order to prevent the particles from communicating with one another then it is necessary to stop collecting their moments on the grids. However, in order to interpolate the EM fields onto the particle positions, moment gathering is required (a computational choice rather than a physical limitation). By holding the EM fields constant, moments can still be gathered on the EM grid, however these have no impact on the models operations, effectively halting particle-particle communications.

Examining the option of vastly reducing the number of particles in the domain, hence lowering the density, it is recalled that when a low number of particles are present within a cell that the assumptions used to form the model are broken. These assumptions are used in the construction of the EM fields, with particle solutions derived from the equation of motion for an individual kinetic ion. A solution is implemented to allow small parts of the model to temporarily become depleted without disrupting the overall operations of the domain. However, this is not suitable for use over long time periods or over large spatial sections. By fixing the EM fields within the domain the problems caused by low densities are also resolved, allowing for the single particle tests to be run with just an individual ion in the computational domain.

6.1.1 Gyro-Motion

The parameters selected for analysis within this set of physical benchmarks are the gyro-radii and period, r_g and T_g respectively, for an ion in the simulated region. These are

simple to obtain analytically with stationary background EM fields using the eqns 1.5 & 1.6. From these it can be seen that with the magnetic field held constant and a null electric field (i.e. $E = 0$ V m^{-1}) across the domain, and of course the particle's mass & charge constant, that as long as the particle's initial velocity is known these parameters can be determined exactly.

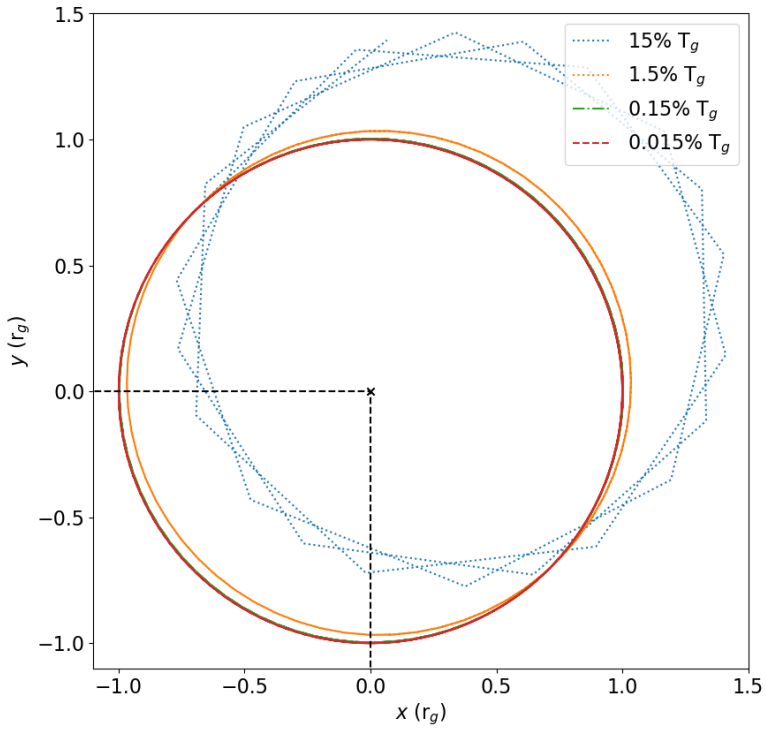

Figure 6.1: Ray trace of a single ion's motions over 240 s, $\approx 3.6T_g$, through a model domain containing a uniform magnetic field. Spatial coordinates are transformed using the analytic solution for the ion gyro-radii with the origin shifted to the centre of the particle's gyro-motion, indicated by a black cross and lines. 4 separate traces are visible with the blue, orange, green and red lines corresponding to a temporal resolution of 15%, 1.5%, 0.15%, 0.015% of the ion's gyro-period respectively.

Figure 6.1 contains a set of four ray-traces showing the path of a single ion over a 240 s simulation period. Ray-traces are a tool often utilised when examining the path taken by elements within a computational model, in this case that element being a single ion. Essentially the method takes the position of the element at each time step within a given simulation run and connects these, in temporal order, using a line plot. Hence, the path of an element followed through the system can be readily examined. By using multiple simulations with background fields in identical configurations, and by starting particles at the same initial location, a set of ray traces can be constructed to examine the effects of varying computational parameters on the models operations.

For this simple initial test the only physical parameters that require setting are that of the ion species and the magnetic field strength. The ion selected is that of a Hydrogen ion, H^+, (i.e. a singular proton) and the magnetic field set at 1 nT. The initial velocity of the particle is manually set with both velocity components equal ($v_x = v_y$) for computational ease. Using these parameters it is readily determinable that the 240 s of simulation time translates to approximately $3.6T_g$. With a uniform magnetic field and a null electric field the guiding centre will remain stationary as previously noted.

Figure 6.1 contains 4 separate ray-traces, each trace corresponding to a different temporal resolution, changing the size of step taken in time (Δt) each iteration of the main model loop. It was discussed previously (see §5) that in order to accurately reproduce the ion motions the temporal step size must be at least an order of magnitude smaller than the gyro-period of the ion (ie $\leq 10\%\ T_g$). Therefore, we are able to verify that this rule is applicable to JERICHO's operations by comparing this set of ray-traces, with the blue dotted line advancing with temporal steps above the theorised upper limit. Each of the other traces are below this limit, decreasing the model temporal resolution by an order of magnitude between runs.

Examining first the blue dotted line in figure 6.1, it can be seen that the path of the particle in this run diverges greatly from the solution obtained analytically, with the axes used centred on the particles guided centre and all values obtain via direct computation. The first notable difference is the shift in the particle's guiding centre at this resolution, with the centre of the gyration being offset by approximately $0.5r_g$ in both spatial directions. Further, the trace can be seen to form a shape with defined edges rather than a smooth circle as the space between steps causing the particle to move large distances in the spatial domain between each step. It can be concluded that the particle motions at this temporal resolution do not closely match those obtained analytically.

The orange dotted, green dashed & dotted and red dashed lines each are ray traces at temporal resolutions postulated as viable for a model in production. Examining the orange line, the numerical solution produced can be seen to match more closely with the analytical. On its own the deviation between the particles guiding centre and that obtained analytically is difficult to see, with the shift less than $0.1r_g$ in both spatial directions. However, using the green and red lines for comparison this offset is made obvious. Looking at the form of the line traced it is clear that the temporal resolution allows for a smooth circular path to be produced, though of course small sections of the particles orbit when examined in detail still consist of straight lines.

Examining last the green and red lines together it is immediately apparent that the green line appears to be missing from the plot. This is because the red line sits over top of the green, showing that the solution produced by the model has converged at these temporal resolutions. Using the black dotted lines to identify the guiding centre of the green & red ray-traces, we see that this sits exactly on that calculated analytically. This shows that at high enough resolutions the particle paths produced using numerical approximations iteratively converges on the analytic solution, providing confidence that the particle's equations of motion are physically accurate.

6.1.2 ExB Drift

Of course to this point, although the particles have been orbiting their guiding centre, the plasma as a whole can be considered stationary as those centres are fixed. The introduction of an electric field incudes $\underline{E}\times\underline{B}$ drift motions, breaking this simplistic set up and causing the plasma to move. Again the analytic values associated with this drift are readily computable, with the equations needed to quantise these motions proved in §1.1.2, with eqn 1.7 giving the drift velocity. The initial gyro-radius and period remain unchanged from the previous configuration, with no dependency on the electric field, however it is work noting that the gyro-radii of the particle will change over the course of the simulation as its position in velocity-space changes.

Placing a uniform 0.1 nV m^{-1} electric field over the entire spatial domain (with a 1 nT magnetic field), once again a proton is placed within the computational domain and advanced 240 s through the temporal domain. These motions can be seen in figure 6.2a with the particle drifting from the left to the right-hand side of the plot. Once again a ray-trace has been produced to visualise the trajectory of the particle. A set of 4 ray-traces

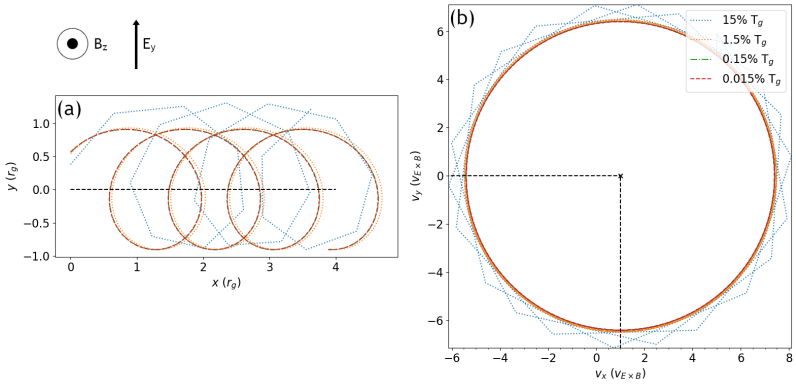

Figure 6.2: Ray trace of a single ion's motion over 240 s through a model domain containing both a uniform magnetic and electric field, shown in the top left. Motions through the spatial domain are shown in (a), with coordinates transformed using the gyro-radii and the origin shifted to the initial guiding centre, and their corresponding position in velocity space in (b), with coordinates transformed using the ion's $\underline{E}\times\underline{B}$ drift velocity. A set of 4 traces can be seen in both (a) and (b) with the blue, orange, green and red lines corresponding to a temporal resolution of 15%, 1.5%, 0.15%, 0.015% of the ion's gyro-period respectively. The black line in (a) indicates the guiding centre of the ion as it moves through the domain and in (b) the black cross shows the centre of the ion's path through velocity space.

can be seen, each corresponding to a separate simulation run with the temporal resolution varied in the same manner as for the stationary particle. The axes of the plot are expressed in gyro-radii, obtained analytically using the particle's initial velocity and the particles are initialised in the same location within the computational domain, to facilitate comparison.

The motions of the particles are traced as they move through this domain and can be seen to differ significantly from those contained in figure 6.1. The guiding centre can be seen to move in a straight line in the x-direction causing the particle's orbit to be deformed from a circle into a cycloid that travels about this line. It is worth noting that despite the particle having velocity components in both spatial directions, the guiding centre only moves in one, causing the bulk plasma to convect in only a single direction.

Figure 6.2b contains another set of 4 ray-traces tracking the particles movement through velocity phase space. Examining the form of these traces it can be seen that they orbit around some central point (like a guiding centre), unlike the spatial paths that now spiral around their drifting centre. Determining the location of this centre it is found to sit exactly at $1v_{E\times B}$ in the v_x-domain and 0 in the v_y, meaning the particles guiding centre sits exactly at the analytically obtained drift velocity.

Each of the 4 ray-traces again correspond to a set of simulation runs with varying temporal resolutions. Examining this set of solutions they are found free of the offset found in the stationary gyrating particle paths as resolution decreased. Hence, the yellow, green & red line all sit on top of one another, converged on the same values. The blue line differs in that rather than forming a smooth circle it can be seen to take a spiked shape as the low resolution causes an overestimate of the particle's velocity. However, it can be concluded that any temporal resolution $\leq 0.1T_g$ will produce the same results.

Using the set of tests performed in figures 6.1 & 6.2 it is can be concluded that the earlier assertion of the suitability of a temporal resolution $\sim 0.1T_g$ for model operations proves adequate in terms of particle motions. However, it is further concluded that where computational resources allow, a resolution of $\sim 0.01T_g$ is preferred as at this value there is only minor difference between the modelled solutions and those determined analytically.

Since so much of the model physics is driven by particle motions, with the fluid electrons essentially following these, then it is important to ensure these motions are as accurate as possible.

6.1.3 ∇B Drift

With stationary particle gyration as well as E×B drift motions examined, it is sensible to extend this physical analysis to motions introduced by a gradient in the magnetic field ($\nabla \underline{B}$). The mechanism and equations to describe the motions introduced by this have been detailed (see §1.1.2, eqn 1.10) and will be utilised in order to analyse the simulated results. We will limit the maximum resolution of the set of simulations performed in this case to $0.1T_g$ in order to inspect the model's accuracy precisely at the maximum permissible temporal resolution.

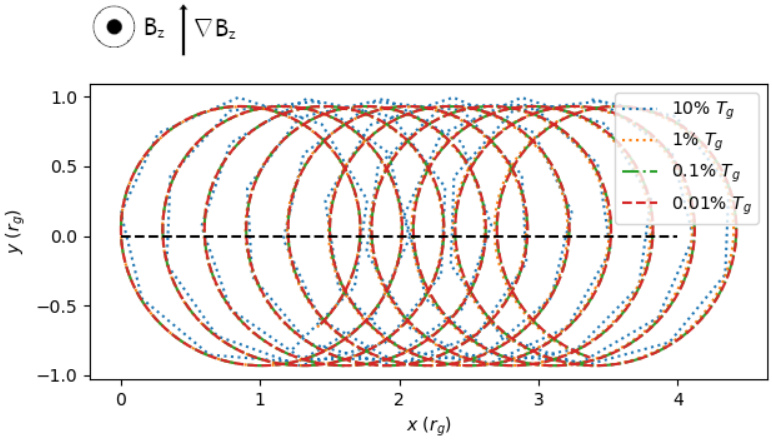

Figure 6.3: Ray trace of a single ion's motions over 240 s through a model domain containing a magnetic field with a uniform gradient, shown in the top left. Spatial coordinates are transformed using the analytic solution for the average ion gyro-radii with the origin shifted to the centre of the particle's initial guiding centre, indicated by a black dotted line. 4 separate traces are visible with the blue, orange, green and red lines corresponding to a temporal resolution of 10%, 1%, 0.1%, 0.01% of the ion's average gyro-period respectively.

Figure 6.3 contains the set 4 ray-traces corresponding to 4 separate simulation runs. These traces track the trajectory of the particles as they move through the spatial domain of the modelled region. Each of these regions contain prescribed static EM fields, with the magnetic field increasing positively as the y coordinate increases to introduce the gradient needed to induce drift. The magnitude of this gradient is 0.1 nT m^{-1} with the average field strength equalling 2.5 nT. The spatial coordinates on the plot have been transformed in terms of the particle's gyro-parameters using this average field strength. It is worth noting that the electric field is set to the null vector for this physical examination. A black dashed line has again been included to indicate the drift of the particles guiding centre through the model domain.

Examining the set of traces included it can be seen that each gyrates about its guiding centre with this drifting in the direction perpendicular to that of the gradient, the x-domain. With a higher average magnetic field strength than the uniform fields used in the previous two tests the particle is seen to gyrate more rapidly, completing more 'orbits' in the 240 s simulated period. From its initial position the particle can once again be seen to spiral about its drifting guiding centre, giving a result similar to that observed in the $\underline{E}\times\underline{B}$ examination. With the gradient in the magnetic field confined to purely the y-domain, the

drift in the particles guiding centre can be seen to be purely in the x-domain as expected.

It was noted that the set of 4 ray-traces presented here differ from those in the previous two tests, with the maximum temporal resolution at $0.1T_g$, $0.05T_g$ less than the previous maximum. Comparing the set of traces it can be seen that a reduction of this maximum to the hypothesised upper limit eliminates the obvious outlier visible in figures 6.1 & 6.2. However, that is not to say that the trace corresponding to the lowest temporal resolution is indistinguishable from the higher. Once again this trace fails to resolve a smooth orbital path, giving it a 'spiky' appearance and it can be seen to over-estimate the maximum spatial position on the y-axis through-out the course of the simulation.

Analysing the 3 remaining traces, it can be readily seen that once a temporal resolution of $\leq 1\%$ T_g is utilised then the solutions produced by the model converge, with the ray-traces essentially laying on top of one another. Examining the trajectory of the model run at 10% T_g it is seen to diverge beyond the lack of smoothness caused by the relatively few points to trace between, with the solution over estimating the maximum position of the particle in the y-domain. However, it is notably closer to the higher resolution solutions than in figures 6.1 & 6.2. Therefore, from this test no reasons can be determined to change the conclusions drawn from analysis particle motions drift via $\underline{E}\times\underline{B}$, with temporal resolutions of $\leq 0.1T_g$ clearly able to accurately capture $\nabla\underline{B}$ drift motions.

The tests on the particle's equation of motion performed in this section are limited to the components contributed to it by the Lorentz force. That is not to say that the application of the centrifugal & Coriolis pseudo-forces have not been tested. Rather, due the relatively simple mathematical form of their contributions in the equations, the tests for these are much simpler and find exact agreement between the simulated and analytic solution at any reasonable temporal resolution. Additionally, as these forces are free of EM fields they are not bound to the domain grid and are hence independent of any choices made for spatial-resolution.

6.2 Energy Conservation

Analysing the motions of single particles in specified, static EM fields, provided the information required to create rules for selecting the temporal resolution of a simulation preformed by JERICHO. However, the usage of static EM fields in this meant that the gyro-parameters of the charged particle moving through the domain remained constant (or varied constantly in the case of the $\underline{E}\times\underline{B}$ & $\nabla\underline{B}$ drifts) throughout the course of the simulation run. In the construction of the model, performed in §5 following the recipe in §4, self-consistent dynamic EM fields were selected and implemented. Therefore, in a simulation run using the unaltered codebase, the EM fields will vary across the modelled domain and hence the gyro-parameters will. It should also be noted that usually a statistical method is used to initiate particles in order to fully populate velocity phase space, hence this will also vary specific gyro-parameters independent of the EM fields.

The time-step utilised in JERICHO is constant (see eqn 5.36), though it is certainly possible to vary the size of the temporal step in response to model conditions (i.e. Gunell et al., 2013), this selection is made for computational ease within the model codebase. Therefore, it is possible to envisage regions within a simulation where the EM fields induce particle motions with trajectories that diverge from the analytic solution. Hence, errors will be introduced into the simulation which propagate through all modelled parameters as these values are self-consistently calculated.

Further, the methods used to obtain the parameters (i.e. the magnetic field, particle velocities & positions) are numerical approximations. By their very nature these methods contain divergences from the analytic solutions as there are only an approximation of these, though methods have been carefully selected in the construction of the model to

ensure that ones utilised are suitable for describing the dynamics of interest. Therefore, the numerical methods used to approximate these parameters are another source through which error is introduced into the solutions obtained within the simulation. Typically, the higher-order the numerical method used, the more facets of the analytic solution it is able to capture. However, this may be undesirable as it may introduce phenomena such as turbulence, incorporating non-linear effects into the calculations causing the solutions to more rapidly diverge from the analytic than a lower-order approximation would.

The final source of error, at least that will be discussed here, is that which is introduced computationally. The machine it is deployed upon is imperfect and therefore introduces error into the solutions obtained by the model. The most well known example of these computational errors are floating-point errors, arising from the limitation of variable data-types to be bound to a finite amount of precision (essentially number of trailing decimal places, see Microprocessor Standards Committee, 2019). However, many other errors contribute to this source, with even point defects in a machine's memory substrate a possible mechanism for error to enter. Hence, it is not feasible to eliminate the introduction of errors into even fully analytic models constructed using computational codebases and therefore striving to fully eliminate error is fundamentally not possible.

Considering the impact of the errors on the solutions obtained across the entire domain, it is clear individually effects of these will be small and localised, imperceivable when looking at the solution as a whole. For example, an error that causes a deflection to a particle's trajectory, this could be anything up to a few metres in size, considered on the spatial scales of interest, closer to the order of planetary radii, make this deflection negligible on its own. However, considering that there are likely to be many particles in the region where trajectories are diverging from their true solution, the moments of which are then gathered, informing the updated configuration of the EM fields, it can be seen how errors can feedback into themselves, self-perpetuating. These are compounded at each time step within the simulations run, with errors introduced with each cycle through the main logical loop.

Fully eliminating error from the model is clearly not possible, however the introduction of errors does not invalidate solutions produced by it. The example presented before demonstrates although errors may change a small portion of the model solution, the overall form of it remains unchanged, allowing it to still capture the dynamics of interest within the system as a whole. What is important is ensuring that the dynamics being created are representative of the physical system being modelled and not the configuration of the numerical errors that have been introduced. Typically, once errors have begun to overpower the physical effects within a simulation run, then the solutions produced for the modelled parameters become unphysical, the model is therefore deemed to be unstable.

Therefore, one must consider how it is best to quantise the amount of error that has entered a simulation performed by JERICHO as it progresses. In order to do this, the mechanisms through which errors are introduced must be identified. Particles can introduce errors every time their parameters are updated, but analysing these is almost impossible as their true trajectory through the model domain is not known. Therefore it does not make sense to examine error introduced at the level of individual particles. Rather, one must group these parameters and treat them using a statistical method. Grouping the particle parameters is a function already performed by the model as their moments are gathered on the EM grid and these are used to self-consistently calculate the EM fields. Therefore, by quantising the amount of error that enters the EM fields, one gains an understanding of the amount of error in the model as a whole.

Examining the calculations utilised to obtain the EM fields, it is seen that the electric field is obtained analytically, whereas the magnetic is obtained via numerical approximation, performed taking the curl of the electric field. One may assume therefore that only

an understanding of the error in the magnetic field is necessary. However, this is not the case as it is recalled that in regions of the model where plasma density drops below a critical value, an alternate method is used for obtaining the electric field which is numerical in nature. Hence, an understanding of the error in both the electric & magnetic fields is required.

It is worth noting here that within JERICHO errors which are introduced into the magnetic field are found to lead to the model becoming unstable most rapidly, especially when errors increase the field strength. The reason for this is linked to the discussion of the range of gyro-parameters able to be accurately captured by the model numerical schemes. This is compounded by the numerical method used to obtain the magnetic field being non-diffusive, hence there is no mechanism to disperse errors into the background, creating a feedback loop. Hence, this is the motivation for including artificial smoothing over the magnetic field, in order to make the model as a whole more robust.

With it identified that the EM field can be utilised to understand the amount of error introduced into a simulation run, the question is then what metric is appropriate for this analysis. In order to do this, one must consider the impacts of the errors on our obtained solutions. Impacts broadly fall into two categories (though these are not physically distinct). The first of these is the difference of the values calculated within our domain of the modelled parameters (i.e. the electric or magnetic field strength at a grid point). The second is the impact of these divergences on the form of the modelled solution as a whole (i.e. changing the topology of the magnetic field).

Examining how one measures these categories in reverse, first we determine how to ensure the form of the EM fields do not change in unphysical ways over the course of a simulation. If we select a region in either the Jovian or Saturnian magnetosphere in which we know no dynamics of interest should occur, within a specified temporal scale, then we can configure the region with the known values for physical parameters. One can then analyse the results modelled within the simulation and it should be seen that there is little deviation at any point from this initial configuration. Key indicators of error becoming dominant in the model would be deformation of the magnetic field from its dipolar configuration or large coherent structures in the electric field that the model equations are not able to dissipate. This can be seen performed by JERICHO in figure 6.4 for a region far out in the Jovian magnetosphere (49-50 R_J).

The simulation results contained within figure 6.4 shows the temporal evolution of a plasma from initialisation at 0 Ω_i^{-1} (0 hr) to 50 Ω_i^{-1} ($\sim$1.5 hr) across a 1$\times$1 R_J domain with the base placed at 49 R_J. A 100$\times$100 grid for the discretisation of the EM fields is placed across the domain, with 50 macroparticles per grid cell used to populate the domain. The plasma has a initial number density of 1×10^5 m^{-2} and is configured so that plasma pressure gives a 0.01 β_i (see §5.4 for how other values are obtained). A time-step of $\Delta t = 0.005\ \Omega_i^{-1}$ ($\sim$0.17 s) is selected as a compromise between our maximum step size of 0.01 Ω_i^{-1} and ideal size of 0.001 Ω_i^{-1}.

Frome analysis of the results shown in this figure we can see that both the electric field and ion charge (this is the charge of all the macroparticles gathered on the EM grid, not considering the electron neutralising fluid) contain a number of localised transient structures in the field strength and charge distribution respectively. The important thing to note is that these structures are able to naturally dissipate, without overpowering the simulation run, leaving the overall configuration of the field unchanged. It is noted that there is a growth in the electric field strength with time, this is due to centrifugal forces accelerating the ions, a phenomenon that will be examined in detail later in this section. The magnetic field can be seen to remain unchanged (without the background field removed) over the course of the entire simulation, this is as expected in a configuration where magnetic forces are dominant (recall low beta). From the behaviour observed within

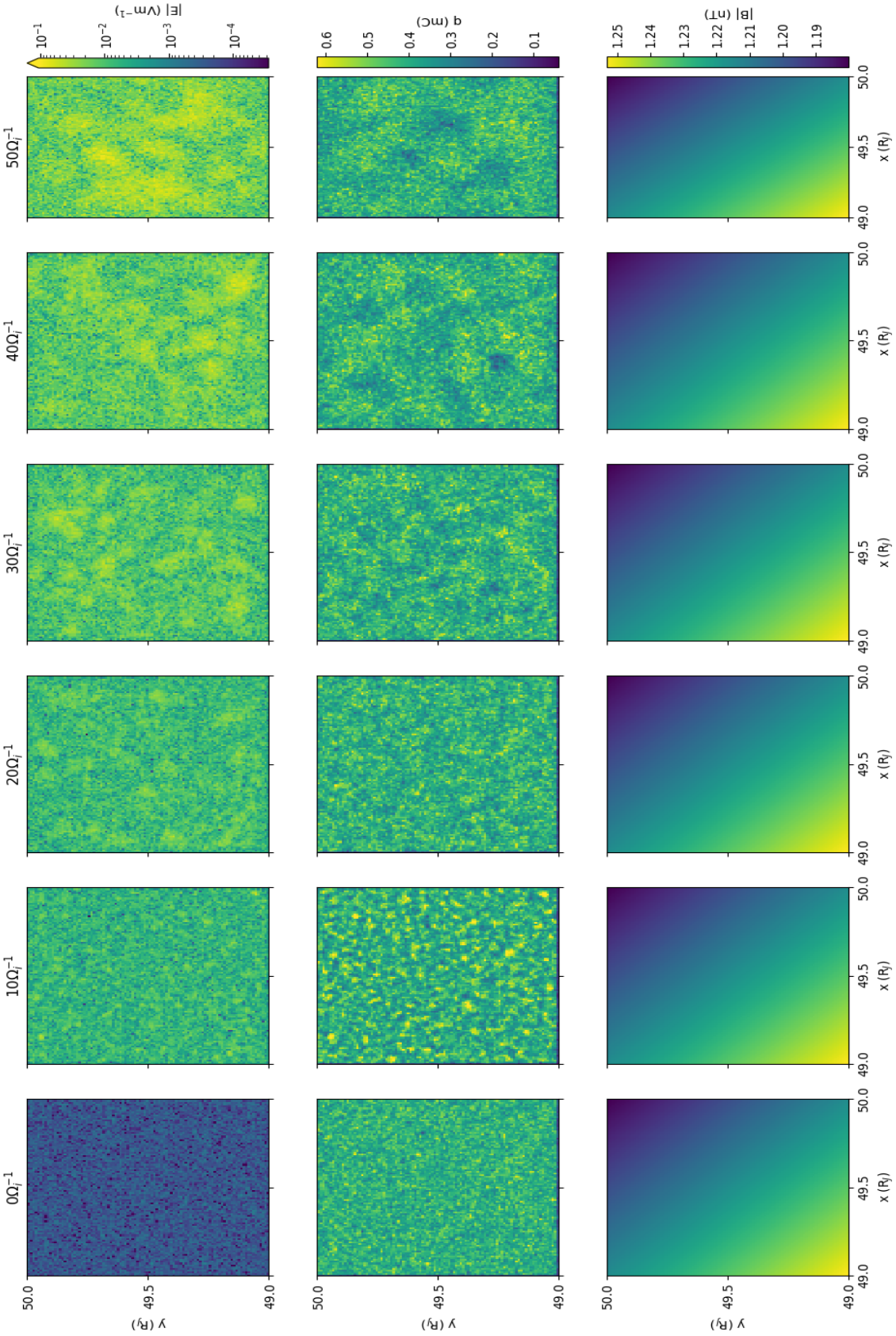

Figure 6.4: Evolution of the electric field ($|\underline{E}|$, top row), ion charge (q, middle row) and magnetic field ($|\underline{B}|$, bottom row) over a period of 50 Ω_i^{-1} (∼1.5 hr) with a 0.005 Ω_i^{-1} (≈0.17 s) time-step (Δt). Modelled domain is from 49-50 R_J in both the x & y-coordinates with EM fields discretised on a 100×100 grid containing 50 macroparticles per grid cell (N_{PPC}), initialised with 0.01 β_i

these results it can be concluded that the large scale topology of the fields do not diverge from expected configurations in typical quiet simulations.

It is noted that the structures seen best in the ion charge seem to shift to larger and larger spatial scales, becoming less sharp, as the model progresses. This is attributed to the source of these initial perturbations being created by shot noise (a function of using a finite number of randomly initiated macroparticles), through time these perturbations are naturally damped by the numerical schemes utilised in the construction of JERICHO. This can be thought of as the constituent plasma particles attempting to reconfigure themselves into the lowest energy state.

Next a method is required to quantise the amount of change local variations introduce into the simulation. The quantity that is identified for this measure is that of total energy contained within the EM fields. This is used as fundamentally energy is required to be conserved in all physical systems, however errors are introduced by non-physical sources so will act to change this. It is noted that $\nabla \cdot \underline{B} = 0$ (Guass' law for magnetism) is conserved by definition through the 2.5D topology, with no mechanism for errors to introduce divergences.

It is recalled that total energy stored in EM fields, Φ_{EM}, is calculated using (Griffiths, 2017),

$$\Phi_{EM} = \frac{1}{2} \int \left(\epsilon_0 \left| \underline{E} \right|^2 + \frac{1}{\mu_0} \left| \underline{B} \right|^2 \right) dV, \tag{6.1}$$

where dV is some unit volume assuming 3 spatial dimensions. This can be obtained from the discretised EM grid in the model by performing,

$$\Phi^n_{EM} = \frac{1}{2} \sum_i \sum_j \epsilon_0 \left| \underline{E}^n \right|^2_{i,j} + \frac{1}{\mu_0} \left(B^n_{z\,i,j} \right)^2, \tag{6.2}$$

where the magnitude of the electric field is obtained in the usual manner. The change is total energy is then measured by computing the percentage change between the total initial energy (Φ^0_{EM}) and the total energy contained within the fields at a particular time step (Φ^n_{EM}).

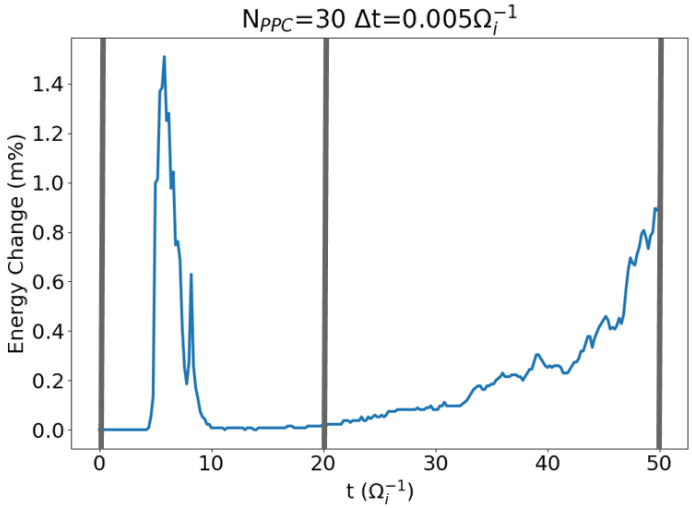

Figure 6.5: Percentage change in total energy (in $\% \times 10^{-3}$) stored within the EM fields obtained in the simulation shown in figure 6.4 as it progresses. The change can be subdivided into 2 distinct epochs, switching at $\approx$20 Ω_i^{-1}, with these bounded by the vertical grey lines. Change between 0-20 Ω_i^{-1} relates to shot noise, where as change after this period, >20 Ω_i^{-1}, is related to centrifugal force.

Figure 6.5 uses this method to compute the total energy change in the simulation shown in figure 6.4. The total change in energy can be seen to create an initial peak, from 0-20 Ω_i^{-1}, followed by a sustained growth phase between 20-50 Ω_i^{-1}. These two epochs are readily distinguishable from one another and this is attributed to two separate mechanisms being responsible for them. It is worth noting that total energy change peaks in the initial epoch at $\approx 1.5\times10^{-3}$%, re-enforcing the conclusion reached in previous analysis that error induced features have not significantly altered results in the quiet simulation.

Examining the sharp peak that occurs initially, it can be seen that total energy change rapidly increases up to its peak value ($\approx 1.5\times10^{-3}$%), before more slowly reducing back to the initial amount of energy. The mechanisms attributed for the creation of this peak is that of shot noise (Bagdonat, 2005), discussed previously. It is the reordering of the particles locally in order to create a more natural distribution of them in response to the global configuration of the EM fields, as this configuration is reached the total energy change returns to ≈ 0. Therefore, it is preferable to include a 'start-up' or 'spin-up' period at the beginning of any simulation to allow this phenomena to occur.

After this response in the total energy to shot noise, the amount of change remains approximately 0 until after 20 Ω_i^{-1}. After this point in simulation time, the amount of energy within begins to increases once again. However, it is seen in this temporal segment that error increases more slowly, with noise obscuring the exact rate form of this growth. Between 20 & 50 Ω_i^{-1} it is seen that total energy changes by $\approx 1\times10^{-3}$ %, giving a energy change rate of $\approx 3\times10^{-5}$ % Ω_i^{-1}, assuming linear growth.

The mechanism that is responsible for this sustained growth is centrifugal force, accelerating the particles and hence increasing the strength of the EM fields. It is noted that the growth rate obtained assume linear growth, examining the form of the contribution in the particles' equation of motion (eqn 5.5) this assumption seems sensible as the centrifugal pseudo-force applied is obtained using a linear combination of a particle's position. The position of the simulated domain, with its base at 49 R_J is much further from the planet then any domain utilised to simulate RI instability, hence the rate of energy growth in this system is more rapid than one placed closer to the planetary body.

In the configuration utilised for the simulated domain used in this test, the particles will continue to accelerate until reaching speeds above those possible for simulation (i.e. $v_\xi > \Delta\xi$) and triggering a break condition in the model codebase. This is due to the use of periodic boundary conditions on the limits of both spatial-dimensions, making them essentially infinite in length. This means no matter what direction a particle travels it will continue to move across the surface of the domain, when compared to a surface in nature with these properties it is found to resemble the behaviour one would expect on a sphere. Therefore, it is said when all boundaries are periodic that the domain is spherical. Hence, total energy will continue to steadily increase from its initial total as the particles velocity increase. However, this is not the case in simulation runs used in the analysis of the RI instability.

Simulation runs analysing the RI instability use a combination of open, periodic and source boundaries, with open boundaries placed at the radial maximum of the domain. Therefore, particles initialised and emitted into the simulated domain are accelerated by the centrifugal force radially outwards, but are removed after reaching the radial top of the domain. Hence, it can be seen if a steady stream of particles are emitted by our source boundary that an equilibrium will be reached where the total energy will reach a constant value, perturbed only by computational noise.

6.3 Ion Acoustic Wave

The motions of single particles have been analysed along with the conservation of energy within a domain simulated by JERICHO. These tests have ensured that the model is capable of producing physically accurate solutions, with regions within the model's parameter space identified which simulated values must remain within in order to ensure the produced solutions are accurate. They have also ensured that self-consistent solutions are capable of capturing the spatial scales of the desired physical phenomena on time-scales of interest without cumulative numerical errors interfering with the obtained results.

However, all tests so far have dealt with well quantised linear phenomena, whereas the physical mechanism of interest to this thesis, namely the RI-instability, is intrinsically a non-linear effect. Therefore, it is necessary to devise a test that is able to ensure that the model codebase can accurately capture higher-order effects. Further, the model should be able to do this multiple times in a single simulation run without previously induced dynamics interfering with fresh (well-spaced) effects.

The method used to perform this is the initialising of a wave that propagates through the model domain, hence ensuring that higher-order effects can be captured by the numerical solver, allowing for the incorporation of linear & non-linear dynamics. Further, by inducing a plasma wave with well known properties, then it is possible to determine analytical metrics to ensure the wave is behaving physically. It should be noted that unlike the paths of single particles in stationary EM fields, it is not expected that these metrics will aligned exactly with the analytic values. This is due to the nature of physical assumptions used when constructing the model and the numerical approximations made by the solvers used to obtain various values within the codebase.

A full exploration of the vast zoo of plasma waves is beyond the scope of this thesis, however details of these can be found in Swanson (2003), with more limited reviews in Baumjohann and Treumann (1996) & Treumann and Baumjohann (1997). Often, when selecting a wave to test the performance of a model the (typical) MHD waves are used (i.e. Alfvén, slow & fast). However, these are used by testing their wave speed as a function of inclination to the background magnetic field. In the 2.5D configuration used by JERICHO it is found that only the fast wave solution is permissible travelling at a characteristic speed. This speed can be varied, but it is found that this is not as computationally simple to implement in the model configuration as other plasma waves, that also will travel at a characteristic velocity through the domain.

The wave that is selected for the test is an ion acoustic wave, which as the name suggests is reminiscent of a sound wave in a standard fluid or gas and can in fact be found to be analogous in the plasma medium. Hence, the ion acoustic wave is longitudinal in nature and is found to be propagated by density perturbations within a plasma medium. Recalling that the RI-instability deals with dynamics of regions of different densities within a domain, this allows confidence that density perturbations can propagate physically through within a simulation.

In order to generate an ion-acoustic wave a velocity enhancement, φ, is introduced, acting upon the ions within a magnetised domain, in order to create a density perturbation. The function used to introduce this perturbation takes the form

$$\varphi(x,t) = A\cos(\omega t)e^{-x}, \tag{6.3}$$

where A controls the amplitude and ω the frequency of the perturbation. An example of how this function varies across a domain, with an amplitude of 10 m s^{-1}, can be seen in figure 6.6a, with the velocity contribution rapidly dropping to 0. It is noted here that the form of this contribution is dependent only on the x-domain and is applied across the entire y-domain, this can be seen in figure 6.6b. It can also be seen that the function

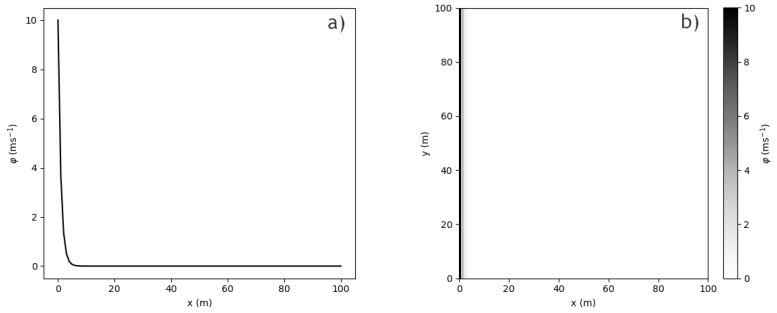

Figure 6.6: Form of a perturbation with an amplitude of 10 m s^{-1} used to introduce an ion-acoustic wave within a simulated domain of 100×100 m. Panel a) shows the form in purely the x-domain and b) shows the contour of the perturbation in both the x & y-domains.

is dependent on the temporal domain, with the frequency at which waves are launched controlled simply using ω.

The speed of the ion-acoustic wave can be calculated using (Baumjohann and Treumann, 1996),

$$v_{ia} \approx \left(\frac{\gamma_e k_B T_e + \gamma_i k_B T_i}{m_i} \right)^{\frac{1}{2}},$$

where γ_e & γ_i are the adiabatic indexes for an electron & ion fluid respectively. However, in our framework utilised to construct our model it was assumed that only the electrons were formed into a fluid continuum, whilst the ions were treated individually. Fortunately, it is found when making the assumption that electron velocities in the models are much greater than the ions, the following simplified equation is obtained for the wave speed of the ion acoustic wave, v_{ia},

$$v_{ia} \approx \left(\frac{\gamma_e k_B T_e}{m_i} \right)^{\frac{1}{2}}. \tag{6.4}$$

Clearly this assumption is excellent when using JERICHO as the electron fluid is massless and able to react instantly in response to dynamics within the ion distribution.

Using this approximation for the ion-acoustic wave speed, it is possible to perform a direct comparison between the wave speeds observed in the simulations to those calculated analytically. This is done by varying $k_B T_e$ by altering the amplitude of the velocity enhancement introduced by eqn 6.3. When the density perturbation is induced this creates a large pressure gradient with the maximum pressure found aligned with the wave. The pressure of the electron fluid can be readily obtained by performing post-processing upon the results from a model run as detailed in §4. Pressure can be used to obtain the temperature of the electron fluid by considering the continuum as an ideal gas.

The simulated domain is initialised with $5{\times}10^5$ particles and a 10^2x10^2 grid is utilised. The particles are initialised assuming a uniform distribution throughout the region and their velocities are configured with no bulk flow. Periodic boundary conditions are applied at the edges of the domain, once again creating essentially a spherical model geometry. Each simulation is 3 s long, with the first 2 s utilised to allow the model to settle into a steady-state (i.e. let shot noise dissipate), and progressed for the final second at a temporal resolution (Δt) of 1×10^{-3} s. It is noted that the time here is expressed in seconds rather than gyro-periods for easier analysis of the wave velocities, however the temporal resolution is $< 0.01\Omega_i^{-1}$ in all simulation runs.

A total of 5 separate simulated runs are analysed in order to examine the behaviour of the ion-acoustic wave as it propagates across the domain and ensure that the analytical

value of interest, the wave speed, varies as expected. The amplitude of the velocity is varied as detailed, with larger initial amplitudes corresponding to higher peak pressures and hence a larger wave speed. The driving frequency for the waves is held constant at 3.2 Hz, ensuring that the wave fronts are launched at the same times in each simulation.

In order to determine the wave speed from within the simulation results and use them for analysis, a method is required for the automatic detection and fitting of a wave as it moves through the domain. The ion-acoustic wave is a density perturbation that propagates through the domain, therefore ion density, gathered on the grid vertices, is utilised for this detection. The function used to introduce the perturbation (eqn 6.3) acts solely in the x-domain. Hence, the spatial-dimensionality of the simulated results is reduced by performing a line-of-sight integration from the y origin, essentially summing each column, j. This reduced dataset is then simply plotted against temporal domain.

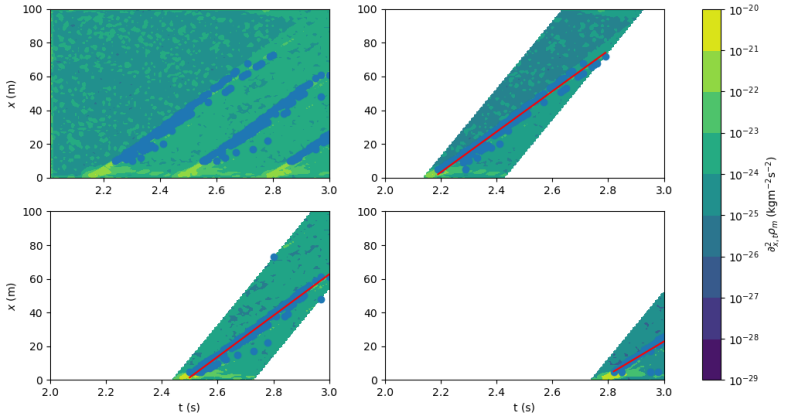

Figure 6.7: Automated detection of 3 ion acoustic waves moving through the model domain. Rate of change of mass density shown, with 1 s of simulation time against the line-of-sight integrated x-domain. The wave is identified by select points within the integrated domain that are $> 10^2$ above the median run value. The domain is then decomposed into 3 subdomains based on when the waves are launched with the wave speed obtained using linear regression on the points identified within an individual subdomain.

To assist with the automated detection of the waves, it is found beneficial to take the rate of change of mass density (i.e. the acceleration of mass density change) in the integrated x-domain, which is then plotted against time, this can be seen seen in the top left panel of figure 6.7. The wave fronts are automatically identified by dividing each domain into 3 subdomains using eqn 6.3 to identify the point in the time domain at which the wavefronts will be generated, seen in the remaining 3 panels of figure 6.7. Once sub-divided the wave front is identified by selecting points which are $> 10^2$ orders of magnitude than the median value of the domain. A first order polynomial can then be fitted, the gradient of which is the velocity of the wave front. Uncertainties originating in the fitting of the polynomial give an uncertainty in the wave speed. These wave speeds and uncertainties are combined in order to yield a single characteristic value for a simulation run.

This technique for the automatic detection of the wave front moving through the model domain and calculation of the wave speed is then repeated on the 5 separate simulation runs. A subset of 4 of the runs containing the ion-acoustic waves can be seen in figure 6.8 with red lines indicated the fitted waves. The top left panel has the lowest velocity enhancement, hence the smallest perturbation and slowest wave speed, with an amplitude of 10 m s^{-1} utilised. The size of this amplitude is increased in each panel, left to right, top to bottom.

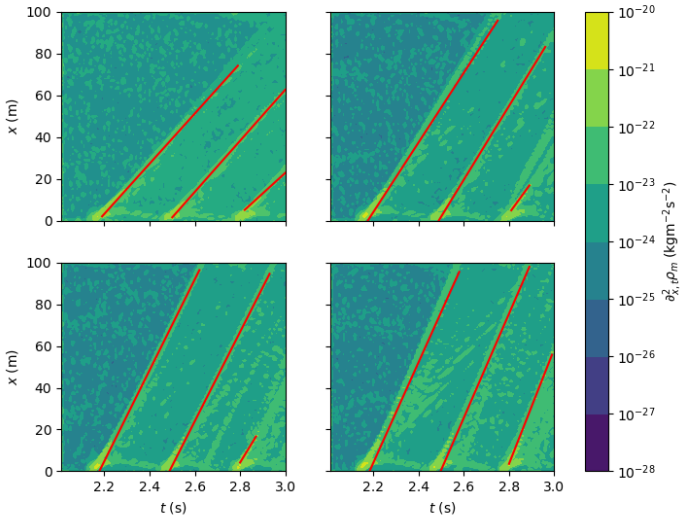

Figure 6.8: Rate of change in mass density across a 100×100 m domain, line-of-sight integrated into x-plane, over a 1 s period, from 2 to 3 s, within which 3 ion acoustic waves are generated. Each panel shows a separate simulation run in which the magnitude of the initial perturbation is increased, from top left to bottom right. Red lines fit the path of each ion-acoustic wave front through the domain.

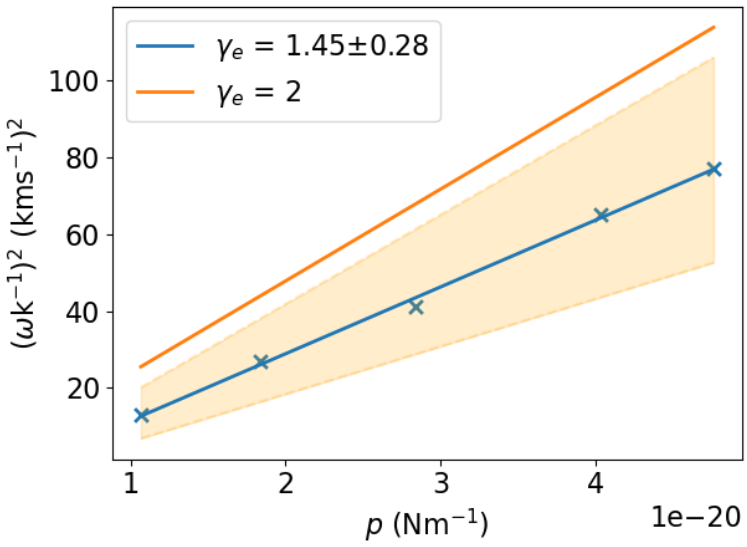

Figure 6.9: Speed at which ion acoustic wave front propagates across a 100×100m domain against the pressure in the region from which it was generated. 5 separate simulations are utilised with each containing 3 wave fronts, these 3 fronts are combined and averaged to yield a single value indicated by the blue crosses. A first-order polynomial is fitted to these values, the gradient of which is equal to γ_e determined to be 1.45 ± 0.28. The uncertainty in this value is a product of determining the path of the wave front. This is compared to a fluid with a γ_e equal to 2, indicated by the orange line.

Figure 6.9 shows the wave speed squared against the pressure in the region in which it is launched, recalling each simulation contains 3 ion-acoustic waves which are averaged to form a single value. It is clear from eqn 6.4 this leaves γ_e as the only free parameter.

Fitting a first-order polynomial to these values γ_e it is determined to be 1.45 ± 0.28 from the simulations. This is compared to a fluid with a γ_e of 2, as would be expected for a fluid with two degrees of freedom. The uncertainty in the index calculated for the modelled electron fluid is introduced by the function constructed to track the wave front as it propagates through the domain. This difference between the index of the ideal gas and our modelled fluid is due to a number of factors. The first of the these is that in the model although the fluid is contained within a 2-dimensional plane it responds to forces for 3-dimensional vectors. Additionally, the modelled fluid is far from ideal with particles interacting electro-dynamically as well as being influenced by both regional and global electromagnetic forces.

The results from this test provide confidence that the model codebase can reproduce higher-order effects with properties that accurately capture mechanisms observed within plasmas. Although the precise values obtained vary from the analytic, it should be noted that the form of the solution obtained matches exactly. It is not surprising the precise numerical values of properties vary with the number of assumptions and approximation utilised in the construction of the model. Hence, we can conclude that the model is suitable for the analysis of large scale non-linear dynamics within a simulated region, though physical properties calculated from these should be treated with more care.

Chapter 7

Application to Saturnian Magnetosphere

In §3 a number of open science questions were identified which related to the bulk transport of plasma in the magnetospheres of both the gas giants in our solar system, Jupiter & Saturn. More specifically these questions related to the mechanism postulated as being responsible for the transport of this material through these systems, the radial-interchange (RI) instability. In order to answer these questions it was hypothesised that a hybrid plasma physics model would be necessitated, one specifically designed for operation in the outer-planetary magnetospheres.

A new hybrid kinetic-ion, fluid-electron plasma model for the study of plasma transport in the magnetospheres of Jupiter and Saturn (JERICHO) was presented in §4 & 5. The assumptions and parametrisation were discussed and justified, additionally it was shown that JERICHO is able to accurately reproduce single particle motions and physics associated with collective motion (so that ions could feel the effects of their neighbours through the grid) via the simulation of wave propagation. Constraints on parameter regimes, such as time step, were also explored.

With a model now constructed that is able to perform hybrid plasma simulations in the outer-planetary magnetospheric systems, it is possible to return to the questions identified in §3.5 and begin to configure simulation runs that will yield results from which these questions can be answered. In particular, the first, and perhaps most fundamental, question is explored within this chapter. This question is *'What are the local spatial & temporal scales of RI instabilities and which local plasma parameters control these?'*

In order to explore this a set of parameters with which to configure JERICHO's ICs must first be identified, this is done in §7.1. Results from initial simulation runs are then examined in §7.2, with features related to the RI instability identified and categorised. §7.2.2 varies key parameters related to the RI instability, performing a parameter survey, in order to identify which control properties of the instability. Finally, findings from the simulations performed throughout the chapter, with physical interpretations, are summarised in §7.3.

7.1 A Saturnian Configuration for 7.5-9.5 R_S

When configuring a model domain with JERICHO the most fundamental selection that is required is that of the planetary magnetosphere. This selection sets a number of key parameters which influence all other aspects of the simulation's configuration, these being the mass & radius of the planetary body, as well as its equatorial magnetic field strength and planetary rotation rate. After this, it is necessary to configure other model parameters and ICs to reflect the system within which the simulation is being performed. These

include properties such as ion species, plasma density & β.

	Jupiter	Saturn
Radial distance of peak interchange signatures	6-8 R_J (Kivelson et al., 1997; Thorne et al., 1997)	7-9 R_S (Azari et al., 2018)
Ion species	S^{++}or O^+ ($\frac{m}{q} = 16$)	W+ ($\frac{m}{q} = 17$)
Rotation Period (hrs)	9.97	10.5
Magnetic field strength (nT)	800-2000	30-60
Gyro-period (s)	0.002-0.005	0.06-0.1
Typical thermal speed (km s^{-1})	29	34
Typical gyro-radius (km)	2.4 (6×10^{-5} R_J)	150 (2×10^{-3} R_S)

Table 7.1: Comparison of key parameters considered when selecting, between Jupiter & Saturn, the initial system in which to simulate RI motions. Detailed overviews of the planetary systems can be found in §2.2.1 & 2.2.2.

Comparing the key parameters of Jovian & Saturnian systems (see summary in table 7.1), it is evident that Saturn possesses characteristics that makes it preferential both physically & computationally. The primary motivation for the selection of Saturn is the number of observations of RI events is simply much greater within this system than the Jovian, with hundreds of these events observed (see §3.3). There are more observations in the Saturnian system due to the much larger dataset of observations, provided predominantly by the Cassini mission, and due to lower $\nabla\underline{B}$ drifts leading to lower ion dispersions rates (Hill et al., 2005). From analysis of the events identified, it is determined that the region of 7-9 R_S is most preferential for RI motions (Azari et al., 2018), hence this is used for the selection of the location to place the simulated domain.

The lower drifts are intrinsically linked to Saturn having a lower magnetic field strength, this leads to the next reason for the selection of the Saturnian system. Comparing magnetic field strengths within the main Saturnian region of interest (7-9 R_S) to that of the Jovian ($\sim$6 R_J), it is immediately evident that field strength in the Saturnian system is much less than the Jovian. Consequently, the simulation run configured is able to use larger temporal steps and has less chance of becoming numerically unstable (see §5 & 6). Additionally, the smaller planetary radius of the body naturally increases the spatial resolution of the simulation due to the spatial step size being set as a denomination of this radius. Hence, the Saturnian system allows for more simulations to be performed, with longer simulated temporal lengths, therefore is preferential for the analysis performed.

With the system for experimentation determined, it is then necessary, following §5.4, to select other properties required for simulation configuration. The first property selected is that of the ion species of interest. For the ease of computational implementation all simulations performed within this analysis assume a single species plasma. Using the review of plasma sources in §2.2.2 it is determined that Enceladus is the main contributor, with the ions belonging to the water group (W^+). From this group, singular ionised oxygen is selected (O^+) as it has the same mass-charge ratio as doubly ionised sulphur (S^{++}), a main constituent in the Jovian system (see §2.2.1).

Next, the location of the domain is selected, with this already identified as 7-9 R_S, due to conditions in this region being highly susceptible to RI instabilities. Of course RI motions are thought responsible for the bulk transport of plasma from the inner to outer magnetosphere, therefore a small region is included above the identified sub-domain to ensure nothing specific within it is controlling the motions. For computational efficiency (i.e. allowing longer time-steps) a lower bound of 7.5 R_S is selected in the y-domain which

extends 2 R_S, placing the upper bound at 9.5 R_S. The x-domain is given a length of 1 R_S, ranging from 0-1 R_S. From this configuration it is possible to make a small angle approximation, determining the y-domain is aligned with the radial coordinate. Hence, moving in the positive y direction is approximately equivalent to moving radially outwards from the planetary body.

The selection of the number of spatial steps (and hence the spatial resolution) at this stage reflects that the motivation for it is often tied to computational reasoning rather than physical. This is because the number of spatial steps controls the number of grid cells and as the number of particles within the model is a function of the total number of cells, then the higher resolution the longer each temporal step takes to compute. However, using §1.2 it is seen that spatial steps should be equal to or smaller than an ion gyro-radii. It is determined that the ion gyro-radii of O^+ in the configured domain is $\sim 10^3$-10^4 km, therefore a selection of 0.01 R_S ($\sim 5 \times 10^3$ km) is made for the resolution in both spatial domains. This gives a grid of 200×100 cells.

The magnetic field is now specified as a simple dipolar field. The calculations that require a magnetic field strength when determining other parameters in the domain's configuration assume a worse case and hence utilise the highest value. This can be readily calculated using eqn 5.35 as $\approx$50 nT within the prescribed domain.

With the ion species identified and the maximum magnetic field strength obtained the temporal step size can now be specified, as accorded by eqn 5.36, with the ion gyro-frequency readily determinable as $\approx 0.3\ s^{-1}$. A simulation run is set to progress temporally through 1000 Ω_i^{-1}, which equates to $\approx$1 hr. Analysis performed in §3.3 found RI motions had a radial velocity of $\sim$100 km s^{-1}, hence it is permissible that two injections being transported by RI motions could travel across the simulated domain.

In order to populate the computational domain with particles both plasma density & β are required. To ensure the simulated results are physically accurate then the values used for these parameters are required to reflect those found within the prescribed region of the Saturnian magnetospheric system. Therefore, the use of observations, again mainly obtained by the Cassini mission, are utilised. Obviously these observations vary, hence are different each time spacecraft take measurements within the region, so values are determined from steady state models fitted to these observations, essentially providing physical quantities representative of the region at quiet periods.

The fitted models selected for use in this work are those provided by Wilson et al. (2017) & Persoon et al. (2020), with a selection of the profiles calculated shown in figure 7.1. Wilson et al. (2017) uses forward modelling to fit a range of parameters, whereas Persoon et al. (2020) uses a diffusive equilibrium model. However, the results obtained by both agree on the approximate values for the parameters of interest in steady state. It should be noted that when configuring JERICHO the centre position of 8.5 R_S is selected as being representative of the entire simulated region. Using figure 7.1a & b (top panel) the density of water group ions is found to be 3 cm^{-3}. Figure 7.1b (bottom panel) is used to determine a plasma β of 0.1.

It is noted that the values for density obtained here are in 3-dimensional space, whereas the magnetospheric plane constructed by JERICHO is 2-dimensional by definition. Therefore, when configuring the model parameters a selection could be made to specify the distance (or height) from the centrifugal equator to integrate into the plane. However, examining the model constructed in §4 & 5, it can be seen that no mechanism has been provided to control this height. Hence, a thin slice of the plasma sheet is simulated here, representing the region aligned exactly with the rotational & magnetic equators. The height of the simulated plasma sheet is therefore controlled by the dimensionality of the model equations, yielding a thickness of 1 m. It is determined, using experimentation later in this chapter, that the motions of interest observed in the simulation are independent

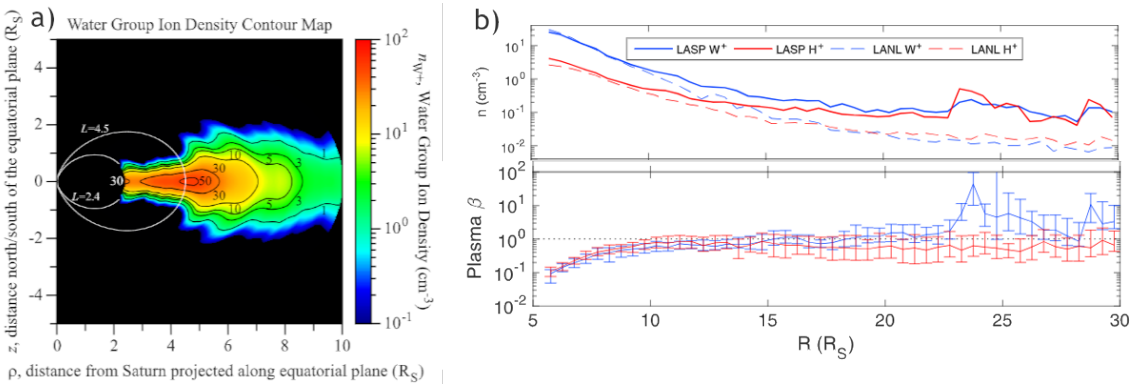

Figure 7.1: Profiles of plasma density and β as a function of radial distance in the Saturnian magnetosphere obtained using steady state modelling techniques to fit measurements made using in-situ spacecraft. a) is obtained by Persoon et al. (2020) using a diffusive equilibrium model and shows contours of water group ion density as both a function of radial distance and height from the equilibrium plane. b) is obtained by Wilson et al. (2017) using a forward modelling technique showing profiles of water group & hydrogen ion densities purely as a function of radial distance (top panel) and the profile of associated plasma β's (bottom panel).

of the magnitude of density gradient utilised (see 7.2.2). Therefore, this assumption is hypothesised to impact little on the analysis of RI motions and the conclusions drawn.

With the required physical parameters all now specified it is necessary to select remaining computational parameters, these in general are not intrinsically linked to the physical. The first of these is the number of macroparticles per grid cell, a value of 50 is selected for this as it was found to yield acceptable levels of errors in §6.2. The next is the amount of smoothing to be applied to the magnetic field, a value of $N_{NS} = 0.15$ (see eqn 5.30) is found sufficient for this work. This value is determined through the use of computational experimentation, rather than from Saturn's physical parameters. The amount of artificial smoothing is kept to the minimum needed to provide robustness within the simulations, in order to allow RI motions to transport magnetic flux through the system.

Following §5.4 all the parameters required for the configuration of the model domain are now specified, therefore the constructed region can now be populated by an initial distribution of macroparticles. These macroparticles use a uniform distribution in both spatial dimensions to statistically populate all grid cells. However it is noted from figure 7.1 that the density of the plasma varies significantly from 7.5-9.5 R_S. It is seen over this distance that density can be approximated as falling linearly with radial position and can be fitted by a power law of $-\frac{9}{2}$. Hence, the domain population is modified to scale the weights of the macroparticles using this determined relation based on their initial position within the simulated domain.

Macroparticle initial velocities are determined using from a Maxwell-Boltzmann distribution (constructed by utilising a set of normal distributions) in both spatial dimensions. Macroparticle mass is now a function of its initial position within the domain and temperature is obtained from the specified plasma β. The only additional parameter required to populate the velocity-space is the bulk flow velocity of the plasma in both dimensions, this is once again obtained using the profiles by Wilson et al. (2017). From these a flow velocity of 0 km s^{-1} is selected in the x-direction and 1 km s^{-1} in the y-direction. The selection of these bulk flow velocities is also beneficial in the analysis of the RI instability as it helps prohibit the induction of other instabilities such as the Kelvin-Helmholtz, as they ensure large scale velocity sheers are not included in an unperturbed configuration.

Finally, with the domain configured and populated it is required to specify what hap-

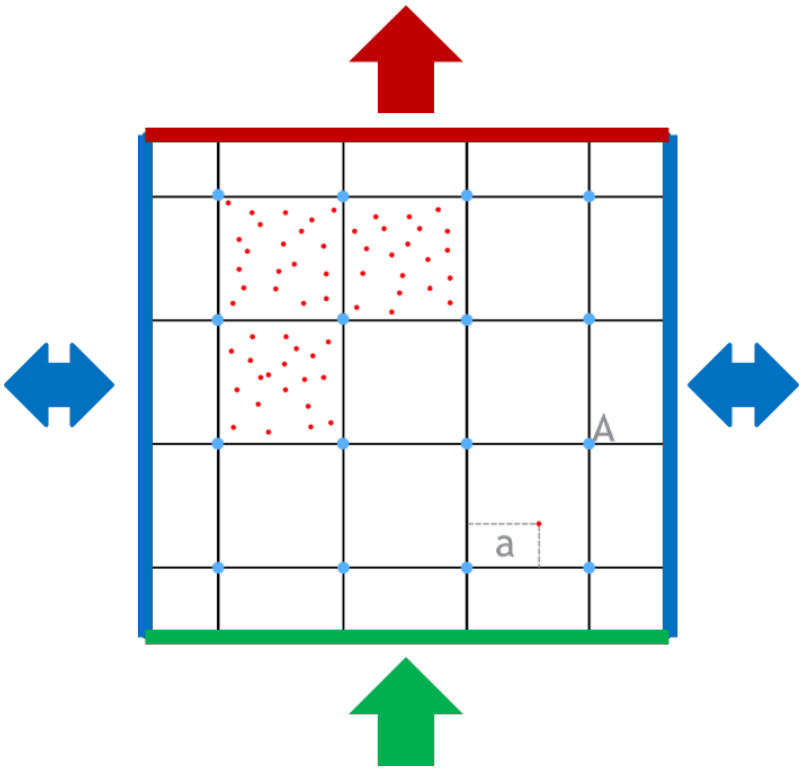

Figure 7.2: BCs utilised in the configuration of the simulation domain in which RI instabilities are examined. The grid with red particles in the centre represents the domain constructed by the model framework with coloured bars placed on the edges to indicate BC. The x_{min} & x_{max} (left & right) edges have periodic boundaries (blue), y_{min} (bottom) has an inflow (green) and y_{max} has an open (red). Coloured arrows represents the general flow of particles at these edges.

pens to the macroparticles (henceforth macroparticles are referred to as particles) and fields at the edges of the model domain. This is configured using the set of BCs described in §5.5. The simulations performed here utilise periodic boundaries on the x_{min} & x_{max} edges, inflow (source) at y_{min} and open at y_{max}. This can be seen summarised in figure 7.2. Essentially, this creates the skin of a cylinder with particles entering from the base and exiting from the top.

The inflow boundary at the y_{min} (bottom) edge of the domain emits particles (macroparticles with properties typical of 8.5 R_S) randomly distributed across the entire x-domain and over the distance of the first spatial step in the y-domain. In order to generate RI instabilities sufficiently large gradients in density are required (see §3.1), with the magnitude of these postulated as proportional to the rate of instability growth. Therefore, it is convenient to use this inflow boundary to introduce additional gradients into the simulated region. This is done by 'injecting' two regions of plasma an order of magnitude denser than the background between 0-200 Ω_i^{-1} & 400-600 Ω_i^{-1}. The source is set to enforce background densities, representative of the middle (8.5 R_S) of the domain, outside of these time intervals.

7.2 Simulation Results

Results from the simulation run configured as described in the previous section can be seen in figures 7.3, 7.4, 7.5 & 7.6 with these showing the ion charge distribution (q), electric field strength ($|\underline{E}|$), magnitude of current densities ($|\underline{J}|$) & induced magnetic effects (B_{z1})

respectively. Each figure contains 21 panels containing a snapshot of their associated simulated parameter at the time indicated above it. These panels span the entire simulated time period, 0-1000 Ω_i^{-1} (≈1 hr), spaced evenly throughout this time and separated by 50 Ω_i^{-1} (≈3 mins). A comparison of each of these parameters, with snapshots separated by 250 Ω_i^{-1} can be readily performed using figure 7.7.

Analysing figure 7.3 the evolution of the total ion charge distribution across the EM grid can be examined over the course of the simulated time period. It is worth noting that due to each temporal snapshot sharing the same colourbar for their contours, the initial gradient created by scaling macroparticles is not visible (at 0 Ω_i^{-1}) as the two later plasma injections overpower it. A cursory initial examination of the dynamics found in the 21 panels contained within the figure readily finds the two plasma injections, occurring between 0-200 & 400-600 Ω_i^{-1}. These can clearly be seen moving in the positive y-direction, which is recalled to be aligned with the radial direction, hence the injections propagate radially outwards. On both the leading and trailing edges of these injections, seen in this figure as areas of enhanced charge, are a number of instabilities.

By focusing analysis on these instabilities it can be determined that approximately the same number are formed on both the edges of both injections, this being $\sim 10^1$. These features grow in size as time progresses as the injected regions of increased density move radially outwards. Using the number of instabilities created on the leading & trailing edges (see figure 7.8) of the injected regions (1 R_S in width) it can be readily determined that the spatial scale associated with them is $\sim 10^{-1}$ R_S, matching exactly the scales determined using spacecraft observations (Azari et al., 2018). However, determination of the temporal scales associated with them is much more difficult to estimate, with the region of enhanced density moving out of the simulated domain whilst the instability is still developing.

It can be seen that these instabilities develop into large dense fingers interspersed with narrower channels of more tenuous plasma which appear to move into the injected region. It is also noted that if these channels of tenuous plasma are closed, then an island of more tenuous plasma is left inside the injected region continuing to move with it. This can be best seen in snapshots 550-750 Ω_i^{-1}, where a depleted island is created at approximately (0.25, 9.25) R_S and can be readily tracked through time as the simulation progresses. An overview of the described features developing over the course of a simulation run can be found in figure 7.8, the identified island is seen clearly in the snapshot at 650 Ω_i^{-1} along with a second developing island labelled. This behaviour matches closely to that reported in §3.3 & 3.4, with bundles of plasma from further in the magnetosphere are transported inwards, remaining coherent in the local background plasma. It is worth examining at this point how certain it is that the instabilities being observed within the simulation are RI.

Considering the instabilities associated with plasma flows of this nature (though a detailed review is outside the scope of this thesis) we find the Kelvin-Helmholtz (KH) and the Rayleigh-Taylor (RT) are most likely. Taking first the RT, this can immediately be discounted from consideration as the restoring force for it is gravity, a force omitted in the configuration of our model domain. Examining the KH it can be determined from the domain configuration that the instabilities on the leading and trailing edges of the injected regions develop without a velocity shear across their interfaces. Therefore, it is also possible to discount KH as the mechanism for their creation. The gaining of a bulk velocity (deflecting fingers left or right) occurs after the instabilities are triggered due to the induced magnetic effects (see figure 7.7).

Hence, by a process of elimination only the RI instability is left and must be responsible for the dynamics observed along these interfaces. This conclusion is re-enforced when it is recalled that centrifugal acceleration is acting across the domain, which is the driver for RI motions. It should also be noted here that it is postulated that the inclusion of a velocity shear along the interface between the injection region and background plasma

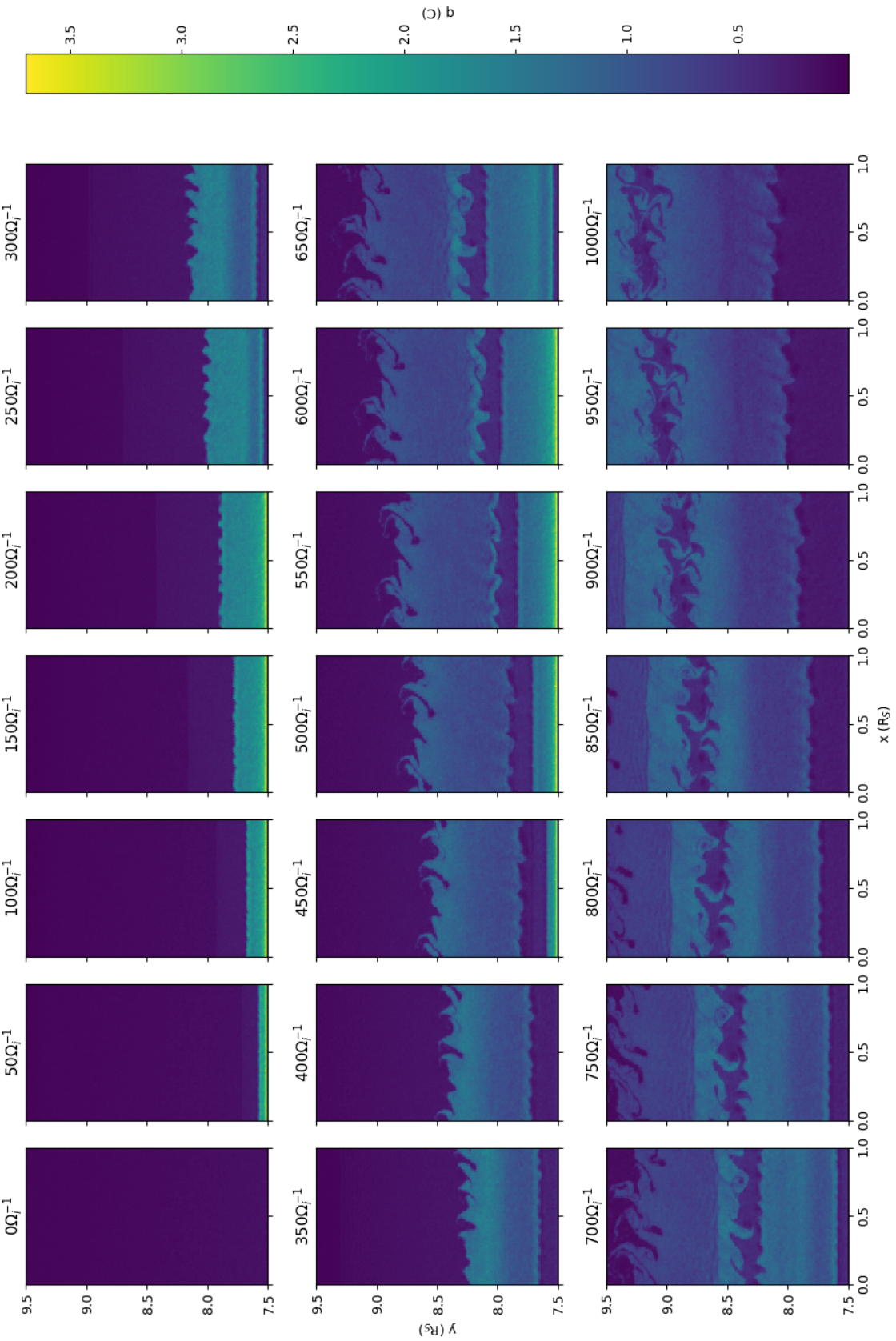

Figure 7.3: Evolution of ion charge distribution (q) within a 2×1 R_S domain placed at 7.5-9.5 R_S. 21 panels, separated by 50 Ω_i^{-1}, show snapshots of the charge distribution over the course of the simulated 1000 Ω_i^{-1} period. Over this period 2 plasma 'injections' are introduced from the bottom boundary and can be seen to move through the y-domain (radially outwards) inducing RI instabilities both on their leading and trailing interfaces.

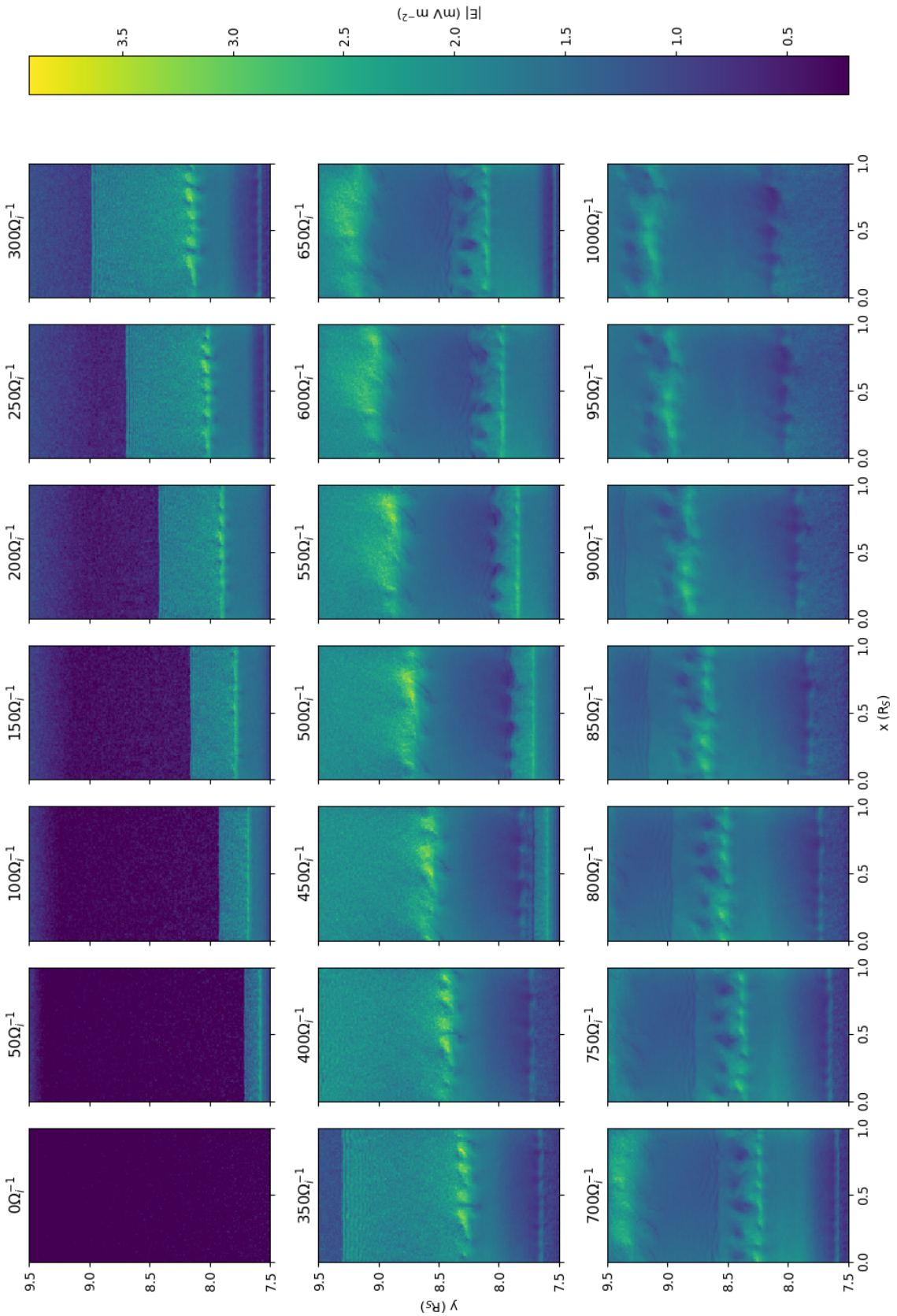

Figure 7.4: Evolution of electric field strength ($|\underline{E}|$) within a 2×1 R_S domain placed at 7.5-9.5 R_S. 21 panels, separated by 50 Ω_i^{-1}, show snapshots of the electric field strength over the course of the simulated 1000 Ω_i^{-1} period. The effects of two plasma 'injections' introducing RI instabilities on the electric field can be seen.

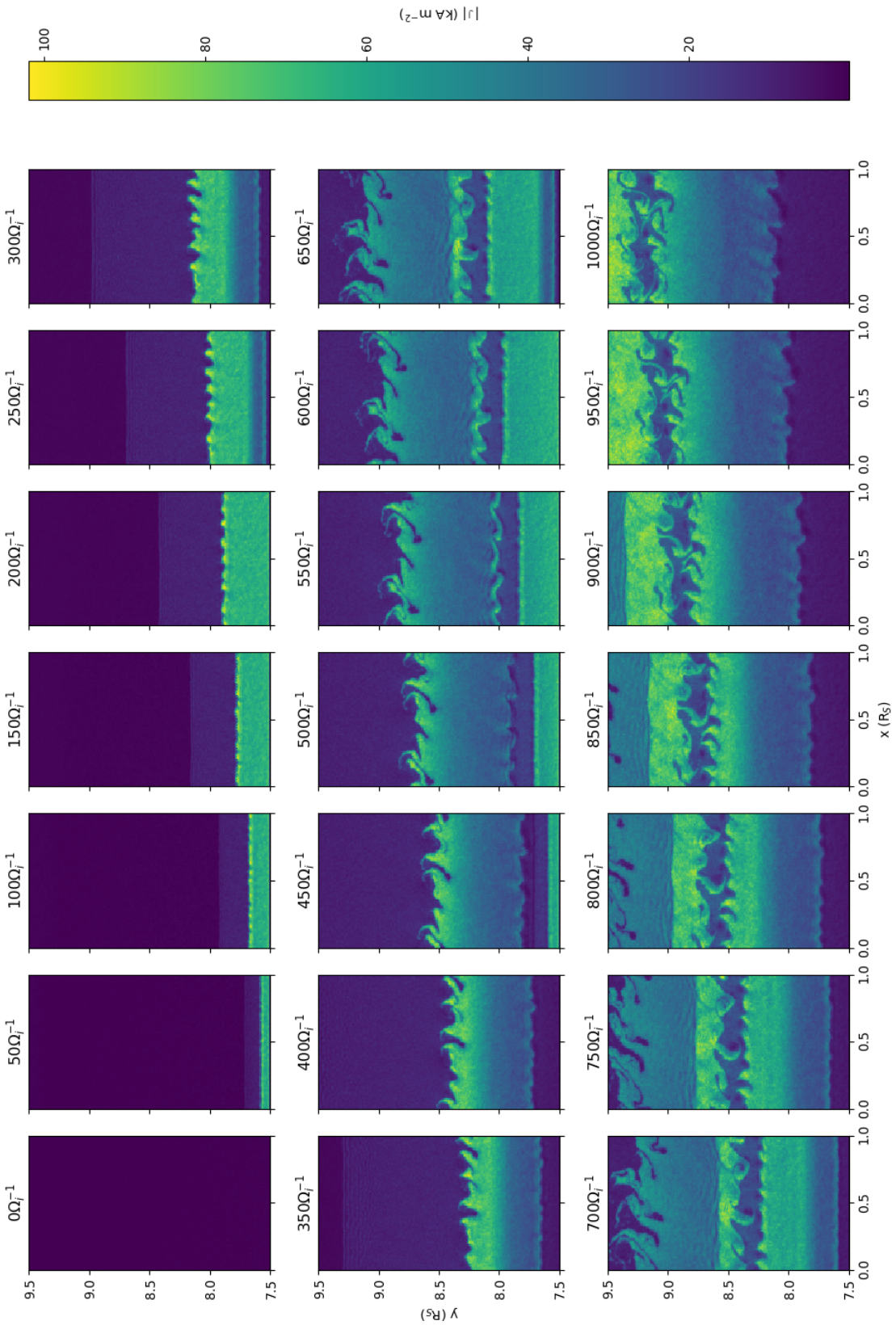

Figure 7.5: Evolution of the magnitude of current densities ($|\underline{J}|$) within a 2×1 R_S domain placed at 7.5-9.5 R_S. 21 panels, separated by 50 Ω_i^{-1}, show snapshots of the current densities over the course of the simulated 1000 Ω_i^{-1} period. The introduction of 2 plasma 'injections' from the bottom boundary can be seen to create RI instabilities on both the leading of trailing edges of these regions.

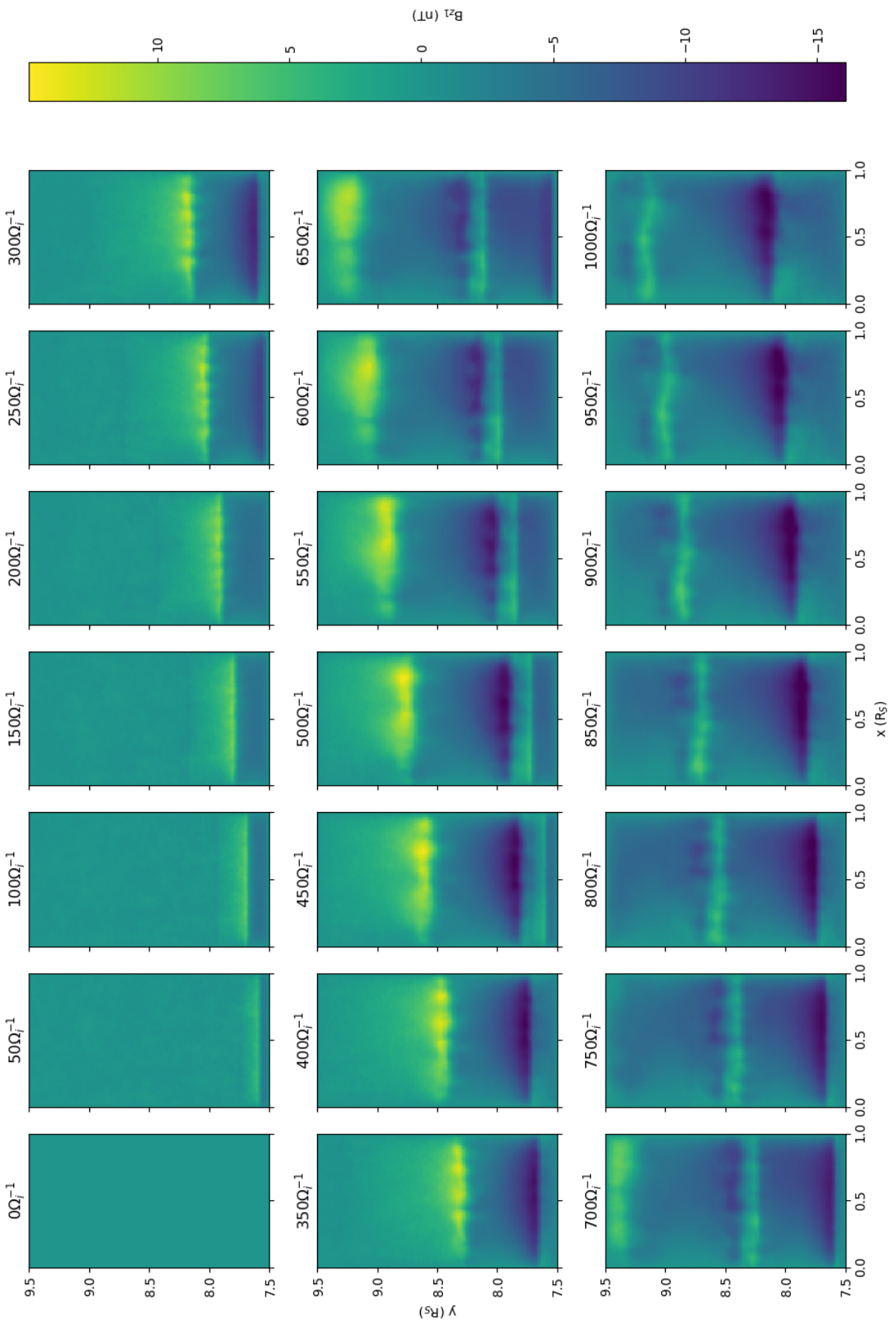

Figure 7.6: Induced magnetic effects (B_{z1}) within a 2×1 R_S domain placed at 7.5-9.5 R_S. 21 panels, separated by 50 Ω_i^{-1}, show snapshots of the perturbed magnetic field over the course of the simulated 1000 Ω_i^{-1} period. The effects induced by 2 plasma 'injections' introducing RI instabilities within the magnetic field can be seen.

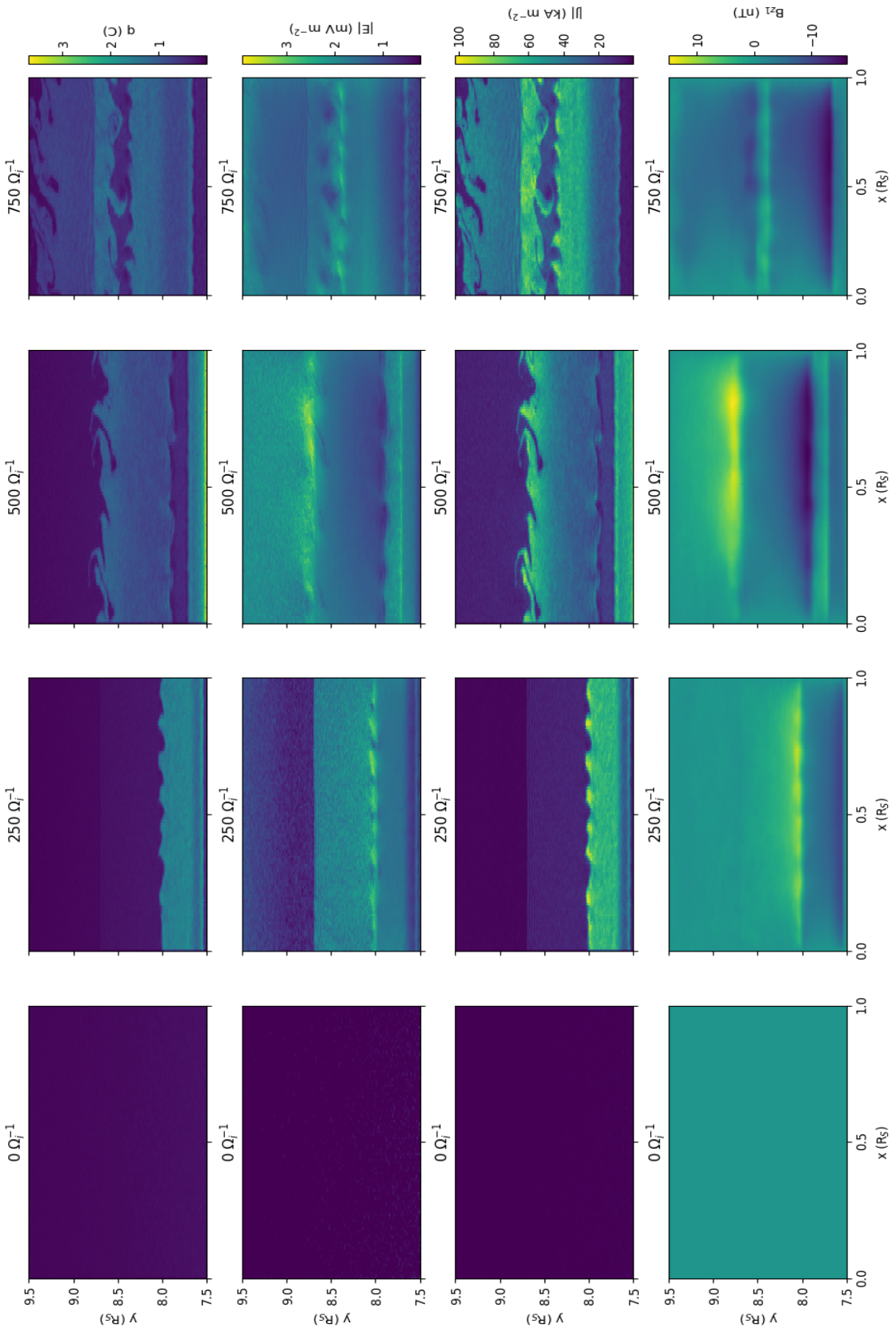

Figure 7.7: A series of snapshots at 0, 250, 500 & 750 Ω_i^{-1} for ion charge distribution, electric field strength, magnitude of current densities and induced magnetic effects taken from the simulation run contained within figures 7.3-7.6.

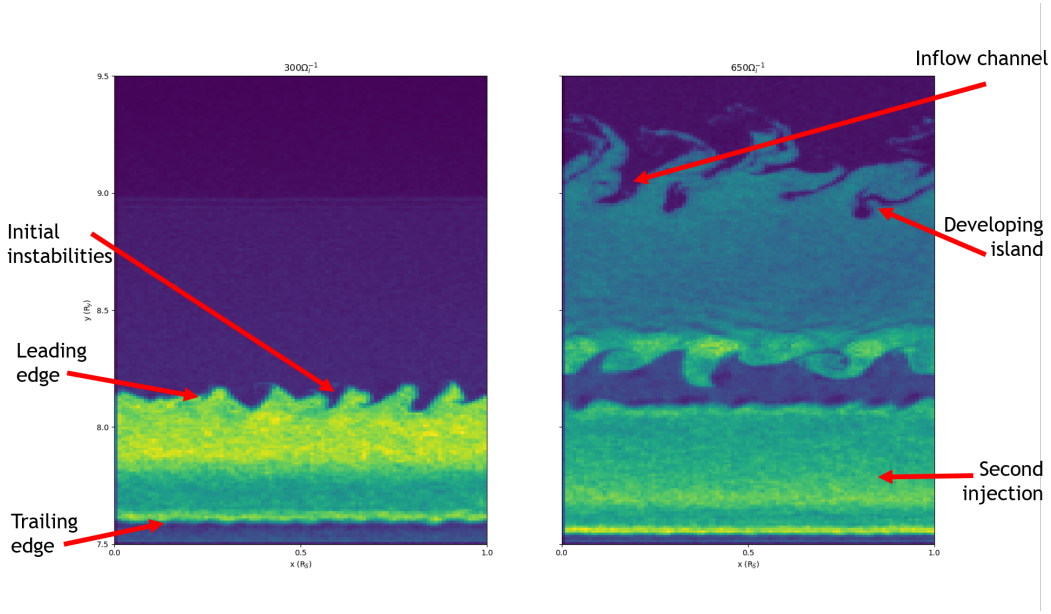

Figure 7.8: Two snapshots of ion charge distribution taken at 300 (left) & 650 (right) Ω_i^{-1} from the simulation run contained within figures 7.3-7.6. Key features related to the description of injected plasma region, as well as the developed RI motions are labelled.

will either act to enhance or damp RI inabilities depending the direction of this shear.

Analysing the evolution of ion charge distribution, combined with knowledge of domain configuration, it has been possible to examine RI motions developing on the leading & trailing edges of two plasma injections. However, there remain features in the simulation that are better examined using other modelled parameters. From this it is determined that the ion charge distribution is the parameter in which pure RI motions are best seen. Hence, when performing a parameter survey to understand what controls these motions the ion charge distribution is the simulated parameter selected for examination.

Figure 7.4 shows the evolution of electric field strength over the simulated 1000 Ω_i^{-1} period. RI motions are much less visible in the electric field, with their effects more evident than the motions themselves. These effects can be seen as regions of enhanced or depleted field strength moving along an injection's interface, growing in size as the instabilities develop, the mechanism associated with these can be seen in figure 7.9. These are most clearly observed in panels containing temporal snapshots of 700 Ω_i^{-1} onwards and can be seen to reach a characteristic spatial scale of $\sim$0.1 R_S in the x-domain. This supports the spatial scale of the instabilities inferred from motions in the ion charge distributions, noted once again to align with values determined using spacecraft measurements.

The feature best visible using the electric field strength is that of a region of the enhanced field strength that propagates radially outwards, ahead of plasma injection, with a velocity of $\approx$90 km s^{-1}. This feature is also seen in the other parameters shown, though barely visible in the ion charge distribution and induced magnetic effects. The physical interpretation of the propagating enhancement is that it is a shock front associated with the sudden introduction of a dense plasma injection, this front represents the speed at which the modelled background plasma can reorganise itself in response to the injection. The precise physical mechanism that is responsible for the generation of this front is yet to be determined, though it appears linked to magnetic field strength in some way. It should be noted that the second injection also introduces a front of enhanced field strength, but its propagation speed is substantially slowed once it encounters the first injection region, though whether this is linked to the increased plasma density of the region or the reduced

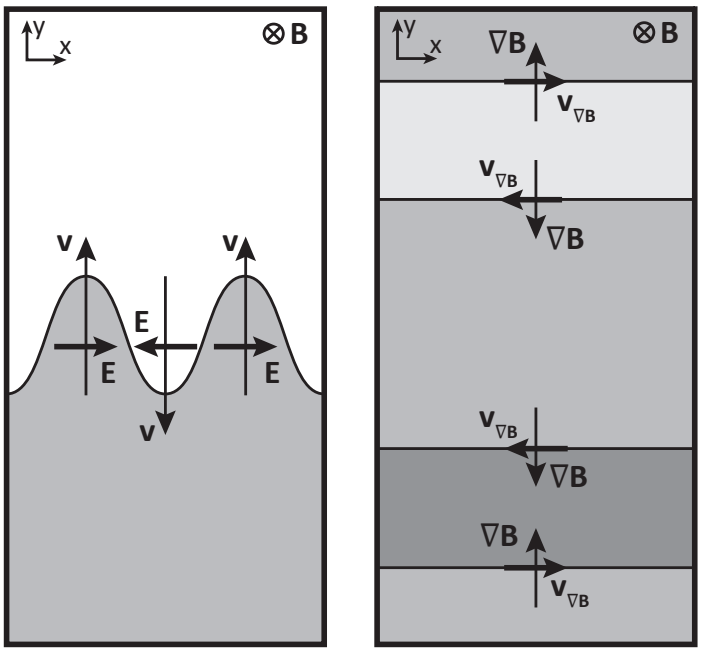

Figure 7.9: Sketch of how plasma dynamics associated with developing RI motions effect EM fields, domain & magnetic configuration can be seen at the top of the panels. On the injection interface (left) it can be seen how the development of plasma fingers with channels in-between create oppositely directed electric effects. The deflection of the fingers on the leading & trailing edge (right) is caused by drifts induced by gradients in the magnetic field. Credit: Arridge and Wiggs.

magnetic field strength along its trailing edge is unknown.

However, figure 7.5, the magnitude of current densities, shows the interaction between the propagating front and the first injected region better than the the electric field. Panels 700-900 Ω_i^{-1} clearly show this enhancement propagating through the first injected dense region, with longitudinal waves created in the plasma ahead of it, though these appear to be at the grid resolution. What is also clearly shown by the current densities is the spreading of the second injected region in the y-domain as it moves radially outwards. This behaviour is attributed to the plasma within the injected region possessing a higher number density and hence a higher thermal (plasma) pressure. Therefore, the injection spreads over time to minimise this pressure gradient as would be typically expected.

Focusing analysis back to the motions of interest, RI instabilities, these can clearly be seen to form on the leading and trailing edges of the plasma injections with their structure matching exactly those seen in the ion charge distributions (as is expected). However, the features better seen using the current densities are narrow channels of high density plasma at the tips of the dense plasma fingers formed. What is interesting about these is as they exit the region of induced magnetic effects, which give the interface a flow direction in the x-domain, they are swept back from the finger, reminiscent of spray off the crest of a wave. This can be best seen at the leading interface of the first injection in panels 600-700 Ω_i^{-1}.

Finally, the induced magnetic effects can be examined in figure 7.6. It should be noted that since only first order effects are shown the dipolar structure of the background field is omitted. The key feature that is observed in the magnetic effects is a region of enhanced field strength that is created at the top of the leading interface edge, which is closed by a region of depleted field strength at the bottom of its trailing edge. The gradients

introduced by these effects induce a bulk flow velocity in the x-domain, deflecting the created RI fingers to the left and right of the simulated domain.

Using figure 7.9 it is possible to examine the exact configuration of these induced drift motions. The fingers created on the leading edge move into regions of enhanced field strength, hence experiencing a positive gradient in the y-domain. This induces $\nabla\underline{B}$-drift motions, deflecting the fingers as indicated in the figure. Interestingly, the spray of high density plasma at the tips of the fingers moves through the peak of this gradient and into an oppositely oriented magnetic gradient, causing the swept back configuration observed using the current densities. Conversely, the fingers on the trailing edge move into a region of decreased field strength, hence gaining a bulk drift motion in the opposite direction. The combination of these drifts lead to what appears to be a turning motion of the injected plasma region.

It is noted that in the Saturnian system the magnetic field is in the $-z$ direction. Therefore, the positive induced field effects would represent a decrease in field strength and negative effects would act to enhance field strength. However, the drifts indicated in figure 7.9 would remain unchanged as both the magnetic field & the field gradients would switch directions, making the deflection observed identical in either field configuration.

A process yet to be discussed is mixing of plasma from the first and second injections most visible in the current densities (figure 7.5) and which also impacts the induced magnetic effects (figure 7.6). This is best seen in panels 900 Ω_i^{-1} onwards at the top of the simulated domain and causes the dense plasma fingers to be deflected back towards the region they originated from, trapping narrow regions of depleted plasma. The notable impact of this on the induced magnetic effects is the bending of initially straight field enhancements/depletions to create a more wave-like structure. Although outside the scope of the current question, this region might be most comparable to the postulated region above the Io plasma torus (see §3.1) where RI motions are generated by a randomly varying source, creating inevitably a very mixed, turbulent environment.

7.2.1 Links to Domain Resolution?

A notable omission from the configuration of the interface upon which the RI instability is triggered is that of the perturbation utilised to initiate it. This is because rather than artificially impose some function across it, it is found that the perturbations generated by the use of the EM grid are sufficient to trigger these motions. Therefore, it can be determined that the length scales associated with the perturbation which allows the instabilities to be generated is the spatial resolution of the underlying EM grid (i.e. 10^{-2}).

The question that follows this assertion is '*are the spatial scales of the generated RI motions intrinsically linked to the resolution of the EM grid?*' This can be tested by varying the resolution of the grid specified upon initial construction of the domain (200×100). This resolution is increased by a factor of 2.5 in both spatial dimensions to yield a new grid consisting of 500×250 cells, other than this all other parameters are held constant. The results from this simulation can be examined in figure 7.10. It should be noted that as the parameter examined is total ion charge distribution, the scale of the colourbar has changed due to this being spread over more grid vertices, but the bulk density of the plasma utilised is unchanged.

Examining the motions observed in figure 7.10 it can be seen that initial interchange motions do begin on much smaller spatial scales, however closer inspection determines behaviour that was not found in figures 7.3-7.6. This is the coalescence of the instabilities formed into structures with much larger spatial scales associated than those of the initial motions. This can be seen on the leading and trailing edges of both of the plasma injections, however it takes almost the entire radial distance (and hence simulated time) for the motions to reach their maximum length and hence we do not get to see the motions of

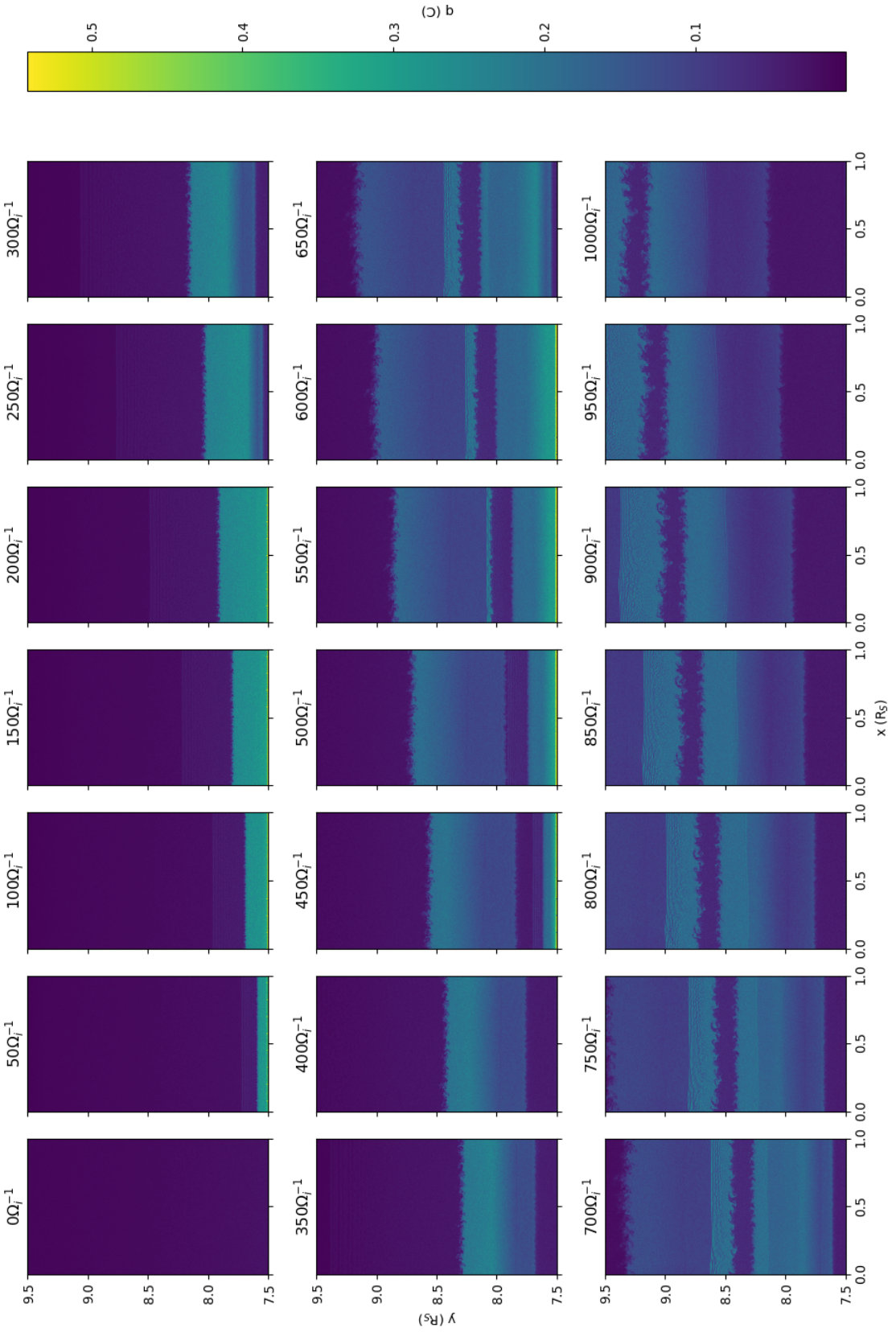

Figure 7.10: Evolution of ion charge distribution (q) within a 2×1 R_S domain placed at 7.5-9.5 R_S utilising an increased spatial resolution of 500×250 cells. 21 panels, separated by 50 Ω_i^{-1}, show snapshots of the charge distribution over the course of the simulated 1000 Ω_i^{-1} period. RI motions are triggered on the leading and trailing edge of plasma injections.

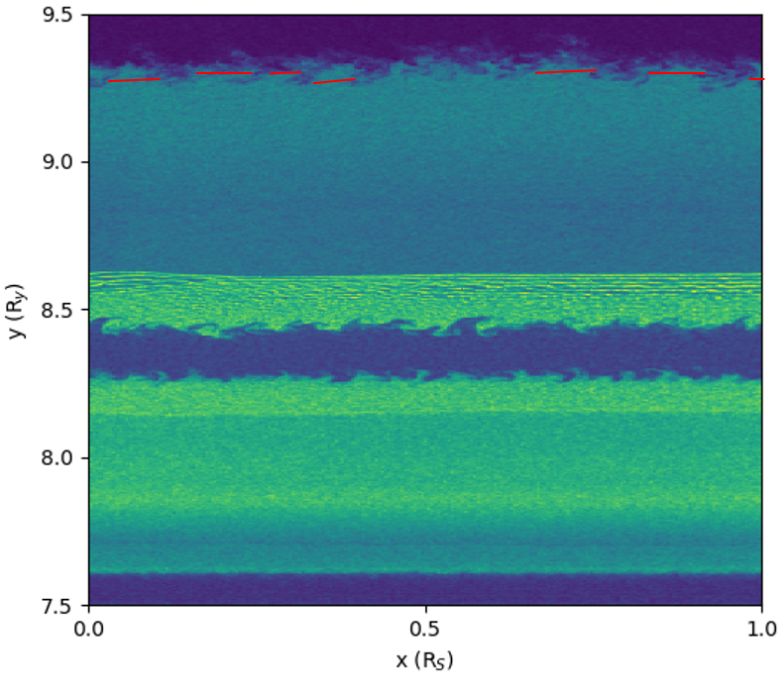

Figure 7.11: Ion charge distribution at 700 Ω_i^{-1} taken from simulation performed in figure 7.10. Red lines highlight the large scale structures that smaller scale RI motions are coalescing into, found to be on length scales of $\sim 10^{-1}$ R_S.

these larger scale structures in the simulation.

Figure 7.11 contains a single snapshot of the ion charge distribution from the simulation presented in figure 7.10 at 700 Ω_i^{-1}. Within this snapshot coherent structures formed of coalesced RI instabilities are determinable, and have been highlighted using red lines. There are found to be $\sim 10^1$ structures with spatial scales of $\sim 10^{-1}$ R_S. These larger instabilities formed do not have chance to evolve from their initial stages before exiting the top of the simulated domain. However, their form mirrors that observed in panels 150-200 Ω_i^{-1} in figure 7.3, giving confidence that the dynamics being examined are functions of the physical parameters utilised when configuring the domain, rather than simply an artefact of grid resolution.

7.2.2 Parameter Survey

It has been shown to this point that JERICHO is capable of producing RI motions, which upon examination are found to have spatial scales that align exactly with those observed by spacecraft in the Saturnian magnetosphere. This is expected as the simulation domain utilised has been configured with physical parameters taken from these spacecraft measurements, therefore it is not surprising that the spatial scales induce also match these observations (though it is reassuring that the model is physically accurate). However, this does not allow one to determine which of these parameters is most important in controlling the scales associated with induced RI motions.

In order to determine which parameter RI motions are sensitive to, and answer the second part of our science question '*and which local plasma parameters control these*', key parameters can be systematically varied. A vast range of physical parameters are selected and tuned when configuring the model domain, hence it is sensible to revisit the review performed in §3.1 to focus the search to variables the instability is known to be related to. The two parameters that are immediately apparent from the instability criterion (eqn

3.7) are that of magnetic field strength and plasma density, therefore these are selected for analysis.

Strength of Planetary Magnetic Field

Initially the magnetic field is selected for variation in order to perform the described parameter survey. This is done by simply applying a multiplier to the equatorial planetary field strength such that,

$$B_{eq,sim} = \mathcal{K} B_{eq,P}, \tag{7.1}$$

where $B_{eq,P}$ is the scaled field strength used in configuration of the varied simulated domain and $\mathcal{K}$ is the scaling factor. The magnetic field is perhaps the most important physical parameter when configuring a domain in JERICHO, with many other parameters calculated as a function of maximum component of the field (see §5.4). However, the two properties most important for consideration to the analysis performed here are the plasma β and the temporal resolution.

The plasma β is important to consider when performing this examination as its value is indicative of the parameters controlling plasma dynamics within the simulation. Therefore, a significant change in this value would represent a shift of controlling physical properties in the simulated domain, with the results obtained difficult to directly compare. However, this problem is avoided as the model configuration uses the (ion) plasma β as a selected parameter when configuring itself, therefore we can be sure that the same physical parameters should be control plasma motions.

Temporal resolution (or time step) is obtained directly by using particle gyro-frequency. Since the same particles are used in each simulated domain, it can be seen that temporal resolution of the model also becomes scaled by $\mathcal{K}$. In the survey performed scaling factors of 0.5, 1.5 & 2 are utilised, therefore at 1000 Ω_i^{-1} the maximum run times of associated simulated domains will be ≈2 hrs, ≈0.75 hrs & ≈0.5 hrs respectively. A reasonable question at this point is to the selection of relatively small scaling factors for the magnetic field, this is for reasons of computational efficiency as it recalled that the model is most sensitive to changes in magnetic fields.

Figure 7.12 shows the evolution of ion charge distribution with a field strength scaled by a factor $\mathcal{K} = 0.5$, associated with a maximum simulation time of ≈2 hrs. Two injections of dense plasma regions can be seen at 0-200 Ω_i^{-1} & 400-600 Ω_i^{-1}, with these injected regions seen to move radially outwards at approximately the same rate (in terms of Ω_i^{-1}) as in an unmodified magnetic field, this can be attributed to the fixed plasma β. Therefore, it is found possible to compare all simulations performed with varied field strength directly using Ω_s^{-1} rather than need to converting back into real time.

Examining the dynamics observed in figure 7.12 it can be found that although spontaneous perturbations are once again found to occur on both the leading and trailing edge of both plasma injections, the induced instabilities appear to experience less growth. However, it is found on all edges that the spatial scales of the induced instabilities are once again on the order of 10^{-1} R_S. Specifically analysing the instabilities on the leading edge of the first plasma injections, the general form of the RI motions appears to be the same. It is clear once again that both large fingers of dense plasma are formed, interspersed with narrow channels of more tenuous plasma between.

Figures 7.13 & 7.14 correspond to equatorial planetary fields scaled by $\mathcal{K} = 1.5$ & $\mathcal{K} = 2.0$, giving them maximum run times of 0.75 & 0.5 hrs respectively. The analysis of the simulations performed in these is joined due to the remarkable similarity in the results observed in them. Though it should be noted that upon close inspection small differences are found between them, such as increased drift in the x-direction in figure 7.14 due to higher field strengths.

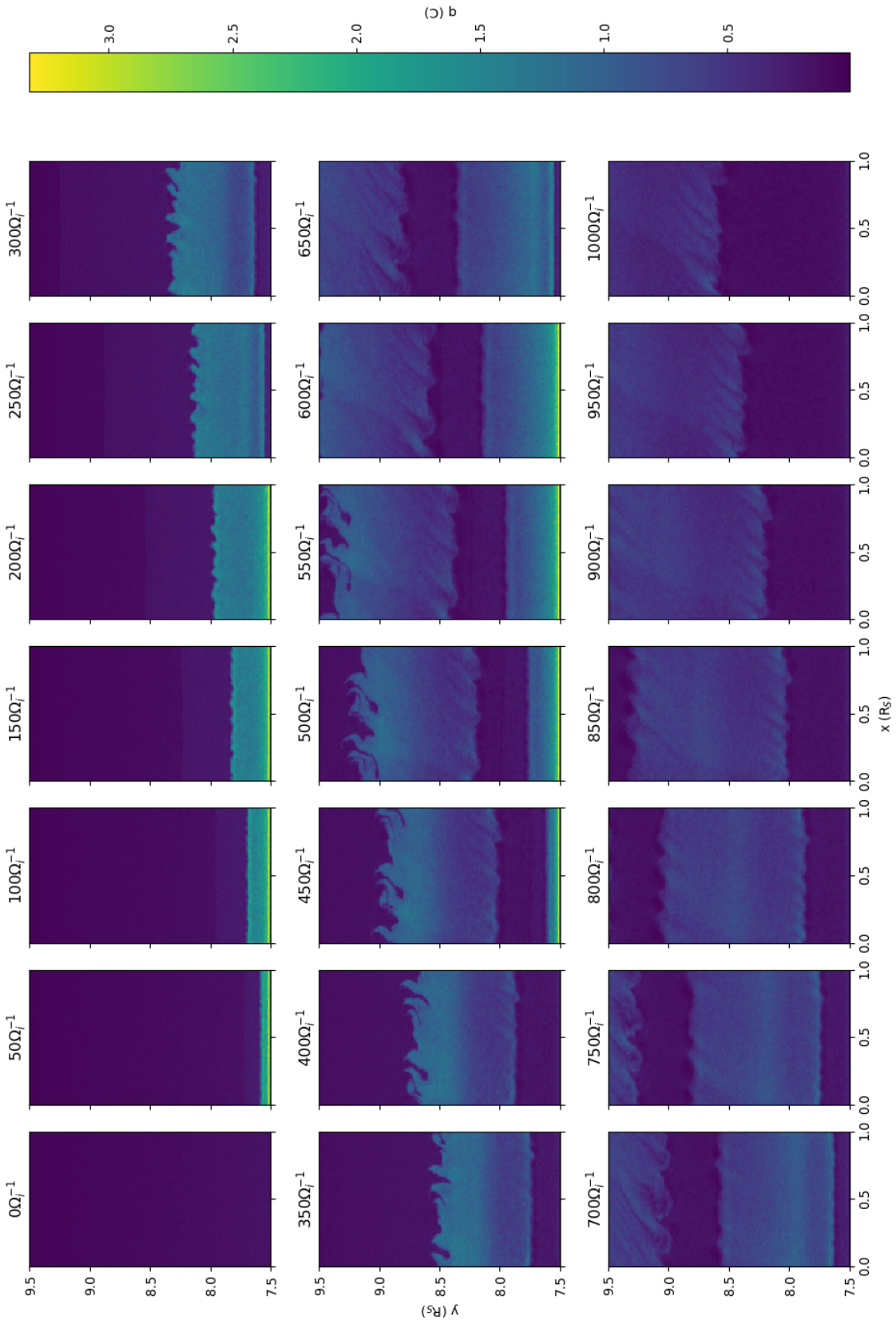

Figure 7.12: Evolution of ion charge distribution (q) within a 2×1 R_S domain placed at 7.5-9.5 R_S with the planetary dipolar field strength modified by a factor of $\mathcal{K} = 0.5$. 21 panels, separated by 50 Ω_i^{-1}, show snapshots of the charge distribution over the course of the simulated 1000 Ω_i^{-1} period, equating to ≈2 hrs.

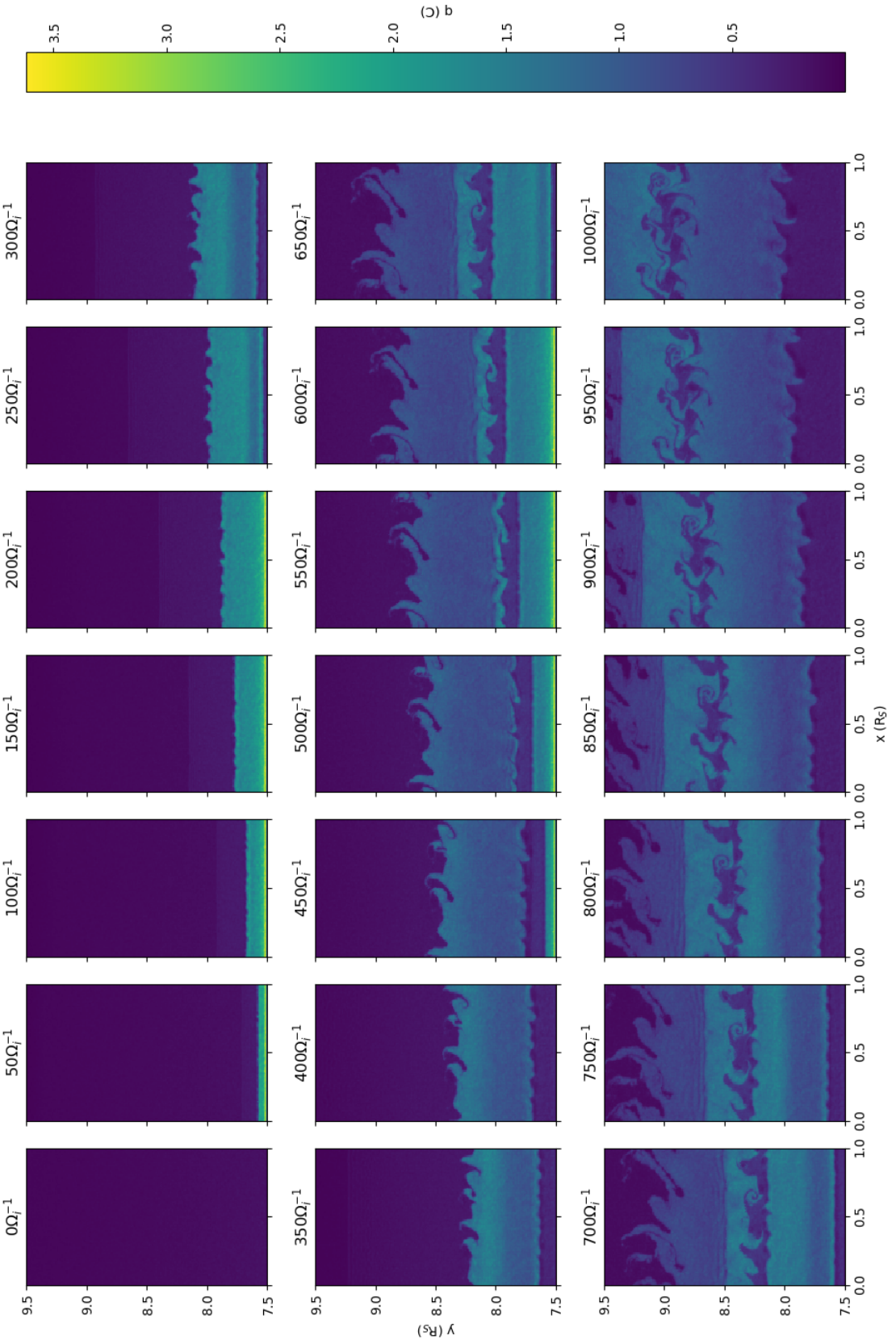

Figure 7.13: Evolution of ion charge distribution (q) within a 2×1 R_S domain placed at 7.5-9.5 R_S with the planetary dipolar field strength modified by a factor of $\mathcal{K} = 1.5$. 21 panels, separated by 50 Ω_i^{-1}, show snapshots of the charge distribution over the course of the simulated 1000 Ω_i^{-1} period, equating to ≈0.75 hrs.

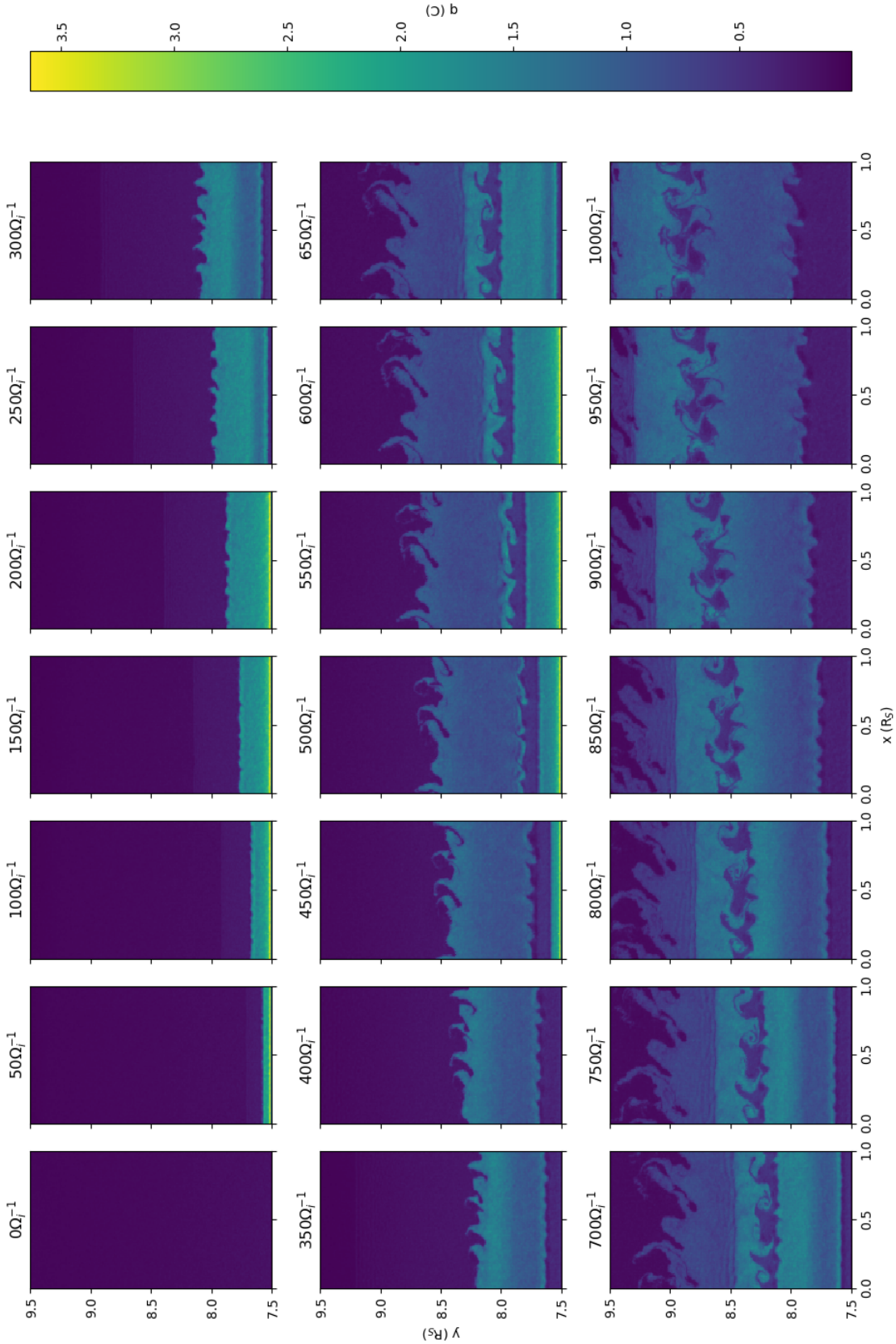

Figure 7.14: Evolution of ion charge distribution (q) within a 2×1 R_S domain placed at 7.5-9.5 R_S with the planetary dipolar field strength modified by a factor of $\mathcal{K} = 2.0$. 21 panels, separated by 50 Ω_i^{-1}, show snapshots of the charge distribution over the course of the simulated 1000 Ω_i^{-1} period, equating to ≈0.5 hrs.

Examining the key features present in these two simulations it is once again found that instabilities spontaneously occur on both the leading and trailing edges of both plasma injections. The spatial scales associated with these is once again found to be 10^{-1} R_S, though it is noted that parameters have now been varied from those obtained from spacecraft measurements. Large fingers of dense plasma are formed with narrow channels of tenuous plasma between. Mixing between the first and second plasma injections is more developed in these simulations, the dense fingers change directions multiple times, creating spirals in the tenuous channels. From this overview it is clear that all the features present in the domain configured with an exact Saturnian field strength are also present in these modified simulations.

However, as previously noted it is the similarity between the simulation results in figures 7.13 & 7.14 that is striking. The solutions produced within the modelled domains are almost exactly the same, with the locations only modified by the rate of drift in the x-domain. Therefore, it is possible to conclude the simulations contain RI motions that have converged on a set of solutions that are unmodified in form by the magnetic field strength. However, the rate at which this solution is reached (i.e. the growth rate of the RI instabilities) changes with field strength, leading to the hypothesis that RI growth rate is enhanced by stronger magnetic fields in the magnetosphere.

It is noted that the magnetospheric plane utilised configured for use here are not linked to an ionospheric plane. Following Southwood and Kivelson (1989) this means that the solutions determined by the simulations performed represent a maximum in terms of the growth rate of RI instabilities, with inclusion of ionospheric effects acting to retard these. Examining the growth rate obtained within their analysis (see eqn 3.9) it was determined that the rate is inversely proportional to the magnetospheric magnetic field strength, the opposite of this is found in the simulations contained within figures 7.13 & 7.14. However, it is not possible to construct any definite conclusions from the two data points represented from these simulations. Therefore, a much larger parameter survey, and more advanced tools for the analysis of the results contained within, is required before it is possible to definitely conclude a direct proportionality between field strength and RI growth rate within JERICHO.

Density of Plasma Injected by Source

The second parameter in the simulation configuration that is identified as potentially controlling the spatial & temporal scales of RI motions is that of the density gradient between the local background medium and the injected dense plasma region. Therefore, this gradient is varied by modifying the density of the injected plasma region by both enhancing and reducing its value. The method selected for creating these variations is the modification of the total number of fresh particles (macroparticles configured with properties representative of 8.5 R_S) introduced at the inflow boundary. The number of fresh particle is altered once again using a coefficient, $\mathcal{L}$, which is varied in each simulation run. The density of the plasma contained within the injected region ($\rho_{sim,inj}$) can be calculated using,

$$\rho_{sim,inj} = \mathcal{L}\rho_{inj}, \tag{7.2}$$

where ρ_{inj} is the density of the region used in the simulation contained within figures 7.3-7.6.

All other parameters used in model configuration are unaltered from those initially determined. It should be noted that unlike the previous survey in which magnetic field strength was varied, which changed the parameters calculated using it (such as temporal resolution), there are no domain parameters dependent on the density of the injected regions. This means the simulated region through which the injection propagates are exactly

the same and the simulation results are by their nature directly comparable between model runs. It should also be noted that for the same reason much more dramatic modifiers can be utilised to vary the injection densities than to alter the magnetic field strength.

Figure 7.15 contains the ion charge distributions corresponding to a simulation run in which the injection density has been decreased by a factor of $\mathcal{L} = 0.5$. The dynamics within this simulation are very similar to these seen in the unmodified configuration with the $\approx 10^1$ instabilities forming on both the leading and trailing edges of the two injections. The instabilities grow at a comparable rate though the fingers of dense plasma appear narrower with the tenuous channels wider.

There are two noticeable differences which are unrelated to the RI motions within this simulation run. First, the injection region spreads less over the course of the run. The reason for this bulk motion of the injection has already been identified as the increase in thermal pressure. Hence, the lower density in the injections compared to those previously utilised corresponds to a smaller thermal pressure gradient, and therefore the particles comprising the plasma regions are slower to act to minimise them. The second difference is in the interaction of the shock front induced by the second plasma injection with the first. This front can be seen to move through the first injected region substantially quicker than in the initial simulation configuration. This suggests that the physical mechanism responsible for its propagation is in some way dependent on the density of the region it is moving through.

Returning focus to the motions of interest to this work, the simulations contained within figures 7.16 & 7.17 can be analysed together. These both correspond to simulations with enhanced densities in the plasma injections, with these scaled by factors of $\mathcal{L} = 5.0$ & $\mathcal{L} = 10.0$ respectively. Unlike the previous survey these are not analysed together due to their inherent similarity, but rather due the dynamics contained within diverging substantially from these observed in the initial configuration. It can be seen that the injected plasma regions spread much more rapidly, inhabiting almost the entire simulated domain before moving out of it.

The reason for this is once again linked to the magnitude of the thermal pressure inside the plasma injections. Using the definition of the plasma β it is found that varying the number density within the injection also varies this parameter, with the simulations contained within figures 7.16 & 7.17 changing it to such an extent that the controlling parameters within them are altered. Hence, the dynamics of motions created by these injections are found to be more closely related with thermal (plasma) pressure rather than magnetic, making it difficult to interpret and compare the results obtained.

However, it is noted that despite the modification of the controlling dynamics over the injected regions motions, a series of instabilities are formed along both the leading and trailing interfaces of the injections. Once again these are found to have spatial scales of $\sim 10^{-1}$ R_S, though the growth and evolution differ due to the reasons identified. It is therefore difficult to draw a conclusion on whether the density gradient modifies the temporal scale of RI motions, however it is determined that it does not modify the spatial scales associated with the RI instabilities induced.

7.3 Discussion & Summary

Utilising a series of simulations, configured for the Saturnian magnetosphere, evidence has been presented that these simulations can produce RI motions within their runs and determine properties relating to the spatial and temporal scales of these induced instabilities. The model domains were placed between 7.5-9.5 R_S, a region selected due to spacecraft observations determining a peak in observed RI events at this distance. The domains were initialised with physical properties obtained to represent the typical values of this region

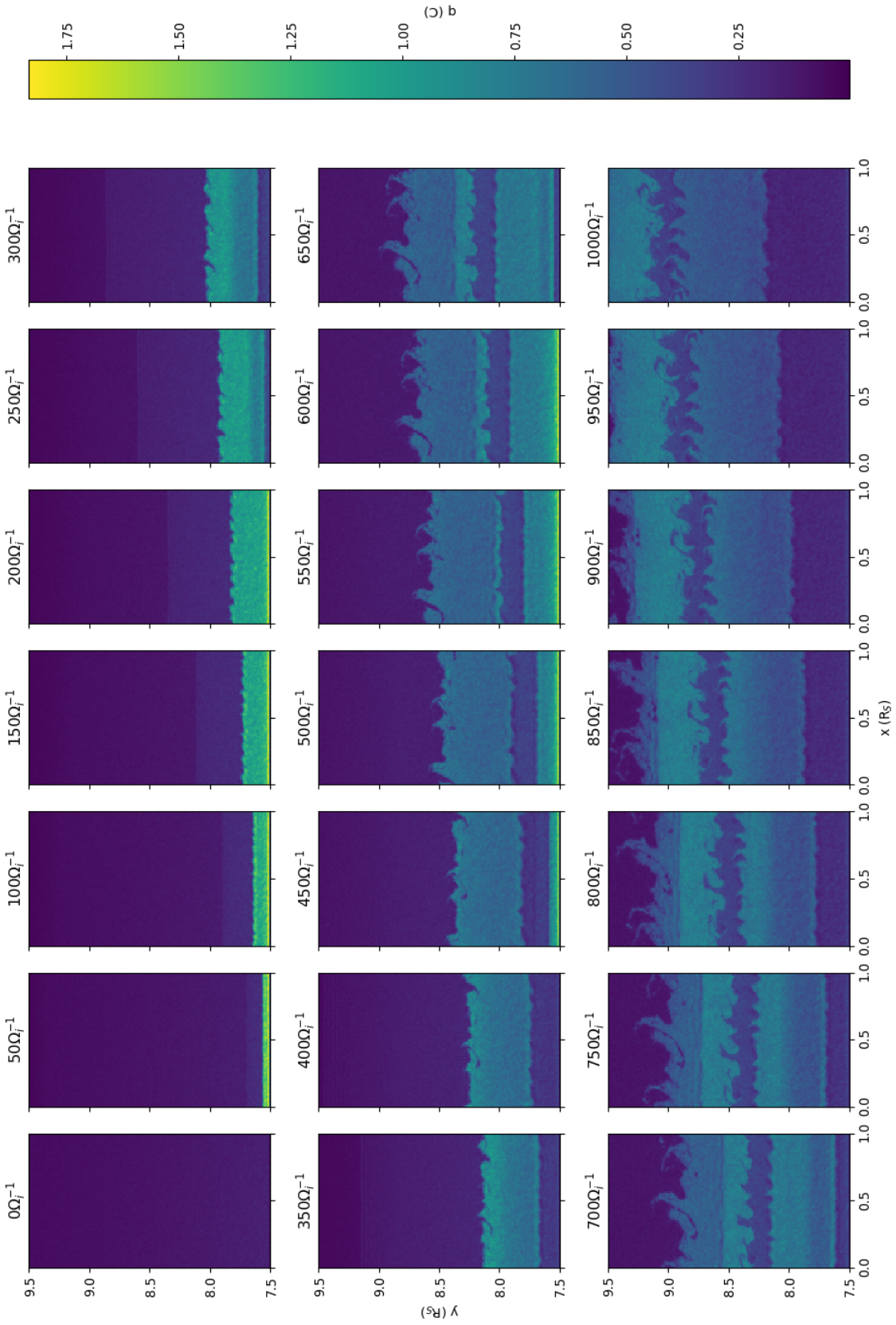

Figure 7.15: Evolution of ion charge distribution (q) within a 2×1 R_S domain placed at 7.5-9.5 R_S with the density of plasma injections at 0-200 & 400-600 Ω_i^{-1} decreased by a factor $\mathcal{L} = 0.5$. 21 panels, separated by 50 Ω_i^{-1}, show snapshots of the charge distribution over the course of the simulated 1000 Ω_i^{-1} period.

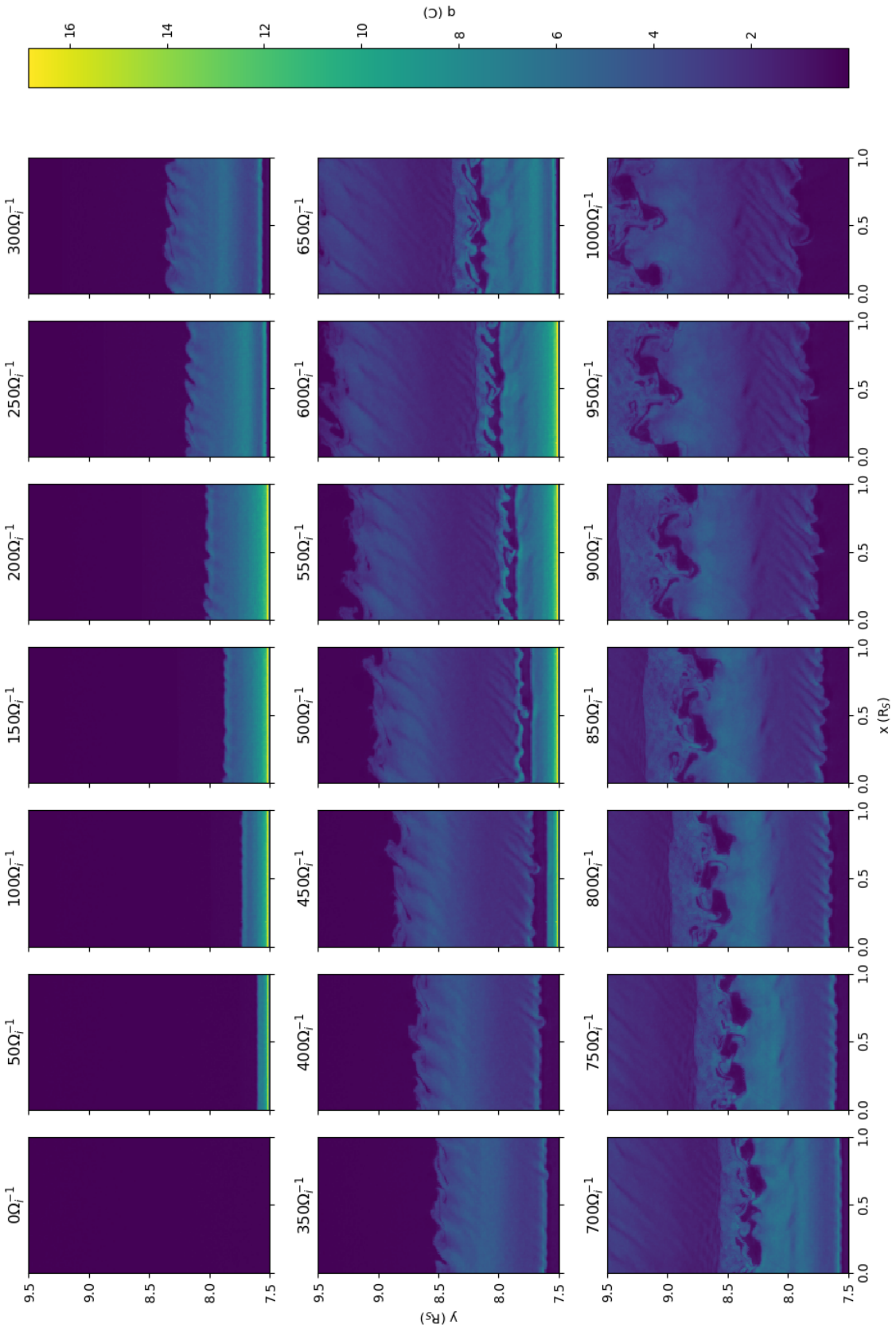

Figure 7.16: Evolution of ion charge distribution (q) within a 2×1 R_S domain placed at 7.5-9.5 R_S with the density of plasma injections at 0-200 & 400-600 Ω_i^{-1} increased by a factor $\mathcal{L} = 5.0$. 21 panels, separated by 50 Ω_i^{-1}, show snapshots of the charge distribution over the course of the simulated 1000 Ω_i^{-1} period.

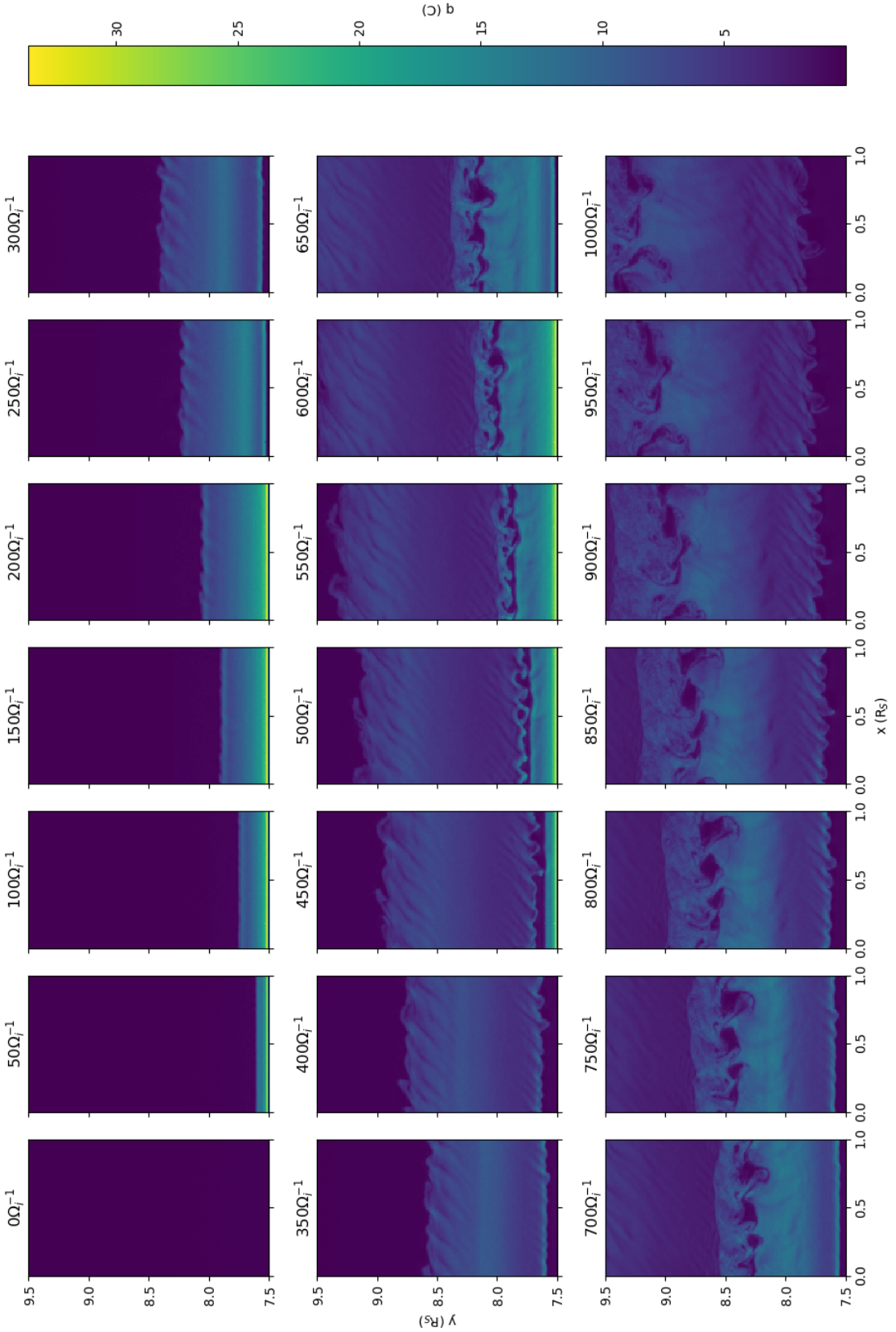

Figure 7.17: Evolution of ion charge distribution (q) within a 2×1 R_S domain placed at 7.5-9.5 R_S with the density of plasma injections at 0-200 & 400-600 Ω_i^{-1} increased by a factor $\mathcal{L} = 10.0$. 21 panels, separated by 50 Ω_i^{-1}, show snapshots of the charge distribution over the course of the simulated 1000 Ω_i^{-1} period.

in a steady state, again determined from spacecraft measurements.

Into this region two injections of dense plasma were introduced from the inflow boundary at the base of the domain, which were allowed to propagate radially outwards. These plasma injections were configured such that the (in)stability criterion (eqn 3.7, see §3.1) was satisfied along the injection-background interface. RI motions are observed occurring on both the leading and trailing edges of the plasma injections, which raises the question of why are instabilities also generated on the trailing edge where density is increasing. However, using the (in)stability criterion the reason can be found tied to the gradient created by the decreased magnetic field strength.

Examination of the dynamics observed on the interfaces between these dense plasma injections and the background medium determined that $\sim 10^1$ RI instabilities formed along them, corresponding to spatial scales of $\sim 10^{-1}$ R_S. These spatial scales associated with the instabilities in the model match exactly with those determined from spacecraft measurement taken in the Saturnian magnetospheric system (see Azari et al., 2018). The calculation of growth rates was found to be inconclusive using these initial results. It was noted that RI motions continued to develop as the injections passed outside of the simulated region. However, as the model is configured to use an open boundary at the maximum radial position, it is not possible to continue tracking these developing RI motions.

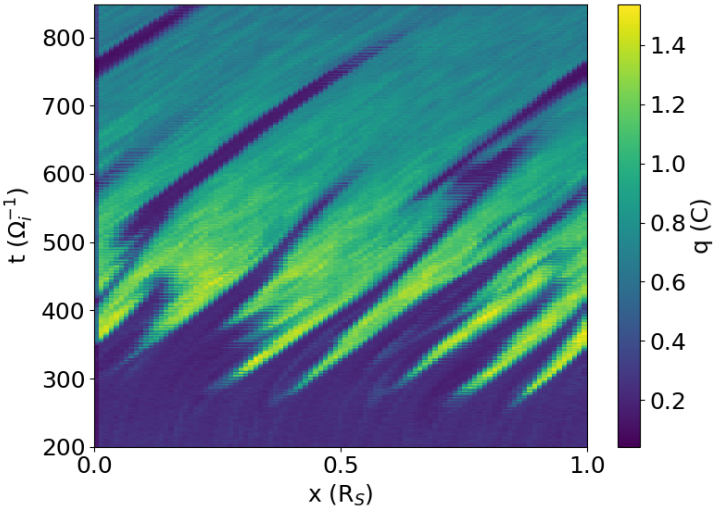

Figure 7.18: Slices of ion charge taken on the leading edge of the first plasma injection from the simulation performed in figure 7.3. Each slice is comprised of the grid points at the indexes closest to the position in the y-domain that the front is calculated to occupy, with simulation time between 200-850 Ω_i^{-1} shown against the simulated x-domain. The perturbations that develop into fingers can be seen with initially wide regions of tenuous plasma that narrow to form diagonal tracks with a width of ~ 0.02 R_S.

The structures created by these RI motions were found to be the creation of large dense fingers of plasma with narrow channels of tenuous background plasma between. These tenuous channels were found to move into the dense region, with it possible for them to close and create isolated regions of depleted plasma, still coherent in a now dense local background. Figure 7.18 allows for an initial analysis of the development process of the structures that form on the leading edge of the initial injection, with the dense fingers and interspersed tenuous channels of particular interest. This is achieved by taking slices of the ion charge distribution at the location in y which the leading edge of the injection

is calculated to occupy at a particular time step (the closest set of grid cells), a method utilised in the analysis of shocks in hybrid simulations (see Burgess et al., 2016). The position of the edge is obtained by making the assumption that it travels at a constant velocity of $\sim$40 km s^{-1}. This assumption is clearly imperfect with the calculated edge being first ahead of the simulated edge which then passes ahead of the calculated edge at later run times. However, the construction of a automatic edge detection method (as seen in §6.3) is extremely challenging due to the continual deformation of the surface by the generated instabilities.

Examining figure 7.18 it can be seen that there are $\sim$10 separate perturbations that form on the leading edge. The regions containing more tenuous plasma thin over time and are deflected in the positive x-direction (azimuthally) due to the created drifts already discussed. The result is a series of tracks that seem to be moving through a dense background, an interesting feature of which is their seemingly characteristic width of $\sim$0.02 R_S. Though at this point it is not possible to determine if this is representative of some associated physical parameter of the domain or an effect of the method used to take the slices. Additionally, the angle of deflection seems largely uniform for each of the tracks, perhaps hinting that this is also determined by some physical characteristic of the simulated region. The length of these tracks varies but most eventually thin and close as the dense fingers bend sufficiently to sever the connection between the tenuous channels and the background medium of which they are created from.

The creation of these fingers is consistent with behaviour observed in simulations using the RCM-J (Yang et al., 1994) & -S (Liu et al., 2010; Liu and Hill, 2012) and in the multi-fluid approach used by Kidder et al. (2009). However, the spatial scales of the created plasma fingers differs significantly in JERICHO, which contains smaller fingers measuring 10^{-1} R_S in width. Further, the fingers created in the RCM are found to be deflected azimuthally by the inclusion of the Coriolis pseudo-force. A direct comparison cannot be made with those in this work as they are found to be deflected by induced magnetic effects, which cannot be included in the RCM due to its use of a prescribed magnetic field. However, the spontaneous outbreak of these structures in all models supports them being natural products of RI motions, rather than purely numerical effects (as suggested by Vasyliunas, 2019).

RI motions observed in the Saturnian magnetosphere are often broken into two categories, as described in Mitchell et al. (2015) (see §3.3). Though it is not possible from the analysis of the simulations performed in this work to determine if the motions described by these categories are created by the same plasma dynamics, it is possible to find localised regions of tenuous plasma parcels moving radially inwards. These parcels, or islands, are created in the simulations when the tenuous channels between plasma fingers are closed by their deflections. The isolated regions of more tenuous background plasma then begin to slowly move into the dense plasma injection as it is transported radially outwards.

Examples of these isolated parcels of plasma, with properties distinct from the local background medium, are found in observations taken in both the Jovian (Bolton et al., 1997; Kivelson et al., 1997; Thorne et al., 1997) & Saturnian systems Rymer et al. (2009). These plasma parcels are characterised in both magnetospheric systems by a decrease in the number density and increases in both temperature & field strength. From the analysis performed in the previous section, it is seen that the plasma islands created in the simulations are more tenuous then their local background. Figure 7.19 contains a set of cuts at a distance of 9 R_S at simulation time of 650 Ω_i^{-1} (with panel a) showing the familiar ion charge distribution). These cuts are just behind the leading edge of the first plasma injection as it moves through the domain. Across the cut there are 3 tenuous plasma regions with channels that still connect them back to the background medium from which they are created and one isolated plasma parcel (at $\approx$0.3 R_S). Fig 7.19b & d

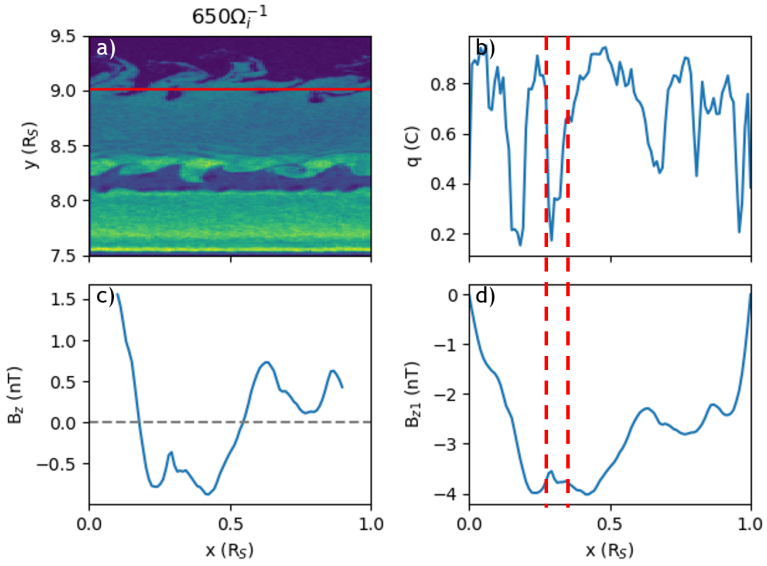

Figure 7.19: Snapshot at 650 Ω_i^{-1} selected from the simulation performed in figure 7.3 with panel a) containing the ion charge distribution and the red line at 9 R_S indicating where the cuts contained in panels b)-d) are taken. b) shows the ion charge against the simulated x-domain. c) shows the magnetic field (B_z) between 0.1-0.9 R_S with the average field value across these locations subtracted. Finally, d) shows the induced magnetic effects (B_{z1}) and is placed below b) to allow for direct comparison with ion charge distribution. The red dashed lines show the location of the isolated region of tenuous plasma in the snapshot.

contain the ion charge distribution & induced magnetic effects respectively and are placed to allow for direct comparison between them. Interestingly it can be seen that each of the connected plasma regions seem associated with decreases in the local field strength other than the isolated parcel (indicated by red dashed lines), which conversely seems associated with a small enhancement of ∼0.5 nT, an increase of ∼2 % from the background field.

Figure 7.19c contains a cut of the magnetic field with the average background field subtracted. This is calculated by taking all values between 0.1-0.9 R_S in the x-domain at 9 R_S in the y and taking a mean, utilising the approximation made when constructing the model coordinates that aligns y with the radial direction and hence allowing the assertion to be made that field strength should be constant at a fixed position in y. However, since the boundaries are held constant at the initial dipole values the edges must be excluded from the examination. The profile contained within this plot can be used to gain an understanding of what a spacecraft might see as it passes through the isolated parcel of tenuous plasma. It would see a sudden increase in field strength (in relation to its local background) as it entered the region corresponding with a drop in the plasma density, followed by a sudden transition back to background values as it exits. These virtual observations would match those reviewed in §3.3, however the magnitude of the magnetic field increase is closer to those reported in the Jovian system to the Saturnian, with the size of the region ∼10^{-2} R_S also being smaller than those determined by Azari et al. (2018).

Considering the limitations of the simulations presented, these being mainly that the created isolated tenuous plasma parcels are formed relatively late into the run time of the simulations presented and that smoothing is applied to the magnetic field. It is evident that further examination is required to determine if these islands accurately capture the observed characteristics, with it difficult to isolate a magnetic field enhancement as-

sociated with the tenuous channels from the larger scale induced effects. Additionally, ion temperature is not immediately available from the variables examined, however local profiles could be created from the hybrid kinetic-ions simulated.

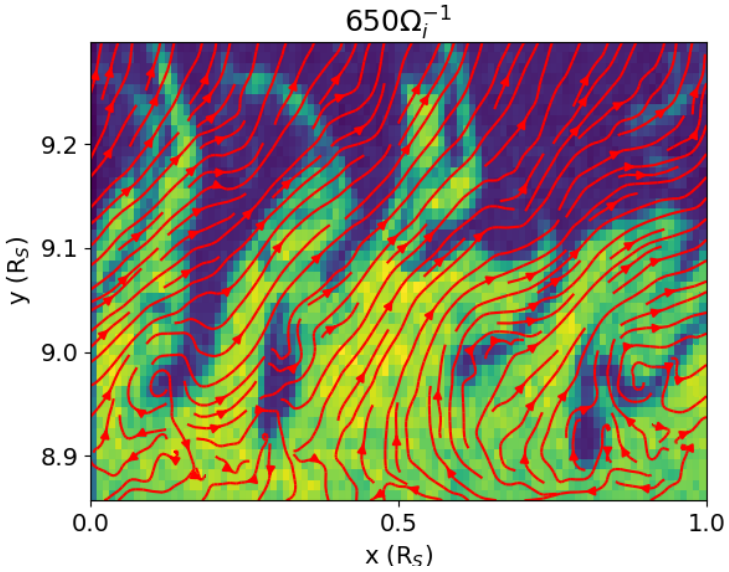

Figure 7.20: Streamlines of ion flow velocity across the leading edge of the plasma injection contained within the simulation performed in figure 7.3 at 650 Ω_i^{-1}. Ion charge distribution is also shown to allow for comparison between the ion flows and the structures created on the edge. Ion flow velocities are transformed into a reference frame approximately at rest with the flows on the leading edge to prevent the bulk motion radially outwards overwhelming the finer dynamics created by RI instabilities, generating the clearly visible structures.

Examining the environment created at the leading edge of the plasma injection there are find to be continually changes in the local number density, which are only enhanced by the introduction of multiple perturbations in close proximity along it. Comparing to the theoretical frameworks presented in §3 it could be argued that this environment is closer to that expected above the Io plasma torus. Figure 7.20 contains streamlines created from the ion flow velocities on the ion charge distribution at the leading edge of the initial plasma injection from the standard Saturnian configuration. The ion flow velocities are transformed into a reference frame at rest with the leading edge by taking the average of the velocity components in both spatial domains. This is required in order to prevent the bulk outward radial motion dominating the streamlines. Comparing with figure 3.2 it can be seen that the region between 8.9-9.0 R_S has some similarity with streamlines moving both into and out of the region and swirling associated with the RI instabilities. However, looking outside this region the chaotic mixture of flows both radially inwards and out in not observed with the dominant motion still being radially outwards. Inwards motions shown by the streamlines (outside the region below the leading edge) are all associated with the tenuous plasma channels created between the dense fingers, however the rate of these motions is slow compared to those moving the bulk injection.

To test if determined spatial scales for RI motions were tied to the spatial resolution of the underline EM grid, a simulation was performed with the resolution increased by a factor of 2.5. No perturbation is applied to the injection interface in order to induce RI instabilities, rather grid level effects are found sufficient. From this test it was determined that the instabilities were induced on shorter spatial scales initially, but coalesced into larger finger-like structures of the characteristic spatial scale ($\sim 10^{-1}$ R_S). This behaviour is

consistent with that of RT instabilities examined using hybrid & non-ideal MHD modelling, where it was found that motions started at shorter wavelengths in hybrid models and then transitioned to longer. However, it was concluded that ultimately close agreement is found between the solutions produced by the two modelling techniques on long enough time-scales (Winske, 1996; Huba and Winske, 1998). This is the same behaviour as is postulated as occurring in the higher resolution simulation, hence it is expected that in a larger domain (i.e. permitting a longer run time) the same dense finger and narrow channel structure will be formed.

In order to try and find the key parameters responsible for determining the spatial & temporal scales of the RI instabilities, as identified in the (in)stability criterion & growth rates (see §3.1), the magnetic field strength and density of the plasma injection were varied and surveyed. From these surveys a possible link between the instability growth rate and the magnetic field strength was determined, with the instability appearing to grow more rapidly in higher field strengths. However, it was noted that the results obtained in the limited survey performed were inconclusive and a more expansive range of field strengths would require examining before any definite rules could be drawn. The impact of the increased injection density on growth rate were inconclusive due to the varying of the thermal pressure associated with them. It was found that modifying either of these parameters had no impact on the spatial scales associated with the RI instabilities. Therefore, the question of what parameter controls this remains open, however it is postulated that it may be linked to centrifugal effects (the instabilities' restoring force). This highlights the need for further work utilising hybrid modelling techniques in order to continue increasing our understanding of how these motions are responsible for the transport of material in the magnetospheres of the outer planets.

Chapter 8

Summary

The work contained within this thesis has been primarily focused on the motion of plasma contained within the magnetospheres of the outer planets, at Jupiter & Saturn. Each of these magnetospheric systems are internally loaded with plasma, with the source of material located at natural satellites. In the Jovian system this is primarily the volcanic moon of Io, emitting $\approx$1000 kg s^{-1} of material into the magnetosphere, which is then rapidly ionised and brought into corotation to form the Io plasma torus. At Saturn it is primarily the icy moon of Enceladus that is the emitter of material providing a source of $\approx$300 kg s^{-1}, though the processes responsible for ionising this material occur over longer temporal scales and hence the 'neutral' tori is formed, with ionisation occurring throughout the region creating the plasma medium of interest to this work. More complete descriptions and reviews of the processes associated with the creation of these regions and their impacts on global magnetospheric dynamics can be found in §2.2.1 for the Jovian system and §2.2.2 for the Saturnian.

Both the described tori can be considered permanent, stationary features found within their corresponding planetary magnetosphere. With both moons constantly emitting new material into these regions it is readily determined, since the tori are not found to be continually inflating, that there must be loss processes associated with them. Both regions are found to have the same two main loss mechanisms, these are ejection as ENAs or bulk transport into sink regions in the outer magnetosphere. The process of interest to this work is bulk transport, more specifically the mechanism thought to be to be responsible for the transport, the radial-interchange (RI) instability.

The RI instability is analogous, both physically and mathematically, to the Rayleigh-Taylor instability with the centrifugal force replacing gravity as a driving force. The source of cold dense plasma in the inner magnetosphere and hotter tenuous plasma in the outer magnetosphere plays the role of a dense fluid on top of a less dense fluid and is thus in an unstable configuration. Essentially, RI motions allow magnetic flux tubes filled with hot, tenuous plasma to exchange places with tubes containing cold, dense plasma, without affecting the overall magnetic configuration. These motions have been observed by spacecraft in both the Jovian & Saturnian systems, with the number of observed events much greater in the Saturnian system due to a larger dataset of measurements and the advantageous configuration of the physical properties of the region. Modelling work previously performed to examine RI motions, primarily by the RCM, has proved successful in capturing them. The key predictions from the results obtained by the simulations are that outbreak of dense interchange fingers with narrow channels of tenuous plasma interspersed between, which are bent azimuthally by the inclusion of the Coriolis force.

A comprehensive review of the literature exploring the theory, observations and modelling that examine the RI instability in the outer-planetary system can be found in chp 3. A number of questions that remain unanswered by work performed to date are identified

and the need for a hybrid kinetic-ion, fluid-electron plasma model, specially designed for operation in the magnetospheres of the outer planets is determined. This is to allow the examination of flow patterns on planetary length scales, whilst retaining the ability to resolve physical effects down to the ion-inertial (see §1.2) length scales.

Chp 4 details the methods taken and combined together in order to form a recipe for a hybrid model. Specially, the ions within the model are chosen to be treated kinetically, moving them each time-step by solving their equation of motions, utilising a PIC methodology. The electrons are formed into a massless, neutralising fluid that follows the ion motions. EM fields are discretised onto the same grid vertices that particle moments are collected. The main difference in most hybrid models proves to be obtaining the fully advanced ion flow velocities (due to the temporal leap-frogging of particle positions & velocities), the recipe created utilises the CAM technique to obtain these.

Taking the recipe created, the methods contained can be taken and solutions obtained to form a computational model able to self-consistently progress through time. The exact derivation of these solutions in a 2.5-dimensional geometry constructed specifically for use within the Jovian & Saturnian systems is presented in chp 5. Of note is the inclusion of the rotation pseudo-forces (centrifugal & Coriolis) in the solution obtained for the ion's equation of motion, with the full derivation found in appendix B. These solutions form the **J**ovian magn**E**tosphe**RIC** kinetic-ion, fluid-electron **H**ybrid plasma m**O**del (JERICHO), with the techniques used to obtain these methods being accurate to the second-order in both time & space and hence able to resolve plasma instabilities. Therefore, JERICHO provides the tool required to investigate the questions pertaining to RI motions previously identified.

After constructing the framework of the model, the order in which to configure its initial parameters is provided with hypotheses presented on how to make these selections. Additionally, the statistical methods utilised to initially populate configuration & velocity space with generated particle distributions are detailed. A set of BCs are devised for dealing with both particles and EM fields at the edge of the computational domain with comment provided on how they impact the physical accuracy of the model configuration. Finally, a description of the software architecture used to execute JERICHO is detailed, providing details of the practicalities of using the model codebase.

Of course any insights provided by JERICHO into RI motions would have little value if it cannot be shown that the results obtained accurately represent physical effects. The solvers used by the model codebase have their computational correctness ensured using unit tests, but this on its own does not mean simulated solutions recreate physical effects precisely. Therefore, a series of benchmarks are developed to ensure simulation results reach the level of physical accuracy expected. These benchmarks are detailed in chp 6 and form three separate test configurations.

The first of these benchmarks examines the trajectory of particles through a domain with prescribed EM fields, a special configuration of the model is used to hold the fields constant. It is determined that the simulated trajectories converge to the analytic solution when a model time step of $\leq 0.01\Omega_i^{-1}$, motivating the selection of temporal resolution used in subsequent simulations. Next energy conservation in a domain placed within the outer Jovian magnetosphere is tested in order to quantise & examine the amount of error introduced into a simulation run. This benchmark determines that simulations, with 50 particles-per-cell or higher, experience two epochs in relation to the errors introduced, the first is related to shot noise created by our statistically methods for initialising particle distributions and the second is related to energy gained from centrifugal acceleration. Additionally, it is found be analysing the simulation results that local structures are able to transiently form and be dissipated by the solvers. It is concluded from this test that JERICHO is capable of simulating on temporal scales of interest to RI motions. The final

benchmark ensures that the model is capable of capturing higher-order effects by launching an ion acoustic wave from one edge of the simulated domain. It is found that the wave travels coherently across the simulated region, with associated signatures clearly visible in simulation results as it travels. Analysing the characteristic speed of wave propagation it was found possible to determine the adiabatic index of the electron fluid, with a value obtained of 1.45 ± 0.28. The exact value diverges from the analytic but the form of the function varying with pressure is found to match.

With the accuracy of simulated solutions ensured, JERICHO was applied to the Saturnian magnetosphere to perform an initial analysis of RI motions. The question selected for exploration in chp 7 was '*What are the local spatial & temporal scales of RI instabilities and which local plasma parameters control these?*' The region of 7.5-9.5 R_S was selected as it was found to be the most susceptible to RI motions, with the largest number of RI events observed here. The physical parameters of the model were configured to represent this region using steady state solutions fitted to spacecraft observations. Two plasma injections were introduced from the base of the domain, creating dense regions of plasma travelling radially outwards.

Examining the results obtained by JERICHO, it was determined that RI instabilities were created on the leading and trailing edges of both plasma injections. The spatial scales (in the x-domain) associated with these instabilities was determined to be 10^{-1} R_S, though it was not possible to determine precisely the temporal scale. The ion charge distribution was determined to be the most useful in the identification & analysis of RI motions within simulation results. However, the impacts of these motions on all key simulated parameters was examined, with them clearly identifiable in each. There was a range of other physical phenomena captured by the simulations, with physical interpretations of these presented.

It was noted that no perturbation was applied to the interfaces created at the leading and trailing edges of the injected plasma regions to induce RI motions. Rather, these were introduced at the grid cell spatial scale. Therefore, it was necessary to vary the spatial resolution of the simulated region, increasing it by a factor of 2.5 to ensure determined scales associated with the instabilities were not purely a function of model resolution. It was determined that though instabilities are induced on a smaller spatial scale in higher resolutions, that these then coalesces to create larger structures, with characteristic spatial scales of $\sim 10^{-1}$ R_S. A comparison between the results obtained using these simulations and those contained from previous examination of spacecraft measurements & from other models can be found in §7.3.

To identify which parameters controlled the spatial & temporal scales associated with the induced RI motions two parameters were selecting for testing using the theoretical framework obtained in chp 3. These were the strength of the magnetic field and the density of the injected plasma regions, which were systematically varied (or surveyed) by applying modifying coefficients to their values. From the series of simulations produced and subsequentially analysed a potential dependency was found between RI growth rate and magnetic field strength, though not enough data was present for definite conclusions. No correlation was found with the injection density. It was notable that the variation of both parameters had little impact on the spatial scales associated with the RI instabilities, which remained at $\sim 10^{-1}$ R_S. It is postulated that a stronger connection may be found between spatial scales and centrifugal force, the restoring force for RI motions, which could be tested by varying the spin rate of the planetary body.

The simulations examined throughout chp 7 show that JERICHO is capable of accurately resolving RI motions. This demonstrates that a new hybrid kinetic-ion, fluid-electron model has been developed, detailed in chps 4-6, which can be utilised in the exploration of plasma dynamics in the magnetospheres of the outer planets. The work presented in this thesis represents a start in the examination of RI motions with a hybrid

plasma physics model with vast scope for future development and experimentation.

8.1 Future Work

The avenues for continued work utilising JERICHO can be separated into two distinct categories. These are not isolated from one another, being possible to perform tasks in both of these simultaneously with one adding value to the other. First, is the continued development of the model solutions, solvers and codebase, which includes the use of more sophisticated (higher-order) numerical techniques as well as the inclusion of additional physical phenomena. The model presented in this thesis should be thought of as an initial release, with it expected to improve with further development. The second category is the configuration of different experiments utilising the existing model, with current work only considering a small section of a much larger system.

Examining first the prospects for future development of the model itself, it is worth considering what the primary limiting factor is in simulating larger magnetospheric regions for longer times. This is the amount of computational resources that are required to execute the computations which form the model. Currently the amount of computational resources that can be leveraged in the operation of JERICHO is limited by the serial design of its code. Therefore, the application of libraries that permit the decomposition of the model domain into smaller subdomains upon which multiple processors can be used in parallel would alleviate this limitation. With a parallelised model codebase, the size of domain that can be simulated and the length of the simulated time becomes a function of the amount of computational resources (i.e. node hours) available.

The geometry selected for model configuration is by design restrictive in nature. The grid constructed for the discretisation of EM fields and the collection of particle moments is Cartesian, which does not naturally align with the coordinates used to describe a planetary magnetosphere (r, ϕ, θ). Hence, the transformation of the grid structure to utilise polar-cylindrical or curviliniear coordinates may prove beneficial to the examination of plasma motions in a magnetospheric environment. It was noted that Cartesian coordinates were selected as it was postulated that they would provide an adequate description of plasma motions whilst being the easiest to implement computationally. Therefore, a comparison between coordinates systems to identify the benefits provided by them, weighted again any disadvantages is required.

The numerical methods selected for use in the construction of JERICHO's codebase were, once again, largely selected for computational ease, rather than through rigorous physical benchmarking. This is particularly true for the solutions to derivatives approximated using Euler differencing methods (i.e. advancing particle positions in configuration space). Hence, a comprehensive analysis of the impacts of more sophisticated numerical methods could identify the best for application within each solution that requires calculation. Any improvements proved in numerical accuracy of the solutions obtained would require careful comparison with the decrease in computational efficiency associated with the implementation of a more sophisticated method, ensuring an appropriate balance is reached between the two.

The model framework presented in this work details the construction a magnetospheric plane, with the methodology contained for the calculation of field aligned current (along the magnetic field lines). However, this work does not contain the construction of a corresponding ionospheric plane and the mechanism for communicating the response of the ionosphere to the magnetosphere. In terms of RI motions, it is postulated that the inclusion of this response would act to retard the growth of the instability. Complications arise in the coupling of the magnetosphere to the ionosphere, along magnetic field lines, in the calculation of corresponding potentials in the ionospheric plane. Further, most

coupled ionospheric-magnetospheric models assume that the communication between the two regions occurs instantaneously, clearly this is not physical but a scheme could be developed to communicate responses at the characteristic Alfvén velocity of the system.

Finally, previous modelling work determined that the inclusion of electron pressure gradients acted to alter the growth rates of RI instabilities. Currently these pressure gradients are only obtainable from JERICHO's model runs via post-processing. Therefore, the development & inclusion of additional logic to allow for these gradients to be used in the model solutions may increase the accuracy of simulation results.

Shifting focus onto the second category of continued work that could be pursued, this contains the configuration of different physical experiments utilising the existing model codebase. Of course any simulation results obtained would benefit from the additional development work described in the first category. However, all the configurations detailed here could be created within the model codebase contained in this thesis.

A sensible location for the start of continued work examining RI motions is to extend the parameter survey described in chp 7. Exploring a wider range of magnetic field strength would allow more definite conclusions to be drawn between its strength and RI growth rates. Additionally, it was postulated that varying of the applied centrifugal force, controlled by the rate of planetary rotation, may reveal a link between this parameter and the spatial scales associated with RI instabilities.

All simulations containing RI motions were performed in the Saturnian magnetosphere, in the spatial region identified as most susceptible to RI motions. Therefore, it is sensible to use the same logic and construct a configuration that captures the equitable region in the Jovian magnetosphere, identified as distances just above the Io plasma torus. This would require the obtention of a completely new of the set of ICs used to determine the initial physical parameters within the modelled region and to populate configuration & velocity space with macroparticles. However, it should be noted that observations currently being collected by the JUNO spacecraft mission motivate the undertaking of this work, with the opportunity to compare predictions obtained from simulations with the latest available data and even inform the future directions of the mission.

The simulations performed in this thesis all assume the planetary magnetic field is dipolar and aligned with the spin axis. Although the adaption of solutions used to approximate the magnetic field would fall into the first category, it would be possible to give some consideration for this offset by modifying the initial field values, scaling their magnitudes based on the size of this axial offset. However, it should be noted that the self-consistently evolving EM fields would still not respect the axial offset, with the assumption of spin alignment fundamentally included in the derivation of their solutions. Further, more precise maps of the planetary magnetic field are available in both the Jovian & Saturnian systems. Hence it would be possible to construct a more physically accurate magnetic field across a simulated domain which would then be discretised onto the EM grid.

The range of options for the continuation of work undertaken in this thesis is by no means exhaustive of all the paths that could be taken to improve the hybrid model. Nor does it describe every conceivable configuration that could be devised to examine RI motions, or even other plasma dynamics within a rotationally dominated environment. Rather, these capture the views of the author on the most exciting development opportunities and computational experiments that lie before JERICHO.

Bibliography

Achilleos, N., André, Nicolas amd Blanco-Cano, X., Brandt, P. C., Delamere, P. A., and Winglee, R. (2015). 1. transport of mass, momentum and energy in planetary magnetodisc regions. *Space Science Reviews*, 187(1):229–299.

Achilleos, N., Arridge, C. S., Bertucci, C., Jackman, C. M., Dougherty, M. K., Khurana, K. K., and Russell, C. T. (2008). Large-scale dynamics of saturn's magnetopause: Observations by cassini. *Journal of Geophysical Research: Space Physics*, 113(A11).

Achilleos, N., Guio, P., and Arridge, C. S. (2010). A model of force balance in saturn's magnetodisc. *Monthly Notices of the Royal Astronomical Society*, 401:2349–2371.

Achilleos, N., Guio, P., Hardy, F., Paranicas, C., and Sorba, A. M. (2021). *The Magnetodisk Regions of Jupiter and Saturn*, chapter 29, pages 453–469. American Geophysical Union (AGU).

Acuna, M. H. and Ness, N. F. (1976). The main magnetic field of jupiter. *Journal of Geophysical Research (1896-1977)*, 81(16):2917–2922.

Alfvén, H. (1942). Existence of electromagnetic-hydrodynamic waves. *Nature*, 150:405–406.

Alfvén, H. (1950). *Cosmical Electrodynamics*. Clarendon Press.

André, N. and Ferrière, K. M. (2004). Low-frequency waves and instabilities in stratified, gyrotropic, multicomponent plasmas: Theory and application to plasma transport in the io torus. *Journal of Geophysical Research: Space Physics*, 109(A12).

Arridge, C. and Wiggs, J. (2019). Ikuchi: 3d views of solar system magnetospheres. *10.5281/zenodo.3451443*.

Arridge, C. S., Achilleos, N., Dougherty, M. K., Khurana, K. K., and Russell, C. T. (2006). Modeling the size and shape of saturn's magnetopause with variable dynamic pressure. *Journal of Geophysical Research: Space Physics*, 111(A11).

Arridge, C. S., André, N., McAndrews, H. J., Bunce, E. J., Burger, M. H., Hansen, K. C., Hsu, H.-W., Johnson, R. E., Jones, G. H., Kempf, S., Khurana, K. K., Krupp, N., Kurth, W. S., Leisner, J. S., Paranicas, C., Roussos, E., Russell, C. T., Schippers, P., Sittler, E. C., Smith, H. T., Thomsen, M. F., and Dougherty, M. K. (2011). Mapping magnetospheric equatorial regions at saturn from cassini prime mission observations. *Space Science Reviews*, 164(1):1–83.

Arridge, C. S., Khurana, K. K., Russell, C. T., Southwood, D. J., Achilleos, N., Dougherty, M. K., Coates, A. J., and Leinweber, H. K. (2008a). Warping of saturn's magnetospheric and magnetotail current sheets. *Journal of Geophysical Research: Space Physics*, 113(A8).

Arridge, C. S., Russell, C. T., Khurana, K. K., Achilleos, N., Cowley, S. W. H., Dougherty, M. K., Southwood, D. J., and Bunce, E. J. (2008b). Saturn's magnetodisc current sheet. *Journal of Geophysical Research: Space Physics*, 113(A4).

Azari, A. R., Liemohn, M. W., Jia, X., Thomsen, M. F., Mitchell, D. G., Sergis, N., Rymer, A. M., Hospodarsky, G. B., Paranicas, C., and Vandegriff, J. (2018). Interchange injections at saturn: Statistical survey of energetic h+ sudden flux intensifications. *Journal of Geophysical Research: Space Physics*, 123:4692–4711.

Badman, S. V. and Cowley, S. W. H. (2007). Significance of dungey-cycle flows in jupiter's and saturn's magnetospheres, and their identification on closed equatorial field lines. *Annales Geophysicae*, 25(4):941–951.

Bagdonat, T. (2005). Hybrid simulation of weak comets.

Bagdonat, T. and Motschmann, U. (2002). 3d hybrid simulation code using curvilinear coordinates. *Journal of Computational Physics*, 183:470–485.

Bagenal, F. (1985). Plasma conditions inside io's orbit: Voyager measurements. *Journal of Geophysical Research: Space Physics*, 90(A1):311–324.

Bagenal, F. (1994). Empirical model of the io plasma torus: Voyager measurements. *Journal of Geophysical Research: Space Physics*, 99(A6):11043–11062.

Bagenal, F. (2005). Saturn's mixed magnetosphere. *Nature*, 433(7027).

Bagenal, F. (2013). *Planetary Magnetospheres*, pages 251–307. Springer Netherlands.

Bagenal, F. and Bartlett, S. (2012a). Earth magnetoshere: Basic dipolar magnetosphere with distance to sub-solar magnetopause (r_{mp}). `https://lasp.colorado.edu/home/mop/files/2012/04/1Msphere.jpg`.

Bagenal, F. and Bartlett, S. (2012b). Jupiter's magnetosphere. `https://lasp.colorado.edu/home/mop/files/2012/04/JupMag-8W.jpg`.

Bagenal, F., Crary, F. J., Stewart, A. I. F., Schneider, N. M., Gurnett, D. A., Kurth, W. S., Frank, L. A., and Paterson, W. R. (1997). Galileo measurements of plasma density in the io torus. *Geophysical Research Letters*, 24(17):2119–2122.

Bagenal, F., Dowling, T. E., and McKinnon, W. B. (2007). *Introduction*, chapter 1, pages 1–18. Cambridge University Press.

Bagenal, F., Shemansky, D. E., McNutt Jr., R. L., Schreier, R., and Eviatar, A. (1992). The abundance of o++ in the jovian magnetosphere. *Geophysical Research Letters*, 19(2):79–82.

Bagenal, F., Sullivan, J. D., and Siscoe, G. L. (1980). Spatial distribution of plasma in the io torus. *Geophysical Research Letters*, 7(1):41–44.

Bagenal, F., Wilson, R. J., Siler, S., Paterson, W. R., and Kurth, W. S. (2016). Survey of galileo plasma observations in jupiter's plasma sheet. *Journal of Geophysical Research: Planets*, 121(5):871–894.

Balkanski, M. and Wallis, R. F. (2000). *Semiconductor physics and applications*. Series on semiconductor science and technology ; 8. Oxford University Press.

Bame, S. J., Asbridge, J. R., Felthauser, H. E., Hones, E. W., and Strong, I. B. (1967). Characteristics of the plasma sheet in the earth's magnetotail. *Journal of Geophysical Research (1896-1977)*, 72(1):113–129.

Battarbee, M., Brito, T., Alho, M., Pfau-Kempf, Y., Grandin, M., Ganse, U., Papadakis, K., Johlander, A., Turc, L., Dubart, M., and Palmroth, M. (2021). Vlasov simulation of electrons in the context of hybrid global models: an evlasiator approach. *Annales Geophysicae*, 39(1):85–103.

Baumjohann, W. and Treumann, R. A. (1996). *Basic Space Plasma Physics*. Imperial College Press.

Biesecker, D. A., Webb, D. F., and St. Cyr, O. C. (2007). Stereo space weather and the space weather beacon. *Space Science Reviews*, 136(1).

Bigg, E. K. (1964). Influence of the satellite io on jupiter's decametric emission. *Nature*, 203(4949):1008–1010.

Birdsall, C. and Langdon, A. (1985). *Plasma Physics Via Computer Simulation*. McGraw-Hill.

Bolton, S. J., Thorne, R. M., Gurnett, D. A., Kurth, W. S., and Williams, D. J. (1997). Enhanced whistler-mode emissions: Signatures of interchange motion in the io torus. *Geophysical Research Letters*, 24:2123–2126.

Borderick, J. D. (2010). *Ionospheric Signatures of Ultra Low Frequency Waves*. PhD thesis, University of Leicester, Leicester, UK.

Boyd, T. J. M. and Sanderson, J. J. (2003). *The Physics of Plasmas*. Cambridge University Press.

Broadfoot, A. L., Belton, M. J. S., Takacs, P. Z., Sandel, B. R., Shemansky, D. E., Holberg, J. B., Ajello, J. M., Atreya, S. K., Donahue, T. M., Moos, H. W., Bertaux, J. L., Blamont, J. E., Strobel, D. F., McConnell, J. C., Dalgarno, A., Goody, R., and McElroy, M. B. (1979). Extreme ultraviolet observations from voyager 1 encounter with jupiter. *Science*, 204(4396):979–982.

Brown, L. W. (1975). Saturn radio emission near 1 mhz. *Astrophysical Journal*, 198:L89–L92.

Brown, R. A. (1974). Optical line emission from io. In Woszczyk, A. and Iwaniszewska, C., editors, *Exploration of the Planetary System*, volume 65, pages 527–531.

Brown, S. (2019). The c4 model for visualising software architecture. https://c4model.com.

Burgess, D., Hellinger, P., Gingell, I., and Trávníček, P. M. (2016). Microstructure in two- and three-dimensional hybrid simulations of perpendicular collisionlessÂ shocks. *Journal of Plasma Physics*, 82(4).

Burke, B. F. and Franklin, K. L. (1955). Observations of a variable radio source associated with the planet jupiter. *Journal of Geophysical Research (1896-1977)*, 60(2):213–217.

Burlaga, L. F., Ness, N. F., Berdichevsky, D. B., Park, J., Jian, L. K., Szabo, A., Stone, E. C., and Richardson, J. D. (2019). Magnetic field and particle measurements made by voyager 2 at and near the heliopause. *Nature Astronomy*, 3(11):1007–1012.

Carbary, J. F. and Mitchell, D. G. (2016). Seasonal variations in saturn's plasma sheet warping. *Geophysical Research Letters*, 43(23):11,957–11,962.

Cassidy, T. and Johnson, R. (2010). Collisional spreading of enceladus' neutral cloud. *Icarus*, 209(2):696–703.

Caudal, G. (1986). A self-consistent model of jupiter's magnetodisc including the effects of centrifugal force and pressure. *Journal of Geophysical Research: Space Physics*, 91(A4):4201–4221.

Chapman, S. and Ferraro, V. C. A. (1931). A new theory of magnetic storms. *Terrestrial Magnetism and Atmospheric Electricity*, 36(3):171–186.

Chen, Y. and Hill, T. W. (2008). Statistical analysis of injection/dispersion events in saturn's inner magnetosphere. *Journal of Geophysical Research: Space Physics*, 113(A7).

Connerney, J. E. P., Kotsiaros, S., Oliversen, R. J., Espley, J. R., Joergensen, J. L., Joergensen, P. S., Merayo, J. M. G., Herceg, M., Bloxham, J., Moore, K. M., Bolton, S. J., and Levin, S. M. (2018). A new model of jupiter's magnetic field from juno's first nine orbits. *Geophysical Research Letters*, 45(6):2590–2596.

Connerney, J. E. P., Timmins, S., Oliversen, R. J., Espley, J. R., Joergensen, J. L., Kotsiaros, S., Joergensen, P. S., Merayo, J. M. G., Herceg, M., Bloxham, J., Moore, K. M., Mura, A., Moirano, A., Bolton, S. J., and Levin, S. M. (2022). A new model of jupiter's magnetic field at the completion of juno's prime mission. *Journal of Geophysical Research: Planets*, 127(2).

Cowen, R. (2013). Voyager 1 has reached interstellar space. *Nature*.

Cowley, S. W. H., Bunce, E. J., and Prangé, R. (2004). Saturn's polar ionospheric flows and their relation to the main auroral oval. *Annales Geophysicae*, 22(4):1379–1394.

Cowley, S. W. H., Bunce, E. J., Stallard, T. S., and Miller, S. (2003). Jupiter's polar ionospheric flows: Theoretical interpretation. *Geophysical Research Letters*, 30(5).

Coxon, J. C., Jackman, C. M., Freeman, M. P., Forsyth, C., and Rae, I. J. (2016). Identifying the magnetotail lobes with cluster magnetometer data. *Journal of Geophysical Research: Space Physics*, 121(2):1436–1446.

Daly, A., Li, W., Ma, Q., and Shen, X. (2021). Interchange instability in the jovian magnetosphere using juno observations. Poster presented at the Magnetospheres of the Outer Planets Meeting.

Delamere, P. A. and Bagenal, F. (2003). Modeling variability of plasma conditions in the io torus. *Journal of Geophysical Research: Space Physics*, 108(A7).

Delamere, P. A., Bagenal, F., Dols, V., and Ray, L. C. (2007). Saturn's neutral torus versus jupiter's plasma torus. *Geophysical Research Letters*, 34(9).

Delamere, P. A., Barnes, N. P., Ma, X., and Johnson, J. R. (2021). The kelvin-helmholtz instability from the perspective of hybrid simulations. *Frontiers in Astronomy and Space Sciences*, 8.

Delamere, P. A., Damiano, P. A., Mino, B., Schok, A., Sorathia, K., Sciola, A., Wing, S., Zhang, B., Ma, X., Johnson, J. R., and Bagenal, F. (2022). Structure and dynamics of jupiter's dawnside magnetosphere. Presented at the Magnetospheres of the Outer Planets Meeting.

Developers, T. S. (2022). Sphinx. https://www.sphinx-doc.org/en/master/.

Dialynas, K. (2018). Cassini/mimi observations on the dungey cycle reconnection and kelvin-helmholtz instability in saturn's magnetosphere. *Journal of Geophysical Research: Space Physics*, 123(9):7271–7275.

Dialynas, K., Krimigis, S. M., Decker, R. B., Hill, M., Mitchell, D. G., Hsieh, K. C., Hilchenbach, M., and Czechowski, A. (2022). The structure of the global heliosphere as seen by in-situ ions from the voyagers and remotely sensed enas from cassini. *Space Science Reviews*, 218.

Dungey, J. W. (1961). Interplanetary magnetic field and the auroral zones. *Physical Review. Letters*, 6:47–48.

Eastwood, J. P., Hietala, H., Toth, G., Phan, T. D., and Fujimoto, M. (2015). What controls the structure and dynamics of earth's magnetosphere? *Space Science Reviews*, 188(1).

Eastwood, J. P., Nakamura, R., Turc, L., Mejnertsen, L., and Hesse, M. (2017). The scientific foundations of forecasting magnetospheric space weather. *Space Science Reviews*, 212(3):1221–1252.

Fleshman, B. L., Delamere, P. A., and Bagenal, F. (2010). A sensitivity study of the enceladus torus. *Journal of Geophysical Research: Planets*, 115(E4).

Fleshman, B. L., Delamere, P. A., Bagenal, F., and Cassidy, T. (2012). The roles of charge exchange and dissociation in spreading saturn's neutral clouds. *Journal of Geophysical Research: Planets*, 117(E5).

Fleshman, B. L., Delamere, P. A., Bagenal, F., and Cassidy, T. (2013). A 1-d model of physical chemistry in saturn's inner magnetosphere. *Journal of Geophysical Research: Planets*, 118(8):1567–1581.

Fox, N. J., Velli, M. C., Bale, S. D., Decker, R., Driesman, A., Howard, R. A., Kasper, J. C., Kinnison, J., Kusterer, M., Lario, D., Lockwood, M. K., McComas, D. J., Raouafi, N. E., and Szabo, A. (2016). The Solar Probe Plus Mission: Humanity's First Visit to Our Star. *Space Science Reviews*, 204(1-4):7–48.

Ganushkina, N. Y., Liemohn, M. W., and Dubyagin, S. (2018). Current systems in the earth's magnetosphere. *Reviews of Geophysics*, 56(2):309–332.

Gehrels, N. and Stone, E. C. (1983). Energetic oxygen and sulfur ions in the jovian magnetosphere and their contribution to the auroral excitation. *Journal of Geophysical Research: Space Physics*, 88(A7):5537–5550.

Gold, T. (1959). Motions in the magnetosphere of the earth. *Journal of Geophysical Research*, 64:1219–1224.

Gombosi, T. I., Armstrong, T. P., Arridge, C. S., Khurana, K. K., Krimigis, S. M., Krupp, N., Persoon, A. M., and Thomsen, M. F. (2009). *Saturn's Magnetospheric Configuration*, pages 203–255. Springer Netherlands.

Grasset, O., Dougherty, M., Coustenis, A., Bunce, E., Erd, C., Titov, D., Blanc, M., Coates, A., Drossart, P., Fletcher, L., Hussmann, H., Jaumann, R., Krupp, N., Lebreton, J.-P., Prieto-Ballesteros, O., Tortora, P., Tosi, F., and Van Hoolst, T. (2013). Jupiter icy moons explorer (juice): An esa mission to orbit ganymede and to characterise the jupiter system. *Planetary and Space Science*, 78:1–21.

Green, J., Boardsen, S., and Dong, C. (2021). Magnetospheres of terrestrial exoplanets and exomoons: Implications for habitability and detection. *The Astrophysical Journal Letters*, 907(2):L45.

Griffiths, D. J. (2017). *Introduction to Electrodynamics*. Cambridge University Press, 4 edition.

Griffiths, D. J. and Schroeter, D. F. (2018). *Introduction to Quantum Mechanics*. Cambridge University Press, 3 edition.

Guennebaud, G., Jacob, B., et al. (2010). Eigen v3. http://eigen.tuxfamily.org.

Gunell, H., De Keyser, J., Gamby, E., and Mann, I. (2013). Vlasov simulations of parallel potential drops. *Annales Geophysicae*, 31(7):1227–1240.

Gurnett, D. A. and Kurth, W. S. (2019). Plasma densities near and beyond the heliopause from the voyager 1 and 2 plasma wave instruments. *Nature Astronomy*, 3(11):1024–1028.

Gurnett, D. A., Kurth, W. S., Shaw, R. R., Roux, A., Gendrin, R., Kennel, C. F., Scarf, F. L., and Shawhan, S. D. (1992). The galileo plasma wave investigation. *Space Science Reviews*, 60(1):341–355.

Hameiri, E., Laurence, P., and Mond, M. (1991). The ballooning instability in space plasmas. *Journal of Geophysical Research: Space Physics*, 96(A2):1513–1526.

Hansen, C., Esposito, L., Colwell, J., Hendrix, A., Portyankina, G., Stewart, A., and West, R. (2020). The composition and structure of enceladus' plume from the complete set of cassini uvis occultation observations. *Icarus*, 344.

Harel, M., Wolf, R. A., Reiff, P. H., Spiro, R. W., Burke, W. J., Rich, F. J., and Smiddy, M. (1981). Quantitative simulation of a magnetospheric substorm 1. model logic and overview. *Journal of Geophysical Research: Space Physics*, 86(A4):2217–2241.

Hargreaves, J. K. (1992). *The solar wind and the magnetosphere*, pages 132–207. Cambridge University Press.

Harris, C. R., Millman, K. J., van der Walt, S. J., Gommers, R., Virtanen, P., Cournapeau, D., Wieser, E., Taylor, J., Berg, S., Smith, N. J., Kern, R., Picus, M., Hoyer, S., van Kerkwijk, M. H., Brett, M., Haldane, A., del Río, J. F., Wiebe, M., Peterson, P., Gérard-Marchant, P., Sheppard, K., Reddy, T., Weckesser, W., Abbasi, H., Gohlke, C., and Oliphant, T. E. (2020). Array programming with numpy. *Nature*, 585:357–362.

Hesse, M. and Cassak, P. A. (2020). Magnetic reconnection in the space sciences: Past, present, and future. *Journal of Geophysical Research: Space Physics*, 125(2).

Hill, T. (1976). Interchange stability of a rapidly rotating magnetosphere. *Planetary and Space Science*, 24:1151–1154.

Hill, T. (1979). Inertial limit on corotation. *Journal of Geophysical Research: Space Physics*, 84(A11):6554–6558.

Hill, T. W. (1980). Corotation lag in jupiter's magnetosphere: Comparison of observation and theory. *Science*, 207(4428):301–302.

Hill, T. W., Dessler, A. J., and Maher, L. J. (1981). Corotating magnetospheric convection. *Journal of Geophysical Research: Space Physics*, 86(A11):9020–9028.

Hill, T. W., Dessler, A. J., and Michel, F. C. (1974). Configuration of the jovian magnetosphere. *Geophysical Research Letters*, 1(1):3–6.

Hill, T. W., Rymer, A. M., Burch, J. L., Crary, F. J., Young, D. T., Thomsen, M. F., Delapp, D., André, N., Coates, A. J., and Lewis, G. R. (2005). Evidence for rotationally driven plasma transport in saturn's magnetosphere. *Geophysical Research Letters*, 32.

Hones Jr., E. W. (1977). Substorm processes in the magnetotail: Comments on 'on hot tenuous plasmas, fireballs, and boundary layers in the earth's magnetotail' by l. a. frank, k. l. ackerson, and r. p. lepping. *Journal of Geophysical Research (1896-1977)*, 82(35):5633–5640.

Horowitz, E. J., Shumaker, D. E., and Anderson, D. V. (1989). Qn3d: A three-dimensional quasi-neutral hybrid particle-in-cell code with applications to the tilt mode instability in field reversed configurations. *Journal of Computational Physics*, 84:279–310.

Huba, J. D. (2003). *Hall Magnetohydrodynamics - A Tutorial*, pages 166–192. Springer Berlin Heidelberg, Berlin, Heidelberg.

Huba, J. D. (2013). *NRL Plasma Formulary*. Naval Research Laboratory.

Huba, J. D. and Winske, D. (1998). Rayleigh-taylor instability: Comparison of hybrid and nonideal magnetohydrodynamic simulations. *Physics of Plasmas*, 5:2305–2316.

Hundhausen, A. J. (1995). *The Solar Wind*, chapter 4, pages 91–128. Cambridge University Press.

Huscher, E., Bagenal, F., Wilson, R. J., Allegrini, F., Ebert, R. W., Valek, P. W., Szalay, J. R., McComas, D. J., Connerney, J. E. P., Bolton, S., and Levin, S. M. (2021). Survey of juno observations in jupiter's plasma disk: Density. *Journal of Geophysical Research: Space Physics*, 126(8).

ISO/IEC TR 19768:2007 (2007). Information technology - programming languages - technical report on c++ library extensions. Technical report, International Organization for Standardization.

Jackman, C. M., Thomsen, M. F., and Dougherty, M. K. (2019). Survey of saturn's magnetopause and bow shock positions over the entire cassini mission: Boundary statistical properties and exploration of associated upstream conditions. *Journal of Geophysical Research: Space Physics*, 124(11):8865–8883.

Jarvinen, R., Kallio, E., SillanpÃ¤Ã¤, I., and Janhunen, P. (2008). Hybrid modelling the pioneer venus orbiter magnetic field observations. *Advances in Space Research*, 41:1361–1374.

Jia, X., Hansen, K. C., Gombosi, T. I., Kivelson, M. G., Tóth, G., DeZeeuw, D. L., and Ridley, A. J. (2012). Magnetospheric configuration and dynamics of saturn's magnetosphere: A global mhd simulation. *Journal of Geophysical Research: Space Physics*, 117(A5).

Joy, S. P., Kivelson, M. G., Walker, R. J., Khurana, K. K., Russell, C. T., and Ogino, T. (2002). Probabilistic models of the jovian magnetopause and bow shock locations. *Journal of Geophysical Research: Space Physics*, 107(A10).

Jurac, S., Johnson, R., and Richardson, J. (2001). Saturn's e ring and production of the neutral torus. *Icarus*, 149(2):384–396.

Kallio, E. and Janhunen, P. (2003). Modelling the solar wind interaction with mercury by a quasi-neutral hybrid model. *Annales Geophysicae*, 21:2133–2145.

Kennelly, T. J., Leisner, J. S., Hospodarsky, G. B., and Gurnett, D. A. (2013). Ordering of injection events within saturnian sls longitude and local time. *Journal of Geophysical Research: Space Physics*, 118(2):832–838.

Khurana, K. K., Kivelson, M. G., Vasyliunas, V. M., Krupp, N., Woch, J., Lagg, A., Mauk, B. H., and Kurth, W. S. (2004). *The configuration of Jupiter's magnetosphere*, chapter 24, pages 593–616. Cambridge University Press.

Kidder, A., Winglee, R. M., and Harnett, E. M. (2009). Regulation of the centrifugal interchange cycle in saturn's inner magnetosphere. *Journal of Geophysical Research: Space Physics*, 114(A2).

Kivelson, M. G., Khurana, K. K., Means, J. D., Russell, C. T., and Snare, R. C. (1992). The galileo magnetic field investigation. *Space Science Reviews*, 60(1-4):357–383.

Kivelson, M. G., Khurana, K. K., Russell, C. T., and Walker, R. J. (1997). Intermittent short-duration magnetic field anomalies in the io torus: Evidence for plasma interchange? *Geophysical Research Letters*, 24:2127–2130.

Kivelson, M. G. and Southwood, D. J. (2005). Dynamical consequences of two modes of centrifugal instability in jupiter's outer magnetosphere. *Journal of Geophysical Research: Space Physics*, 110(A12).

Krimigis, S. M., Mitchell, D. G., Hamilton, D. C., Dandouras, J., Armstrong, T. P., Bolton, S. J., Cheng, A. F., Gloeckler, G., Hsieh, K. C., Keath, E. P., Krupp, N., Lagg, A., Lanzerotti, L. J., Livi, S., Mauk, B. H., McEntire, R. W., Roelof, E. C., Wilken, B., and Williams, D. J. (2002). A nebula of gases from io surrounding jupiter. *Nature*, 415(6875):994–996.

Krimigis, S. M., Mitchell, D. G., Roelof, E. C., Hsieh, K. C., and McComas, D. J. (2009). Imaging the interaction of the heliosphere with the interstellar medium from saturn with cassini. *Science*, 326(5955):971–973.

Krupp, N., Kollmann, P., Mitchell, D. G., Thomsen, M., Jia, X., Masters, A., and Zarka, P. (2018). *Global Configuration and Seasonal Variations of Saturn's Magnetosphere*, pages 126–165. Cambridge University Press.

Krupp, N., Vasyliūnas, V. M., Woch, J., Lagg, A., Khurana, K. K., Kivelson, M. G., Mauk, B. H., Roelof, E. C., Williams, D. J., Krimigis, S. M., Kurth, W. S., Frank, L. A., and Paterson, W. R. (2004). *Dynamics of the Jovian Mangetosphere*, pages 617–638. Cambridge University Press.

Kundu, P. K. and Cohen, I. M. (2004). *Fluid Mechanics*. Elsevier Academic Press, 3 edition.

Lai, H. R., Russell, C. T., Jia, Y. D., Wei, H. Y., and Dougherty, M. K. (2016). Transport of magnetic flux and mass in saturn's inner magnetosphere. *Journal of Geophysical Research: Space Physics*, 121(4):3050–3057.

Landau, L. D. and Lifshitz, E. M. (1976). *Mechanics*. Butterworth-Heinemann, 3 edition.

Lapenta, G., Schriver, D., Walker, R. J., Berchem, J., Echterling, N. F., Alaoui, M. E., and Travnicek, P. (2022). Do we need to consider electrons' kinetic effects to properly model a planetary magnetosphere: The case of mercury. *Journal of Geophysical Research: Space Physics*, 127(4).

Lavraud, B. and Trattner, K. J. (2021). *The Polar Cusps of the Earth's Magnetosphere*, chapter 11, pages 163–176. American Geophysical Union (AGU).

Lellouch, E., McGrath, M. A., and Jessup, K. L. (2007). *Io's atmosphere*, chapter 10, pages 231–264. Springer Berlin Heidelberg.

Li, W. and Hudson, M. (2019). Earth's van allen radiation belts: From discovery to the van allen probes era. *Journal of Geophysical Research: Space Physics*, 124(11):8319–8351.

Liu, X. and Hill, T. W. (2012). Effects of finite plasma pressure on centrifugally driven convection in saturn's inner magnetosphere. *Journal of Geophysical Research: Space Physics*, 117(A7).

Liu, X., Hill, T. W., Wolf, R. A., Sazykin, S., Spiro, R. W., and Wu, H. (2010). Numerical simulation of plasma transport in saturn's inner magnetosphere using the rice convection model. *Journal of Geophysical Research: Space Physics*, 115.

Liuzzo, L., Feyerabend, M., Simon, S., and Motschmann, U. (2015). The impact of callisto's atmosphere on its plasma interaction with the jovian magnetosphere. *Journal of Geophysical Research: Space Physics*, 120(11):9401–9427.

Louarn, P., Mauk, B. H., Kivelson, M. G., Kurth, W. S., Roux, A., Zimmer, C., Gurnett, D. A., and Williams, D. J. (2001). A multi-instrument study of a jovian magnetospheric disturbance. *Journal of Geophysical Research: Space Physics*, 106(A12):29883–29898.

Lucek, E. A., Constantinescu, D., Goldstein, M. L., Pickett, J., Pinçon, J. L., Sahraoui, F., Treumann, R. A., and Walker, S. N. (2005). The magnetosheath. *Space Science Reviews*, 118(1).

Lyon, J., Fedder, J., and Mobarry, C. (2004). The lyon-fedder-mobarry (lfm) global mhd magnetospheric simulation code. *Journal of Atmospheric and Solar-Terrestrial Physics*, 66(15):1333–1350.

Lyon, J., Sorathia, K., Zhang, B., Merkin, V. G., Wiltberger, M. J., and Daldorff, L. K. S. (2017). GAMERA - The New Magnetospheric Code. In *AGU Fall Meeting Abstracts*, pages SM13C–2394.

Lyons, L. R. and Thorne, R. M. (1973). Equilibrium structure of radiation belt electrons. *Journal of Geophysical Research (1896-1977)*, 78(13):2142–2149.

Macek, W. M., Kurth, W. S., Lepping, R. P., and Sibeck, D. G. (1992). Distant magnetotails of the outer magnetic planets. *Advances in Space Research*, 12(8):47–55.

Markidis, S., Lapenta, G., and Rizwan-uddin (2010). Multi-scale simulations of plasma with ipic3d. *Mathematics and Computers in Simulation*, 80(7):1509–1519.

Matthews, A. P. (1994). Current advance method and cyclic leapfrog for 2d multispecies hybrid plasma simulations. *Journal of Computational Physics*, 112:102–116.

Mauk, B. H., Clark, G., Allegrini, F., Bagenal, F., Bolton, S. J., Connerney, J. E. P., Haggerty, D. K., Kollmann, P., Mitchell, D. G., Paranicas, C. P., and Rymer, A. M. (2020). Juno energetic neutral atom (ena) remote measurements of magnetospheric injection dynamics in jupiter's io torus regions. *Journal of Geophysical Research: Space Physics*, 125(5).

Mauk, B. H., Clarke, J. T., Grodent, D., Waite, J. H., Paranicas, C. P., and Williams, D. J. (2002). Transient aurora on jupiter from injections of magnetospheric electrons. *Nature*, 415(6875):1003–1005.

Mauk, B. H., Gary, S. A., Kane, M., Keath, E. P., Krimigis, S. M., and Armstrong, T. P. (1996). Hot plasma parameters of jupiter's inner magnetosphere. *Journal of Geophysical Research: Space Physics*, 101(A4):7685–7695.

Mauk, B. H., Hamilton, D. C., Hill, T. W., Hospodarsky, G. B., Johnson, R. E., Paranicas, C., Roussos, E., Russell, C. T., Shemansky, D. E., Sittler, E. C., and Thorne, R. M. (2009). *Fundamental Plasma Processes in Saturn's Magnetosphere*, pages 281–331. Springer Netherlands.

Mauk, B. H., Williams, D. J., and McEntire, R. W. (1997). Energy-time dispersed charged particle signatures of dynamic injections in jupiter's inner magnetosphere. *Geophysical Research Letters*, 24(23):2949–2952.

Mauk, B. H., Williams, D. J., McEntire, R. W., Khurana, K. K., and Roederer, J. G. (1999). Storm-like dynamics of jupiter's inner and middle magnetosphere. *Journal of Geophysical Research: Space Physics*, 104(A10):22759–22778.

McComas, D. J., Bagenal, F., and Ebert, R. W. (2014). Bimodal size of jupiter's magnetosphere. *Journal of Geophysical Research: Space Physics*, 119(3):1523–1529.

McLaughlin, J. A., Thurgood, J. O., Botha, G. J. J., and Wiggs, J. A. (2019). 3d wkb solution for fast magnetoacoustic wave behaviour within a separatrix dome containing a coronal null point. *Monthly Notices of the Royal Astronomical Society*, 484(1):1390–1400.

Microprocessor Standards Committee (2019). Ieee standard for floating-point arithmetic. *IEEE Std 754-2019 (Revision of IEEE 754-2008)*, pages 1–84.

Millas, D. (2022). Private Communication.

Mitchell, D. G., Brandt, P. C., Carbary, J. F., Kurth, W. S., Krimigis, S. M., Paranicas, C., Krupp, N., Hamilton, D. C., Mauk, B. H., Hospodarsky, G. B., Dougherty, M. K., and Pryor, W. R. (2015). Injection, interchange, and reconnection.

Mitchell, D. G., Carbary, J. F., Cowley, S. W. H., Hill, T. W., and Zarka, P. (2009). *The Dynamics of Saturn's Magnetosphere*, pages 257–279. Springer Netherlands.

Müller, J., Simon, S., Motschmann, U., Schüle, J., Glassmeier, K. H., and Pringle, G. J. (2011). A.i.k.e.f.: Adaptive hybrid model for space plasma simulations. *Computer Physics Communications*, 182:946–966.

Müller, D., St. Cyr, O. C., Zouganelis, I., Gilbert, H. R., Marsden, R., Nieves-Chinchilla, T., Antonucci, E., Auchère, F., Berghmans, D., Horbury, T. S., Howard, R. A., Krucker, S., Maksimovic, M., Owen, C. J., Rochus, P., Rodriguez-Pacheco, J., Romoli, M., Solanki, S. K., Bruno, R., Carlsson, M., Fludra, A., Harra, L., Hassler, D. M., Livi, S., Louarn, P., Peter, H., Schühle, U., Teriaca, L., del Toro Iniesta, J. C., Wimmer-Schweingruber, R. F., Marsch, E., Velli, M., De Groof, A., Walsh, A., and Williams, D. (2020). The solar orbiter mission - science overview. *Astronomy & Astrophysics*, 642:A1.

Narita, Y., Plaschke, F., and Vörös, Z. (2021). *The Magnetosheath*, chapter 9, pages 137–152. American Geophysical Union (AGU).

Nichols, J. D., Achilleos, N., and Cowley, S. W. H. (2015). A model of force balance in jupiter's magnetodisc including hot plasma pressure anisotropy. *Journal of Geophysical Research: Space Physics*, 120(12):10,185–10,206.

Northrop, T. G. (1961). The guiding center approximation to charged particle motion. *Annals of Physics*, 17:79–101.

Northrop, T. G. (1963). Adiabatic charged-particle motion. Technical Report UCRL-10750, Lawrence Berkeley National Laboratory.

Northrop, T. G. and Teller, E. (1960). Stability of the adiabatic motion of charged particles in the earth's field. *Physical Review*, 117:215–225.

Ofman, L., Viñas, A.-F., and Moya, P. S. (2011). Hybrid models of solar wind plasma heating. *Annales Geophysicae*, 29(6):1071–1079.

Ogino, T., Walker, R. J., and Kivelson, M. G. (1998). A global magnetohydrodynamic simulation of the jovian magnetosphere. *Journal of Geophysical Research: Space Physics*, 103(A1):225–235.

Olshevsky, V., Lapenta, G., and Markidis, S. (2013). Energetics of kinetic reconnection in a three-dimensional null-point cluster. *Physical Review Letters*, 111.

Opher, M., Loeb, A., Drake, J., and Toth, G. (2020). A small and round heliosphere suggested by magnetohydrodynamic modelling of pick-up ions. *Nature Astronomy*, 4(7):675–683.

Orton, G. S., Baines, K. H., Cruikshank, D., Cuzzi, J. N., Krimigis, S. M., Miller, S., and Lellouch, E. (2009). *Review of Knowledge Prior to the Cassini-Huygens Mission and Concurrent Research*, pages 9–54. Springer Netherlands.

Paranicas, C. P., Mauk, B. H., and Krimigis, S. M. (1991). Pressure anisotropy and radial stress balance in the jovian neutral sheet. *Journal of Geophysical Research: Space Physics*, 96(A12):21135–21140.

Parker, E. N. (1955). The formation of sunspots from the solar toroidal field. *Astrophysical Journal*, 121:491–507.

Parks, G. K., Lee, E., Yang, Z. W., Lin, N., Fu, S. Y., and Liu, Y. (2021). *Solar Wind Interaction with Earth's Bow Shock*, chapter 8, pages 123–135. American Geophysical Union (AGU).

Paty, C., Arridge, C. S., Cohen, I. J., DiBraccio, G. A., Ebert, R. W., and Rymer, A. M. (2020). Ice giant magnetospheres. *Philosophical Transactions of the Royal Society A: Mathematical, Physical and Engineering Sciences*, 378(2187).

Peng, I. B., Markidis, S., Laure, E., Johlander, A., Vaivads, A., Khotyaintsev, Y., Henri, P., and Lapenta, G. (2015a). Kinetic structures of quasi-perpendicular shocks in global particle-in-cell simulations. *Physics of Plasmas*, 22(9).

Peng, I. B., Markidis, S., Vaivads, A., Vencels, J., Amaya, J., Divin, A., Laure, E., and Lapenta, G. (2015b). The formation of a magnetosphere with implicit particle-in-cell simulations. *Procedia Computer Scence.*, 51:1178–1187.

Peng, I. B., Vencels, J., Lapenta, G., Divin, A., Vaivads, A., Laure, E., and Markidis, S. (2015c). Energetic particles in magnetotail reconnection. *Journal of Plasma Physics*, 81(2).

Persoon, A. M., Kurth, W. S., Gurnett, D. A., Faden, J. B., Groene, J. B., Morooka, M. W., Wahlund, J. E., Wilson, R. J., and Menietti, J. D. (2020). Distribution in saturn's inner magnetosphere from 2.4 to 10 rs: A diffusive equilibrium model. *Journal of Geophysical Research: Space Physics*, 125:1–15.

Pesnell, W. D., Thompson, B. J., and Chamberlin, P. C. (2012). The solar dynamics observatory (sdo). *Solar Physics*, 275(1-2):3–15.

Phipps, P. H., Withers, P., Vogt, M. F., Buccino, D. R., Yang, Y.-M., Parisi, M., Ranquist, D., Kollmann, P., and Bolton, S. (2020). Where is the io plasma torus? a comparison of observations by juno radio occultations to predictions from jovian magnetic field models. *Journal of Geophysical Research: Space Physics*, 125(8).

Piel, A. (2010). *Plasma Physics: An Introduction to Laboratory, Space, and Fusion Plasmas*. Springer Berlin, Heidelberg.

Pletcher, R. H. (2013). *Computational fluid mechanics and heat transfer*. CRC Press, 3rd ed. edition.

Pollock, C., C:son-Brandt, P., Burch, J., Henderson, M., Jahn, J.-M., McComas, D.J.and Mende, S., Mitchell, D., Reeves, G., Scime, E., Skoug, R., Thomsen, M., and Valek, P. (2020). The role and contributions of energetic neutral atom (ena) imaging in magnetospheric substorm research. *Space Science Reviews*, 109(1).

Pontius Jr., D. H. (1997). Radial mass transport and rotational dynamics. *Journal of Geophysical Research: Space Physics*, 102(A4):7137–7150.

Postberg, F., Schmidt, J., Hillier, J., Kempf, S., and Srama, R. (2011). A salt-water reservoir as the source of a compositionally stratified plume on enceladus. *Nature*, 474:620–622.

Press, W. H., Teukolsky, S. A., Vetterling, W. T., and Flannery, B. P. (2007). *Numerical Recipes: The Art of Scientific Computing*. Cambridge University Press, 3 edition.

Priest, E. (2014). *Magnetohydrodynamics of the Sun*. Cambridge University Press.

Pritchett, P. L. (2003). *Particle-in-Cell Simulation of Plasmas - A Tutorial*, pages 1–24. Springer Berlin Heidelberg, Berlin, Heidelberg.

Pucci, F., Viviani, M., Valentini, F., Lapenta, G., Matthaeus, W. H., and Servidio, S. (2021). Turbulent magnetogenesis in a collisionless plasma. *The Astrophysical Journal Letters*, 922(1).

Raeder, J. (2003). *Global Magnetohydrodynamics - A Tutorial*, pages 212–246. Springer Berlin Heidelberg, Berlin, Heidelberg.

Rajendar, A. (2015). *Multifluid Magnetohydrodynamic Investigation of the Global Dynamics of Saturn's Magnetosphere*. PhD thesis, Georgia Institute of Technology.

Ridley, A. J., De Zeeuw, D. L., and Rastätter, L. (2016). Rating global magnetosphere model simulations through statistical data-model comparisons. *Space Weather*, 14(10):819–834.

Riley, K. F., Hobson, M. P., and Bence, S. J. (2002). *Mathematical Methods for Physics and Engineering: A Comprehensive Guide*. Cambridge University Press, 2 edition.

Russell, C. T. (2000). The polar cusp. *Advances in Space Research*, 25(7):1413–1424.

Russell, C. T. (2003). *The Cassini-Huygens Mission: Overview, Objectives and Huygens Instrumentarium*, volume 1. Springer Dordrecht.

Russell, C. T., Khurana, K. K., Huddleston, D. E., and Kivelson, M. G. (1998). Localized reconnection in the near jovian magnetotail. *Science*, 280(5366):1061–1064.

Russell, C. T., Luhmann, J. G., and Strangeway, R. J. (2016). *Space Physics: An Introduction*. Cambridge University Press.

Rymer, A., Mauk, B., Hill, T., André, N., Mitchell, D., Paranicas, C., Young, D., Smith, H., Persoon, A., Menietti, J., Hospodarsky, G., Coates, A., and Dougherty, M. (2009). Cassini evidence for rapid interchange transport at saturn. *Planetary and Space Science*, 57(14):1779–1784.

Rymer, A. M. (2021). *Fast Rotating Magnetospheres*, chapter 30, pages 471–483. American Geophysical Union (AGU).

Saur, J., Mauk, B. H., Kaßner, A., and Neubauer, F. M. (2004). A model for the azimuthal plasma velocity in saturn's magnetosphere. *Journal of Geophysical Research: Space Physics*, 109(A5).

Saur, J., Neubauer, F. M., Connerney, J. E. P., Zarka, P., and Kivelson, M. G. (2004). *Plasma interaction of Io with its plasma torus*, chapter 22, pages 537–560. Cambridge University Press.

Saur, J., Schilling, N., Neubauer, F. M., Strobel, D. F., Simon, S., Dougherty, M. K., Russell, C. T., and Pappalardo, R. T. (2008). Evidence for temporal variability of enceladus' gas jets: Modeling of cassini observations. *Geophysical Research Letters*, 35(20).

Saur, J., Strobel, D. F., Neubauer, F. M., and Summers, M. E. (2003). The ion mass loading rate at io. *Icarus*, 163(2):456–468.

Sazykin, S. (2000). *Theoretical Studies of Penetration of Magnetospheric Electric Fields to the Ionosphere*. PhD thesis, University of Utah.

Schneider, N. M. and Bagenal, F. (2007). *Io's neutral clouds, plasma torus, and magnetospheric interaction*, chapter 11, pages 265–286. Springer Berlin Heidelberg.

Schriver, D. (2003). *Kinetic Simulation of Inhomogeneous Plasma with a Variable Sized Grid System*, pages 93–108. Springer Berlin Heidelberg, Berlin, Heidelberg.

Sciola, A., Sorathia, K., Wing, S., Delamere, P., Clark, G., Zhang, B., Ma, X., Mino, B., Neupane, B., Johnson, J., Damiano, P., Smith, A., Kaminker, V., and Coffin, D. (2022). Particle entry, escape, and energization at saturn through global convection and wind-magnetosphere interaction. Presented at the Magnetospheres of the Outer Planets Meeting.

Seidelmann, P. K. and Divine, N. (1977). Evaluation of jupiter longitudes in system iii (1965). *Geophysical Research Letters*, 4(2):65–68.

Shadowitz, A. (1975). *The Electromagnetic Field*. Dover Publications Inc.

Shi, C. (2018). Generalized ohm's law of a mhd plasma. `https://chenshihelio.github.io/notes/generalized_ohms_law.pdf`.

Shi, F., Lin, Y., Wang, X., Wang, B., and Nishimura, Y. (2021). 3-d global hybrid simulations of magnetospheric response to foreshock processes. *Earth, Planets and Space*, 73.

Shprits, Y. Y. and Thorne, R. M. (2004). Time dependent radial diffusion modeling of relativistic electrons with realistic loss rates. *Geophysical Research Letters*, 31(8).

Sibeck, D. G. and Murphy, K. R. (2021). *Large-Scale Structure and Dynamics of the Magnetosphere*, chapter 2, pages 15–36. American Geophysical Union (AGU).

Simon, S. (2019). Private Communication.

Siscoe, G. L. and Summers, D. (1981). Centrifugally driven diffusion of iogenic plasma. *Journal of Geophysical Research: Space Physics*, 86(A10):8471–8479.

Slavin, J. A., Imber, S. M., and Raines, J. M. (2021). *A Dungey Cycle in the Life of Mercury's Magnetosphere*, chapter 34, pages 535–556. American Geophysical Union (AGU).

Slavin, J. A., Smith, E. J., Spreiter, J. R., and Stahara, S. S. (1985). Solar wind flow about the outer planets: Gas dynamic modeling of the jupiter and saturn bow shocks. *Journal of Geophysical Research: Space Physics*, 90(A7):6275–6286.

Smith, A. G. and Carr, T. D. (1959). Radio-frequency observations of the planets in 1957-1958. *Astrophysical Journal*, 130:641–647.

Smith, H. T., Johnson, R. E., Perry, M. E., Mitchell, D. G., McNutt, R. L., and Young, D. T. (2010). Enceladus plume variability and the neutral gas densities in saturn's magnetosphere. *Journal of Geophysical Research: Space Physics*, 115(A10).

Somov, B. V. (2006). *Plasma Astrophysics, Part I: Fundamentals and Practice*. Springer New York, NY.

Sonnerup, B. U. O. and Laird, M. J. (1963). On magnetospheric interchange instability. *Journal of Geophysical Research (1896-1977)*, 68(1):131–139.

Sorathia, K. A., Merkin, V. G., Panov, E. V., Zhang, B., Lyon, J. G., Garretson, J., Ukhorskiy, A. Y., Ohtani, S., Sitnov, M., and Wiltberger, M. (2020). Ballooning-interchange instability in the near-earth plasma sheet and auroral beads: Global magnetospheric modeling at the limit of the mhd approximation. *Geophysical Research Letters*, 47(14).

Southwood, D. J. (2021). *A Brief History of the Magnetosphere*, chapter 1, pages 1–13. American Geophysical Union (AGU).

Southwood, D. J. and Kivelson, M. G. (1987). Magnetospheric interchange instability. *Journal of Geophysical Research*, 92:109.

Southwood, D. J. and Kivelson, M. G. (1989). Magnetospheric interchange motions. *Journal of Geophysical Research*, 94:299.

Spencer, J. (2013). Saturn's tides control enceladus' plume. *Nature*, 500:155–156.

Spencer, J. R. and Schneider, N. M. (1996). Io on the eve of the galileo mission. *Annual Review of Earth and Planetary Sciences*, 24(1):125–190.

Spilker, L. (2019). Cassini-huygens' exploration of the saturn system: 13 years of discovery. *Science*, 364(6445):1046–1051.

Stern, D. P. (1970). Euler potentials. *American Journal of Physics*, 38.

Strauss, R. D. T. (2019). Voyager 2 enters interstellar space. *Nature Astronomy*, 3(11):963–964.

Summers, D. and Siscoe, G. L. (1985). Coupled low-energy - ring current plasma diffusion in the jovian magnetosphere. *Journal of Geophysical Research: Space Physics*, 90(A3):2665–2671.

Summers, D., Thorne, R. M., and Mei, Y. (1988). Theory of centrifugally driven magnetospheric diffusion. *The Astrophysical Journal*, 328:358.

Swanson, D. G. (2003). *Plasma Waves*. Institute of Physics, 2 edition.

Swift, D. W. (1995). Use of a hybrid code to model the earth's magnetosphere. *Geophysical Research Letters*, 22(3):311–314.

Taylor, F. W., Atreya, S. K., Encrenaz, T., Hunten, D. M., Irwin, P. G. J., and Owen, T. C. (2004). *The composition of the atmosphere of Jupiter*, chapter 4, pages 59–78. Cambridge University Press.

Terasawa, T., Maezawa, K., and Machida, S. (1978). Solar wind effect on jupiter's non-io-related radio emission. *Nature*, 273(5658):131–132.

Thomas, N., Bagenal, F., Hill, T. W., and Wilson, J. K. (2004). *The Io neutral clouds and plasma torus*, chapter 23, pages 561–591. Cambridge University Press.

Thorne, R. M., Armstrong, T. P., Stone, S., Williams, D. J., McEntire, R. W., Bolton, S. J., Gurnett, D. A., and Kivelson, M. G. (1997). Galileo evidence for rapid interchange transport in the io torus. *Geophysical Research Letters*, 24:2131–2134.

Toffoletto, F., Sazykin, S., Spiro, R., and Wolf, R. (2003). Inner magnetospheric modeling with the rice convection model.

Toffoletto, F., Sazykin, S., Spiro, R., Wolf, R., and Lyon, J. (2004). Rcm meets lfm: initial results of one-way coupling. *Journal of Atmospheric and Solar-Terrestrial Physics*, 66(15):1361–1370.

Tokumaru, M., Kojima, M., and Fujiki, K. (2010). Solar cycle evolution of the solar wind speed distribution from 1985 to 2008. *Journal of Geophysical Research: Space Physics*, 115(A4).

Tóth, G., Chen, Y., Gombosi, T. I., Cassak, P., Markidis, S., and Peng, I. B. (2017). Scaling the ion inertial length and its implications for modeling reconnection in global simulations. *Journal of Geophysical Research: Space Physics*, 122(10):10,336–10,355.

Treumann, R. A. and Baumjohann, W. (1997). *Advanced space plasma physics*. Imperial College Press.

Tseng, W.-L., Johnson, R. E., Thomsen, M. F., Cassidy, T. A., and Elrod, M. K. (2011). Neutral h2 and h2+ ions in the saturnian magnetosphere. *Journal of Geophysical Research: Space Physics*, 116(A3).

van Heesch, D. (2022). Doxygen. https://www.doxygen.nl/index.html.

Vasyliunas, V. M. (2008). Comparing jupiter and saturn: dimensionless input rates from plasma sources within the magnetosphere. *Annales Geophysicae*, 26(6):1341–1343.

Vasyliunas, V. (2019). Observational constraints on theoretical description of plasma and magnetic flux transport in the io torus. Poster presented at the AGU FAll Meeting.

Vasyliunas, V. M. (1970). Mathematical models of magnetospheric convection and its coupling to the ionosphere. In *Particles and Fields in the Magnetosphere*, pages 60–71. Springer Netherlands.

Vasyliunas, V. M. (1975). Theoretical models of magnetic field line merging. *Reviews of Geophysics*, 13(1):303–336.

Vasyliunas, V. M. (1983). *Plasma distribution and flow*, pages 395–453. Cambridge Planetary Science. Cambridge University Press.

Vasyliūnas, V. M. (2009). *Fundamentals of planetary magnetospheres*, pages 256–294. Cambridge University Press.

Vogt, M. F., Connerney, J. E., DiBraccio, G. A., Wilson, R. J., Thomsen, M. F., Ebert, R. W., Clark, G. B., Paranicas, C., Kurth, W. S., Allegrini, F., Valek, P. W., and Bolton, S. J. (2020). Magnetotail reconnection at jupiter: A survey of juno magnetic field observations. *Journal of Geophysical Research: Space Physics*, 125(3).

Vogt, M. F., Kivelson, M. G., Khurana, K. K., Joy, S. P., and Walker, R. J. (2010). Reconnection and flows in the jovian magnetotail as inferred from magnetometer observations. *Journal of Geophysical Research: Space Physics*, 115(A6).

Vogt, R. E., Chenette, D. L., Cummings, A. C., Garrard, T. L., Stone, E. C., Schardt, A. W., Trainor, J. H., Lal, N., and McDonald, F. B. (1981). Energetic charged particles in saturn's magnetosphere: Voyager 1 results. *Science*, 212(4491):231–234.

Vogt, R. E., Chenette, D. L., Cummings, A. C., Garrard, T. L., Stone, E. C., Schardt, A. W., Trainor, J. H., Lal, N., and McDonald, F. B. (1982). Energetic charged particles in saturn's magnetosphere: Voyager 2 results. *Science*, 215(4532):577–582.

von Alfthan, S., Pokhotelov, D., Kempf, Y., Hoilijoki, S., Honkonen, I., Sandroos, A., and Palmroth, M. (2014). Vlasiator: First global hybrid-vlasov simulations of earth's foreshock and magnetosheath. *Journal of Atmospheric and Solar-Terrestrial Physics*, 120:24–35.

Williams, D. A. and Howell, R. R. (2007). *Active volcanism: Effusive eruptions*, pages 133–161. Springer Berlin Heidelberg.

Williams, D. J., McEntire, R. W., Jaskulek, S., and Wilken, B. (1992). The galileo energetic particles detector. *Space Science Reviews*, 60(1):385–412.

Williams, D. R. (2021a). Jupiter fact sheet. `https://nssdc.gsfc.nasa.gov/planetary/factsheet/jupiterfact.html`.

Williams, D. R. (2021b). Saturn fact sheet. `https://nssdc.gsfc.nasa.gov/planetary/factsheet/saturnfact.html`.

Wilson, R. J., Bagenal, F., and Persoon, A. M. (2017). Survey of thermal plasma ions in saturn's magnetosphere utilizing a forward model. *Journal of Geophysical Research: Space Physics*, 122:7256–7278.

Wilson, R. J., Tokar, R. L., and Henderson, M. G. (2009). Thermal ion flow in saturn's inner magnetosphere measured by the cassini plasma spectrometer: A signature of the enceladus torus? *Geophysical Research Letters*, 36(23).

Wilson, R. J., Tokar, R. L., Henderson, M. G., Hill, T. W., Thomsen, M. F., and Pontius Jr., D. H. (2008). Cassini plasma spectrometer thermal ion measurements in saturn's inner magnetosphere. *Journal of Geophysical Research: Space Physics*, 113(A12).

Winske, D. (1996). Regimes of the magnetized rayleigh-taylor instability. *Physics of Plasmas*, 3:3966–3974.

Winske, D. and Omidi, N. (1996). A nonspecialist's guide to kinetic simulations of space plasmas. *Journal of Geophysical Research: Space Physics*, 101(A8):17287–17303.

Winske, D., Yin, L., Omidi, N., Karimabadi, H., and Quest, K. (2003). *Hybrid Simulation Codes: Past, Present and Future - A Tutorial*, pages 136–165. Springer Berlin Heidelberg.

Wolf, R. A. (1983). The quasi-static (slow-flow) region of the magnetosphere.

Wolfe, J. H., Mihalov, J. D., Collard, H. R., McKibbin, D. D., Frank, L. A., and Intriligator, D. S. (1980). Preliminary results on the plasma environment of saturn from the pioneer 11 plasma analyzer experiment. *Science*, 207(4429):403–407.

Yang, Y. S., Wolf, R. A., Spiro, R. W., and Dessler, A. J. (1992). Numerical simulation of plasma transport driven by the io torus. *Geophysical Research Letters*, 19(10):957–960.

Yang, Y. S., Wolf, R. A., Spiro, R. W., Hill, T. W., and Dessler, A. J. (1994). Numerical simulation of torus-driven plasma transport in the jovian magnetosphere. *Journal of Geophysical Research*, 99.

Young, D. T., Berthelier, J.-J., Blanc, M., Burch, J. L., Bolton, S., Coates, A. J., Crary, F. J., Goldstein, R., Grande, M., Hill, T. W., Johnson, R. E., Baragiola, R. A., Kelha, V., McComas, D. J., Mursula, K., Sittler, E. C., Svenes, K. R., Szegö, K., Tanskanen, P., Thomsen, M. F., Bakshi, S., Barraclough, B. L., Bebesi, Z., Delapp, D., Dunlop, M. W., Gosling, J. T., Furman, J. D., Gilbert, L. K., Glenn, D., Holmlund, C., Illiano, J.-M., Lewis, G. R., Linder, D. R., Maurice, S., McAndrews, H. J., Narheim, B. T., Pallier, E., Reisenfeld, D., Rymer, A. M., Smith, H. T., Tokar, R. L., Vilppola, J., and Zinsmeyer, C. (2005). Composition and dynamics of plasma in saturn's magnetosphere. *Science*, 307(5713):1262–1266.

Yu, Z. J. and Russell, C. T. (2009). Rotation period of jupiter from the observation of its magnetic field. *Geophysical Research Letters*, 36(20).

Zhang, B., Delamere, P. A., Yao, Z., Bonfond, B., Lin, D., Sorathia, K. A., Brambles, O. J., Lotko, W., Garretson, J. S., Merkin, V. G., Grodent, D., Dunn, W. R., and Lyon, J. G. (2021). How jupiter's unusual magnetospheric topology structures its aurora. *Science Advances*, 7(15).

Zhang, B., Sorathia, K. A., Lyon, J. G., Merkin, V. G., Garretson, J. S., and Wiltberger, M. (2019). GAMERA: A three-dimensional finite-volume MHD solver for non-orthogonal curvilinear geometries. *The Astrophysical Journal Supplement Series*, 244(1):20.

Appendix A

JERICHO Variables

A.1 Constants

Variable	Variable Name in Model	Meaning	Units
R_P	R_J or R_S	Planetary radius	m
M_P	M_J or M_S	Planetary mass	kg
Ω_P	Omega	Planetary spin velocity	rad s^{-1}
$B_{eq,P}$	B_eq	Equatorial strength of planetary magnetic field	T
q_s	q_c	Charge of macroparticle	C
m_s	m	Mass of macroparticle	kg

A.2 Domain

Variable	Variable Name in Model	Meaning	Units
x_{min}	x_min	Position of minimum boundary in the x direction	m
x_{max}	x_max	Position of maximum boundary in the x direction	m
y_{min}	y_min	Position of minimum boundary in the y direction	m
y_{max}	y_max	Position of maximum boundary in the y direction	m
t_{min}	t_min	Point in time of model initialisation	s
t_{max}	t_max	Point in time of model completion	s
N_x	nx	Number of grid vertices in the x direction	-
N_y	ny	Number of grid vertices in the y direction	-
N_t	nt	Number of time steps	-
-	T_c	Total number of grid cells	-
N_{PPC}	PPC	Number of particles per cell	-
N_{TPPC}	T_PPC	Total number of macroparticles	-
Δx	dx	Distance between grid vertices in the x direction	m
Δy	dy	Distance between grid vertices in the y direction	m
Δt	dt	Size of the time step	s

x	x	Dimensional vector for the x coordinate	m
y	y	Dimensional vector for the y coordinate	m
t	t	Dimensional vector for t coordinate	s
E_x^{back}	E_x_back	x-component of the background electric field	V m^{-1}
E_y^{back}	E_y_back	y-component of the background electric field	V m^{-1}
B^{back}	B_z_back	Background magnetic field	T
B_{max}	B_max	Maximum strength of the magnetic field	T
$\omega_{g,max}$	gyro_freq	Maximum ion gyro frequency	rad s^{-1}
ρ	num_density	Number density of the initial plasma	m^{-2}
β_i	Beta_i	Ion plasma beta	-
v_A	v_A	Alfvén velocity	m s^{-1}
N_{NS}	smoothing_factor	Numerical smoothing factor	-
M_S	Macro_N	Macro number for weighting particles	-
v_{th}	v_th	Thermal velocity of plasma	m s^{-1}
T_p	T	Temperature of plasma	k

A.3 Modelled Field Parameters

Variable	Variable Name in Model	Meaning	Units
E_x^n	E_x_n	x-component of electric field at current time-step	V m^{-1}
E_y^n	E_y_n	y-component of electric field at current time-step	V m^{-1}
E_x	E_x_new	x-component of newly calculated electric field	V m^{-1}
E_y	E_y_new	y-component of newly calculated electric field	V m^{-1}
E_x^{mix}	E_x_mix	x-component of electric field at mixed CAM time-step	V m^{-1}
E_y^{mix}	E_y_mix	y-component of electric field at mixed CAM time-step	V m^{-1}
$E_x^{n+\frac{1}{2}}$	E_x_phalf	x-component of electric field advanced half a time-step	V m^{-1}
$E_y^{n+\frac{1}{2}}$	E_y_phalf	y-component of electric field advanced half a time-step	V m^{-1}
B^n	B_z_n	Magnetic field at current time-step	V m^{-1}
B_{ind}^n	B_z_ind_n	Induced component of magnetic field at current time-step	T
$B_{ind}^{n+\frac{1}{2}}$	B_z_ind_n_phalf	Induced component of magnetic field advanced half a time-step	T
$B_{ind}^{n-\frac{1}{2}}$	B_z_ind_n_mhalf	Induced component of magnetic field at previous half time-step	T
$B^{n+\frac{1}{2}}$	B_z_n_phalf	Magnetic field advanced half a time-step	T
J_x^n	J_x_n	x-component of current density at current time-step	A m^{-2}
J_y^n	J_y_n	y-component of current density at current time-step	A m^{-2}

J_x^-	J_x_minus	x-component of current density at mixed CAM time-step	A m^{-2}
J_y^-	J_y_minus	y-component of current density at mixed CAM time-step	A m^{-2}
J_x^+	J_x_plus	x-component of current density at mixed CAM time-step	A m^{-2}
J_y^+	J_y_plus	y-component of current density at mixed CAM time-step	A m^{-2}
$\rho_{c,i}^n$	q_grid_n	Ion charge density at current time-step	C m^{-2}
$\rho_{c,i}^{n+\frac{1}{2}}$	q_grid_n_phalf	Ion charge density advanced half a time-step	C m^{-2}
$\rho_{c,i}^{n+1}$	q_grid_n_pone	Ion charge density advanced a time-step	C m^{-2}
U_x^n	U_x_n	x-component of ion flow velocity at current time-step	m s^{-1}
U_y^n	U_y_n	y-component of ion flow velocity at current time-step	m s^{-1}
$U_x^{n+\frac{1}{2}}$	U_x_n_phalf	x-component of ion flow velocity advanced half a time-step	m s^{-1}
$U_y^{n+\frac{1}{2}}$	U_y_n_phalf	y-component of ion flow velocity advanced half a time-step	m s^{-1}
$U_x^{n-\frac{1}{2}}$	U_x_n_mhalf	x-component of ion flow velocity at previous half time-step	m s^{-1}
$U_y^{n-\frac{1}{2}}$	U_y_n_mhalf	y-component of ion flow velocity at previous half time step	m s^{-1}
U_x^-	U_x_minus	x-component of ion flow velocity at mixed CAM time-step	m s^{-1}
U_y^-	U_y_minus	y-component of ion flow velocity at mixed CAM time-step	m s^{-1}
U_x^+	U_x_plus	x-component of ion flow velocity at mixed CAM time-step	m s^{-1}
U_y^+	U_y_plus	y-component of ion flow velocity at mixed CAM time-step	m s^{-1}
Λ^{n+1}	Lambda_n_pone	Moment gathered for CAM method	C^2 kg^{-1}
Γ_x^{n+1}	Gamma_x_n_pone	x-component of moment gathered for CAM method	C^2 m kg^{-1} s^{-1}
Γ_y^{n+1}	Gamma_y_n_pone	y-component of moment gathered for CAM method	C^2 m kg^{-1} s^{-1}

A.4 Modelled Particle Parameters

Variable	Variable Name in Model	Meaning	Units
B_p	B_z	Magnetic field strength at particle location	T
$E_{x,p}$	E_x	x-component of electric field at particle location	V m^{-1}
$E_{y,p}$	E_y	y-component of electric field at particle location	V m^{-1}
h	h	see eqn 5.8	-

α	alpha	see eqn 5.7	-
k	k	see eqn 5.6	-
$v_{x,p}^{n+\frac{1}{2}}$	v_x_n_phalf	x-component of particle at half-integer time-step	m s^{-1}
$v_{y,p}^{n+\frac{1}{2}}$	v_y_n_phalf	y-component of particle at half-integer time-step	m s^{-1}
x_i	x_i	x index of grid cell particle occupies	-
y_i	y_i	y index of grid cell particle occupies	-
-	hx	Distance of particle from x location of grid cell	m
-	hy	Distance of particle from y location of grid cell	m
$f_{i,j}$	f_ij	Weight factor for grid cell (i, j) for moment gathering	-
$f_{i+1,j}$	f_i1j	Weight factor for grid cell $(i + 1, j)$ for moment gathering	-
$f_{i+1,j+1}$	f_i1j1	Weight factor for grid cell $(i + 1, j + 1)$ for moment gathering	-
$f_{i,j+1}$	f_ij1	Weight factor for grid cell $(i, j + 1)$ for moment gathering	-

Appendix B

Ion Equation of Motion in a Rotating Reference Frame

The equation to obtain the motion of particles in a 2.5D rotational reference frame (described in §5) can be worked though to the following state with little rigorous mathematical effort required,

$$\underline{v}^{n+\frac{1}{2}} - \frac{q\Delta t}{m}\left[\underline{v}^{n+\frac{1}{2}} \times \left(\frac{1}{2}\underline{B}^n + \frac{m}{q}\underline{\Omega}\right)\right] =$$
$$\underline{v}^{n-\frac{1}{2}} + \frac{q\Delta t}{m}\left[\underline{E}^n + \underline{v}^{n-\frac{1}{2}} \times \left(\frac{1}{2}\underline{B}^n + \frac{m}{q}\underline{\Omega}\right)\right] + \Delta t\left(\left|\underline{\Omega}\right|^2 \underline{x}^n - \frac{GM_p\underline{x}^n}{\left|\underline{x}^n\right|^3}\right).$$

It is possible given this to obtain the final form of the equation, contained in eqns 5.5, 5.6, 5.7, 5.8, readily. However, a substantial amount of rearranging is required to obtain this final form of the particles equation of motion. Here, the operations required to perform this rearrangement are detailed.

Examining this form of the equation of motion in component form, in 2.5D [i.e. $\underline{v} = (v_x, v_y, 0)$, $\underline{x} = (x, y, 0)$, $\underline{E} = (E_x, E_y, 0)$, $\underline{B} = (0, 0, B_z)$, $\Omega = (0, 0, \Omega)$], we can first attempt to isolate $v_x^{n+\frac{1}{2}}$ in the x domain. This yields,

$$v_x^{n+\frac{1}{2}} - \frac{q\Delta t}{m} v_y^{n+\frac{1}{2}}\left(\frac{1}{2}B_z^n + \frac{m}{q}\Omega_z\right) =$$
$$v_x^{n-\frac{1}{2}} + \frac{q\Delta t}{m}\left[E_x^n + v_y^{n-\frac{1}{2}}\left(\frac{1}{2}B_z^n + \frac{m}{q}\Omega_z\right)\right] + \Delta t\left[\left|\Omega\right|^2 x^n - \frac{GM_p}{(x^n)^2}\right],$$

$$v_x^{n+\frac{1}{2}} = v_x^{n-\frac{1}{2}}$$
$$+\frac{q\Delta t}{m}\left[E_x^n + \left(v_y^{n+\frac{1}{2}} + v_y^{n-\frac{1}{2}}\right)\left(\frac{1}{2}B_z^n + \frac{m}{q}\Omega_z\right)\right] + \Delta t\left[\left|\Omega\right|^2 x^n - \frac{GM_p}{(x^n)^2}\right].$$

However, although $v_x^{n+\frac{1}{2}}$ has been successfully isolated, this solution is impractical for use as it is reliant on knowing $v_y^{n+\frac{1}{2}}$. If this process is repeated to isolate $v_y^{n+\frac{1}{2}}$ in the y domain, it is found that this solution is simultaneously dependant on $v_x^{n+\frac{1}{2}}$. Hence, using our usual mathematical toolkit one must plug one solution into the other to remove this dependency.

Therefore, it is necessary to rearrange to isolate $v_y^{n+\frac{1}{2}}$,

$$v_y^{n+\frac{1}{2}} = v_y^{n-\frac{1}{2}}$$
$$+\frac{q\Delta t}{m}\left[E_y^n - \left(v_x^{n+\frac{1}{2}} + v_x^{n-\frac{1}{2}}\right)\left(\frac{1}{2}B_z^n + \frac{m}{q}\Omega_z\right)\right] + \Delta t\left[\left|\Omega\right|^2 y^n - \frac{GM_p}{(y^n)^2}\right].$$

Examining the isolated forms of $v_x^{n+\frac{1}{2}}$ & $v_y^{n+\frac{1}{2}}$ above, then it can be seen them the EM term on the RMS are now simplified by using the definitions made in eqns 5.7 & 5.7. Using these gives,

$$\begin{aligned} v_x^{n+\frac{1}{2}} &= v_x^{n-\frac{1}{2}} + h\left[E_x^n + \left(v_y^{n+\frac{1}{2}} + v_y^{n-\frac{1}{2}}\right)\alpha\right] + \Delta t\left[|\Omega|^2 x^n - \frac{GM_p}{(x^n)^2}\right], \\ v_y^{n+\frac{1}{2}} &= v_y^{n-\frac{1}{2}} + h\left[E_y^n - \left(v_x^{n+\frac{1}{2}} + v_x^{n-\frac{1}{2}}\right)\alpha\right] + \Delta t\left[|\Omega|^2 y^n - \frac{GM_p}{(y^n)^2}\right]. \end{aligned}$$

Now, substituting $v_y^{n+\frac{1}{2}}$ into $v_x^{n+\frac{1}{2}}$,

$$\begin{aligned} v_x^{n+\frac{1}{2}} &= v_x^{n-\frac{1}{2}} \\ &+h\left\{E_x^n + \left[\left(v_y^{n-\frac{1}{2}} + h\left[E_y^n - \left(v_x^{n+\frac{1}{2}} + v_x^{n-\frac{1}{2}}\right)\alpha\right] + \Delta t\left[|\Omega|^2 y^n - \frac{GM_p}{(y^n)^2}\right]\right) + v_y^{n-\frac{1}{2}}\right]\alpha\right\} \\ &+\Delta t\left[|\Omega|^2 x^n - \frac{GM_p}{(x^n)^2}\right]. \end{aligned}$$

Expanding and cancelling terms leaves,

$$\begin{aligned} v_x^{n+\frac{1}{2}} + h^2\alpha^2 v_x^{n+\frac{1}{2}} &= v_x^{n-\frac{1}{2}} - h^2\alpha^2 v_x^{n-\frac{1}{2}} + hE_x^n + 2h\alpha v_y^{n-\frac{1}{2}} + h^2\alpha E_n^2 \\ &+\Delta t\,|\Omega|^2 x^n + \Delta th\alpha\,|\Omega|^2 y^n - \Delta t\frac{GM_P}{(x^n)^2} - \Delta t\,h\alpha\frac{GM_P}{(y^n)^2}. \end{aligned}$$

Grouping alike terms together allows for this to be simplified further. It is also noted here that isolating $v_x^{n+\frac{1}{2}}$ on the LHS by removing it as a common factor yields the substitution given in eqn 5.6. Hence,

$$\begin{aligned} v_x^{n+\frac{1}{2}} = K\Bigg\{&\left(1-h^2\alpha^2\right)v_x^{n-\frac{1}{2}} + h\left(E_x^n + 2\alpha v_y^{n-\frac{1}{2}}\right) + h^2\alpha E_y^n \\ &+\Delta t\,|\Omega|^2\left(x^n + h\alpha y^n\right) - \Delta tGM_P\left[\frac{1}{(x^n)} + \frac{h\alpha}{(y^n)^2}\right]\Bigg\}. \end{aligned}$$

It is also possible to substitute $v_x^{n+\frac{1}{2}}$ into $v_y^{n+\frac{1}{2}}$ and rearrange using the same steps as above. This yields,

$$\begin{aligned} v_y^{n+\frac{1}{2}} = K\Bigg\{&\left(1-h^2\alpha^2\right)v_y^{n-\frac{1}{2}} + h\left(E_y^n - 2\alpha v_x^{n-\frac{1}{2}}\right) - h^2\alpha E_x^n \\ &+\Delta t\,|\Omega|^2\left(y^n - h\alpha x^n\right) - \Delta tGM_P\left[\frac{1}{(y^n)} - \frac{h\alpha}{(x^n)^2}\right]\Bigg\}. \end{aligned}$$

Using the pair of solutions determined above it is possible to find the generalised solution for the particles' equation of motion in 2.5D with the gravitational term retained,

$$\begin{aligned} \underline{v}^{n+\frac{1}{2}} = K\Bigg\{&\left(1-h^2\alpha^2\right)\underline{v}^{n-\frac{1}{2}} + h\left[\underline{E}^n + 2\alpha\left(\underline{v}^{n-\frac{1}{2}} \times \hat{\underline{z}}\right)\right] + h^2\alpha\left(\underline{E}^n \times \hat{\underline{z}}\right) \\ &+\Delta t\,|\underline{\Omega}|^2\left[\underline{x}^n + (\underline{x}^n \times h\alpha\hat{\underline{z}})\right] - \Delta tGM_P\left[\frac{\underline{x}^n}{|\underline{x}^n|^2} + \left(\frac{\underline{x}^n}{|\underline{x}^n|^3} \times h\alpha\hat{\underline{z}}\right)\right]\Bigg\}. \end{aligned}$$